Export and lateral advection of organic matter within the biological carbon pump

Dissertation

zur Erlangung des akademischen Grades eines Doktors der Naturwissenschaften

-Dr. rer. nat.-

im Fachbereich Geowissenschaften der Universität Bremen

Vorgelegt von

Steffen Swoboda

Bremen, Juli 2022

Bremen

marum
Center for Marine
Environmental Sciences
University of Bremen

Die vorliegende Dissertation wurde im Zeitraum von Januar 2019 bis Juli 2022 an der Universität Bremen durchgeführt. Die Ergebnisse der Arbeit wurden am MARUM – Zentrum für Marine Umweltwissenschaften im Rahmen des Exzellenzcluster „Der Ozeanboden – unerforschte Schnittstelle der Erde“ in der Arbeitsgruppe „Receiver“, und dem Fachbereich der Geowissenschaften erarbeitet.

Erstgutachter: Prof. Dr. Morten Hvitfeldt Iversen

Zweitgutachter: Prof. Dr. Lars Stemmann

Datum des Prüfungskolloquiums: 09.09.2022

„…Dass ich nicht mehr mit saurem Schweiß
Zu sagen brauch was ich nicht weiß;
Dass ich erkenne, was die Welt
Im Innersten zusammenhält…“

“…And thus the bitter task forego
Of saying the things I do not know;
That I may detect the inmost force
Which binds the world, and guides its course…”

Johann Wolfgang von Goethe

Table of Contents

Summary

The biological carbon pump (BCP) exports organic carbon from the surface to the deep ocean through which it drives the oceanic carbon storage of atmospheric CO_2. The majority of this exported carbon is mediated by sinking marine particles, which are mostly formed by primary producers i.e. phytoplankton, and detrital material including dead zoo- and phytoplankton as well as fecal pellets. The efficiency at which these marine particles are exported is largely dependent on the interplay between their degradation and the duration the particles settle through the water column. Particle and aggregate degradation is largely driven by attached microbes and zooplankton grazing, which is most prominent in the upper few hundred meters of the water column. Settling velocities of particles or aggregates are largely determined by their density and thus composition. Therefore, fast settling aggregates or particles sink more rapidly through the upper water column, which increases the efficiency for carbon export. The incorporation of ballasting components, such as sediments or minerals, during particle aggregation may increase the size-specific settling velocities of the aggregates and are thus an important process for carbon export via the biological pump. The manuscripts within this dissertation focus on the impact of aggregate morphology and ballasting on settling velocities and how carbon export is mediated by slow versus fast settling aggregates. We investigated the horizontal relocation of slow vs. fast settling aggregates in form of particle clouds, aggregate ballasting through the incorporation of minerals and the role of the aggregate microstructure on settling.

In **Manuscript I** we developed a method for the observation of the internal and external structure of marine snow which is crucial for the understanding of its settling behaviour and exchange rates of solutes with the surrounding environment. Due to its small size and fragile nature, small scale observations of marine snow have been restricted to a resolution of whole aggregates without the possibility to observe three-dimensional structures within single aggregates, e.g. micropores, channels or hollow spaces. In this project we use magnetic resonance imaging to develop a three-dimensional imaging method that can visualize surface

and internal microstructures within individual aggregates. For the first time, we are able to visualize the three-dimensional internal and external structure of an aggregate. These observations indicate that commonly used approaches to derive aggregate sizes and volume using geometric model shapes such as an ellipsoid, underestimate true aggregate sizes. Using a flow model, we compared the effect of the aggregate shape with ellipsoid and spherical model shapes to observe differences in settling behaviour. Surface vorticity fields on the aggregate were more pronounced as for model shapes. Generated drag forces by the aggregate were over a magnitude larger as for the model shapes. Despite the occurrence of connecting channels in the aggregate pore space, we did not observe any indications for internal flow by our flow model. Our results suggest that current parameterizations of particle size may bias estimations of microbial degradation and settling velocity of aggregates. This may have large implications for current estimations of carbon export via the biological pump.

In **Manuscript II**, we combined inter-annual and -seasonal flux measurements between 1989 - 2017 with a ship-based process study from 2019 to deduce forcing factors for the formation of shelf produced particle clouds and their contribution to deep ocean carbon export in the Canary current-EBUS (CC-EBUS). Our results from deep ocean carbon fluxes show that particle clouds formed at the continental shelf continuously supply 4.2 - 6.0 times more carbon than vertically exported local surface primary production. Microscopic observations and measured size and settling velocities imply that mineral ballasting of offshore advected particles and aggregates drives the formation of a fast-settling benthic particle cloud while non-ballasted particles and aggregates form a slower settling intermediate particle cloud. These observations suggest that common approaches that only consider vertical downward movement of settling particles and aggregates are prone to overestimate carbon flux and turnover by not including the contribution of horizontal advected slow settling particles and aggregates throughout the water column. The recognition of horizontal advected particle clouds in modelling efforts will thus help improve our ability to accurately quantify carbon export and sequestration via the biological pump.

In **Manuscript III**, we describe the role of sea-ice mediated aggregate ballasting as driver for carbon export in the vicinity of the ice-edge in the Arctic. By combining 13-years of continuous

flux measurements with benthic eDNA analysis, laboratory-based ballasting experiments and sea-ice distributions, we show that the release of cryogenic gypsum and terrigenous material from melting sea-ice ballasts organic matter in the water column, which enhances carbon export. The ballasting experiments showed that size-specific aggregate settling velocities where up to 10-fold higher that non-ballasted aggregates, which resulted in >30% higher carbon export at the ice-edge. Further, eDNA samples from the sea-floor showed that the slow settling phytoplankton genus *Phaeocystis* spp., which generally does not contribute significantly to carbon export, was efficiently exported to the sea floor in sea-ice associated areas. As cryogenic gypsum is primarily formed in first-year sea-ice, its effect on aggregate ballasting is expected to continue as long as phytoplankton phenology matches the distribution of sea-ice. However, the flux of terrigenous material continuously decreased over the past decades and is expected to cease with progressing sea-ice loss since the future Arctic sea-ice is projected to be formed in the open ocean and not on the Siberian shelf where terrigenous sediment is incorporated into the ice. We therefore expect that the ongoing loss of sea-ice with global warming will limit aggregate ballasting and thus reduce carbon export in the future Arctic Ocean.

Zusammenfassung

Die biologische Kohlenstoffpumpe exportiert organischen Kohlenstoff von der Ozean Oberfläche in die Tiefsee, und treibt somit die Speicherung von atmosphärischem CO2 in den Ozeanen an. Der Großteil des organischen Kohlenstoffs wird in Form von sinkenden Partikeln exportiertet, welche aus Bestandteilen der Primärproduktion in der Wasseroberfläche bestehen, wie etwa Algen und Detritus welches z.b. aus totem Phyto-, Zooplankton oder Kotballen bestehet. Die Effizienz mit der diese Partikel exportiert werden ist in großem Maße abhängig von der Partikelsinkgeschwindigkeit und der Abbaurate. Der Abbau von Partikeln geschieht Großteiles im oberen Teil der Wassersäule und wird durch mikrobiellen Abbau und Zooplankton Fraß verursacht. Die Sinkgeschwindigkeit der Partikel ist wiederum hauptsächlich von der Partikeldichte aber auch der Morphologie und somit der Zusammensetzung abhängig. Somit führen schnell absinkende Partikel zu einem verhältnismäßig geringen Abbau, da die Partikel schnell aus dem oberen Teil der Wassersäule sinken. Das Einbauen von Ballastmaterialien wie z.b. Sedimente oder Mineralien, kann die Sinkgeschwindigkeiten von Partikeln erhöhen und ist somit ein wichtiger Faktor der den Export von Kohlenstoff über die Biologische Pumpe beeinflusst. Die Studien innerhalb der vorgelegten Dissertation beziehen sich deshalb auf die Morphologie von Partikeln, den Einfluss durch das Beschweren über Ballastmaterialien und Unterschiede zwischen dem Export von Kohlenstoff durch langsam und schnell absinkende Partikel. Hierfür untersuchten wir den horizontalen Transport von schnell und langsam absinkenden „Partikelwolken“, das beschweren von Partikeln durch die Integration von Mineralien, und den Einfluss der internen und externen Mikrostruktur von Partikeln auf ihre Sinkgeschwindigkeit und Aggregationspotential.

In **Manuskript I** entwickelten wir eine Methode zur Darstellung von internen und äußeren Strukturen von marinen Partikeln, welches essentiell für das Verständnis und die Vorhersage von Partikelsinkgeschwindigkeiten und austauschraten von gelösten Stoffen mit der Umgebung ist. Durch ihre kleine Größe und fragilem Aufbau sind Untersuchungen von marinen Partikeln limitiert auf ganze Partikel, ohne die Möglichkeit die internen Porenstrukturen aus Tunnel und Hohlräumen mit einzubeziehen. In diesem Projekt ist uns als erste gelungen eine Methode zu entwickeln um die interne und äußere Struktur inklusive von Poren mit Hilfe von Magnetresonanztomographie dreidimensional darzustellen. Unsere Beobachtungen deuten darauf hin das regulär verwendete Methoden zur Bestimmung der Größe von Partikeln mithilfe von geometrischen Formen wie z.b. einer Ellipse, fehlerbehaftet sind. Mithilfe eines Strömungsmodels, verglichen wir den Einfluss der Form von dem Partikel mit elliptischen und sphärischen geometrischen Formen um den Einfluss der Struktur auf das sinkverhalten festzustellen. Die Wirbelstärke im Fluss über der Oberfläche des Partikels war stärker ausgeprägt als bei den geometrischen Formen. Der generierte Strömungswiederstand des Partikels war um das 10-fache erhöht im Vergleich zu den geometrischen Formen. Trotz der Präsenz von Tunnelstrukturen durch den Partikel, haben wir keine Indizien für internen Fluss über unser Model feststellen können. Unsere Ergebnisse deuten darauf hin das regulär verwendete Methoden zur Parametrisierung von Partikelgrößen, Annahmen zu Abbauraten und Partikelsinkgeschwindigkeiten verfälschen könnten. Diese Beobachtungen könnte weitreichende Implikationen für aktuelle Schätzungen zum Export von Kohlenstoff über die Biologische Pumpe haben.

Im **Manuskript II** kombinierten wir jährliche und saisonale Kohlenstoff Export Messungen zwischen 1989 und 2017 im Auftriebsgebiet vor Westafrika mit einer schiffsbasierten Prozessstudie aus dem Jahre 2019, um die vorherrschenden Faktoren für die Bildung von Partikelwolken zu identifizieren und ihren Anteil am Kohlenstoffexport in der Tiefsee zu bestimmen. Unsere Ergebnisse haben gezeigt, dass der Anteil vom Kohlenstoffexport über lateral eingetragene Partikelwolken den vom vertikalen Export aus der Oberfläche um das 4.2-6.0 fache übersteigt. Ergebnisse von Mikroskop-basierten Beobachtungen und Messungen von Partikelgrößen und Sinkgeschwindigkeiten zeigen, dass der Einbau von Mineralien Partikel beschwert und somit zur Bildung von schnell sinkenden Partikelwolken führt, während Partikel die nicht beschwert wurden langsam sinkende Partikelwolken bildeten. Unsere Beobachtungen deuten darauf hin, das gängige Methoden zur Bestimmung vom Kohlenstoffexport dazu neigen den Kohlenstoffexport und Abbauraten zu überschätzen, da in diesen der Eintrag von lateralem material nicht berücksichtigt wird. Das integrieren von lateralem Kohlenstoffeintrag über Partikelwolken in Modellen zur Bestimmung des

Kohlenstoffexports ist somit ein wichtiger Schritt um den Kohlenstoffexport und die darauffolgende Sequestrierung über die Biologische Pumpe bestimmen zu können.

Im **Manuskript III** beschreiben wir, wie die Freisetzung von eingeschlossenem Material aus schmelzendem Meereis den Kohlenstoffexport entlang der Meereiskante in der Arktis antreibt. Durch die Kombination von 13-jahre andauernden Kohlenstoffexport Messungen mit benthischen e-DNA Analysen, Laborexperimenten zur Beschwerung von Partikeln und Daten zur Meereisausdehnung, zeigen wir das die Freisetzung von kryogenem Gips und terrigenem Material, Partikel in der Wassersäule beschweren und somit den Kohlenstoffexport erhöht. Die Experimente zur Beschwerung von Partikeln zeigten das aufgenommenes Material die Partikelsinkgeschwindigkeiten um das 10-fache erhöhen. Dies spiegelte sich in einem 30% höheren Kohlenstoffexport in der Nähe der Meereiskante wider. Des weiteren haben benthische e-DNA Analysen gezeigt das die Alge *Phaeocystis* spp. in Regionen mit regelmäßiger Meereisbedekung bis zum Meeresboden gesunken ist, obwohl diese dafür bekannt ist durch ihre langsame Sinkgeschwindigkeit nicht nennenswert zum Kohlenstoffexport in tiefere Wasserschichten beizutragen. Mit Bezug auf dem Klimawandel erwarten wir, dass, solange die Phänologie der frühjährlichen Planktonblüte mit dem Beginn der Meereisschmelze übereinstimmt, das Freisetzen von kryogenem Gips Partikel in der Wassersäule beschweren wird. Jedoch zeigten die Exportmessung das mit der fortschreitenden Reduktion der Meereisausdehnung der Einschluss und somit das freisetzen von terrigenem Material aus Meereis sich immer weiter reduziert. Wir erwarten somit, dass die beständige Reduktion der Meereisbedeckung durch den Klimawandel den Kohlenstoffexport im Arktischen Ozean reduzieren wird.

Introduction

Marine carbon pumps

Carbon transfer between the global carbon reservoirs

The global carbon cycle describes the transfer of carbon within and between the four main global carbon reservoirs, including the land, atmosphere, geological reserves i.e. fossil fuels and the ocean (Houghton 2014). Carbon transfer between the main carbon reservoirs occurs through a multitude of abiotic and biotic processes in which carbon is transferred as a "carbon flux". Whenever a net influx of carbon to a is higher than its release, it is considered a "carbon sink".

From the four major carbon reservoirs, the ocean is a key component in the regulation of the global climate through a net influx of atmospheric CO_2, thus acting as a net carbon sink (Lal 2008). The net ocean influx of atmospheric CO_2 at the air-sea interface is driven by a gradient of a higher CO_2 partial pressure (pCO_2) in the atmosphere which leads to an accumulation of dissolved inorganic carbon (DIC) in the surface ocean (Volk and Hoffert 1985). This gradient is maintained by "carbon pumps" which actively transport DIC from the surface ocean to the ocean interior. Therefore, the oceans carbon pumps are a driving force that regulate atmospheric CO_2 concentrations and thus the global climate.

Carbon pumps in the ocean

The ocean carbon pumps are distinguished in the solubility pump and the biological pump. The solubility pump is based on the increase of seawater density and CO_2 solubility with colder water temperatures. As part of the global ocean circulation, commonly referred to as the global conveyer belt, relatively cold DIC enriched surface water sinks into the ocean interior at high latitudes which leads to the formation of DIC enriched deep water.

In contrast, the biological pump exports carbon from the ocean surface into its interior in form of particulate organic carbon (POC). The accumulated DIC in the surface ocean is transformed into POC through photosynthesis by marine autotrophs, in particular marine phytoplankton. When phytoplankton collide, they may stick together, aggregate and form what is referred to as "marine aggregate". If the equivalent spherical diameter of such a marine aggregates is larger than 500 µm, it may also be termed "marine snow". Together with "fecal pellets" which are excreted from heterotrophs e.g., zooplankton, these two marine particle types transport the assimilated DIC as POC into the ocean interior and thus drive the uptake of atmospheric CO_2 in the surface ocean.

Combined, the solubility pump and the biological pump drive an estimated total CO_2 uptake of ~ 92.5 Gt C year^{-1} from the atmosphere, which amounts to ~25 Gt of carbon per year (Lal et al. 2008). However, the contribution of the biological pump to the transfer of DIC to the deep ocean is estimated to cover ~ 70% of the total carbon export (Passow & Carlson 2012). Therefore, the biological pump accounts for the majority of carbon export to the deep ocean and thus CO_2 regulation of the global atmosphere.

Mechanisms of particle transport in the biological pump

The export of marine POC is mediated by varying export pathways including abiotic and biotic processes (Boyd et al. 2019). Approximately 6.5 ± 2.5 Gt of the global POC export can be attributed to gravitational settling i.e. the particle density is higher as that of the surrounding water. In addition, 4 ± 3.5 Gt of global POC export is suggested to be partly mediated by so called particle-injection pumps (PIP) that actively transport particles to greater depth. However, as PIP export settling- as well as suspended particles, a unknown fraction of carbon export mediated by PIP can also be accounted to export via gravitational settling. The combined total export of approximately 17 Gt is therefore likely an overestimation due to double accounting. The underlying processes to these PIP include 5 different mechanisms of which 3 are physical and 2 biological based. Physical based mechanisms include: (I) the mixed-layer pump, which is driven by the accumulation of marine aggregates and particles in summer months and subsequently diluted as the mixed layer depth increases during winter. In the following spring, only a fraction of the diluted particles is reintroduced into the mixed layer with the onset of surface stratification. (II) The large scale subduction pump which covers the passive transport of marine aggregates and particles along the global conveyer belt and (III) the eddy-subduction pump which subducts surface waters on scales of up to 10 km by vertical circulation in eddy fronts. The biological based mechanisms include: (IV) the mesopelagic migrant pump which describes the excretion of fecal pellets from vertically migrating zooplankton in deeper water layers and (V) the seasonal lipid pump which describes the respiration of lipid reserves from hibernating zooplankton in deep water layers. Therefore, POC export via the biological pump is mediated by a combination of factors, including the particles density, the prevailing biota and the physical conditions of the water column.

Carbon remineralisation of exported particles

From the estimated global net primary production of 50 Gt C year^{-1} (Steinberg & Landry 2017), the suggested carbon export of the biological pump is 6-17 Gt C year^{-1} of which approx. 0.66 GT C year^{-1} reaches 2000 m depth or greater (Boyd et al. 2019, Henson et al. 2012). Therefore, carbon fluxes in the water column generally decrease with increasing depth. This strong attenuation of POC export is due to zooplankton grazing and microbial remineralisation.

Zooplankton grazing occurs predominantly in the upper few hundred meters of the water column (Jackson & Checkley 2011, Iversen et al. 2010). In addition, marine particles are hotspots for microbial activity (Azam et al. 1993, Thiele et al. 2019, Arnosti et al. 2011) which degrade particles and thus reduce POC export while settling through the water column. As a result, POC attenuation is suggested to reduce export flux by 30 - 80% within the top 100 m (Buessler et al. 2020) and only an estimated 1 - 10% of primary production is exported to a depth of ≥ 2000 m (Henson et al. 2012).

Depth dependent sequestration efficiency of exported carbon

The sequestration timescale of the exported POC is determined by the duration until the exported POC is relocated back to the surface ocean. Therefore, a greater export depth leads to a higher sequestration efficiency (Passow & Carlson 2012, Boyd et al. 2019). Estimations for the sequestration time of a given export depth are highly variable e.g. for an export depth of 1000 m, the estimated sequestration timescale ranges between 100 years (Passow & Carlson 2012) and 300 – 400 (Boyd et al. 2019) years. Suspended particles tend to have a lower sequestration efficiency than settling particles. This is because suspended particles are dependent on PIPs to be actively transported to deeper water layers and thus contribute to carbon export (Boyd et al. 2019). Due to this limitation of suspended particles to reach great depths, settling particles have a larger potential for long-term carbon sequestration.

The fundamental parameters to estimate carbon export

The accurate determination of carbon fluxes from the surface to the deep ocean is essential to assess carbon export via the biological pump and thus understanding its implications for climate functioning. Numerous studies over the past decades have identified a multitude of processes which affect the export via the biological pump. However, experimental and theoretical based observations have shown that the main parameters for the regulation of carbon export are the settling velocity and rate of degradation (e.g., Martin et al. 1987, Iversen & Ploug 2013). Therefore, relevant implications of particle and aggregate settling velocities and degradation will be discussed separately in the following chapters.

Particle degradation

The pelagic food web plays a central role in the cycling and export of carbon. In particular, microbes and zooplankton play a fundamental role by recycling organic carbon from marine aggregates and transferring it into the dissolved organic and inorganic pool, as well as linking higher and lower trophic levels as predators and food source (Steinberg & Landry 2017). The degradation and consumption of marine aggregates can loosely be separated into two vertical domains: Zooplankton grazing of marine aggregates is mostly pronounced in the upper few hundred meters of the water column (Jackson & Checkley 2011, Iversen et al. 2010, van der Jagt et al. 2020), while the degradation by particle attached microbes is prominent throughout the entire water column (Iversen and Ploug 2013, Iversen et al. 2010).

Zooplankton degradation

The majority of zooplankton feeding occurs in the euphotic zone and is estimated to consume 75 – 91% of carbon produced from primary production (Steinberg & Landry 2017). Hereby, the consumed carbon is metabolically respired, fixed within the organism or excreted as fecal pellets. Fecal pellets are particularly relevant since they are reintegrated into carbon export as fast settling and compact aggregates and contain approximately up to half of the carbon consumed by the zooplankton (Steinberg & Landry 2017). Therefore, the rate at which these are exported and degraded by microbial remineralisation and/or zooplankton coprophagy is a determining factor if zooplankton grazing results in an increase or decrease of carbon fluxes. For instance, rapidly exported fecal pellets from dense swarms of Antarctic krill (*Euphausia superba*) were observed to locally contribute up to 72% of carbon flux in the water column and deposit >60% of carbon stored in the sea floor. In contrast, fecal pellets produced from salps (*Salpa thompsoni*) in the same region contained 4-fold more carbon than krill fecal pellets, yet microbial degradation and disaggregation retained 80% in the mixed layer (Iversen et al. 2017, Pauli et al. 2021). Therefore, the "repackaging" of organic carbon from the water column into efficiently exported fecal pellets and the rate at which these are exported and recycled may fundamentally impact the export efficiency of the biological pump.

Microbial degradation

Marine aggregates host distinct microbial communities (Thiele et al. 2019) which can be two- to threefold more abundant compared to the surrounding water column, thus enabling a rapid remineralisation. The key determinants for microbial carbon turnover within marine aggregates is the in- and efflux of O_2, nutrients and dissolved organic matter (Ploug & Bergkvist 2015, Zetsche et al. 2021). Herewith, microbial grazing and extracellular enzyme release are maintained, thus driving heterotrophic production on the aggregate and the release of unutilized DOC to the surrounding water column (Arnosti et al. 2011).

In-situ measurements of aggregate degradation indicate that microbial remineralisation of marine aggregates is temperature dependent, with increasing degradation rates at higher temperatures (Iversen and Ploug 2013). This has been supported by deep ocean carbon fluxes, which could be replicated with flux calculations by taking the temperature dependent microbial degradation into account (Iversen & Ploug 2013). However, experimental studies have also shown that the increase in ambient pressure decreases the concentration and respiratory activity of particle attached microbes, especially when reaching ambient pressure equivalent to 3000 m depth and below (Grossart & Gust 2009, Stief et al. 2021). This indicates, that the temperatures marine aggregates experience while settling through the water column may be a good indicator for microbial degradation rates in depths above 3000 m, while at deeper depths, pressure induced effects are expected to further decrease respiratory activity of particle attached microbes.

The microbial communities of marine aggregates sampled from the deep ocean showed similar microbial compositions as for the surface ocean, suggesting that microbial colonization occurs mainly in the surface ocean (Thiele et al. 2015, Boeuf et al. 2019). This may suggest that particle attached microbial activity is related to the water temperatures in the upper water column. Therefore, the temperature dependence of the microbial activity and thus aggregate degradation during settling may be more affected in tropical or subtropical regions as for polar regions, since aggregates sink from relatively warm surface waters to the cold deep ocean, as suggested by trends towards a more efficient microbial remineralization in regions with cold waters (Marsay et al. 2015).

Aggregate formation and its implications on settling velocities

Marine aggregate formation envisioned from aggregation- and coagulation theory

Particle aggregation is a primary process of the biological pump as it alters the physical properties of organic matter by forming aggregates that allows the transfer of material from the dissolved into the particulate phase and suspended/slow-settling single cells into fast-settling aggregates (Burd & Jackson 2009). Extensive theoretical and empirical based findings have proposed two major hypothesis that describe aggregation behaviour of particulate material and are based on the aggregation of material by collision (aggregation theory) and the spontaneous assembly of DOM polymers to larger sized gel polymers (polymer gel theory; Verdugo et al. 2004).

According to the aggregation theory, the particle aggregation rate is dependent on the particle size, concentration, adhesion force i.e. stickiness and encounter rate which depends on differential settling, turbulent or laminar fluid shear and, for sub-micron sized particles, Brownian motion (Burd & Jackson 2009).

In the polymer gel theory, aggregation is explained by self-induced assembly to networks of random or (semi)ordered structures via chemical or physical bonds, including covalent bonds, hydrogen bonding, van der Waals forces, electrostatics, entanglement etc. (Verdugo et al. 2004).

The extent to which the aggregation theory and polymer gel theory overlaps and complements each other is not fully clear, however, a size-dependent relevance can be expected and would suggest polymer gel theory to explain primarily sub-micron coagulation processes including particle precursor material such as nano- and microgels, while the aggregation theory is more suitable for the description of particle aggregation in the larger size ranges, hence marine snow.

The hydrodynamic environment from aggregates impacts bacterial attachment

In addition to the aggregation parameters defined from aggregation theory, the hydrodynamic environment around a settling aggregate may affect the encounter of particles (Secchi et al. 2021). As marine aggregates settle through the water column, the surrounding water generates a drag force i.e. fluid resistance which forms a thin layer of water around the aggregate, with a steep gradient of flow velocities i.e. shear rate. When particles are to encounter, the shear rate around the settling aggregate may act as a limiting barrier by "pushing away" the colliding particle and thus decelerate the collision speed. Thereby, the encountering particles trajectory may be redirected by the flow surrounding the aggregate, thus deflecting the encountering particle and preventing aggregation (Zetsche et al. 2020, Secchi et al. 2021). This implies that the hydrodynamic environment of a settling aggregate must be overcome in order for colliding particles to successfully encounter and potentially attach.

Studies have shown that the hydrodynamic environment may deflect bacteria (Secchi et al. 2020). In addition to size, the bacterial motility/sinking velocities affects the rate at which small sized particles overcome the boundary layer and hence, attach to the particle.

Non-motile/truly suspended bacteria are attached less frequent and in the windward direction of a settling particle. In contrast, motile bacteria, attach more frequent and predominantly in the leeward position of a particle (Secchi et al. 2020). This is because motile bacteria are able to penetrate into the high shear layer as they are deflected, if their motility velocity is higher as the wake flow behind the aggregate (Secchi et al. 2020). However, the mentioned bacterial motility is a chemotactically driven movement towards the particle. Therefore, motile bacteria actively approach the surface of the aggregate independent of their orientation towards the aggregate.

In addition, the surface heterogeneity of settling aggregates creates local vorticity, which creates a rotational water flow towards the aggregate surface. This is particularly pronounced if the structures are located lateral on the settling particle (Zetsche t al. 2020). The vortexes created from surface structures may thus enhance the aggregation potential of small sized particles by dragging the particle towards the aggregates surface.

Particle ballasting increases aggregate settling velocities

The incorporation of relatively dense ballasts minerals increases the size-specific settling velocities of marine aggregates (e.g. Iversen and Ploug 2010, Ploug et al. 2008a, Ploug et al. 2008b, van der Jagt et al. 2018). This particle ballasting is a commonly observed process and can be mediated by material of organic and inorganic origin.

Ballasting sources of organic origin comprise mainly phytoplankton groups that form shells of biogenic minerals, including calcium carbonate (coccolithophores) and opal (diatoms; Iversen & Ploug 2010, Ploug et al. 2008). Further, the incorporation of relatively dense fecal pellets into marine aggregates can increase particle settling velocities (Ploug et al. 2008).

Inorganic particle ballasting includes the incorporation of minerals or sediments (Iversen & Robert 2015, van der Jagt et al. 2018). These materials are sourced by the deposition of atmospheric dust on the ocean surface, e.g. Saharan dust deposition in the Atlantic (Iversen et al. 2010, Nowlad et al. 2015, van der Jagt et al. 2018), sediment plumes from river or glacial discharge (Halbach et al. 2019, Mouyen et al. 2018) or the resuspension of sediments in shallow shelf areas (Fahl & Nöthig 2007).

Differences between slow and fast settling aggregates for carbon export

As the majority of organic matter turn-over occurs within the upper few hundred meters (e.g. Iversen et al. 2010), the retention time within these depths largely determines the efficiency at which POC is exported to greater depth. Fast particle and aggregate settling velocities may transition organic matter efficiently to greater depths which limits zooplankton grazing and microbial degradation at shallow depths. Further, colder water temperatures limit the respiration rate of particle attached microbes thus limiting particle degradation (Iversen & Ploug 2013). Hence, a fast particle settling into deeper and colder water layers (excluding polar regions with cold surface waters, see section Microbial degradation) reduces the degradation by attached microbes in the deep ocean (Marsay et al. 2015). Therefore, fast particle and aggregate settling velocities are a determining factor for the efficiency of POC export.

In contrast, slow-settling particles and aggregates are generally considered to be degraded more efficiently at shallow depths due to their longer residence times and, thus, exposure to grazing zooplankton and microbial degradation in the upper part of the water column. For example, the phytoplankton species *Phaeocystis* spp. forms colonies with high amounts of gelatinous polysaccharides, which lower their settling velocity to approx. ~10 m day^{-1} (Skreslet 1988, Ploug et al. 1999). Due to this low settling velocity, *Phaeocystis* spp. is generally attenuated within the top 100 m of the water column and therefore only contributes to carbon flux in negligible amounts (Reigstad & Wassmann 2007, Wolf et al. 2016). Further, slow-settling particles and aggregates are strongly affected by water currents. Therefore, resuspension and vertical mixing are more likely to maintain slow-settling particles in the surface ocean. However, lateral advection may relocate slow settling particles and aggregates over far distances and thus change the area that the they are exported to from their production origin. This is particularly relevant in shelf regions, where the limited water depth leads to a short sequestration time when compared with the deep ocean (Boyd et al. 2019, Karakas et al. 2005). A lateral relocation of particles from shallow to deep areas may therefore extend the sequestration timescale of particles and thus increase the amount of POC exported via the biological pump.

Aims of the doctoral thesis

Great efforts have been undertaken over the past decades to identify and describe the principal mechanisms that control and drive the carbon export via the biological pump. In particular, the interplay between particle degradation and settling velocity have been identified as determining factors for carbon export (e.g., Martin et al. 1987, Iversen et al. 2013). However, until now, particle aggregation and its consequential implications on particle settling velocities are not fully understood. Specifically, methodological constraints on the sub-aggregate level limit our understanding of aggregation processes. In addition, highly dynamic environments such as polar and shelf regions encompass complex environmental properties that affect particle formation, composition and ballasting with varying consequences for particle sinking velocities and the time available for organic matter turn-over in the water column.

In this thesis, I aim to investigate knowledge gaps regarding aggregate structure and aggregation on the sub-aggregate level and the settling behaviour of particles in highly dynamic yet globally relevant environments for carbon export. The questions addressed in this thesis are:

I. How does lateral advection and vertical transport contribute to deep ocean carbon flux?
II. What are the implications of mineral ballasting on settling marine aggregates?
III. How does aggregate structure affect microbial degradation and aggregation potential?

References

Arnosti, C. (2011). Microbial extracellular enzymes and the marine carbon cycle. *Annual Review of Marine Science*, *3*, 401–425. https://doi.org/10.1146/annurev-marine-120709-142731

Azam F, Martinez J, Smith DC (1993) Bacteria-organic matter coupling on marine aggregates. In: Guerrero R, PedrósAlió C (eds) Trends in microbial ecology. Spanish Society for Microbiology, Barcelona, p 410–414

Buesseler, K. O., Boyd, P. W., Black, E. E., & Siegel, D. A. (2020). Metrics that matter for assessing the ocean biological carbon pump. *Proceedings of the National Academy of Sciences of the United States of America*, *117*(18), 9679–9687.

Burd, A. B., & Jackson, G. A. (n.d.). *Particle Aggregation*. https://doi.org/10.1146/annurev.marine.010908.163904

Boeuf, D., Edwards, B. R., Eppley, J. M., Hu, S. K., Poff, K. E., Romano, A. E., Caron, D. A., Karl, D. M., & DeLong, E. F. (2019). Biological composition and microbial dynamics of sinking particulate organic matter at abyssal depths in the oligotrophic open ocean. *Proceedings of the National Academy of Sciences of the United States of America*, *116*(24), 11824–11832. https://doi.org/10.1073/pnas.1903080116

Boyd, P. W., Claustre, H., Levy, M., Siegel, D. A., & Weber, T. (2019). Multi-faceted particle pumps drive carbon sequestration in the ocean. *Nature*, *568*(7752), 327–335.

Fahl, K., & Nöthig, E. M. (2007). Lithogenic and biogenic particle fluxes on the Lomonosov Ridge (central Arctic Ocean) and their relevance for sediment accumulation: Vertical vs. lateral transport. *Deep-Sea Research Part I: Oceanographic Research Papers*, *54*(8), 1256–1272. https://doi.org/10.1016/j.dsr.2007.04.014

Grossart, H. P., & Gust, G. (2009). Hydrostatic pressure affects physiology and community structure of marine bacteria during settling to 4000 m: An experimental approach. *Marine Ecology Progress Series*, *390*, 97–104. https://doi.org/10.3354/meps08201

Halbach, L., Vihtakari, M., Duarte, P., Everett, A., Granskog, M. A., Hop, H., Kauko, H. M., Kristiansen, S., Myhre, P. I., Pavlov, A. K., Pramanik, A., Tatarek, A., Torsvik, T., Wiktor, J. M., Wold, A., Wulff, A., Steen, H., & Assmy, P. (2019). Tidewater Glaciers and Bedrock Characteristics Control the Phytoplankton Growth Environment in a Fjord in the Arctic. *Frontiers in Marine Science*, *6*(May), 1–18. https://doi.org/10.3389/fmars.2019.00254

Henson, S. A., Sanders, R., & Madsen, E. (2012). Global patterns in efficiency of particulate organic carbon export and transfer to the deep ocean. *Global Biogeochemical Cycles*, *26*(1), 1–14.

Houghton, R.A. (2014) 10.10 - The Contemporary Carbon Cycle, Treatise on Geochemistry (Second Edition),Elsevier, Pages 399-435,

Iversen, M. H., Nowald, N., Ploug, H., Jackson, G. A., & Fischer, G. (2010). High resolution profiles of vertical particulate organic matter export off Cape Blanc, Mauritania: Degradation processes and ballasting effects. *Deep-Sea Research Part I: Oceanographic Research Papers*, *57*(6), 771–784.

Iversen, M. H., & Ploug, H. (2010). Ballast minerals and the sinking carbon flux in the ocean: Carbon-specific respiration rates and sinking velocity of marine snow aggregates. *Biogeosciences*, *7*(9), 2613–2624. https://doi.org/10.5194/bg-7-2613-2010

Iversen, M. H., & Ploug, H. (2013). *Temperature effects on carbon-specific respiration rate and sinking velocity of diatom aggregates – potential implications deep ocean Earth for*. 4073–4085.

Iversen, M. H., & Robert, M. L. (2015). Ballasting effects of smectite on aggregate formation and export from a natural plankton community. *Marine Chemistry*, *175*, 18–27. https://doi.org/10.1016/j.marchem.2015.04.009

Iversen, M. H., Pakhomov, E. A., Hunt, B. P. V., van der Jagt, H., Wolf-Gladrow, D., & Klaas, C. (2017). Sinkers or floaters? Contribution from salp pellets to the export flux during a large bloom event in the Southern Ocean. *Deep-Sea Research Part II: Topical Studies in Oceanography*, *138*(December 2016), 116–125. https://doi.org/10.1016/j.dsr2.2016.12.004

Jackson, G. A., & Checkley JR, D. M. (2011). Deep-Sea Research I Particle size distributions in the upper 100 m water column and their implications for animal feeding in the plankton. *Deep-Sea Research Part I*, *58*(3), 283–297.

Karakaş, G., Nowald, N., Blaas, M., Marchesiello, P., Frickenhaus, S., & Schlitzer, R. (2006). High-resolution modeling of sediment erosion and particle transport across the northwest African shelf. *Journal of Geophysical Research: Oceans*, *111*(6), 1–13. https://doi.org/10.1029/2005JC003296

Lal, R. (2008). Sequestration of atmospheric CO2 in global carbon pools. *Energy and Environmental Science*, *1*(1), 86–100.

Marsay, C. M., Sanders, R. J., Henson, S. A., Pabortsava, K., Achterberg, E. P., & Lampitt, R. S. (2015). Attenuation of sinking particulate organic carbon flux through the mesopelagic ocean. *Proceedings of the National Academy of Sciences of the United States of America*, *112*(4), 1089–1094. https://doi.org/10.1073/pnas.1415311112

Martin, J. H., Knauer, G. A., Karl, D. M., & Broenkow, W. W. (1987). VERTEX: carbon cycling in the northeast Pacific. *Deep Sea Research Part A, Oceanographic Research Papers*, *34*(2), 267–285.

Mouyen, M., Longuevergne, L., Steer, P., Crave, A., Lemoine, J. M., Save, H., & Robin, C. (2018). Assessing modern river sediment discharge to the ocean using satellite gravimetry. *Nature Communications*, *9*(1), 1–9. https://doi.org/10.1038/s41467-018-05921-y

Nowald, N., Iversen, M. H., Fischer, G., Ratmeyer, V., & Wefer, G. (2015). Time series of in-situ particle properties and sediment trap fluxes in the coastal upwelling filament off Cape Blanc, Mauritania. *Progress in Oceanography*, *137*, 1–11. https://doi.org/10.1016/j.pocean.2014.12.015

Pauli, N. C., Flintrop, C. M., Konrad, C., Pakhomov, E. A., Swoboda, S., Koch, F., Wang, X. L., Zhang, J. C., Brierley, A. S., Bernasconi, M., Meyer, B., & Iversen, M. H. (2021). Krill and salp faecal pellets contribute equally to the carbon flux at the Antarctic Peninsula. *Nature Communications*, *12*(1), 1–12. https://doi.org/10.1038/s41467-021-27436-9

Passow, U., & Carlson, C. A. (2012). The biological pump in a high CO2 world. *Marine Ecology Progress Series*, *470*(April 2014), 249–271.

Ploug, H., Stolte, W., Epping, E. H. G., & Jørgensen, B. B. (1999). *Diffusive boundary layers , photosynthesis , and respiration of the colony-forming plankton algae , Phaeocystis sp .* *44*(8), 1949–1958.

Ploug, H., Iversen, M. H., & Fischer, G. (2008a). *Ballast , sinking velocity , and apparent diffusivity within marine snow and zooplankton fecal pellets : Implications for substrate turnover by attached bacteria*. *53*(5), 1878–1886.

Ploug, H., Iversen, M. H., Koski, M., & Buitenhuis, E. T. (2008b). Production, oxygen respiration rates, and sinking velocity of copepod fecal pellets: Direct measurements of ballasting by opal and calcite. *Limnology and Oceanography*, *53*(2), 469–476. https://doi.org/10.4319/lo.2008.53.2.0469

Ploug, H., & Bergkvist, J. (2015). Oxygen diffusion limitation and ammonium production within sinking diatom aggregates under hypoxic and anoxic conditions. *Marine Chemistry*, *176*, 142–149.

Reigstad, M., & Wassmann, Æ. P. (2007). *Does Phaeocystis spp . contribute significantly to vertical export of organic carbon ?* 217–234. https://doi.org/10.1007/s10533-007-9093-3

Secchi, E., Vitale, A., Miño, G. L., Kantsler, V., Eberl, L., Rusconi, R., & Stocker, R. (2020). The effect of flow on swimming bacteria controls the initial colonization of curved surfaces. *Nature Communications*, *11*(1), 1–12. https://doi.org/10.1038/s41467-020-16620-y

Skreslet, S. (1988). Buoyancy in Phaeocystis pouchetii (Hariot) Lagerheim. *Journal of Experimental Marine Biology and Ecology*, *119*(2), 157–166. https://doi.org/10.1016/0022-0981(88)90230-4

Steinberg, D. K., & Landry, M. R. (2017). Zooplankton and the Ocean Carbon Cycle. *Annual Review of Marine Science*, *9*(1), 413–444.

Stief, P., Elvert, M., & Glud, R. N. (2021). Respiration by "marine snow" at high hydrostatic pressure: Insights from continuous oxygen measurements in a rotating pressure tank. *Limnology and Oceanography*, *66*(7), 2797–2809. https://doi.org/10.1002/lno.11791

Thiele, S., Fuchs, B. M., Amann, R., & Iversen, M. H. (2015). Colonization in the photic zone and subsequent changes during sinking determine bacterial community composition in marine snow. *Applied and Environmental Microbiology*, *81*(4), 1463–1471. https://doi.org/10.1128/AEM.02570-14

Thiele, S., Basse, A., Becker, J. W., Lipski, A., Iversen, M. H., & Mollenhauer, G. (2019). Microbial communities in the nepheloid layers and hypoxic zones of the Canary Current upwelling system. *MicrobiologyOpen*, *8*(5), 1–13.

van der Jagt, H., Iversen, M. H., Friese, C., & Stuut, J. W. (2018). *The ballasting effect of Saharan dust deposition on aggregate dynamics and carbon export : Aggregation , settling* ,. https://doi.org/10.1002/lno.10779

van der Jagt, H., Wiedmann, I., Hildebrandt, N., Niehoff, B., & Iversen, M. H. (2020). Aggregate Feeding by the Copepods Calanus and Pseudocalanus Controls Carbon Flux Attenuation in the Arctic Shelf Sea During the Productive Period. *Frontiers in Marine Science*, *7*(September). https://doi.org/10.3389/fmars.2020.543124

Verdugo, P., Alldredge, A. L., Azam, F., Kirchman, D. L., Passow, U., & Santschi, P. H. (2004). The oceanic gel phase: A bridge in the DOM-POM continuum. *Marine Chemistry*, *92*(1–4), 67–85. https://doi.org/10.1016/j.marchem.2004.06.017

Volk, T., & Hoffert, M. I. (1985). EFFICIENCIES IN OCEAN-DRIVEN CARBON PUMPS : ANALYSIS Department of Applied Science , New York University models solubility pump signal , subject to uncertainties in the C : P Redfield changes which lower pCO • atm in the model are vertical carbon Since di. *The Carbon Cycle and Atmospheric CO2: Natural Variations Archean to Present*, *32*, 99–110.

Wolf, C., Iversen, M., Klaas, C., & Metfies, K. (2016). Limited sinking of Phaeocystis during a 12 days sediment trap study. *Molecular Ecology*, *25*(14), 3428–3435. https://doi.org/10.1111/mec.13697

Zetsche, E. M., Larsson, A. I., Iversen, M. H., & Ploug, H. (2020). Flow and diffusion around and within diatom aggregates: Effects of aggregate composition and shape. *Limnology and Oceanography*, *65*(8), 1818–1833. https://doi.org/10.1002/lno.11420

List of manuscripts

Manuscript I

Three-dimensional visualization of marine snow using magnetic resonance imaging

Steffen Swoboda, Ekkehard Küstermann, Gerhard Bartzke, Ricarda Gatter, Nasrollah Moradi, Anna Biastoch, Wolfgang Dreher, Morten H. Iversen

SS, EK, GB, WD, NM and MHI conceptualized the study; SS performed laboratory measurements and aggregate embedding; EK performed the magnetic resonance imaging; SS, EK, RG and GB performed the image processing and image analysis; GB performed the flow model analyses; SS and AB performed laboratory culture work; SS performed the data analysis with help of GB and EK; SS drafted the manuscript; All authors revised the manuscript.

Manuscript in preparation

Manuscript II

Lateral advection of shelf produced organic matter is the main contributor to deep ocean carbon flux in the Cape Blanc Upwelling region

Steffen Swoboda, Hannah Marchant, Soeren Ahmerkamp, Jan-Hendrik Hehemann, Hagen Buck-Wiese, Farooq Moin Jalaluddin, Marius Becker, Arjun Chennu, Oscar E. Romero, Kai Schwalfenberg, Simon Ramondenc, Morten H. Iversen

SS, HM and MHI conceptualized the study; SS, HM, SA, JH, HB, KS and MHI performed the field work; SS, HB and FMJ performed the laboratory analysis; SS, SR and MHI performed data analyses; SS drafted the manuscript. All authors revised and approved the manuscript for submission.

Under revision at Global Biogeochemical Cycles (GBC)

Manuscript III

Release of ballast material during sea-ice melt enhances carbon export in the Arctic Ocean

Steffen Swoboda, Thomas Krumpen, Eva-Maria Nöthig, Katja Metfies, Simon Ramondenc, Jutta Wollenburg, Kirsten Fahl, Ilka Peeken, Morten H. Iversen

SS, EN and MHI conceptualized the study; SS, EN, KM, JW and KF performed the field work; SS performed the ballasting experiments; EN performed the sediment trap analysis; KM preformed DNA-analysis; KF performed terrigenous marker analysis; SS performed data analyses with the help of SR and TK; TK performed sea-ice backtracking analysis; SS drafted the manuscript. All authors revised and approved the manuscript for submission.

Under consideration at Proceedings of the National Academy of Sciences (PNAS)

Manuscript I

Three-dimensional visualization of marine snow using magnetic resonance imaging

Steffen Swoboda[1*], Ekkehard Küstermann[2], Gerhard Bartzke[1], Ricarda Gatter[1], Nasrollah Moradi[1], Anna Biastoch[1], Wolfgang Dreher[2], Morten H. Iversen[1,3]

[1]MARUM – Centre for Marine Environmental Sciences, University of Bremen, 28359 Bremen, Germany.

[2]Chemistry Department, University of Bremen, 28359 Bremen, Germany.

[3]Section for Polar Biological Oceanography, Alfred Wegener Institute Helmholtz Centre for Polar and Marine Research, 27570 Bremerhaven, Germany.

Corresponding authors:

Steffen Swoboda

Morten Iversen

Abstract

Oceanic carbon storage is largely mediated by organic aggregates which sink from the surface ocean to the deep sea. Since carbon flux is determined by the concentration and settling velocity of organic aggregates, it is vital to understand how aggregate composition, size and shape impact their size-specific carbon content and sinking velocity. However, we still struggle to visualize and quantify the three-dimensional structure within settling aggregates as well as how transparent components of the aggregates affect their size and shape. Here, we suggest a method to visualize both the internal and external three-dimensional structure of individual aggregates using magnetic resonance imaging (MRI). We compared microscopic and MRI measurements and found that aggregate size, volume and surface area were larger when determined via MRI compared to microscopy. If this discrepancy is correct, it has implications for previous size-based measurements on aggregates, such as volumetric carbon content, microbial respiration derived from microsensor profiles, carbon-specific degradation, and size-specific settling velocities. Accompanied with the high-resolution size measurements, the MRI allowed visualization of small-scale structure on the aggregate surface. When implementing these surface structures into a flow model, we found that they caused strong vorticity fields, which may enhance microbial colonization downstream of the structure. Further, the small-scale surface structures increased the drag forces on the settling aggregate to a magnitude higher than would be expected from a smooth sphere with a similar volume. The internal structure of the aggregate showed connecting channels throughout the entire aggregate. Though these channels connected to the surface of the aggregate, the flow model still suggested that flow and advection did not occur through the channels, suggesting diffusion as the main mechanism for solute transport to and from settling aggregates. Our preliminary results suggest that MRI based structural analyses of settling aggregates is a powerful tool to link small-scale structures and processes within single aggregates to large-scale processes, such as biogeochemical cycles and oceanic carbon sequestration.

Introduction

The world's oceans regulate the global carbon cycle through the uptake and storage of atmospheric CO_2. The biological carbon pump is a key mechanism to regulate atmospheric CO_2 uptake via the export of organic matter from the surface to the deep ocean: Phytoplankton in the surface ocean fix dissolved atmospheric CO_2 into particulate organic carbon (POC) via photosynthesis and, by sinking through the water column, transport the fixed POC to the deep ocean where it may be sequestered (Volk & Hoffert 1985, Turner 2015, Boyd et al. 2019).

The export of POC is largely mediated by sinking aggregates, such as zooplankton fecal pellets pellets and marine snow aggregates (Alldredge and Silver 1988). Marine snow often contains a gel like matrix of polysaccharides which are collectively termed transparent exopolymer particles (TEP; Passow & Alldredge 1994, Flintrop et al. 2018, Zetsche et al. 2020). These TEP arrange to a sticky web-like structure to which the material prevailing in the water column adheres to, thus forming a highly heterogenous and porous aggregation of whole phytoplankton cells or their fragments, detrital material and inorganics such as minerals or sediments (Flintrop et al. 2018, van der Jagt et al. 2018).

Marine aggregates host diverse microbial communities which degrade the aggregates while settling through the water column. These communities primarily form on single phytoplankton cells and small aggregates during aggregate formation in the upper water column (Thiele et al. 2015). However, it is possible that some motile bacteria colonize settling aggregates throughout the water column (Secchi et al. 2020), though most studies suggest that this is only a minor fraction of the microbial communities associated with the aggregates at depth (Thiele et al. 2015, Bachmann et al. 2018, Mestre et al. 2018, Fadeev et al. 2020). The aggregate associated microbial communities can be two- to threefold more abundant compared to those in the surrounding water, making marine aggregates hotspots for microbial activity (Thiele et al. 2019). During the microbial degradation, organic matter is solubilized and remineralized under the release of carbon dioxide (respiration), dissolved organic matter (DOM, solubilization) and nutrients (remineralization) to the surrounding water column (Arnosti et al. 2010, Zetsche et al. 2020). Therefore, along with zooplankton grazing, microbial degradation is a determining factor for the efficiency with which organic matter, including carbon, is attenuated from the surface to the deep ocean, thus regulating atmospheric CO_2 sequestration via the biological pump.

Over the past decades, a multitude of approaches have been developed to estimate carbon export and sequestration via the biological pump. (e.g. Iversen et al. 2010, McDonnell & Buesller 2010, Kiko et al. 2017, Guidi et al. 2008, Iversen & Ploug 2013). While these approaches may utilize varying equipment and sources for data acquisition, the variables that are universally necessary to estimate vertical carbon fluxes are the quantity of particulate organic carbon, the rate of its degradation and the speed at which it settles through the water column. However, the fundamental parameter defining each of these variables is the aggregate size and structure, i.e. aggregate diameter, volume, surface area, and internal and external physical structures such as surface roughness and internal pore-space. Often aggregate volume is used to derive carbon-to-volume ratios of different types of aggregates (Iversen et al. 2010, Iversen and Ploug 2010, Iversen and Ploug 2013), which can be used to estimate the carbon content of different aggregate types and sizes using optical measurements of in situ particle abundance and distribution (e.g. Guidi et al. 2008, Iversen et al. 2010, Kiko et al. 2017). Furthermore, total respiration rate of microbial communities within aggregates are often determined from the product between aggregate surface area and oxygen flux at the aggregate surface which is measured using microsensors (Ploug et al. 1999, Iversen & Ploug 2013, Ploug & Grossart 2000, Zetsche et al. 2020). Size-specific settling velocities of marine aggregates are typically related to the equivalent spherical diameter of the aggregates (Iversen and Ploug 2010, McDonnell & Buesseler 2010, Guidi et al. 2008 Iversen and Robert 2015). All of these measurements are reliant on our ability to determine aggregate size accurately across a multitude of methods, including microscope, in situ camera systems, and laser scanning systems. However, despite the crucial role particle volume and surface area have for understanding and predicting the functioning of the biological pump, there is no method to date that allows for the accurate determination of the true volume and surface area of a marine particle.

The common approach to estimate aggregate volume and surface area is to measure the aggregate dimensions and fit a matching geometric volume i.e. an ellipsoid or sphere from which the volume and surface area are derived (e.g. Ploug & Grossart 2000, Gärdes et al. 2011, Iversen & Ploug 2013, Zetsche et al. 2020). However, the composition of marine aggregates is highly heterogenous and contains internal pore spaces and ruff surface areas (Zetsche et al. 2020, Flintrop et al. 2018, Rogge et al. 2018, Ploug & Passow 2007). Therefore, the established methods for the approximation of surface area and volume are inevitably biased, thus affecting our capability to understand and predict carbon cycling and export within the biological pump.

In this study, we present for the first time a new approach to visualize in 3D the internal and external structures of an aggregate. We combine these observations with lab-based measurements of size, settling velocity and oxygen consumption in order to compare the accuracy of established approaches with precise volume and area measurements from the magnetic resonance imaging (MRI). We combine our MRI derived aggregate sizes with a computational fluid dynamics (CFD) based numerical model to estimate the impact of the aggregate structure on hydrodynamic properties including boundary layer thickness and drag forces. Our findings suggest that estimations based on aggregate surface area and volume which are derived from geometric shapes involves significant differences compared to our 3D reconstructed aggregate, indicating that the use of MR imaging can be a powerful tool to improve the structural analysis of marine aggregates.

Material and Methods

Algae cultures

Cultures of *Phaeocystis antarctica*, *Chetoceros debilis* and *Pseudonitzschia turgidula* were grown for 25 days at 2 °C in artificial sea water with 35 PSU according to Kester et al. (1976), and was enriched with nutrients according to f/2 medium (Guillard 1975). The cultures were kept under a constant light irradiation equivalent to 150 µmol photons m^{-2} s^{-1}.

Aggregate formation

An algal concentration of 7000 cells ml^{-1} of *Phaeocystis antarctica*, *Chetoceros debilis* and *Pseudonitzschia turgidula* respectively, were transferred into phosphate and trace elements limited artificial seawater (F1/4) and filled into roller tanks (14 x 7.5 cm; 1.15 l tank^{-1}). Roller tanks were placed on a roller table set at 3 rpm in a temperature-controlled cabinet set at 2 °C until aggregates had formed after 5 days.

Measurements of aggregate settling and oxygen consumption

To determine the aggregate settling velocity, size, settling orientation and oxygen consumption, aggregates were placed into a flow chamber (5 cm diameter) which keeps aggregates suspended by creating an upward flow, thus mimicking aggregate settling (Ploug & Jørgensen 1999). The water in the flow chamber was aerated to ensure oxygen saturation, and cooled to the incubation temperature of the algal culture (2°C) with a thermostat (Julabo). Once the flow was adjusted to maintain the aggregate suspended, the settling velocity was determined in triplicates by dividing the flow rate with the diameter of the flow chamber. Aggregate sizes were determined in their length, width and height with a retical mounted on an ocular and the settling orientation of individual aggregates was captured with a camera (Sony alpha 7 II with a mounted Carl Zeiss Makro-Planar T 100 mm f/2 ZF2).

The microbial oxygen consumption of aggregates was measured as vertical profiles in 100 µm steps from 1 mm above the aggregate until the aggregate centre using a clark-type oxygen microsensor (Unisense, OX-12, 10 µm tip diameter) mounted on a micromanipulator. To ensure that no photosynthetic O_2 production from phytoplankton within the aggregates affected the measurements, oxygen profiles were taken in the dark. The oxygen flux of individual aggregates was calculated in nmol O_2 cm^{-2} h^{-1} by using the model from Moradi et al. (2021) and then multiplied by the surface area to O_2 h^{-1} agg^{-1}. From the obtained oxygen consumption, the microbial respiration of individual aggregates was derived assuming a one-to-one molar ratio of O_2 flux to CO_2 flux.

Aggregate preparation for MR imaging measurements

After the measurements in the flow chamber, marine snow particles from the roller tank experiments were embedded in agarose following a modified procedure according to Rogge et al. (2018). A 0.5% weight contribution of agarose (SERVA, research grade, gel strength min. 1700 g/cm^2) was added to filtered sea water and heated to boiling temperature while stirring until fully dissolved. The hot agar was then filled into an embedding mould which was subsequently placed on a tissue cooler (Jürgens Tissue cool plate COP 20) set at 0°C. The tissue cooler was used to ensure that the agar cured in a gradient from bottom to top. After approx. 4 min, when the agar in the lower half of the embedding mould was firm and in the upper half still liquid, individual aggregates where gently placed into the liquid agar and let to settle on the cured agar within the moulding block. After the agar fully cured a small agar block containing the freely embedded aggregate was cut out of the embedding mould. To control for structural alterations from the embedding process, dimensions of width, length and height of the embedded aggregate were measured once more with a retical mounted on a stereo loupe (xxx) before the agar block was gently transferred into a 2 ml reaction tube. Afterwards, the reaction tube was filled with a contrast agent (0.5 mmol Magnevist solution; Schering) which was let to diffuse into the agar block for a minimum of 24h. Embedded aggregates where then stored at 7°C until the conduction of MRI measurements.

MRI measurements

MR imaging was done on a Biospec 70/20 USR (Bruker Biospin MRI GmbH, Ettlingen, Germany) with a magnetic field strength of 7T working at 300MHz. The system ist equipped with a magnetic field gradient insert BGA12S2 (*inner diameter* = 116 mm, max. gradient strength = 441 mT m^{-1}). Signal excitation and reception was done using a custom-build radio frequency (RF) loop-gap resonator (inner diameter: 21mm, length: 25mm) inductively coupled to the RF-system. In order to derive 3-dimensional maps of T2-relaxation and diffusion of water molecules, MR imaging measurements were done using the following parameters: (1) T2 map: Multi-Spin-Echo sequence with 15 spin-echos separated by 10ms, TE = [10 20 ... 150] ms, TR = 3.0s, two times signal averaging, total experimental time = 13:39 hours:min. (2) Diffusion map: Stejskal-Tanner pulsed gradient Spin-Echo sequence (Stejskal & Tanner 1965), TE=27.5ms TR=3.0s, 12 signal averages, total experimental time = 28:19 h:m, b-values = [0 600] s mm^{-2}.

Both data sets were acquired with identical geometrical parameter at an isotropic spatial resolution of 78 µm (data matrix size: 128x128x64 points, field of view (FOV): 10x10x5mm^3). Data were stored in the generic format of the vendor.

Image pre-processing

Image reconstruction was done offline using custom written scripts in Julia programming language (Version 1.7.1, https://julialang.org/) as follows: The acquired MR-time domain data were arranged to 4D-data sets where the first 3 dimensions represent the data k-space, while the 4th dimension corresponds to volumes acquired at different echo times (T2-measurement) or b-values (diffusion measurements). Next, the individual 3D-data sets were zerofilled along all three k-space axes prior to 3D-Fourier-Transformation (3D- FT) using the "FFTW"-package of Julia. These FT-processed data were saved as magnitude data with an isotropic spatial resolution of 39 µm in the Nifti-format (https://nifti.nimh.nih.gov/) using the Julia "NIfTI"-package. The final T2-relaxation map was calculated using a least-squares fitting algorithm as implemented in Julias "LsqFit"-package by a pixelwise estimation of two parameters (S0,T2) to fit the data points at the measured TE-times according the following equation: S(x,y,z,TE) = S0(x,y,z) * exp{-TE/T2(x,y,z)} where S(x,y,z,TE) := signal time course at voxel position (x,y,z) measured at TE and S0(x,y,z) as well as T2(x,y,z) are pixel-wise estimated values. This results in a 3-dimensional map representing the sampled volume by T2-relaxation values in ms. These estimated T2-values are known to be smaller as compared to the intrinsic T2 relaxation times - this effect is due to the diffusion weighting introduced by the transient magnetic field gradients used for spatial encoding the images (Edzes et al. 1998).

Analogous to this protocol, the diffusion data were processed. Here, the diffusion constant (DC) and the S0 are estimated by fitting the signal to the following equation: S(x,y,z,b) =

S0(x,y,z) * exp{-b*DC(x,y,z)} where S(x,y,z,b) := signal at voxel position (x,y,z) measured with the corresponding b-value and S0(x,y,z) as well as DC(x,y,z) are pixel-wise estimated values.

After image pre-processing, respective aggregate images from T2 measurements and diffusion maps were converted to an 8-bit grey scale (pixel values ranging from 1 - 256), and stacked in a z-plane using the open-source image processing software image J (fiji, version 2.1.9/1.53c). Low pixel values represented embedded structures i.e. the embedded aggregate, while high values represented the surrounding agar and water pockets within the aggregate. In order to differentiate between aggregate structures and surrounding medium, we used the minimum detectable voxel value for noise grain to define a threshold value.

The data were processed with the Avizo software (version 2021.2). The measured aggregate was segmented with a marker-based watershed algorithm (Watershed module). Markers were set with the Segmentation Editor by threshold segmentation (threshold of 222). The resulting structure was further manually corrected by including and excluding individual voxels to account for the aggregate and background, respectively. This was necessary, because some parts of the aggregate had voxel values that lay outside the threshold value, while parts of the background noise lay within the threshold value. As guideline for the addition and removal of voxels we followed the principle that noise is a random artifact and does not form coherent structures. Therefore, it can be expected that detected structures with a coherent appearance, e.g. a detected sharp edge over multiple voxels, are part of the embedded aggregate structure and vice-versa (comparison shown in Fig. S1). Thus, it should be noted, that due to the detection limitations of our MRI setup, the defined contour of the aggregate may locally vary within the size range of a voxel, i.e., 39 μm^3. The Material Statistics and Label Statistic modules were used to characterize the aggregate and calculate the aggregate's volume and surface area.

Flow model setup

A numerical CFD (Computational Fluid Dynamics) model was used to simulate the flow in the direct vicinity of the aggregate. The model is based on the open-source toolbox OpenFOAM version 2112 (Open Field Operation and Manipulation, www.openfoam.com). In order to resolve the flow equations OpenFOAM uses the Finite Volume Method (FVM). In the present case a SIMPLE (Semi-Implicit Method for Pressure-Linked Equations) solver that allows to couple the Navier-Stokes equations with an iterative procedure was used (Ferzinger & Peric 2001). The domain (DX = 0.02 m, DY = 0.02 m, DZ = 0.06 m) was discretized into a grid of three-dimensional hexagonal elements. The flow was driven by inlet and outlet boundary conditions that were assigned at the top and bottom of the domain. All sides walls were discretized with recycling boundary conditions. In order to resolve the flow in high resolution each aggregate was embedded by six mesh refinement zones. In total three aggregate geometries were discretized into the domain at X = 0.01 m, Y = 0.01 m and Z = 0.04 m (Fig. 1). Two geometries were designed as simplified shape models (sphere and ellipsoid) and served model validation (Fig. 2). Both geometries were created with the opensource software Blender and implemented into the CFD environment as STL files. Please note that the size ranges of the ellipsoid and the sphere based onto the equal spherical diameter. The STL (stereo lithography file) file of the natural aggregate, was also positioned at the same location as the sphere and the ellipsoid. The orientation of the MR imaged aggregate was set to match the orientation of the aggregate in the flow chamber. The settling velocity values under which all aggregates were tested was Uz = 60.25 m day^{-1}. Each model run was stopped after the flow field was in steady state, whereby all model runs converged after 1200 iteration steps. Each simulation was run in parallel on 48 cores and took 39 hours of computation time on a Beowulf cluster.

Images created from the model output were generated using the 3D open-source imaging software Paraview (Kitware). Boundary layer sizes were defined as flow velocities within the upper 10% of the terminal settling velocity of the aggregate from flow chamber measurements. An isovolume Filter was used to derive the exact location of the boundary layer. From the derived boundary layer, the volume and surface area where derived using Paraview.

Excess density of aggregates

From the measurements in the flow chamber, we calculated the excess density ($\Delta\rho$) of aggregates according to Iversen and Ploug (2010):

$$\Delta\rho = \frac{C_D \, \rho_{\varpi} \, \omega^2}{\frac{4}{3} g \, D} \qquad (1)$$

where ρ_{ϖ} is the density of seawater at 2 °C at a salinity of 35 PSU (1.0280 in g cm^{-3}), ω is the measured aggregate settling velocity in cm s^{-1}, g is the gravitational acceleration (981 cm s^{-2}) and D is the aggregate diameter (cm) in direction of the Z-axis which was derived from the respective shapes within the model. C_D is the dimensionless drag force which was experimentally derived from the flow model.

Results

A list of aggregate properties including the aggregate shape (volume, area and pore space), microbial respiration as well as hydrodynamic properties (boundary layer, drag force and excess density) are summarized in table 1.

Aggregate formation

Aggregates from a phytoplankton culture mix with equal parts of *Phaeocystis antarctica*, *Chetoceros debilis* and *Pseudonitzschia turgidula* were formed at a total algal cell concentration of 21000 cells ml^{-1}. The formed aggregates were highly porous and very fragile (Fig. S2), thus falling apart regularly which made the handling difficult.

Aggregate volume, area and shape

An overview figure of the shape and internal pore of the aggregate derived from MRI is shown in Fig. 3. The volume of the MRI derived aggregate model with added pore space volume was 3.86 mm^3 and therefore 37% larger as the optically fitted sphere with 2.43 mm^3 and 45% larger as the derived sphere with 2.14 mm^3. By excluding the measured pore space volume of 0.68 mm^3, the resulting MRI derived true aggregate volume was 3.18 mm^3 with a minimum estimate of 3.08 mm^3 and a maximum estimate of 3.23 mm^3.

The outside surface area of the MRI derived aggregate model was 0.189 cm^2, while surface areas of the optically derived ellipsoid and sphere were approximately half with 0.091 cm^2 and 0.080 cm^2 respectively. The pore space area of the MRI derived aggregate model was 0.170 cm^2, resulting in a total surface area of 0.358 cm^2 with minimum and maximum estimates of 0.35 cm^2 and 0.42 cm^2, respectively. Therefore, the total surface area of the MRI derived aggregate model was ~4 fold larger as the optically derived surface area of the ellipsoid and sphere.

The volume of the optically derived ellipsoid from the embedded aggregate was 2.55 mm^3 which amounts to a ~5% increase compared to the ellipsoid volume derived from flow chamber measurements. The shape of the embedded aggregate appeared overall more flattened with a height, width and depth of 1.71 mm, 2.75 mm & 1.04 mm, while the shape of the suspended aggregate in the flow chamber was narrower but more elongated in height with dimensions of 2.125 mm, 1.75 mm and 1.25 mm, respectively (Fig. 2).

Flow velocity, boundary layer size and vorticity

The aggregate settling velocity measured in the flow chamber was 60 m day^{-1}. The flow fields derived from the model output showed parallel running streamlines which were deflected from the surface of the respective shape, smoothly followed the surface and afterwards converged back to in-parallel running streamlines with no indication for the formation of vortices in the leeward direction of the respective shapes (Fig. S3). For the MRI derived aggregate model, streamlines showed no indication for flow through the internal pore structures.

The boundary layer area of the MRI derived model aggregate was 0.67 cm^2 with a total volume of 6.11 mm^3. The boundary layer area of the ellipsoid was 0.20 cm^2 with a volume of 3.25 mm^3 while the boundary layer of the sphere had an area of 0.20 cm^2 with a volume of 3.12 mm^3. This results in an ~2-fold larger surface area and ~3-fold larger total volume of the boundary layer by the MRI derived model aggregate when compared to the boundary layer of the ellipsoid and the sphere (Fig 5).

The respective windward and leeward distance of the boundary layer along the z-axis was 0.028 cm and 0.024 cm for the model derived aggregate, while the ellipsoid was 0.012 cm and 0.02 cm and the sphere was 0.02 cm and 0.028 cm. When dividing the combined distance of the boundary layer along the z-axis with the diameter of the respective shape, the boundary layer fraction was 0.245 for the MRI derived aggregate, while the ellipsoid had the smallest fraction with 0.157 and the sphere the largest with 0.300.

Vorticity fields clearly pronounced on the surface of the MRI derived aggregate while the surface of the ellipsoid and the sphere formed barely any vorticity (Fig. 4a-c). The intensity of vorticity fields for the MRI derived aggregate varied depending on the heterogeneity of the surface structure and where most intense at structures that extended lateral from the aggregate (Fig. 4a).

Drag force, drag coefficient and excess density

The total drag force generated on the sphere by our model was 0.683 N (Fig. 6). These observations matched well the theoretical based drag coefficients of 0.651 N according to White et al. 2005, suggesting that our model was capable to represent the hydrodynamic forces on the respective shapes with a precision of ~95%. Compared to the sphere, the drag force generated on the ellipsoid was only 0.494 N which amounts to a ~30% lower drag force generated on the sphere, while the drag force from the MRI derived model aggregate was 8.11 N resulting in an ~12-fold increase compared to the sphere.

The derived drag coefficient for the MRI derived aggregate was 298.2 from which 176.7 was formed by viscous drag and 121.5 by pressure drag. The drag coefficient for the ellipsoid was lowest with 18.2 from which 13.9 was formed by viscous drag and 4.2 by pressure drag, while the sphere generated a drag coefficient of 25.1 which composed of a viscous drag by 16.8 and pressure drag of 8.3.

Using the model derived drag coefficients, the calculated excess density of the MRI derived aggregate model was $5.37 \bullet 10^{-3}$ g cm^{-3}. This was ~10-fold higher as for the sphere with $5.98 \bullet 10^{-4}$ g cm^{-3}, while excesses density of the ellipsoid was lowest with $3.33 \bullet 10^{-4}$ g cm^{-3}.

Respiration rate

The oxygen microsensor measurements of the aggregate while settling in the flow chamber showed an O2 flux of 5.5278 nmol O_2 cm^{-2} h^{-1}. Assuming a 1 to 1 molar conversion of O_2 to CO_2 from microbial respiration, the area integrated CO_2 flux of the sphere was 10.65 nmol C agg^{-1} d^{-1}. The area integrated CO_2 flux of the ellipsoid was similar with 12.08 nmol C agg^{-1} d^{-1}, while the larger area of the MRI derived aggregate formed a 2-fold higher CO_2 flux of 25.07 nmol C agg^{-1} d^{-1}.

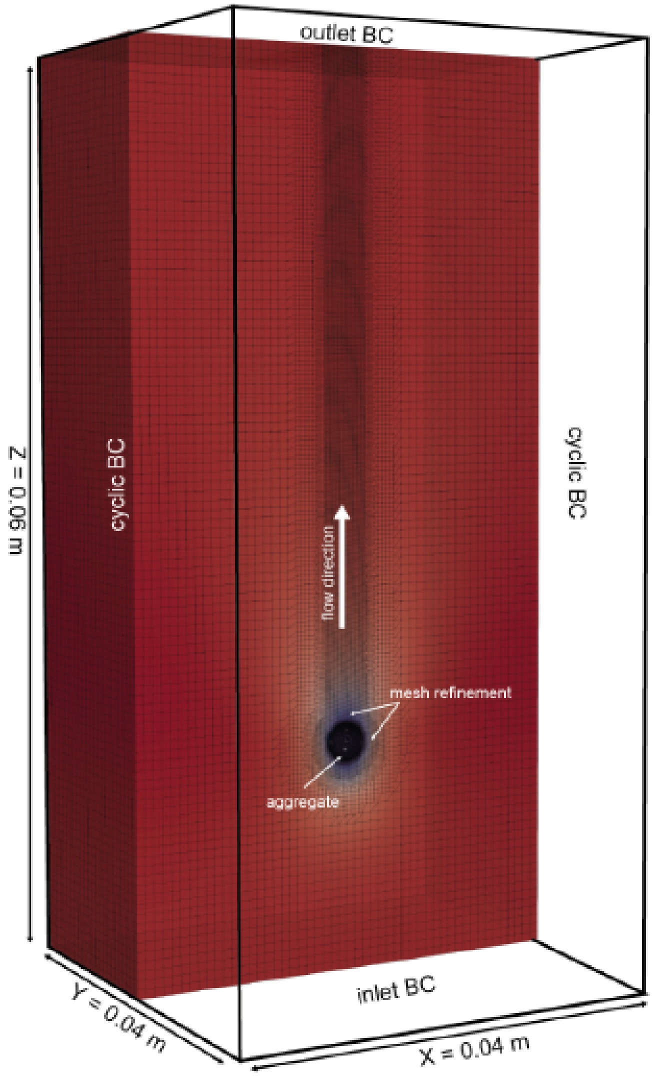

Fig 1: Numerical model setup indicating the model dimensions, boundary conditions as well as the mesh distribution.

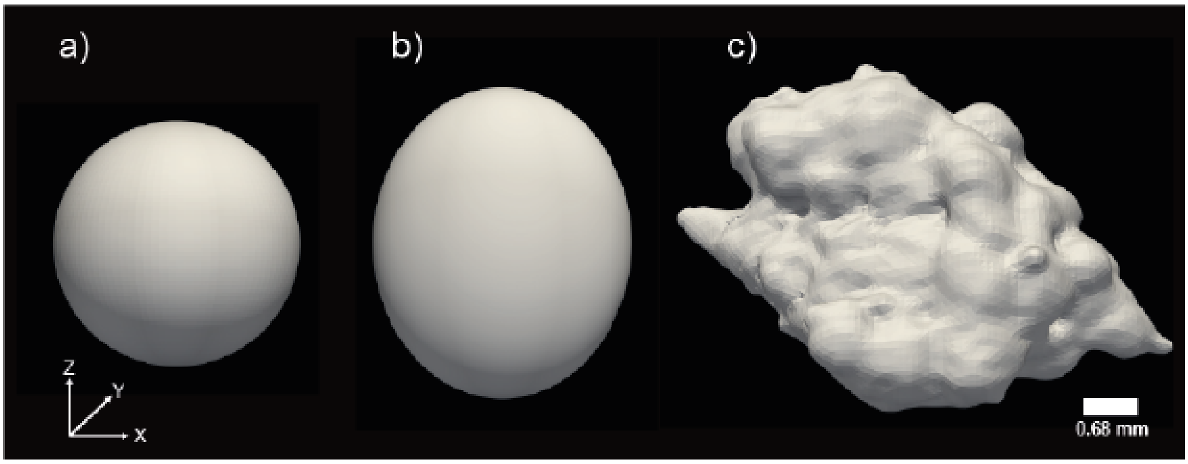

Fig 2: Overview of the tested aggregate shapes: a) Sphere b) Ellipsoid c) Aggregate

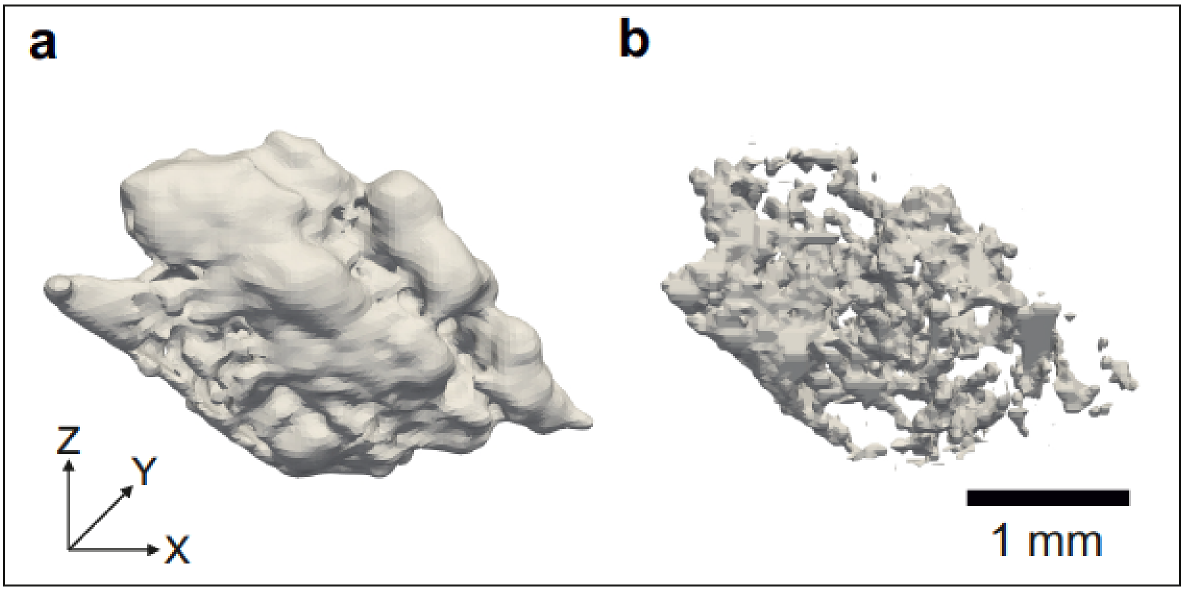

Fig. 3. Aggregate model of the internal and external aggregate shape, derived from measurements with magnetic resonance imaging (MRI).

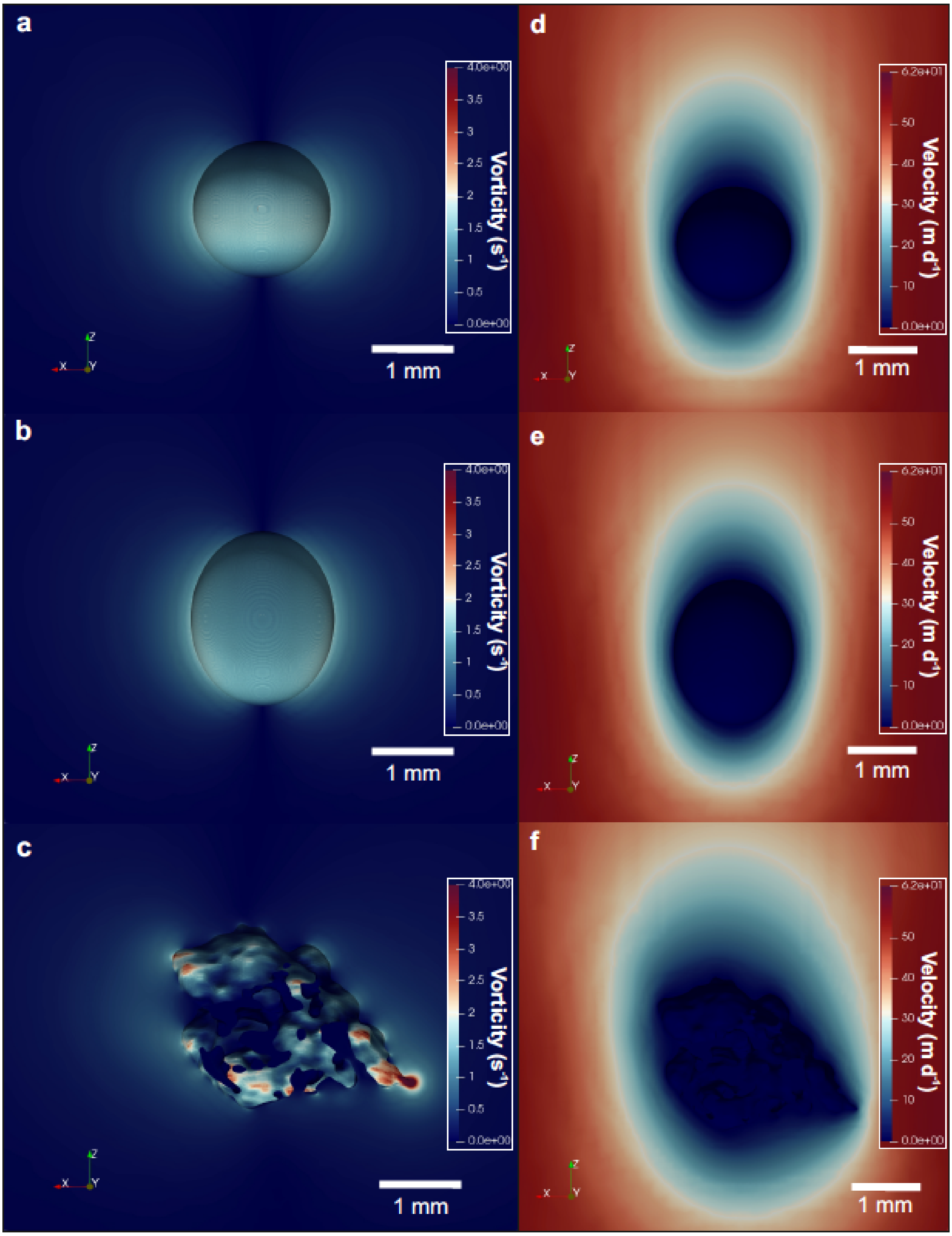

Fig. 4. Model derived vorticity fields (a-c) and flow velocity along the Z-axis (d-f) for the sphere (a & d), ellipsoid (b & e) and aggregate (c & f). The coordinate axes shows the orientation at which the model output is depicted.

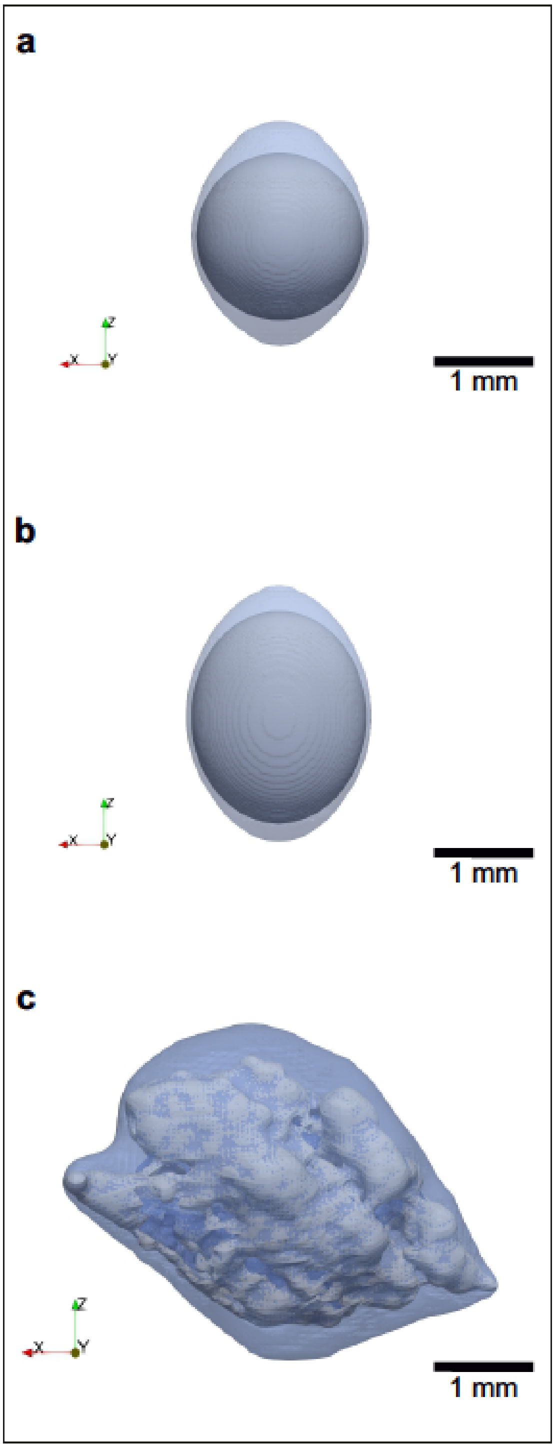

Fig. 5. Model derived boundary layer shape for the sphere (a), ellipsoid (b) and aggregate (c). The depicted boundary layer was defined as water velocities which are within ≥90 - 100% of the terminal settling velocity. The coordinate axes shows the orientation at which the model output is depicted.

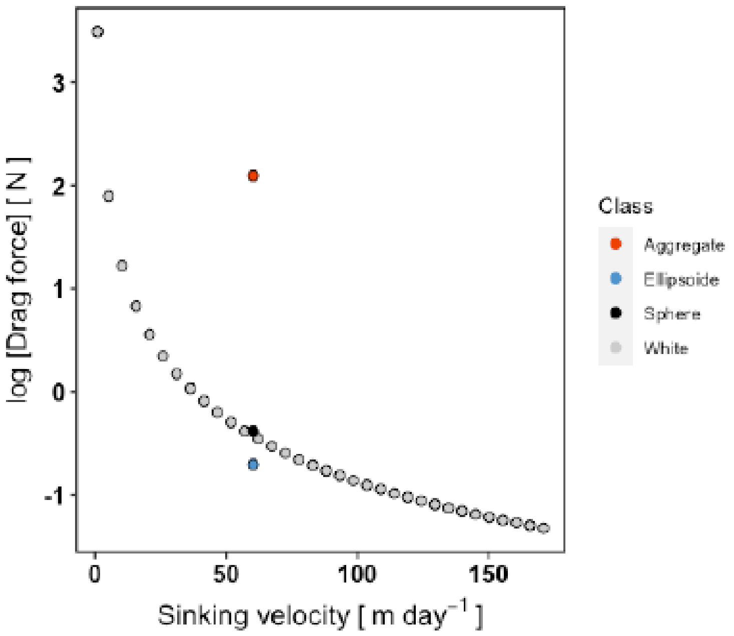

Fig. 6. Generated drag force of theoretical and model derived settling for different shapes. Light grey dots depict theoretical values for generated drag force with increasing settling velocities according to White et al. 2005. The remaining dots show the generated drag force on the aggregate (red), ellipsoid (blue) and sphere (black), which was derived from the model output.

Table. 1. Comparative overview table of sphere, ellipsoid and aggregate properties regarding shape, respiration and hydrodynamic features. The 10% value for the boundary layer variables indicates that the boundary layer was defined water velocities which are within ≥90 - 100% of the terminal settling velocity. Details on respective variables can be obtain from the material & methods section.

	Sphere	**Ellipsoid**	**Aggregate**
Surface area (excluding pore space)	0.080 cm^2	0.091 cm^2	0.189 cm^2
Surface area (including pore space)			0.358 cm^2
Volume (excluding pore space)	2.14 mm^3	2.43 mm^3	3.86 mm^3
Volume (including pore space)			3.18 mm^3
Z axis diameter	0.160 cm	0.208 cm	0.212 cm
Total drag coefficient	25.093	18.164	298.238
Pressure drag coefficient	8.255	4.247	121.500
Viscous drag	16.838	13.917	176.737
Drag	0.683 N	0.494 N	8.110 N
Excess density	$5.988 * 10^{-4}$ g cm^{-3}	$3.334 * 10^{-4}$ g cm^{-3}	$5.373 * 10^{-3}$ g cm^{-3}
Boundary layer area (10%)	0.20 cm^2	0.20 cm^2	0.67 cm^2
Boundary layer volume (10%) (including pore space)	3.12 mm^3	3.25 mm^3	6.11 mm^3
Area integrated O_2 flux	10.61 nmol O_2 agg^{-1} d^{-1}	12.08 nmol O_2 agg^{-1} d^{-1}	25.07 nmol O_2 agg^{-1} d^{-1}
Volumetric O_2 flux	4.96 nmol O_2 mm^{-3} d^{-1}	4.96 nmol O_2 mm^{-3} d^{-1}	6.49 nmol O_2 mm^{-3} d^{-1}

Discussion

In this study, we show for the first time a three-dimensional representation of the internal and external structures of a soft embedded aggregate using magnetic resonance imaging (MRI). A major constrain in the study of marine aggregates is their highly sensitive structure. This makes the study of single aggregates challenging as minor disturbances may already result in the alteration or disruption of the aggregate structure, thus affecting the outcome of measurements. In the case of our study, it is possible that the aggregate structure was affected by the aggregate embedding into agar. Embedding of marine aggregates in media such as cryogels (Ebersbach and Trull 2008; Laurenceau-Cornec et al. 2015; Wiedmann et al. 2016, Flintrop et al. 2018), hard resin, or agar (Rogge et al. 2018) have previously been used to fix and preserve single aggregates for analyses with minimal impact on their structure. The utilized method of soft-embedding in agar for the fixation of the marine aggregate was suggested to be minimal invasive (Rogge et al. 2018). To further minimize structural disturbances, we used a gradient embedding which dampened the impact of the settling aggregate on the cured agar during the embedding process.

Repeated measurements of the length, width and height of the embedded aggregate resulted in a volume increase of the fitted ellipsoid of ~5%, which is within an expected range of measuring error and suggests that no condensation or swelling of the aggregate occurred after embedding. However, it should be noted that in comparison to the length measurements obtained in the flow chamber, measurements of the aggregate height where smaller in the cured agar block while the measured width was larger. Due to the sensitive structure of the aggregate, the hydrodynamic forces while settling will deform an aggregates structure into a more streamline shape. The observed difference in aggregate height and width are therefore likely a result of embedding the aggregate in a quasi-suspended state, which also explains the relatively more elongated shape of the aggregate along the z-axis when compared to the shape derived from MRI (Fig. 2). The amount of deformation between measurements of the settling aggregate in the flow chamber and the sedimented aggregate in the embedding medium strongly depends on the composition of the embedded aggregate. We formed aggregates from phytoplankton cultures of diatoms and *Phaeocystis antarctica* which produce very porous aggregates with high quantities of TEP (Transparent exopolymer particles; Passow 2000, Reigstad & Wassmann 2007, Fig. S2.). However, we expect the effect of hydrodynamic deformation of the aggregate structure to be less in more compact aggregates and to be non-existing for zooplankton fecal pellets. While this caveat should be considered for the interpretation of the embedded aggregate, we observed discrepancies between the microscope and MRI that were larger than what could be explained by the embedding procedure alone. Hence, we consider the combination of MRI with soft embedding in agar as a powerful new tool to study marine aggregates on the sub-aggregate level.

Impact of geometric volume estimations on total aggregate volume

In experimental setups, aggregate size is determined from measurements of aggregate length, width and height and the equivalent spherical diameter is calculated from the aggregate volume, typically by assuming that the aggregate has an ellipsoidal shape (e.g. Ploug and Grossart 2000, Iversen & Ploug 2010, Iversen & Robert 2015). While most marine snow aggregates tend to have ellipsoidal shapes, they can have many other shapes including spherical, tubular, cylindrical, and even comet shapes, meaning that the aggregate has a spherical front with a comet tail in its wake.

The aggregate volume we obtained from MRI measurements was 60% larger with a 2-fold larger outside surface area, compared to the optically fitted ellipsoid. As aggregate shapes can be highly divers, the utilized geometric shape will impact how well the true aggregate volume and surface area are represented. The volume derived from a fitted rectangle, for instance, showed a better fit for our aggregate by only overestimating the MRI derived volume by ~20% and underestimating the surface area by ~10%. It is expected, however, that different aggregate shapes would yield different results, thus implying that estimations of volume and surface area of individual aggregates may bear large errors depending on the fitted shape.

This observations in turn may have large consequences for various practices which are based on volume and area estimates that are derived from fitted geometric shapes. For instance, the respiratory CO_2 flux of the microbial community on an aggregate is commonly derived from measurements of oxygen concentration profiles through the aggregate-water interface of the diffusive boundary layer (e.g. Ploug et al. 2008, Iversen & Ploug 2013). To determine the total CO_2 respiration, the respiratory CO_2 flux is then integrated by the area of the aggregate which commonly is derived using a fitted ellipsoid and thus will alter in accordance to the derived surface area (Ploug et al. 2008, Iversen & Ploug 2013). Another example are particle camera systems that detect particle distributions throughout the water column and are commonly used to estimate aggregate sizes throughout the water column by fitting geometric shapes to the aggregates captured in the images. With these derived size estimations, budgets of carbon content throughout the water column (Kiko et al. 2017) and estimates of vertical carbon flux are commonly computed (Guidi et al. 2008, Iversen et al. 2010, McDonnell & Buesseler 2010). It should be noted though that a multitude of empirical observations showed coherent predictions with estimates from ellipsoid shape approximations. For instance, deep ocean fluxes from a global spanning list of sediment trap records could be accurately predicted from aggregate respiration rates that are based on ellipsoid shape approximations (Iversen & Ploug 2013). However, controversial observations of oceanic carbon budgets and bathypelagic respiration rates have frequently been observed (Burd et al. 2010). Considering that the mentioned examples are fundamental for global oceanic carbon flux and budget estimates, the observed mismatch between the MRI and ellipsoid derived aggregate surface area and volume demonstrate that the applied method for aggregate size determination is fundamental for the analysis and conclusions regarding the biological pump, and should be considered carefully.

Impact of vorticity fields on aggregate colonization

The modelled flow velocity fields followed the surface of the sphere, ellipsoid and aggregate smoothly along the Z-axis. This is in line with previous observations of sphere and aggregate velocity flow fields at Reynolds numbers < 5 (Kiørboe et al. 2001, Zetsche et al. 2020). Experimental and model-based observations of microbial colonization on a pillar as well as protruding surfaces show, that attachment of motile bacteria occurs primarily in the downstream direction of the flow (Secchi et al. 2020). This downstream attachment of motile bacteria was suggested to be promoted by the formation of local vorticity which drives the attachment of the bacteria by creating a local rotation towards the surface (Zetsche et al. 2020, Secchi et al. 2020). Our flow model showed overall higher vorticity on the rough surfaces of the aggregate compared to the ellipsoid and sphere with both smooth surfaces

(Fig. 4 a-c). At lateral extensions along the surface of the aggregate, the model showed local maxima of vorticity (Fig. 4 c), which is in line with previous observations using particle image velocimetry (PIV, Zetsche et al. 2020). This may therefore suggest, that the rough surface areas of marine aggregates may enhance the potential for microbial colonization and potentially particle scavenging. This also suggests that the attachment and colonization of motile bacteria occurs at different regions of individual aggregates and that the colonization mechanisms are different between aggregates with smooth versus rough surfaces, i.e. colonization on smooth aggregates mostly occurs downstream, while attachment to aggregates with rough surfaces occur downstream of the aggregate itself and downstream of laterally extending structures.

Visualization of internal pore space - implications for microbial communities and flow

MRI allowed us to visualize the internal pore spaces of an aggregate. The visualisation of the internal pore space showed isolated chambers and tunnels that spread and connected throughout the aggregate as well as far reaching depressions on the surface. Compared to the smooth surface of the ellipsoid, the highly heterogenous structures of the aggregate resulted in surface area estimates which were 2-fold larger when only considering the outside surface and 4-fold larger when additionally taking the internal pore space into account. This suggests that marine aggregates have larger areas for microbial colonization than what is estimated when calculating the surface area of a smooth ellipsoid. Further, aggregates have been observed to host divers and distinct microbial communities (Thiele et al. 2015). Heterogenous structures such as individual pores or local depressions may stimulate the formation of diverse communities on a relatively small spatial scale, as indicated by the heterogenous distribution of individual bacterial clades throughout aggregate structures (Flintrop et al. 2018). Surface heterogeneity from structures of marine aggregates may therefore be crucial for the diversity of microbial communities which is likely to affect particle degradation and nutrient cycling within aggregate attached microbial communities.

Internal flow and consequential solute transport through aggregates has been suggested through connecting tunnel structures (Li & Logan 2001, Ploug et al. 2002). However, so far there has been no direct observation of flow through marine aggregates (Ploug & Passow 2007, Zetsche et al. 2020). Our model observations of fluid flow around the MRI derived aggregate did not show any indications for flow through the internal pore space despite the presence of connecting channels. This suggests that the viscous forces of water at low Reynolds numbers within the aggregate boundary layer decelerates the flow velocity of oncoming water and therefore prevents flow within the pore channels (Fig. 4f). This indicates that flow as a mechanism for solute transport can likely be neglected and suggests that diffusion is the main mechanism for solute transport within settling aggregates.

Previous estimations of the pore water fraction in diatom aggregates ranged between 88 – 98% of the total aggregate volume (Ploug & Passow 2007). The total volume of the MRI derived internal pockets, tunnels and depressions in the aggregate only amounted to ~18% of the total aggregate volume. However, it is important to consider that the detection limit of our MRI measurements was 39 µm^3 per voxel. This implies that in order to detect a pore structure, a coherent signal of multiple voxels is necessary, thus suggesting that the true detection limit for internal pore spaces within the aggregate is above 78 µm^3 using MRI. Considering that aggregates contain pores with sizes well below our detection limit (Flintrop et al. 2018, Radic et al. 2011), this suggests that we only observe the upper size fraction of aggregate pore spaces from our MRI measurements. However, the MRI derived pore space shows larger sized structures that do not contain organic matter i.e. are filled with water. Therefore, the combination of calculated estimates for aggregate pore space with larger sized and water filled pore structures from the MRI would give a more accurate estimate of the porewater fraction in marine aggregates.

By combining the experimentally derived regression of pore water fraction per aggregate size from Ploug & Passow (2007) with aggregate volume and pore space measurements derived from the MRI, we obtain a total pore water fraction of 0.899. These findings are well within the range of pore water fractions from diatom aggregates (Ploug & Passow 2007) and are expected, considering that the water fraction for large scale pore spaces only shifted from a previously assumed pore water fraction of ~0.90 (Ploug & Passow 2007) to 1.00 in our case. We therefore suggest that our observations do not considerably alter previous estimations on aggregate porosity, but are more relevant for processes regarding microbial colonization and degradation.

Implications of drag force on the excess density of particles

The model derived output of the drag force which was generated for a smooth sphere was in accordance to theoretically based estimates according to White et al. 2005 (Fig. 6). This suggests that our model is capable to accurately represent the forces that are generated by an object that settles through water. The modelled drag force for the smooth ellipsoid was lower than it was for the sphere. This was expected, as ellipsoidal objects tend to have optimised streamline properties when the length along the z-axis exceeds that of the x- and y-axis (White et al. 2005), as it did in our case. In contrast, the generated drag force on the model aggregate exceeded that of the sphere by 12-fold (Fig. 6). This was partially due to a higher proportion of pressure drag which accounted for ~40% of the total drag on the aggregate and was formed from hydrodynamically blunt areas of the heterogenous surface structure. In addition, the modelled viscous drag was ~10-fold higher for the aggregate compared to the sphere. This was likely due to the larger body of water which was moved by the settling aggregate compared to the sphere, as indicated from the larger sized boundary layer (table. 1). It should therefore be considered that heterogenous surface structures of settling aggregates generate substantially higher drag forces than idealized spherical and ellipsoidal model aggregates with smooth surfaces.

Calculations for the excess density of settling aggregates are directly tied to the amount of generated drag via the drag coefficient (equation 1). Therefore, the excess density of the aggregate was 12-fold higher than the excess density of the sphere and 16-fold higher than it was for the ellipsoid. The excess density of our aggregate was comparable to previous measurements of aggregates with settling velocities of ~220 m day^{-1} i.e. four times higher than the measured settling velocity of ~60 m day^{-1} (Iversen & Ploug 2010). In contrast, the excesses densities of the sphere and ellipsoid were within the range of aggregates with similar settling velocities to our aggregate i.e. ~60 m day^{-1} (Iversen & Ploug 2010). The drag coefficient of aggregates is commonly derived from the theoretical drag coefficients derived for a sphere, and hence Stokes law, since an accurate determination of drag coefficients from particles with heterogenous surface structures was so far not possible. This implies that pressure drag was previously not accounted for, since Stokes law only considers the forces from viscous or friction drag. This suggests that excesses densities of aggregates are underestimated when the drag coefficient is derived from a sphere using Stokes law. Hence, it seems that excesses densities of more natural aggregates with heterogenous surface structures should be a magnitude larger than previously estimated. These observations may have implications on flux estimations where particle settling velocities are derived from Stokes law by assuming a spherical shape (Guidi et al. 2008, McDonnell & Buesseler 2012). Following these assumptions, the underestimated drag force would result in an overestimation for particle settling velocities which would therefore increase estimations of carbon flux.

Conclusion

In this study, we were for the first time able to accurately visualize the internal and external structures of an aggregate in a minimal invasive and three-dimensional manner. Our obtained results of the aggregate volume and surface area indicated large discrepancies with established practices that fit geometric shapes e.g. ellipsoids or spheres, according to length or area measurements of individual aggregates. These results therefore suggest, that fitted geometric shapes may introduce biases to estimations which are based on aggregate size, such as aggregate carbon content, export fluxes or aggregate settling velocities. In addition, the shifts in hydrodynamic properties due to the heterogenous shapes may have implications on particle colonization from ambient bacteria and community distributions throughout the aggregate. However, it should be considered that the presented and discussed implications of our findings stem from measurements based on a single aggregate and are therefore expected to vary. None the less, our results demonstrate how crucial the correct parameterization of aggregate volume and surface area are for various practices and processes, including microbial colonization and respiration, calculations of oceanic carbon export fluxes and hydrodynamic forcing around settling aggregates. Future work should therefore carefully consider the shape of the aggregate when calculating volume and surface area. MRI may be a helpful tool for aggregate studies and has a great potential to improve our knowledge on aggregate structures, both internal and external, and how they impact small-scale processes within aggregates as well as the settling through and solute exchange with the surrounding water.

References

Alldredge, A. L., & Silver, M. W. (1988). Characteristics, dynamics and significance of marine snow. *Progress in Oceanography*, *20*(1), 41–82. https://doi.org/10.1016/0079-6611(88)90053-5

Arnosti, C. (2011). Microbial extracellular enzymes and the marine carbon cycle. *Annual Review of Marine Science*, *3*, 401–425. https://doi.org/10.1146/annurev-marine-120709-142731

Azam F, Martinez J, Smith DC (1993) Bacteria-organic matter coupling on marine aggregates. In: Guerrero R, PedrósAlió C (eds) Trends in microbial ecology. Spanish Society for Microbiology, Barcelona, p 410–414

Bachmann, J., Heimbach, T., Hassenrück, C., Kopprio, G. A., Iversen, M. H., Grossart, H. P., & Gärdes, A. (2018). Environmental drivers of free-living vs. particle-attached bacterial community composition in the Mauritania upwelling system. *Frontiers in Microbiology*, *9*(NOV), 1–13. https://doi.org/10.3389/fmicb.2018.02836

Boyd, P. W., Claustre, H., Levy, M., Siegel, D. A., & Weber, T. (2019). Multi-faceted particle pumps drive carbon sequestration in the ocean. *Nature*, *568*(7752), 327–335. https://doi.org/10.1038/s41586-019-1098-2

Burd, A. B., Hansell, D. A., Steinberg, D. K., Anderson, T. R., Arı, J., Buesseler, K. O., Dehairs, F., Jackson, G. A., Baltar, F., Beaupre, S. R., Kadko, D. C., Koppelmann, R., Lampitt, R. S., Nagata, T., Reinthaler, T., Robinson, C., Robison, B. H., Tamburini, C., & Tanaka, T. (2010). *Deep-Sea Research II Assessing the apparent imbalance between geochemical and biochemical indicators of meso- and bathypelagic biological activity : What the @ $] ! is wrong with present calculations of carbon budgets ? 57*, 1557–1571. https://doi.org/10.1016/j.dsr2.2010.02.022

Ebersbach, F., & Trull, T. W. (2008). Sinking particle properties from polyacrylamide gels during the KErguelen Ocean and Plateau compared Study (KEOPS): Zooplankton control of carbon export in an area of persistent natural iron inputs in the Southern Ocean. *Limnology and Oceanography*, *53*(1), 212–224. https://doi.org/10.4319/lo.2008.53.1.0212

Edzes, H. T., Van Dusschoten, D., & Van As, H. (1998). Quantitative T2 imaging of plant tissues by means of multi-echo MRI microscopy. *Magnetic Resonance Imaging*, *16*(2), 185–196. https://doi.org/10.1016/S0730-725X(97)00274-9

Fadeev, E., Rogge, A., Ramondenc, S., Nöthig, E. M., Wekerle, C., Bienhold, C., Salter, I., Waite, A. M., Hehemann, L., Boetius, A., & Iversen, M. H. (2021). Sea ice presence is linked to higher carbon export and vertical microbial connectivity in the Eurasian Arctic Ocean. *Communications Biology*, *4*(1), 1–13. https://doi.org/10.1038/s42003-021-02776-w

Ferziger J. H., Peric M., Computational Methods for Fluid Dynamics, Springer, 3rd Ed., 2001.

Flintrop, C. M., Rogge, A., Iversen, M. H., Miksch, S., Thiele, S., & Waite, A. M. (2018). *OCEANOGRAPHY : METHODS Embedding and slicing of intact in situ collected marine snow. 2.* https://doi.org/10.1002/lom3.10251

Gärdes, A., Iversen, M. H., Grossart, H. P., Passow, U., & Ullrich, M. S. (2011). Diatom-associated bacteria are required for aggregation of Thalassiosira weissflogii. *ISME Journal*, *5*(3), 436–445. https://doi.org/10.1038/ismej.2010.145

Guidi, L., Jackson, G. A., Stemmann, L., Miquel, J. C., Picheral, M., & Gorsky, G. (2008). Relationship between particle size distribution and flux in the mesopelagic zone. *Deep-Sea Research Part I: Oceanographic Research Papers*, *55*(10), 1364–1374. https://doi.org/10.1016/j.dsr.2008.05.014

Guillard, R.R.L. (1975). Culture of Phytoplankton for Feeding Marine Invertebrates. In: Smith, W.L., Chanley, M.H. (eds) Culture of Marine Invertebrate Animals. Springer, Boston, MA. https://doi.org/10.1007/978-1-4615-8714-9_3

Iversen, M. H., Nowald, N., Ploug, H., Jackson, G. A., & Fischer, G. (2010). High resolution profiles of vertical particulate organic matter export off Cape Blanc, Mauritania: Degradation processes and ballasting effects. *Deep-Sea Research Part I: Oceanographic Research Papers*, *57*(6), 771–784. https://doi.org/10.1016/j.dsr.2010.03.007

Iversen, M. H., & Ploug, H. (2010). Ballast minerals and the sinking carbon flux in the ocean: Carbon-specific respiration rates and sinking velocity of marine snow aggregates. *Biogeosciences*, *7*(9), 2613–2624. https://doi.org/10.5194/bg-7-2613-2010

Iversen, M. H., & Ploug, H. (2013). *Temperature effects on carbon-specific respiration rate and sinking velocity of diatom aggregates – potential implications deep ocean Earth for*. 4073–4085. https://doi.org/10.5194/bg-10-4073-2013

Iversen, M. H., & Robert, M. L. (2015). Ballasting effects of smectite on aggregate formation and export from a natural plankton community. *Marine Chemistry*, *175*, 18–27. https://doi.org/10.1016/j.marchem.2015.04.009

Kester, D. R., Duedall, I. W., Connors, D. N., & Pytkowicz, R. M. (1967). Department of Zoology and Plankton Laboratory, University of Southampton, England. *Limnology & Oceanography*, *12*, 176–179.

Kiko, R., Biastoch, A., Brandt, P., Cravatte, S., Hauss, H., Hummels, R., Kriest, I., Marin, F., McDonnell, A. M. P., Oschlies, A., Picheral, M., Schwarzkopf, F. U., Thurnherr, A. M., & Stemmann, L. (2017). Biological and physical influences on marine snowfall at the equator. *Nature Geoscience*, *10*(11), 852–858. https://doi.org/10.1038/NGEO3042

Kiørboe, T., Ploug, H., & Thygesen, U. H. (2001). Fluid motion and solute distribution around sinking aggregates. I. Small-scale fluxes and heterogeneity of nutrients in the pelagic environment. *Marine Ecology Progress Series*, *211*(Kiørboe 2000), 1–13. https://doi.org/10.3354/meps211001

Laurenceau-Cornec, E. C., Trull, T. W., Davies, D. M., Bray, S. G., Doran, J., Planchon, F., Carlotti, F., Jouandet, M. P., Cavagna, A. J., Waite, A. M., & Blain, S. (2015). The relative importance of phytoplankton aggregates and zooplankton fecal pellets to carbon export: Insights from free-drifting sediment trap deployments in naturally iron-fertilised waters near the Kerguelen Plateau. *Biogeosciences*, *12*(4), 1007–1027. https://doi.org/10.5194/bg-12-1007-2015

Li, X. Y., & Logan, B. E. (2001). Permeability of fractal aggregates. *Water Research*, *35*(14), 3373–3380. https://doi.org/10.1016/S0043-1354(01)00061-6

Mcdonnell, A. M. P., & Buesseler, K. O. (2010). *Variability in the average sinking velocities of marine particles*. *55*(5), 1–14. https://doi.org/10.4319/lo.2010.55.5.0000

Mestre, M., Ruiz-González, C., Logares, R., Duarte, C. M., Gasol, J. M., & Sala, M. M. (2018). Sinking particles promote vertical connectivity in the ocean microbiome. *Proceedings of the National Academy of Sciences of the United States of America*, *115*(29), E6799–E6807. https://doi.org/10.1073/pnas.1802470115

Moradi, N., Klawonn, I., Iversen, M. H., Wenzhöfer, F., Grossart, H. P., Ploug, H., Fischer, G., & Khalili, A. (2021). A Novel Measurement-Based Model for Calculating Diffusive Fluxes Across Substrate-Water Interfaces of Marine Aggregates, Sediments and Biofilms. *Frontiers in Marine Science*, *8*(August), 1–12. https://doi.org/10.3389/fmars.2021.689977

Passow, U., & Alldredge, A. L. (1994). *A dye-binding assay for the spectrophotometric measurement of transparent exopolymer particles (TEP)*. 1326–1335.

Passow, U. (2000). Formation of transparent exopolymer particles, TEP, from dissolved precursor material. *Marine Ecology Progress Series*, *192*, 1–11. https://doi.org/10.3354/meps192001

Ploug, H., & Jørgensen, B. B. (1999). A net-jet flow system for mass transfer and microsensor studies of sinking aggregates. *Marine Ecology Progress Series*, *176*(1987), 279–290. https://doi.org/10.3354/meps176279

Ploug, H., & Grossart, H. P. (2000). Bacterial growth and grazing on diatom aggregates: Respiratory carbon turnover as a function of aggregate size and sinking velocity. *Limnology and Oceanography*, *45*(7), 1467–1475. https://doi.org/10.4319/lo.2000.45.7.1467

Ploug, H., & Passow, U. (2007). Direct measurement of diffusivity within diatom aggregates containing transparent exopolymer particles. *Limnology and Oceanography*, *52*(1), 1–6. https://doi.org/10.4319/lo.2007.52.1.0001

Ploug, H., Iversen, M. H., & Fischer, G. (2008). *Ballast , sinking velocity , and apparent diffusivity within marine snow and zooplankton fecal pellets : Implications for substrate turnover by attached bacteria*. *53*(5), 1878–1886.

Radić, T. M., Svetličić, V., Žutić, V., & Boulgaropoulos, B. (2011). Seawater at the nanoscale: Marine gel imaged by atomic force microscopy. *Journal of Molecular Recognition*, *24*(3), 397–405. https://doi.org/10.1002/jmr.1072

Reigstad, M., & Wassmann, Æ. P. (2007). *Does Phaeocystis spp . contribute significantly to vertical export of organic carbon ?* 217–234. https://doi.org/10.1007/s10533-007-9093-3

Rogge, A., Flintrop, C. M., Iversen, M. H., Salter, I., Fong, A. A., Vogts, A., & Waite, A. M. (2018). Hard and soft plastic resin embedding for single-cell element uptake investigations of marine-snow-associated microorganisms using nano-scale secondary ion mass spectrometry. *Limnology and Oceanography: Methods*, *16*(8), 484–503. https://doi.org/10.1002/lom3.10261

Secchi, E., Vitale, A., Miño, G. L., Kantsler, V., Eberl, L., Rusconi, R., & Stocker, R. (2020). The effect of flow on swimming bacteria controls the initial colonization of curved surfaces. *Nature Communications*, *11*(1), 1–12. https://doi.org/10.1038/s41467-020-16620-y

Stejskal E. O. and Tanner J. E., "Spin Diffusion Measurements: Spin Echoes in the Presence of a Time Dependent Field Gradient." J. Chem. Phys. 42, 288 (1965)

Thiele, S., Fuchs, B. M., Amann, R., & Iversen, M. H. (2015). Colonization in the photic zone and subsequent changes during sinking determine bacterial community composition in marine snow. *Applied and Environmental Microbiology*, *81*(4), 1463–1471. https://doi.org/10.1128/AEM.02570-14

Thiele, S., Basse, A., Becker, J. W., Lipski, A., Iversen, M. H., & Mollenhauer, G. (2019). Microbial communities in the nepheloid layers and hypoxic zones of the Canary Current upwelling system. *MicrobiologyOpen*, *8*(5), 1–13. https://doi.org/10.1002/mbo3.705

Turner, J. T. (2015). Progress in Oceanography Zooplankton fecal pellets , marine snow , phytodetritus and the ocean ' s biological pump. *Progress in Oceanography*, *130*, 205–248. https://doi.org/10.1016/j.pocean.2014.08.005

van der Jagt, H., Iversen, M. H., Friese, C., & Stuut, J. W. (2018). *The ballasting effect of Saharan dust deposition on aggregate dynamics and carbon export : Aggregation , settling ,*. https://doi.org/10.1002/lno.10779

Volk, T., & Hoffert, M. I. (1985). EFFICIENCIES IN OCEAN-DRIVEN CARBON PUMPS : ANALYSIS Department of Applied Science , New York University models solubility pump signal , subject to uncertainties in the C : P Redfield changes which lower pCO • atm in the model are vertical carbon Since di. *The Carbon Cycle and Atmospheric CO2: Natural Variations Archean to Present*, *32*, 99–110.

Wiedmann, I., Reigstad, M., Marquardt, M., Vader, A., & Gabrielsen, T. M. (2016). Seasonality of vertical flux and sinking particle characteristics in an ice-free high arctic fjord-Different from subarctic fjords? *Journal of Marine Systems*, *154*, 192–205. https://doi.org/10.1016/j.jmarsys.2015.10.003

White, F. M., & Majdalani, J. (2006). *Viscous fluid flow* (Vol. 3, pp. 433-434). New York: McGraw-Hill.

Zetsche, E. M., Larsson, A. I., Iversen, M. H., & Ploug, H. (2020). Flow and diffusion around and within diatom aggregates: Effects of aggregate composition and shape. *Limnology and Oceanography*, *65*(8), 1818–1833. https://doi.org/10.1002/lno.11420

Competing Interest: The authors declare that they have no competing interest. **Data availability Statement:** Data used in this study are made available at PANGEA.

Manuscript II

Lateral advection of shelf produced organic matter is the main contributor to deep ocean carbon flux in the Cape Blanc Upwelling region

Steffen Swoboda[1*], Hannah Marchant[1,2], Soeren Ahmerkamp[1,2], Jan-Hendrik Hehemann[1,2], Hagen Buck-Wiese[1,2], Farooq Moin Jalaluddin[1,2], Marius Becker[3], Arjun Chennu[4], Oscar E. Romero[1,6], Kai Schwalfenberg[5], Simon Ramondenc[1,6], Morten H. Iversen[1,6*]

[1]MARUM and University of Bremen, Leobener Str. 8, 28359 Bremen, Germany

[2]Max Planck Institute for Marine Microbiology, Celsiusstraße 1 ,28359 Bremen, Germany

[3]Kiel University, Institute of Geosciences, Otto-Hahn-Platz 1, 24118 Kiel, Germany

[4]Leibniz Centre for Tropical Marine Research Fahrenheitstraße 6, 28359 Bremen, Germany

[5]Institute for Chemistry and Biology of the Marine Environment, Carl-von-Ossietzky-Straße 9-11, 26129 Oldenburg, Germany

[6]Alfred Wegener Institute, Alfred Wegener Institute Helmholtz Centre for Polar and Marine Research, Am Handelshafen 12, 27570 Bremerhaven, Germany

*Corresponding authors:

Steffen Swoboda
Morten H. Iversen

Abstract

Sub-surface clouds of particulate matter (nepheloid layers) are a persistent feature in the oceanic Eastern Boundary Upwelling region off Cape Blanc. However, it is unclear to which extent the particulate organic matter within these clouds sinks and contributes to deep ocean carbon export. In this study we combined short-term carbon fluxes from 8 expeditions with process studies and a 23-years time-series of deep ocean carbon fluxes. Thereby we assessed the inter-annual and inter-seasonal contribution of horizontal advected particles to carbon export in the deep ocean off Cape Blanc. Our results revealed that particle clouds are composed of slow sinking material advected offshore from the productive shallow shelf. The particle clouds accounted for ~80% of the total organic carbon export to the adjacent deep ocean waters, with the remainder originating from primary production in open ocean waters. Considering that marine particle clouds are observed throughout the global ocean, our results suggest that the common approaches used to estimate carbon flux attenuation, which only consider a vertical component, will lead to overestimations in carbon flux and turnover. Recognition of particle clouds as an integral part of the biological carbon pump and inclusion of lateral advection in future carbon budgets, will allow more accurate quantifications of export efficiency and biological turnover, hence, improve the data used to model and predict oceanic carbon sequestration.

Plain Language Summary

The biological carbon pump transfers biologically produced organic carbon from the sunlit surface ocean to the deep sea via settling particles. This downward rain of “marine snow” through the water column is an essential component that leads to the uptake and storage of carbon dioxide in the oceans. Generally, this transfer to the deep ocean is considered as a vertical process; wherein organic carbon is formed in the surface ocean by phytoplankton and sinks out directly, in the same region. Here we show that a surprisingly large proportion of the carbon that reaches the deep ocean adjacent to a productive upwelling region is produced on the shallow shelf > 450 km away. This occurs because currents transport carbon rich particles in sub-surface “particle clouds” that sink very slowly. These particle clouds contribute ~80% of the organic carbon flux to the deep ocean, demonstrating that horizontal

transport can be more important than vertical transport for oceanic carbon sequestration. However, despite the importance of horizontal transport for oceanic carbon sequestration and Earth's climate, it is often overlooked in global modelling efforts.

1. Introduction

The biological carbon pump (BCP) mediates the transfer of organic matter from the surface to the deep ocean, fuelling sub-surface ecosystems, as well as contributing an estimated 6-17 Gt to annual carbon sequestration in the deep ocean and seafloor (Boyd et al. 2019). Sinking marine aggregates and fecal pellets are the main vectors of organic matter export within the BCP (Turner 2015), and the efficiency with which these particles are exported is dependent on the interplay between particle degradation and settling velocity (Iversen et al. 2010; Nowald et al. 2015). Particle degradation, and the associated attenuation of carbon flux, is largely driven by zooplankton feeding and microbial remineralization (van der Jagt et al. 2020, Jackson & Checkley 2011, Iversen et al. 2010). Typically, the majority of flux attenuation takes place in the upper few hundred meters of the water column (Martin et al. 1982) and the retention time of settling aggregates at these depths determine their attenuation (Stemmann et al. 2004, Iversen et al. 2010). Therefore, factors which increase the sinking velocity of aggregates directly impact the magnitude of carbon flux (Iversen and Ploug 2010). For example, particle ballasting from Saharan dust, biominerals or clay particles was shown to increase particle settling velocities by 2 to 4-fold, thus increasing the export efficiency by decreasing the time that a ballasted aggregate needed to sink through the water column, i.e. decreasing the time for degradation (Iversen et al. 2010, Iversen and Ploug 2010, Iversen & Robert 2015, van der Jagt et al. 2018).

The time that carbon is removed from exchange with the atmosphere depends on the depth to which it is exported to, with greater export depths leading to a longer sequestration time. This means that slow settling aggregates that are only exported to shallow depths may be transported back up to the surface ocean via resuspension and vertical mixing on daily to seasonal time-scales (Boyd et al. 2019). In this manner, the organic carbon from slow settling aggregates has a higher likelihood of being remineralised in the surface ocean where the produced carbon dioxide can exchange with the atmosphere. Similarly, the limited depths in shallow ocean margins may reduce the sequestration period of exported carbon. This is due to the shallow depth of remineralization for the sedimented aggregates, whereby the produced carbon dioxide may be released back into the atmostphere. If organic matter is advected from the shallow regions to the deep open ocean, the carbon may be sequestrered for long periods (e.g. Karakas et al. 2006, Frischknecht et al. 2018). Consequentially, the horizontal relocation of organic matter produced in shelf regions to the open ocean may dramatically increase the sequestration time of the carbon and thus increase the efficiency of the biological pump. Such horizontal transport mechanisms are typically observed in Eastern Boundary Upwelling Systems (EBUSs) where a fraction of the deep ocean carbon export may originate from production in the shallow ocean margins, i.e. in the shallow shelf region (e.g. Fischer et al. 2009, Romero et al. 2020).

EBUSs are among the most productive regions in the oceans, with the four major EBUSs (Canary, California, Benguela, and Humboldt upwelling system) contributing 10% of global marine primary production and ~20% of fisheries despite covering less than 1% of the ocean's surface (Carr 2002, Behrenfeld and Falkowski 1997, Pauly and Christensen 1995). EBUSs are characterized by strong along-shore trade winds that drive cross-shore Ekman transport which carries nutrient-rich deep waters into the euphotic zone (Garcia-Reyes et al. 2015, Jacox et al. 2015). This leads to high rates of primary production fueled by the high nutrient input and the strong offshore advection creates large surface filaments of phytoplankton resulting in strong lateral displacement of surface production and carbon export (e.g., Van Camp et al. 1991, Pelegrí et al. 2005, Gabric et al. 1993). In addition, intense bottom currents on the shallow continental shelf form so called "nepheloid layers" that, due to their slow settling velocity, are advected into the meso- and bathypelagic depths in the open ocean (e.g., California EBUS: Harlett 1973, Ransom et al. 1998; Canary EBUS: Freudenthal et al. 2001, Karakas et al. 2006, Nowald et al. 2006, Fischer et al. 2009, Ohde et al. 2015; Benguela EBUS: Inthorn et al. 2006, Waldron et al. 2009; Humboldt EBUS: Lam et al. 2018). Traditionally, these nepheloid layers have been considered to be composed from sediments that are resuspended from the shelf and slope seafloor (e.g. Gardner et al. 2018), however, several studies have found that nepheloid layers contain large marine snow particles and labile organic material with distinct microbial communities (Ransom et al. 1998, Santschi et al. 1998, Thiele et al. 2019, Iversen et al. 2010, Roullier et al. 2014, Puig et al. 2013, Romero et al. 2020). The marine snow within nepheloid layers include phytoplankton groups and microbial communities that are related to the pelagic environment (Ransom et al. 1998, Thiele et al. 2019, Romero et al. 2020). This suggests that nepheloid layers are formed from both benthic and pelagic material, which form what we hereafter refer to as “particle clouds” in the water column. These particle clouds transport slow-sinking organic carbon horizontally from the ocean margins to the deep ocean.

Several studies have previously investigated the processes responsible for lateral advection of surface production in EBUSs and the consequent impact on particulate organic carbon (POC) displacement and export via the biological carbon pump (Helmke et al. 2005, Amos et al. 2019, Chabert et al. 2020, Bonino et al. 2021, Lovecchio et al. 2017, Lovecchio et al. 2018, Santana-Fal´con et al. 2020, Frischknecht et al. 2018). However, despite being a persistent feature within EBUSs, the role that particle clouds and horizontal advection play for POC export has so far not been directly quantified from the shallow shelf to the deep open ocean. Here, we utilize POC fluxes obtained from 8 shipbound expeditions as well as a 23-years time-series of deep ocean POC fluxes to assess the inter-annual and inter-seasonal contribution of horizontal advection of particle clouds to carbon export in the deep ocean off Cape Blanc. We combine the long-term measurements with ship-based process studies to understand the mechanisms that shape the transport and distribution of particle clouds and sources and sinks of organic matter in the Canary Current-EBUS (CC-EBUS). Our results suggest that particle clouds are advected offshore from the productive shallow shelf and supply ~80% of the total carbon export to the deep ocean. Hence, a significant fraction of the deep ocean carbon flux is exported via horizontal transport of sub-surface particle clouds from the shelf region to the open ocean. We suggest a reassessment of organic matter fluxes in EBUSs and urge the consideration of off-shore advected particle clouds from ocean margins for global carbon budgets.

2. Material and Methods

2.1. Sampling stations

Field data were obtained during the RV Poseidon cruise (POS531) to the CC-EBUS off Cape Blanc from January 18th to February 1st 2019. Sampling was performed along a transect between 20°46.251' N – 21°12.618' N covering the shelf, slope and open pelagic water column via four key regions; the shallow shelf region (CB_{sh}; 17°10.859' W - 17°37.767' W), the continental slope (CB_s; 17°40.575' W - 17°44.779' W), euphotic open ocean (CB_{eu}; 18°44.219' W – 18°53.648' W), and mesotrophic open ocean (CB_{meso}; 20°51.919' W - 20°53.826' W). Two additional connecting stations were studied between CB_{eu} and CB_{meso} (Transect; 18°04.525' W – 18°24.222' W). Deployed instrumentation and measurements at each key region consisted of: Rosette water sampler, in situ particle camera, marine snow catcher (MSC), free-drifting sediment traps (hereafter referred to as "drifting trap") and measurements of primary production and standing stock of POC through the water column. Deployments at transect stations were limited to the rosette water sampler and in situ particle camera. A detailed sampling overview is given in Figure 1 and table S1 in Supporting Information. The rosette water sampler was equipped with a SBE 9 CTD (Sea-Bird Scientific, Bellevue, USA) for conductivity, temperature and pressure, a WET Labs ECO-AFL/FL (WET Labs Inc., Philomath, USA) for fluorescence and turbidity, and SBE 43 (Sea-Bird Scietific, Bellevue, USA) for dissolved oxygen measurements. Water currents from the surface to 100 m depth were continuously measured with a ship mounted 180 kHz acoustic doppler current profiler (ADCP; Teledyne Technologies, Thousand Oaks, USA) with a measuring interval of 5 Hz.

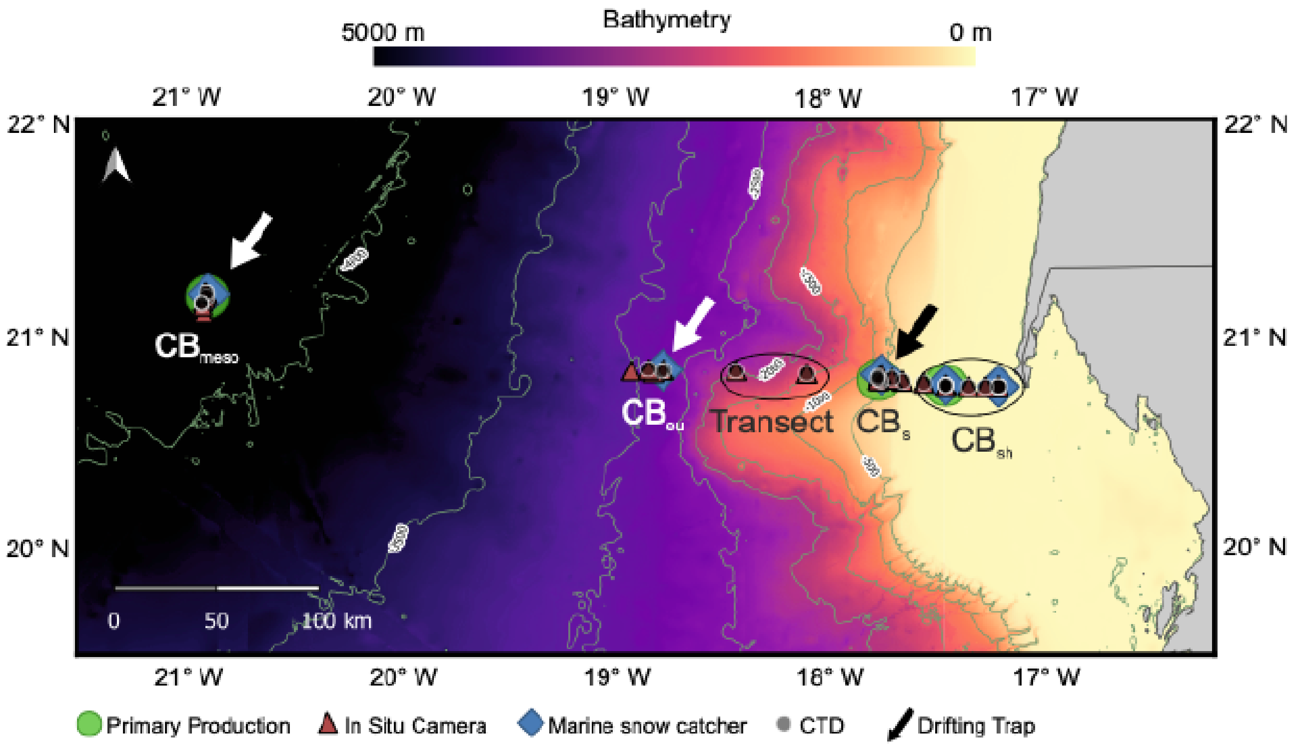

Figure 1. Overview map of the sampling areas and deployed devices during our process study on research expedition POS531 in 2019. Black circles indicate the extent of the CB$_{sh}$ and Transect sampling area. Icons indicate the sampling/deployment carried out at each location.

2.2. Vertical profiling of particle size-distributions and abundance

An underwater camera system was deployed to obtain images of particles every 1 meter along a vertical profile down to 500 m depth. The camera (Canon EOS 60D with a 50 mm prime lens) was set up to image a volume of 606 ml illuminated by a strobe flash. Particles were detected using the Image Processing Toolbox in MatLab (The MathWorks, Markussen et al. 2020) and were then assigned to one of 22 logarithmically-spaced size bins to account for decreasing abundance with increasing particle sizes (Jackson et al. 1997). The area-derived equivalent spherical diameter (ESD) of the particles was computed and the values divided into 22 logarithmically-spaced size bins between 107 µm – 6266 µm. The particle number abundance spectrum (f; # m^{-3} µm^{-1}) was calculated by dividing the concentration of particles per imaged volume (N_F; # m^{-3}) within the respective bin (Δd; µm):

$$f = \frac{N_F}{\Delta d} \qquad \text{(eq 1)}$$

From the resulting particle abundance spectrum (*f*), the derived ESD was then used to calculate the total particle volume of each size bin assuming a spherical shape. The particle camera system accurately quantified particles with ESDs ranging from 107 – 6266 µm. The optical resolution of the camera system could not quantify particles < 107 µm, which resulted in a decrease in particle number size-spectra for smaller particles (Figure S1). Particles larger than 6266 µm were very rare (< 3 particles per bin) and were excluded from further analysis since their numbers were not significantly reliable (Jackson et al. 1997).

2.3. Vertical export fluxes

Vertical export fluxes were measured over a period of 24 h with an array of three drifting traps (Sediment trap 28.400, KC Denmark, Denmark) located at 100, 200 and 400 m depth tethered to surface buoys. At each collection depth, the drifting trap array consisted of four gyroscopically mounted collection tubes (diameter: 11 cm and length: 70 cm), which were filled with filtered seawater prior to their deployment. The filtered seawater was made denser by adding an equivalent of 3 PSU of sodium chloride (NaCl).

Three collection tubes from each depth were used for biochemical analysis, while a fourth tube contained an insert cup that was filled with a viscous cryogel, referred to as gel trap (Tissue-Tek® O.C.T.™ Compound; Sakura Finetek Europe B.V., The Netherlands; hereafter referred to as "gel trap"). The gel trap collected intact marine aggregates without damaging or altering their size and structure (Thiele et al. 2015, Flintrop et al. 2018).

After the drifting traps were recovered, slow-sinking particles in the collection tubes were left to settle for 4h in the dark after which the overlying water was then gently siphoned off. The collected material was preserved with HgCl (0.14% final concentration) and kept at 4°C till further analysis. The cup inserts from the gel trap were removed, imaged and frozen at –20°C.

For measurements of POC and particulate organic nitrogen (PON), subsamples from drift trap samples were filtered onto pre-combusted and pre-weighed GF/F filters (Whatman GF/F 0.7µm, 25mm, GE Healthcare Europe GmbH, Germany). After drying (24h at 40°C), the filters were weighed and acid fumed (24 h with 37% HCl), dried once more (24h at 40°C) and then packed in tin boats for measurements of POC and PON content with a CHN elemental analyser (Elementar vario EL III, precision of ±0.7 µg C or ±0.3%). Values of POC:PON in units of mass where converted to molar units.

For analysis of volumetric particle- and zooplankton fecal pellet flux contribution to the measured drifting trap flux, gel trap samples were imaged (pixel size: 3.47 µm/px) with a custom-built camera setup. The camera setup (Basler acA4600 – 7gc, Basler AG, Germany, with a mounted Edmund Optics 10mm 0.5x inline compact telecentric lens, Edmund Optics, Germany) was attached to a motorized stage with a LED panel beneath on which the gel trap cups where placed and backlit. Processing and analysis of the cup images was performed with the software package Fiji (Schindelin et al. 2012) if not stated differently. Photographs were taken as a grid of 88 frames (12.8 mm x 10.2 mm per image; 8 x 11 images per cup) which covered the entire cup. From each grid frame, eight defined focus depths were imaged respectively to ensure all particles were included and in focus. The eight images of each respective grid frame were stacked using the focus stacking software Zerene stacker (Zerene Systems LLC, USA) and consecutively stitched together to form a 718 megapixel composite image which depicted the contents of the entire gel trap cup. Any collected zooplankton were manually selected and removed. For particle analysis, each image was converted to grey scale and the background was removed using a threshold value of 56 on a grayscale of 256 intensity levels. Fecal pellets were manually marked to analyse separately from phytoplankton aggregates and particles. Measured particles were assigned to one of 14 logarithmically-spaced size bins ranging from 20 µm – 1133 µm as previously described (Markussen et al. 2020).

2.4. Measurements of settling velocity and microbial degradation of particles

For the analysis of single-aggregate settling velocity and microbial respiration, particles were collected using a MSC. Sampling depths were 10 m below the chlorophyll maximum (Chl_{max}) layer which ranged between 20 – 60 m. On deck, captured particles within the MSC were left to settle for a minimum of 8 h before the top ~90 L from the 100 L contained in the MSC was gently drained. Afterwards, the lower collection cylinder of the MSC, in which the particles had settled, was removed and individual aggregates were collected for further analyses.

For measurements of settling velocity and respiration, particles were transferred to a flow chamber (5 cm diameter) which enables to maintain aggregates suspended by an opposing upward flow that was adjusted to the same velocity and the settling velocity of the individual aggregates (Ploug & Jørgensen 1999). The flow chamber was set up in an aquarium with an air diffuser and placed in a temperature-controlled room adjusted to the in situ water temperature in which particles were sampled.

Once the particles were suspended in the flow, settling velocities where measured in triplicates by dividing the flow rate with the area of the flow chamber. Particle size was measured in its length, width and height using an ocular (12x magnification) with a retical. The respective volumes were then calculated assuming an ellipsoid shape from which the ESD was derived.

Using a Clark-type oxygen microsensor (Unisense, OX-12, 10 µm tip diameter) mounted on a micromanipulator, the oxygen concentration was measured every 20 µm from 2 mm above the suspended aggregate's surface to the centre of the aggregate.

The oxygen flux of respective aggregates was calculated in nmol O_2 cm^{-2} h^{-1} using the model of Moradi et al. (2021), and then multiplied by the surface area for each aggregate to nmol O_2 h^{-1} agg^{-1}. The volumetric O_2 flux was then calculated by dividing the O_2 h^{-1} agg^{-1} by the calculated aggregate volume. The volumetric carbon respiration was calculated by assuming a one-to-one molar ratio from O_2 flux to CO_2 flux. Subsequently, the individual aggregates were transferred to an Utermöhl chamber and imaged to visually determine their composition using an inverted microscope (Zeiss, Axiovert 25).

2.5. O_2 fluxes in permeable sediments

Oxygen fluxes from the surficial sandy sediments on the continental shelf were estimated at two stations at CB_{sh} which were located in water depths of 29 m (20°46.352 N 17°11.027 W) and 59 m (20°46.654 N 17°25.675 W). Sediments at both stations consisted of permeable sandy sediments (see Table S2 in Supporting Information for sediment characteristics).

In situ O_2 penetration depth at both stations was determined using a benthic lander (Ahmerkamp et al. 2017). Subsequently, at each station, sediment was sampled using a van Veen Grab, from which the upper 2 cm of sediment was collected, homogenized and filled into acrylic flow through reactors (FTR) in triplicates to measure volumetric O_2 consumption rates (Ahmerkamp et al. 2017, Marchant et al 2016). Briefly, aerated bottom water was pumped upward through the FTR using a peristaltic pump (Cole Palmer MasterFlex) until the entire porewater volume in the FTR was exchanged with the aerated water. Porewater was sampled at ~10 discrete time points over ~120 minutes from an attachment at the bottom of the core equipped with an optode-based measurement system (OXFTC, Pyroscience). From the change in oxygen concentration over time, the volumetric oxygen consumption rates were determined.

Oxygen fluxes were estimated by integrating the volumetric oxygen consumption rates over the penetration depths based on a transport model published by Elliott and Brooks (1997 a & b), previously adapted in Marchant et al. (2016) and Ahmerkamp et al. (2017).

2.6. Measurements of primary production and particulate organic carbon standing stock

CO_2 fixation rates i.e. primary production at 5 m depth, were determined over 12 and 24 hours from water samples collected at each station following Martinez-Perez et al. (2016). For each station seawater was collected at 09:00 am via the ship inlet and filled into ten 620 mL incubation bottles. Subsequently, ^{13}C-DIC (NaH^{13}CO$_{3,}$ ≥98 % Sigma-Aldrich) was added to eight of the bottles to a final concentration of ~5%. The two incubations without added ^{13}C-DIC were terminated immediately to determine the natural abundance of ^{13}C in the POC, along with two ^{13}C-DIC -spiked. The remaining six bottles were filled to the top, closed bubble-free and incubated at surface water temperature via seawater flow-through. Light levels were adjusted to be representative of in-situ conditions by covering the incubator with a filter foil (Ocean Blue; Lee filter 724, 36.2% transmission). After ~12 h and ~24 h, the incubations were terminated for three bottles respectively. A subsample of 6 mL was collected from each bottle and combined with 100 µL of a saturated mercuric chloride solution in a 6 mL glass vial, which was closed bubble-free; these samples were used for determination of ^{13}C-DIC labelling percentage. The remaining sample volume was filtered (KNF Neuberger, <0.4 bar vacuum intensity) onto a pre-combusted (6 hours at 450 °C) 25 mm GF/F filter (Whatman GF/F 0.7µm, 25mm, GE Healthcare Europe GmbH, Germany) and stored at -20 °C.

The GF/F filters were acid fumed overnight (HCL 37% Merck), allowed to dry and packed into tin cups. POC content and isotopic composition was determined using an elemental analyser (Thermo Flash EA, 1112 Series) coupled to an isotope ratio mass spectrometer (Delta Plus XP IRMS; Thermo-Finnigan). ^{13}C-DIC atom percentage in the incubations was determined from an acidified 2 ml subsample (Torres et al, 2005) from the 6 ml glass vial, using cavity ring-down spectroscopy (G2201-i coupled to a Liaison A0301, Picarro Inc., Santa Clara, USA, connected to an AutoMate Prep Device, Bushnell, USA).

Subsequently, CO_2 fixation rates were calculated (Grosskopf et al, 2012) as:

$$CO_{2-fixation\ rate} = \frac{(Atom\%\ POCsample - Atom\%\ POC\ control)}{Atom\%\ DIC - Atom\%\ POC\ control)} \cdot \frac{POC}{t} \qquad \text{(eq.2)}$$

where Atom% POC sample is the atom% ^{13}C in the POC from the labelled sample (n=3); Atom% POC control is the natural abundance of ^{13}C in the POC as determined from the control sample; Atom% DIC is the atom% of ^{13}C-DIC in the DIC pool and POC is the total particulate organic carbon concentration on the filter and t is the duration time of the measurement (day^{-1}).

For the POC standing stock, 1.5 l seawater were collected using a CTD rosette at CB_{meso}, CB_s and CB_{sh} at 1 m, 5 m, 10 m, 50 m and 100 m, provided a sufficient water depth at the respective station. Samples were filtered in triplicates on precombusted (6 hours at 450 °C) 25 mm GF/F filters (Whatman GF/F 0.7µm, 25mm, GE Healthcare Europe GmbH, Germany) and stored at -20°C. For POC analysis, the filters were acid fumed overnight (HCL 37% Merck), dryed at 40°C and subsequently packed into tin cups. POC content was determined using an elemental analyser (Thermo Flash EA, 1112 Series).

2.7. Excess production and export contribution of shelf derived organic matter

To estimate the contribution of laterally advected shelf production to measured export flux in the drift traps, we calculated the projected loss of vertical POC export from 100 m to 400 m based on temperature-dependent microbial degradation for the regions CB_S, CB_{eu} and CB_{meso} according to Lutz et al. (2002), and compared our results with the measured POC flux of the drifting traps (Iversen & Ploug 2013). Thus, the POC flux (*J*; C/m²/h) to the depth (*Z*; m) was calculated by:

$$J = J_{(Z_0)} e^{\left(-\frac{D(T)}{W}\right) Z} \qquad \text{(eq. 3)}$$

where *D(T)* is the temperature dependent rate of microbial degradation (% h^{-1}) and *W* is the settling velocity (m h^{-1}). The temperature dependent rates of microbial degradation were obtained from the literature and on-board measurements (Figure S2 in Supporting Information; Table S3 in Supporting Information). The water temperature *T* for the corresponding depth Z was obtained from temperature measurements of the CTD cast at the station. The settling velocity W is derived from average settling velocities from onboard flow chamber measurements of the respective stations (CB_s = 61.5 m d^{-1} [n = 23]; CB_{eu} = 86 m d^{-1} [n = 20]). Since no size to settling relationship was found, we used an average settling velocity for all aggregate sizes at each region. Missing settling velocities from CB_{meso} were substituted by values from CB_{eu} since POC, PON and C/N export flux at 100 m depth at CB_{eu} and CB_{meso} where similar and microscopic observations of particles at CB_{eu} showed no indications of shelf influence, i.e. we did not observed lithogenic material such as dust or sand in the aggregates. Our calculations for the lateral contribution of shelf material to export flux at depth offshore do not consider the role of zooplankton grazing or dust deposition, which may both impact particle export and attenuation in the region (Iversen et al. 2010, van der Jagt et al. 2018, Nowald et al. 2015). Zooplankton feeding on settling aggregates has been shown to reduce carbon flux in the upper 100 m (e.g. Iversen et al. 2010, Jackson & Checkley 2011), which corroborate with our particle camera profiles which showed that the strong flux attenuation, i.e. rapid decrease in particle abundance and total particle volume, occurred at depths shallower than 100 m for CB_S and CB_{eu}. Additionally, by only taking microbial degradation into account between 100 and 400 m, the calculated carbon flux to 400 m fitted the measured carbon flux to 400 m at CB_{meso}. This suggested that zooplankton grazing on settling aggregates was neglectable at depths below 100 m at CB_{meso} and we consider the same to be true for CB_s and CB_{eu}. The consistently low volumetric contribution of fecal pellets to export flux at all depths between 100 and 400 m at CB_S and CB_{eu} (~4% and ~6% to 100 - 400 m respectively), further supported that zooplankton grazing was of little importance for the flux attenuation below 100 m. Hence, we consider that our flux calculations, which only consider temperature-controlled microbial degradation, are representing the in situ conditions.

To estimate the interseasonal and interannual contribution of laterally sourced shelf material to the open ocean export off Cape Blanc, we applied the calculation (equation 3) to export fluxes collected with short-term drifting trap and long-term deep ocean sediment trap data. For short term drifting trap fluxes, this was done for POC fluxes collected by 18 drifting trap deployments in the upper 400 m of the water column between 2012 – 2019 (Table S4 in Supporting Information). Long-term export fluxes of POC, $CaCO_3$, bpSi and lithogenic material were collected at the station CB_{meso} between 1989 and 2012 (see detailed mooring descriptions in Fischer et al. 2016). The continuous export fluxes cover export measurements for every season at ~3600 m depth and at various depths between ~750 – 4150 m. Seasonal averages of the El Niño/Southern Oscillation (ENSO) index and Atlantic Multidecadal Oscillation (AMO) index during the mooring deployments were obtained from NOAA-ESRL Physical Science Laboratory, Boulder Colorado. We calculated the projected loss of vertical POC export from trap measurements between ~750 - 1250 m to reach 3600 m based on temperature dependent microbial degradation (Iversen and Ploug 2013). Aggregate settling velocities and microbial degradation were utilized as in equation 3 and vertical temperature changes were obtained from CTD profiles during our sampling campaign. Temperature profiles are expected to be stable between years and seasons due to a limited seasonal variability in the region (Fischer et al. 2015)

To estimate if the shallow shelf production of organic matter is sufficient to supply the estimated quantities of lateral advected material, we performed a budget calculation by using measurements of in situ particle camera profiles, POC flux collected by the drifting traps, net community production, in situ particle degradation, POC standing stock and benthic respiration.

Firstly we determined the areal net community production (NCP) within the photic surface ocean by:

$$NCP = VPP \cdot D_P \qquad \text{(eq. 4)}$$

were *VPP* is the net volumetric primary production (mg C m^{-3} day^{-1}) measured over 24 h including community respiration and D_P is the depth of the productive surface layer, which is derived from fluorescence profiles and was defined as 25 m, 65 m and 65 m for CB_{sh}, CB_s and CB_{meso} respectively. We calculated $POC_{aggregated}$ as the POC content of settling particles from the productive surface layer, by multiplying the maesured size specific POC content of in-situ particles with the observed size distribution from particle camera deployments. To estimate the amount of offshore advected POC within the Cape Blanc filament from CB_{sh} to the regions CB_s, CB_{eu} and CB_{meso} respectively, we performed a budget calculation to determine the potential advected POC by:

$$POC_{local} = POC_{up} \cdot R_{microbial}{}^{t} \cdot G_{Zooplankton}{}^{t} \cdot dil^{t} + NCP \qquad \text{(eq. 5)}$$

by which the advected POC (POC_{local}; mg m^{-2} day^{-1}) is derived from the POC standing stock (POC_{up}; mg m^{-2} day^{-1}) within the productive surface layer, including the input of the daily net community production (*NCP*; mg m^{-2} day^{-1}), under the microbial respiration ($R_{microbial}$; d^{-1}), macrozooplankton grazing rate ($G_{zooplankton}$; % d^{-1}) (0.92; Steinberg & Landry 2017) and the loss of POC by the dilution factor (*dil*; %) (Karakas et al. 2006) within the residence time (*t*; d). The microbial respiration rate was set to 0.12 according to an average temperature of 18°C (Iversen et al. 2010, Iversen and Ploug 2010, Iversen and Ploug 2013). The residence time *t* is derived by dividing the average distance between sampling sites of 35 km from CB_{sh} to CB_{s}, 115 km from CB_{s} to CB_{eu} and 205 km from CB_{eu} to CB_{meso} with the average surface advection speed of 6.9 km day^{-1} (Fischer et al. 2015). For the residence time *t* the minimum and maximum distance of 10 - 70 km from CB_{sh} to CB_{s} was used to generate a minimum and maximum estimate of potential advected POC. For the value POC_{up} at CB_{eu} and CB_{meso}, the value of POC_{local} from the previous station was used. The dilution factor *dil* was included for estimates on CB_{eu} and CB_{meso}, but not for CB_{s}.

To estimate the amount of offshore advected POC that was sourced from the shelf ($POC_{advected}$), we performed a similar calculation as for POC_{local} (eq. 5) which did not include the input of the daily net community production *NCP* for the offshore stations CB_{eu} and CB_{meso}. A similar approach was used to estimate the amount of lateral advected POC as subsurface particle clouds from CB_{sh} to the stations CB_{s}, CB_{eu} and CB_{meso}, respectively. The potentially advected POC (POC_{cloud}) was determined by

$$POC_{cloud} = \left(POC_{low} + POC_{aggregated} - R_{benthic}\right) \cdot R_{microbial}{}^{t} \cdot G_{Zooplankton}{}^{t} \cdot dil \qquad \text{(eq. 6)}$$

where the potential advected POC_{cloud} (mg m^{-2} day^{-1}) was derived from the POC standing stock below the mixed layer (POC_{low}; mg m^{-2} day^{-1}) with the added POC input of settling aggregates ($POC_{aggregated}$; mg m^{-2} day^{-1}) from the productive surface layer, under the degradation of the daily benthic respiration ($R_{benthic}$; mg m^{-2} day^{-1}), the microbial respiration factor ($R_{microbial}$; %) a macrozooplankton grazing rate ($R_{zooplankton}$; %) (0.92; Steinberg & Landry 2017) and the dilution factor (*dil*; %) (Karakas et al. 2006) during the residence time (*t*; d). The microbial respiration factor is adjusted to the estimated average temperature during the settling of the subsurface particle clouds, with 0.1 (10°C) between CB_s and CB_{eu} and 0.04 between CB_{eu} and CB_{meso} (~4°C). For the residence time *t* the minimum and maximum distance of 10 - 70 km from CB_{sh} to CB_s was used to generate a minimum and maximum estimate of potential advected POC. For the determination of POC_{low} at CB_{eu} and CB_{meso}, the value of POC_{cloud} from the previous station was used. Further, $R_{benthic}$ and $G_{zooplankton}$ were not considered for CB_{eu} and CB_{meso}, as advected POC is not encountered with sediments past the shelf break and is expected to settle below the depth of zooplankton grazing activity.

3. Results

The sampling campaign was carried out in January 2019 during the winter season off Cape Blanc; an area with strong coastal upwelling and low seasonality (Fischer et al. 2015). Salinity, temperature, density and oxygen profiles at the shelf break and the shallow shelf between CB_s and CB_{sh} showed upwelling of deep water into the shallow shelf as a water layer, covering the bottom 50 m of the water column at the shelf break and gradually thinning to ≤ 10 m, 50 km onto the shelf (Figure S3 in Supporting Information). Based on wind directions and ADCP derived surface currents (data not shown), we observed transport of surface water in a westward offshore direction, indicative of Ekman transport caused by the trade winds (Figure S4 in Supporting Information) representative for a classic state for upwelling in the area (Johnson 1976, Arístegui et al. 2009).

3.1. Vertical turbidity and particle profiles

In situ particle profiling showed high values of particle concentration and volume along the entire transect, from the surface to 100 - 150 m; consistent with high water turbidity values (Figure 2). Average particle concentrations and volume in the top 150 m were highest on the shallow shelf at CB_{sh} with 615 ± 81 particles L^{-1} and 94 ± 14 ppm, decreased at the shelf break at CB_S to 224 ± 40 particles L^{-1} and 35 ± 6 ppm and were lowest in the open ocean at CB_{meso} with 82 ± 16 particles L^{-1} and 12 ± 3 ppm. At the slope stations two distinct peaks in particle abundance, total particle volume and turbidity profiles were observed at intermediate depth and above the sea floor, which showed the presence of the intermediate particle cloud (IPC) and benthic particle cloud (BPC), respectively (Figure 2 & Figure 3).

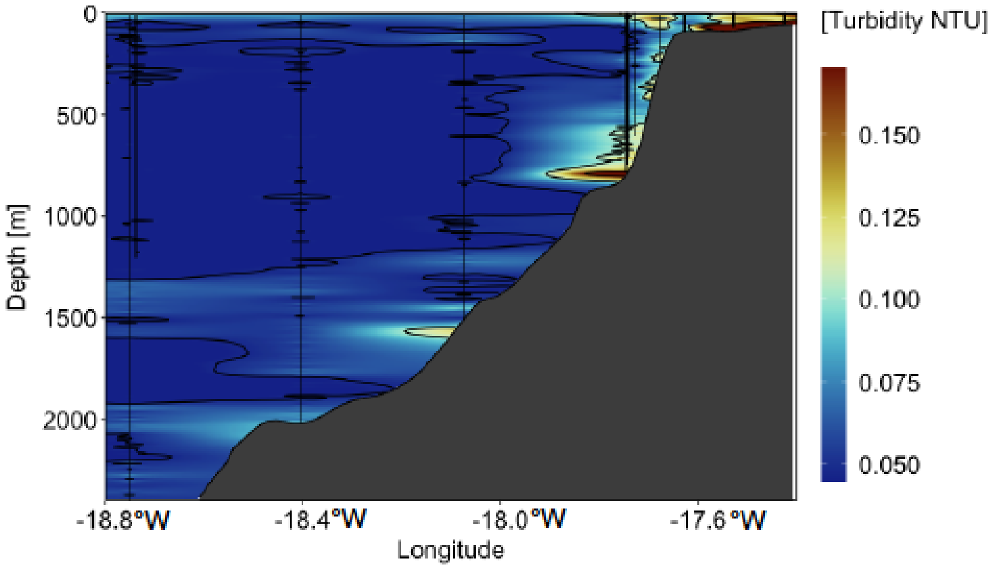

Figure 2. Turbidity based on profiles (black lines) measured on a latitudinal shelf transect during the time period of the process study (January 2019). Particles from the shallow shelf are advected offshore in the surface layers between 100 – 150 m, at intermediate depths between 300 – 900 m meters forming patchy distributed intermediate particle clouds and benthic particle clouds which follow the slope and extend offshore in two layers between 1300 – 1600 m and below 1900 until the seafloor.

The depth of the IPC ranged in depths between 230 – 450 m at CB_S and consisted of individual patches or clouds of mostly 809 – 1587 µm sized particles (Figure 3), with an average concentration of 159 ± 28 particles L^{-1} and volume of 26 ± 5 ppm. Further offshore at the transect stations, the IPC ranged in depths between ~300 – 900 m and was only visible as individual clouds in the turbidity profiles (Figure 2).

The BPC extended from the bottom to ~200 m above the seafloor close to the shelf break at CB_S and separated into two layers ranging between ~1300-1600 m and ~1900 m until the seafloor at ~3000 m at CB_{eu} (Figure 2). The particle size-range of the BPC at CB_S varied from the IPC by containing 4.2 times more volume of 130 – 200 µm sized particles and overall higher average particle concentration of 491 ± 71 particles L^{-1} and volume of 81 ± 13 ppm (Figure S5a & b; profile GeoB23603_31 and GeoB23604_01 in Supporting Information). The peak of the BPC increased with depth and extended below the deployment depth of the particle camera so particle concentrations and volume below 500 m likely exceed those measured in the upper 500 m (Figure 2).

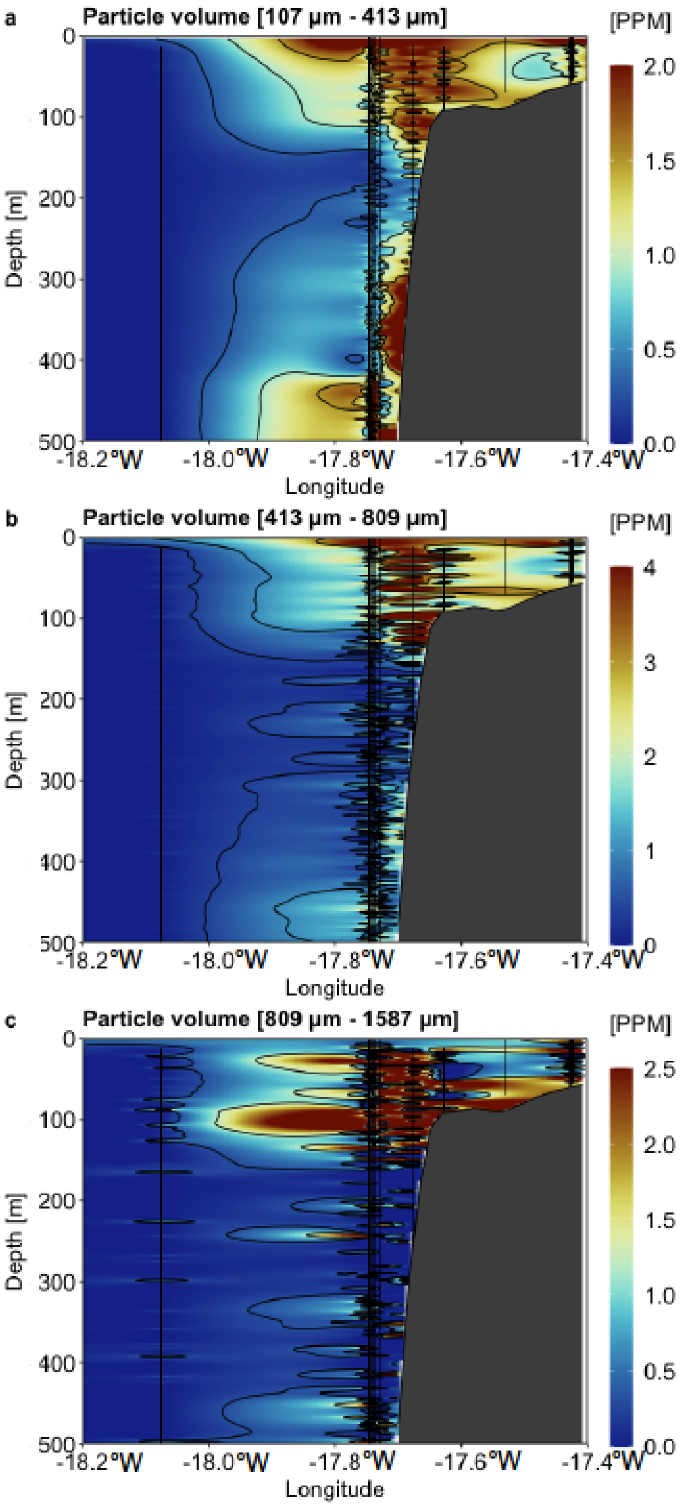

Figure 3. Latitudinal shelf transect of particle volume from 107-413 µm (a), 413-809 µm (b) and 809-1587 µm (c) particle size classes during our process study (January 2019). Particles advected in the surface layers and the benthic particle cloud (which follows the slope), are composed of each of the shown particle size classes. In addition, particles in the 809-1587 µm size range (c) form patchy distributed intermediate particle clouds between 230 – 450 m past the shelf break.

3.2. Drifting trap fluxes

Fluxes of dry weight (DW) and PON showed similar values at 100 m depth across all stations, while POC flux at $\mathrm{CB_{s}}$ was 27-29% higher than at $\mathrm{CB_{eu}}$ and $\mathrm{CB_{meso}}$ (Table 1). In comparison to POC flux to 100 m, the flux at 200 m and 400 m increased by 9-23% and 17-27% at $\mathrm{CB_{S}}$ and $\mathrm{CB_{eu}}$, respectively, but decreased by 7-46% at $\mathrm{CB_{meso}}$. In addition, fluxes at 200 and 400 m were higher at stations closer to the shelf. At $\mathrm{CB_{S}}$ the POC:PON ratios at 400 m were lowest with a value of 6.2 compared to 6.9 at 100 m and 8.3 at 200 m depth, indicating flux to 400 m was largely composed of undegraded organic matter, likely phytoplankton. The POC:PON ratios at $\mathrm{CB_{eu}}$ was 6.7 – 7.1 at all sampled depths. At $\mathrm{CB_{meso}}$, POC:PON ratios showed a steady increase from 7.2 at 100 m to 9.2 at 400 m depth. Particles with ESDs of ~300 μm were the main contributor at $\mathrm{CB_{S}}$ and $\mathrm{CB_{eu}}$, comprising 17% and 20% of the total particulate volume respectively, while at $\mathrm{CB_{meso}}$ particles with ESDs of ~580 μm comprised 21% of the total particulate volume. Furthermore, at $\mathrm{CB_{s}}$ the total volume of particles in the size-range between 20 μm - 413 μm was up to ~2-fold higher in the gel traps collected at 200 and 400 m compared to 100 m (Figure S4 in Supporting Information). In addition, we observed high abundances of particles with ESDs ≤ 20 μm at the 200 m and 400 m gel trap, suggesting the presence of small particles in the two deeper traps.

The contribution of fecal pellets was 3.5 - 7% of the total particle volume for all stations at 100 m. At 200 and 400 m fecal pellets were 18% of the particle volume at $\mathrm{CB_{meso}}$, 4% at $\mathrm{CB_{S}}$ and 6% at $\mathrm{CB_{eu}}$ (Figure S6 in Supporting Information).

Table 1. Fluxes of Dry weight (DW), particulate organic carbon (POC) and particulate organic nitrogen (PON) from drift trap deployments. The calculated vertical POC flux (POC vertical) is derived from temperature dependent microbial degradation under the assumption of vertical export (equation 3). The lateral POC export contribution is the fraction of advected POC to export flux and is derived from the difference between measured and calculated POC.

Station	Depth [m]	DW [mg m^{-2} day^{-1}]	POC [mg m^{-2} day^{-1}]	PON [mg m^{-2} day^{-1}]	POC [%]	PON [%]	POC:PON	POC vertical [mg m^{-2} day^{-1}]	Lateral POC export contribution [%]
$\mathrm{CB_{meso}}$	100	843.90	79.08	9.42	9.3	1.1	7.2	79.08	0
	200	632.93	73.65	7.19	11.6	1.1	8.8	67.10	8.9
	400	389.83	54.11	5.03	13.9	1.3	9.2	50.19	7.2
$\mathrm{CB_{eu}}$	100	848.05	77.31	9.43	9.1	1.1	7.0	77.31	0
	200	897.80	90.14	10.87	10.0	1.2	7.1	66.55	26.16
	400	827.38	98.38	12.54	11.9	1.5	6.7	50.01	49.16
$\mathrm{CB_{S}}$	100	813.29	100.77	12.60	12.4	1.5	6.9	100.77	0
	200	1005.32	110.14	11.37	11.0	1.1	8.3	81.58	25.9

400	1831.93	124.02	17.16	6.8	0.9	6.2	55.40	55.3

3.3. Aggregate composition and settling behaviour

Flow chamber measurements showed no relationship between particle size and settling velocity at any of the stations ($p = > 0.05$). Settling velocities at CB$_{Sh}$ were significantly higher ($p = < 0.001$; 191 m day^{-1}) than at CB$_{S}$ (61 m day^{-1}) and CB$_{eu}$ (86 m day^{-1}). Light microscope observations showed that aggregates from CB$_{Sh}$ were denser and included sand grains, whereas aggregates near the shelf break at CB$_{S}$ were fragile and composed of phytoplankton with little lithogenic material (Figure 4 top). Further off-shore at CB$_{eu}$, aggregates were denser than those observed at CB$_{S}$ and zooplankton fecal pellets were observed inside aggregates.

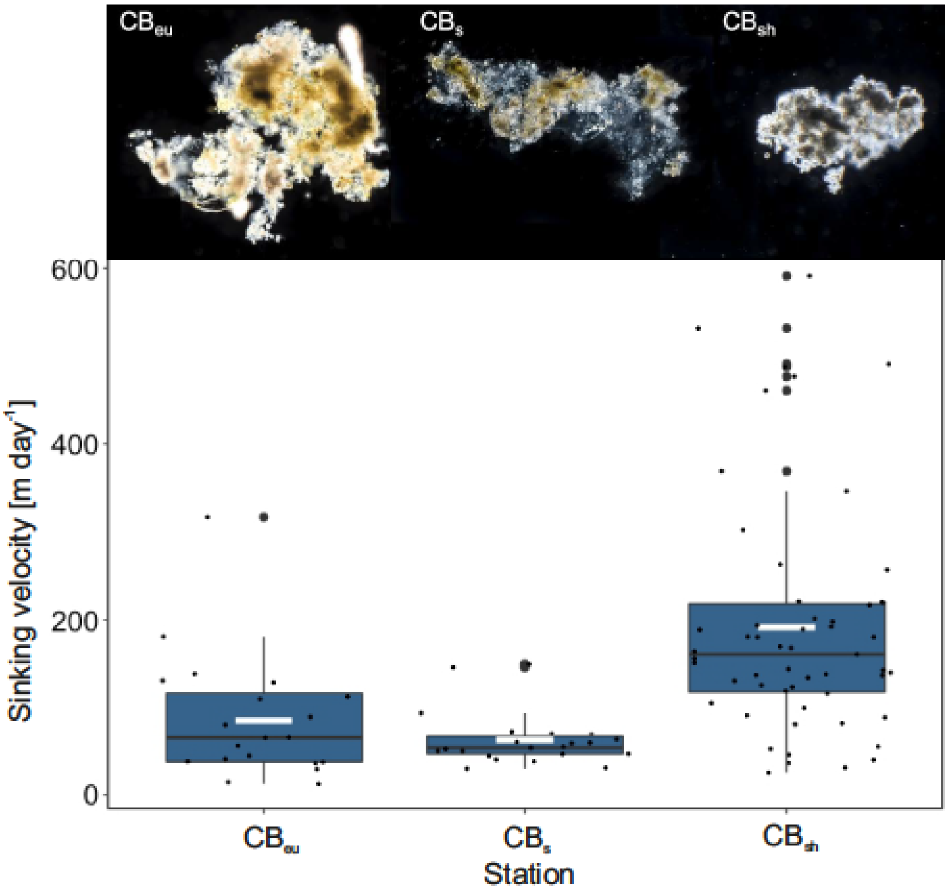

Figure 4. Measured settling velocities of aggregates collected on the shallow shelf (CB$_{sh}$), past the shelf break (CB$_{s}$) and on the slope (CB$_{eu}$) with example images from collected in-situ aggregates above. Boxplots depict the 25–75% quantile range, with the centre line depicting the median (50% quantile). Whiskers encompass data points within 1.5 times the interquartile range. White horizontal bars in boxplots indicate the average. Small points show individuale measurements of aggregate settling velocities. Large points indicate individual measurements that were outliers. Samples were obtained during our process study (January 2019).

3.4. Lateral export contribution during the field campaign

The estimated contribution of lateral advected shelf production to measured POC export from the drifting trap deployments during the field campaign increased with increasing depth at CB_s and CB_{eu} from ~26% at 200 m to ~55% at 400 m. This amounted to a total lateral contribution at 400 m depth of 68.58 mg C m^{-2} day^{-1} and 48.36 mg C m^{-2} day^{-1} at CB_s and CB_{eu} respectively. Further offshore, estimated lateral influence was very low with 9% at 200 m and 7% at 400 m at CB_{meso} (Table. 1).

3.5. Long term contribution of lateral sourced carbon export

Long-term seasonal sediment trap fluxes from 1989 – 2012 at the mooring site at CB_{meso} are obtained from Fischer et al. (2016; Table 2). Average seasonal POC export at 750 – 1250 m was lower or equal to flux measured at 3600 m (Table 2). The estimated lateral contribution of shelf material for the trap collection at 3600 m depth ranged between 3.4 – 4.7 mg POC m^{-2} day^{-1} and covered 76 - 83% of total POC fluxes between all seasons (Figure 5a). Sediment trap fluxes were not correlated to the AMO (Spearman correlation p = 0.66) or ENSO (Spearman correlation p = 0.38) index but significantly correlated to $CaCO_3$ (Spearman p = <0.001), bpSi (Pearson p = <0.001) and lithogenic material fluxes (Pearson p = <0.001).

Values from drifting trap fluxes were obtained between 2011 – 2019 along the slope off Cape Blanc (Table S4 in Supporting Information). The estimated lateral contribution of shelf material increased with shelf proximity and was more pronounced for 400 m compard to 200 m deep flux estimates, though not being statistically significant (Figure 5c; spearman rank correlation; *p* = 0.07 for 400 m and *p* = 0.35 for 200 m fluxes).

Table 2. Seasonal average fluxes of particulate organic carbon (POC) to 750 – 1250 m and 3600 m from 1989 until 2012 at CB_{meso} derived from Fischer et al. 2016, and estimated contribution of lateral advected shelf export and surface derived export.

Season	Av. POC 750-1250 m [mg m^{-2} day^{-1}]	Av. POC 3600 m [mg m^{-2} day^{-1}]	Lateral POC contribution [mg m^{-2} day^{-1}]	Surface POC contribution [mg m^{-2} day^{-1}]	Lateral POC contribution [%]	Surface POC contribution [%]
Spring	4.8	4.8	3.7	1.2	76	24
Summer	3.2	5.2	4.2	1.0	81	19
Autumn	4.0	4.4	3.4	1.1	76	24
Winter	6.2	6.4	4.7	1.7	74	26

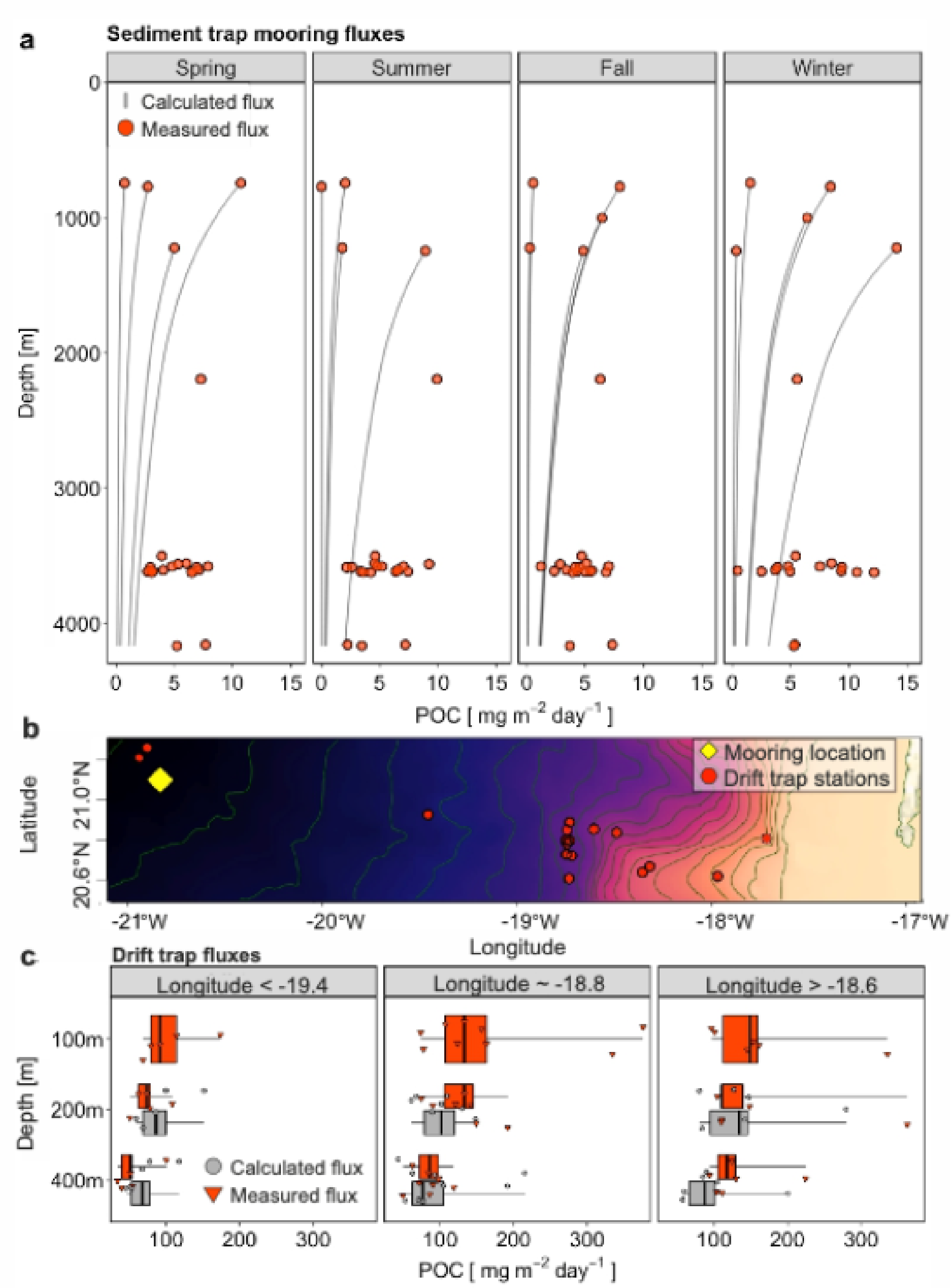

Figure 5. Particulate organic carbon (POC) export fluxes measured off Cape Blanc between 1989 - 2019. Panel a shows sediment trap mooring fluxes at CB_{meso} between 1989 – 2012 which were obtained from Fischer et al. (2015). Yellow points indicate measured carbon fluxes. Grey lines indicate the calculated carbon flux according to Lutz et al. (2002) assuming vertical settling from sediment trap deployments between 750 – 1250 m. Panel b shows sampling locations of the measured POC fluxes off Cape Blanc of sediment trap moorings and drift trap deployments between 1989 - 2019. Panel c shows the flux change from 100 m to 200 m and 400 m as measured (red) and calculated (blue) flux respectively. Carbon flux was calculated according to Lutz et al. (2002) assuming vertical settling from drifting traps deployed at 100 m.

3.6. Budget calculations for offshore transport of shelf produced carbon

Mesurements of primary production at CB_{sh}, CB_s and CB_{meso} amounted for 2404, 3010 and 733 mg C m^{-2} day^{-1}, respectively. The average benthic respiration on the shallow shelf was 188 ± 255 mg C m^{-2} day^{-1}. The total measured POC standing stock on the shallow shelf at CB_{sh} was on average 16098 mg C m^{-2} from which 8240 ± 1341 mg C m^{-2} were contained in the surface productive layer between 0 and 25 m and 7858 ± 2078 mg C m^{-2} within the depths between 25 and 60 m depth.

The estimated amount of advected shelf POC within the Cape Blanc filament was 6671 - 997, 64 – 10 and 0.01 – 0.002 mg C m^{-2} day^{-1} at CB_s, CB_{eu} and CB_{meso}, respectively. When including the daily net community production to the advected POC past the shelf break, the resulting local POC within the Cape Blanc filament was estimated to 12095 - 9075, 12590 - 12560 and 3225 mg C m^{-2} day^{-1} at CB_s, CB_{eu} and CB_{meso}, respectively. The subsurface advection of shelf POC as particle clouds was 12020 - 1915, 226 - 36, and 7 – 1 mg C m^{-2} day^{-1} for CB_s, CB_{eu} and CB_{meso}, respectively. The resulting total advection of 2912 - 18691 mg C m^{-2} day^{-1}, as based on the excess POC, i.e. the POC that was not turnover on the shelf, indicated that the sandy shelf system was a net autotrophic system.

4. Discussion

4.1. Lateral advection is the major source of deep ocean POC flux

Seasonally averaged POC fluxes measured over 23 years at 450 km off the coast of NW Africa (Cape Blanc) at the CB_{meso} site showed that fluxes to intermediate depths (750 m – 1250 m) were either equal to, or lower than fluxes to the deep ocean (3600 m). Similarly, when we calculated potential fluxes to the deep ocean based on the upper trap fluxes, temperature dependent microbial degradation and average particle sinking velocities (Eq. 3), the calculated fluxes to the deep ocean only accounted for 17 – 24% of the measured POC flux (Figure 2a). This mismatch between calculated and measured export flux to 3600 m was of similar magnitude for all seasons and years. In contrast, a similar comparison carried out for globally distributed deep ocean sediment traps showed good correlations between calculated and measured POC flux (Iversen and Ploug 2013). However, that study only included fluxes which decreased with increasing depth, as they assumed that those with higher fluxes at depth were influenced by lateral advection.

The higher measured compared to calculated POC flux to the deep ocean at CB_{meso} could potentially have been caused by high inputs of Saharan dust. Dust input ballasts particles and increases their sinking velocities thereby leading pulse events of high POC export (Nowald et al. 2015, van der Jagt et al. 2018). However, even when assuming a doubled settling velocity in our calculations, the estimated local vertical export from the surface ocean would only explain 32 – 48% of the total measured POC flux to 3600 m depth. Hence, the consistent mismatch throughout the entire 23-years cannot be explained by the irregular occurrence of dust storms. Further, the mismatch was of similar magnitude for all seasons and years and showed no correlation to shifts in the AMO or ENSO, which impact the magnitude of carbon export off Cape Blanc (Fischer et al. 2015, Romero et al. 2021). Therefore, the difference between the calculated and measured POC fluxes indicates that ~75% of the total POC flux to the deep ocean off Cape Blanc is consistently supplied from a source other than local vertical export. Logically this source must be from lateral advection of POC.

To gain a first insight into where the POC was laterally advected from, we compared the calculated and measured fluxes to 200 and 400 m from 18 drift traps deployed between 2011 and 2019 in the region between the shelf and CB_{meso}. The shallow drifting traps deployed in the upper 400 m of the water column close to CB_{meso} (21°W, Fig. 5c) showed an opposite trend to the deep ocean moored traps. Here we observed higher calculated fluxes compared to the measured fluxes, i.e. there was no evidence of laterally advected material to the drifting traps deployed at 200 and 400 m at CB_{meso}. However, with increasing proximity to the shelf, the measured drifting trap fluxes at 200 and 400 m gradually exceeded the calculated POC fluxes (Fig. 5), i.e. there was an increasing fraction of laterally advected POC. From this, we suggest that the gradually decreasing mismatch between measured and calculated drifting trap fluxes was due to offshore advection of slow sinking clouds of particles that originated from the shelf. These particle clouds are frequently observed off Cape Blanc (Nowald et al. 2006, Karakas et al. 2006, Fischer et al. 2009, Helmke et al. 2005) and have been suggested to originate from the shelf region based on the presence of coastal and benthic diatoms in the CB_{meso} deep ocean trap (Romero et al. 2020). Our results suggest that shelf material is consistently transported offshore as particle clouds that slowly sink to the deep ocean.

4.2. Formation of subsurface particle clouds

To better understand the mechanisms by which particles are transported from the shelf to the open ocean as particle clouds, we carried out a process study during January 2019 in the Cape Blanc region. Satellite observations of chlorophyll and Saharan dust showed that no large phytoplankton bloom or dust deposition event had occurred in the month preceeding the sampling campaign (Figure S7 & Figure S8 in Supporting Information). Therefore, our observations were not influenced by an episodic pulse flux which could have decoupled flux mechanisms between the surface and deep ocean.

During the January sampling period, both an intermediate and benthic particle cloud (IPC and BPC, respectively) were observed in the in situ camera and turbidity profiles. Both particle clouds originated on the shelf and diverged at the shelf break (Fig. 3 and 4). During the time of the campaign, the IPC could be observed up to 110 km past the shelf break, which is typical for this region where the IPC has even been shown to extend 400 km offshore (Karakas et al. 2006, Nowald et al. 2006). Using a modelling approach Karakas et al. (2006) suggested that the lateral and vertical extention of the IPC would only be possible if particles sank within it at an average settling velocitiy of 5 m d^{-1}, in contrast particles in the BPC required an average settling velocity of the 35 m d^{-1}. This indicates that the particles within the IPC and BPC separate past the shelf break due to their different settling velocities. The in situ camera profiles revealed differences in particle size-spectra between the two clouds. The BPC mainly consisted of small particles (< 413 µm) while the IPC contained all particle sizes that were detectable by the camera (Fig. 4), which was surprising since small particles are generally considerd to sink slower than large particles if they are composed of similar material. Therefore we hypothesize that the small particles in the BPC were denser than the paricles in the IPC. Indeed both microscopic observations and direct size-specifc settling velocity measurements revealed that the particles formed on the shelf consisted of both ballasted and non-ballasted marine snow aggregates (rather than zooplankton fecal pellets) without a clear size-to-settling relationship (Fig. 5, Fig. S7). This implies that differences in particle density drives the separation of the IPC and BPC at the shelf break, with the fast-settling particles forming the BPC while the slow-settling particles form the IPC.

The slow settling of particles within the IPC could potentially result from limited diffusive exchange between less dense porewater within settling aggregates and the surrounding water at haloclines (Kindler et al. 2010, MacIntyre et al. 1995). However, we did not observe any relationship between peaks in particle concentrations and salinity gradients, which is similar to previous observations that also did not find any indications for halocline driven particle retention off Cape Blanc (Nowald et al. 2006, Iversen et al. 2010). An alternate mechanism for reduced sinking velocities could be high quantities of transparent exopolymeric particles (TEP) in the aggregates (Azetzu-Scott & Passow 2004). TEP has a lower mass density (700 – 800 kg m^{-3}) than seawater and provide buoyancy inside organic aggregates. While we did not directly measure TEP concentration in aggregates, we observed large aggregates that were composed of non-sinking gelatinous material at the shelf (Figure S9 in Suporting Information). This indicates high TEP concentrations in shelf sourced particles may explain the observations of large, seemingly slow-sinking particles within the IPC at 300 m at CB_{eu} (Figure 4c). Considering an average offshore current velocity of ~0.1 m s^{-1} (Karakas et al. 2006), it would take the particles within the IPC between one and two months to reach the CB_{meso} deep ocean trap (450 km from the shelf). This implies that the particles within the ICP are degraded at low rates, which may be a result of their high TEP concentration. The turnover time of TEP is strongly dependent on its chemical composition (Passow 2002). TEP compounds rich in mannose and galactose are rapidly degraded, while fucose containg TEP compounds are more resistant to degradation (Passow et al. 2002, Sichert et al. 2020). Hence, both the slow settling velocities and the long residence time of the organic matter within the IPC supports that the particles are composed of substantial amounts of TEP.

4.3. Implications for global carbon sequestration

By combining auto- and heterotrophic processes, the standing stock of POC on the shelf, and offshore current velocities, we estimated that 1 – 7 mg POC m^{-2} d^{-1} that reached the deep ocean at CB_{meso} originated from the shelf. This matched the independent estimate of lateral advection based on the sediment trap data (3.4 – 4.7 mg POC m^{-2} day^{-1}; Equation 3; Figure 6). Both of these results indicate that offshore advection of organic matter from the shallow shelf relocates large quantities of POC in the form of particle clouds. Considering that the slow-sinking organic matter was observed to reach depths of at least 800 m, i.e. well below the winter mixed layer, horizontal advection is likely an important but overlooked meachnism for oceanic carbon sequestration.

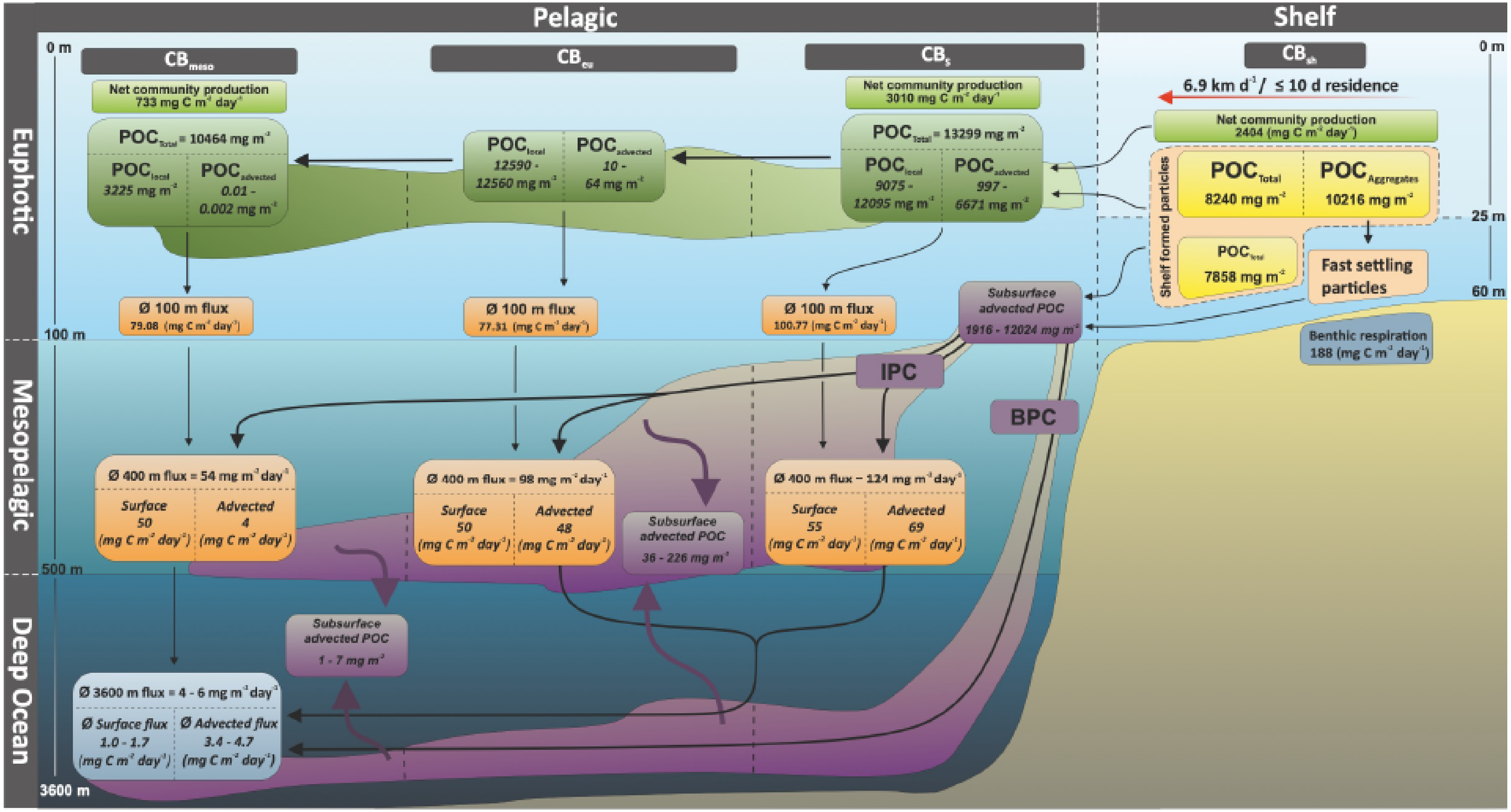

Figure 6. Schematic of particle sources and sinks at the upwelling region off Cape Blanc. Excess production is laterally transported from the shallow shelf to the open ocean as surface- or subsurface advected POC. Surface advected POC forms the CB filament, while subsurface advected POC forms the intermediate particle cloud (IPC) and benthic particle cloud (BPC). Italic font indicates calculated values while regular fonts indicate measured values. POC_{total} is the prevailing measured POC standing stock. POC_{local} shows estimated advected flux including the input from daily primary production, while $POC_{advected}$ shows estimated advected flux originating from the shallow shelf with no input from primary production (eq. 5). Measured deep ocean sediment trap fluxes are obtained from Fischer et al. (2016) and cover measurements from 1989 - 2011, while remaing values are obtained from this process study.

The biological carbon pump (BCP) is estimated to drive a global carbon export of 660 ± 300 Mt C yr^{-1} to 2000 m depth (Henson et al. 2012). Considering that the annual POC deposition of the four major EBUSs was estimated to cover 41 Mt POC (Carr et al. 2002, Jahnke et al. 2009), their total contribution would amount to 4-12% of the global carbon export. Particle clouds are a persistent feature in all of the major EBUSs (e.g. Ransom et al. 1998; Fischer et al. 2009, Inthorn et al. 2006, Lam et al. 2018), and assuming a similar contribution to deep ocean carbon export of 76-83% as we found for the region off Cape Blanc, laterally advected shelf material would sum up to 31-34 Mt C yr^{-1}, resulting in 5-10% of the estimated global carbon export via the BCP. Even though this estimation is based on wide-ranging assumptions, it clearly demonstrates that particle clouds in the major EBUS need to be taken into account in global carbon budgets.

Particle clouds are consistent features that occur independent from EBUSs throughout the global oceans in areas close to continental margins with elevated current velocities (Gardner et al. 2018a, Gardner et al. 2018b). Sediment trap records suggest that particle clouds formed from shelf material contribute substantially to fluxes in the deep ocean, as has been shown in the Canada Basin (Hwang et al. 2015), Fram strait (Lalande et al. 2016), Laptev Sea (Fahl & Nöthig 2007, Shultz et al. 2021), North- and Central Atlantic (Hwang et al. 2017, Conte et al. 2019) and South China Sea (Blattmann et al. 2018). Compositional analyses of deep ocean fluxes indicate that laterally supplied POC contributes 20 to 69% to the total deep ocean POC flux (Hwang et al. 2015, Hwang et al. 2017, Lalande et al. 2016, Fahl & Nöthig 2007). Taken together with the suggestion by Jahnke et al. (2009) who estimated that continental margins may supply ~50% of global deep ocean carbon export, this implies that particle clouds are globally important for the transport of carbon from ocean margins to the open ocean interior and deep ocean sediment. This also suggests that horizontally advected POC may contribute substantially to open ocean benthic communities and to carbon sequestration via the BCP. Considering that marine particle clouds have been observed throughout the global ocean (Gardner et al. 2018a, Gardner et al. 2018b), it seems likely that lateral supply of POC from the continental margins to the deep ocean is not limited to EBUSs. Therefore, only considering a vertical component in carbon flux attenuation estimates, as is done in widely used approaches, such as the “martin curve” (Martin et al. 1987), will lead to overestimations in both total flux and turnover in the water column above the trap (Burd et al. 2010). By recognizing particle clouds and horizontal advection as an integral part of the BCP, we will be able to more accurately quantify export efficiency and biological turnover, hence, improving the data used to model and predict oceanic carbon sequestration.

Acknowledgements

We thank Gerhard Fischer for discussions and critical comments. We thank Gerhard Fischer, Helga van der Jagt, Clara Flintrop, Lili Hufnagel, Nicolas Nowald, Götz Ruhland, Marco Klann, Stefan Thiele, and Isabell Klawonn for support during drifting sediment trap deployments during the past 10 years. We thank the captain and crew of RV *Poseidon* expedition POS531 for their support at sea. This work was fundedby the DFG-Research Center/Cluster of Excellence "The Ocean in the Earth System": EXC-2077-390741603. Soeren Ahmerkamp acknowledges funding from the Max Planck Society (MPG) for the Multiscale Approach on the Role of Marine Aggregates (MARMA) project.

Conflict of Interest

The authors declare no conflict of interest relevant to this study.

Data availability Statement

Data used in this study are made available at PANGEA.

References

Ahmerkamp, S., Winter, C., Krämer, K., Beer, D. de, Janssen, F., Friedrich, J., … Holtappels, M. (2017). Regulation of benthic oxygen fluxes in permeable sediments of the coastal ocean. *Limnology and Oceanography*, *62*(5), 1935–1954. https://doi.org/10.1002/lno.10544

Amos, C. M., Castelao, R. M., & Medeiros, P. M. (2019). Offshore transport of particulate organic carbon in the California Current System by mesoscale eddies. *Nature Communications*, *10*(1), 1–8.

Arístegui, J., Barton, E. D., Álvarez-Salgado, X. A., Santos, A. M. P., Figueiras, F. G., Kifani, S., … Demarcq, H. (2009). Sub-regional ecosystem variability in the Canary Current upwelling. *Progress in Oceanography*, *83*(1–4), 33–48. https://doi.org/10.1016/j.pocean.2009.07.031

Azetsu-Scott, K., & Passow, U. (2004). Ascending marine particles: Significance of transparent exopolymer particles (TEP) in the upper ocean. *Limnology and Oceanography*, *49*(3), 741–748. https://doi.org/10.4319/lo.2004.49.3.0741

Behrenfeld, M. J., & Falkowski, P. G. (1997). Photosynthetic rates derived from satellite-based chlorophyll concentration. *Limnology and Oceanography*, *42*(1), 1–20. https://doi.org/10.4319/lo.1997.42.1.0001

Bonino, G., Lovecchio, E., Gruber, N., Münnich, M., Masina, S., & Iovino, D. (2020). Drivers and impact of the seasonal variability of the organic carbon offshore transport in the Canary Upwelling System. *Biogeosciences Discussions*, 1–30. https://doi.org/10.5194/bg-2020-470

Boyd, P. W., Claustre, H., Levy, M., Siegel, D. A., & Weber, T. (2019). Multi-faceted particle pumps drive carbon sequestration in the ocean. *Nature*, *568*(7752), 327–335. https://doi.org/10.1038/s41586-019-1098-2

Burd, A. B., Hansell, D. A., Steinberg, D. K., Anderson, T. R., Arístegui, J., Buesseler, K. O., … Tanaka, T. (2010). Assessing the apparent imbalance between geochemical and biochemical indicators of meso- and bathypelagic biological activity : What the @ $] ! is wrong with present calculations of carbon budgets? *Deep-Sea Research II*, *57*, 1557–1571.

Busch, K., Endres, S., Iversen, M. H., Michels, J., Nöthig, E. M., & Engel, A. (2017). Bacterial colonization and vertical distribution of marine gel particles (TEP and CSP) in the arctic Fram Strait. *Frontiers in Marine Science*, *4*, 1–14. https://doi.org/10.3389/fmars.2017.00166

Carr, M. E. (2002). Estimation of potential productivity in Eastern Boundary Currents using remote sensing. *Deep-Sea Research Part II: Topical Studies in Oceanography*, *49*(1–3), 59–80.

Chabert, P., d'Ovidio, F., Echevin, V., Stukel, M. R., & Ohman, M. D. (2021). Cross-Shore Flow and Implications for Carbon Export in the California Current Ecosystem: A Lagrangian Analysis. *Journal of Geophysical Research: Oceans*, *126*(2), 1–14. https://doi.org/10.1029/2020JC016611

Elliott, A. H., and N. H. Brooks. 1997a. Transfer of nonsorbing solutes to a streambed with bed forms: Laboratory experiments. *Water Resour. Res.* 33: 137– 151, doi:10.1029/96WR02783

Elliott, A. H., and N. H. Brooks. 1997b. Transfer of nonsorbing solutes to a streambed with bed forms; Theory. *Water Resour. Res.* 33: 123– 136, doi:10.1029/96WR02784

Engel, A., & Passow, U. (2001). Carbon and nitrogen content of transparent exopolymer particles (TEP) in relation to their Alcian Blue adsorption, *Marine Ecology Progress Series 219*(1977), 1–10.

Fahl, K., & Nöthig, E. M. (2007). Lithogenic and biogenic particle fluxes on the Lomonosov Ridge (central Arctic Ocean) and their relevance for sediment accumulation: Vertical vs. lateral transport. *Deep-Sea Research Part I: Oceanographic Research Papers*, *54*(8), 1256–1272. https://doi.org/10.1016/j.dsr.2007.04.014

Fischer, G., Reuter, C., Karakas, G., Nowald, N., & Wefer, G. (2009). Offshore advection of particles within the Cape Blanc filament , Mauritania : Results from observational and modelling studies. *Progress in Oceanography*, *83*(1–4), 322–330.

Fischer, G., Romero, O., Merkel, U., Donner, B., Iversen, M., Nowald, N., Ratmeyer, V., Ruhland, G., Klann, M., Wefer, G. (2015). Deep ocean mass fluxes in the coastal upwelling off Mauritania from 1988 to 2012: Variability on seasonal to decadal timescales. *Biogeosciences Discussions*, *12*(21), 17643–17692. https://doi.org/10.5194/bgd-12-17643-2015

Flintrop, C. M., Rogge, A., Iversen, M. H., Miksch, S., Thiele, S., & Waite, A. M. (2018). Embedding and slicing of intact in situ collected marine snow, *Limnol. Oceanogr.: Methods 00, 2018, 00–00*. https://doi.org/10.1002/lom3.10251

Freudenthal, T., Neuer, S., Meggers, H., Davenport, R., & Wefer, G. (2001). Infuence of lateral particle advection and organic matter degradation on sediment accumulation and stable nitrogen isotope ratios along a productivity gradient in the Canary Islands region, *Marine Geology 177, 93±109*.

Frischknecht, M., Münnich, M., & Gruber, N. (2018). Origin, Transformation, and Fate: The Three-Dimensional Biological Pump in the California Current System. *Journal of Geophysical Research: Oceans*, *123*(11), 7939–7962. https://doi.org/10.1029/2018JC013934

Gabric, A. J., Garcia, L., van Camp, L., Nykjaer, L., Eifler, W., & Schrimpf, W. (1993). Offshore Export of Shelf Production in the Cape Blanc (Mauritania) Giant Filament as Derived From Coastal Zone Color Scanner Imagery. *Journal of Geophysical Research*, *98*(92), 4697–4712.

García-Reyes, M., Sydeman, W. J., Schoeman, D. S., Rykaczewski, R. R., Black, B. A., Smit, A. J., & Bograd, S. J. (2015). Under pressure: Climate change, upwelling, and eastern boundary upwelling ecosystems. *Frontiers in Marine Science*, *2*(DEC), 1–10. https://doi.org/10.3389/fmars.2015.00109

Gardner, W. D., Richardson, M. J., & Mishonov, A. V. (2018a). Global assessment of benthic nepheloid layers and linkage with upper ocean dynamics. *Earth and Planetary Science Letters*, *482*(November 2017), 126–134. https://doi.org/10.1016/j.epsl.2017.11.008

Gardner, W. D., Mishonov, A. V., & Richardson, M. J. (2018b). Decadal Comparisons of Particulate Matter in Repeat Transects in the Atlantic, Pacific, and Indian Ocean Basins. *Geophysical Research Letters*, *45*(1), 277–286.

Gärdes, A., Iversen, M. H., Grossart, H. P., Passow, U., & Ullrich, M. S. (2011). Diatom-associated bacteria are required for aggregation of Thalassiosira weissflogii. *ISME Journal*, *5*(3), 436–445. https://doi.org/10.1038/ismej.2010.145

Großkopf, T., Mohr, W., Baustian, T., Schunck, H., Gill, D., Kuypers, M. M. M., Lavik, G., Schmitz, R. A., Wallace, D. W. R., Laroche, J. (2012). Doubling of marine dinitrogen-fixation rates based on direct measurements. *Nature*, *488*(7411), 361–364. https://doi.org/10.1038/nature11338

Harlett, J. C., & Kulm, L D. (1973). Suspended sediment transport on the northern Oregon continental shelf. *Bulletin of the Geological Society of America*, *84*(12), 3815–3826. https://doi.org/10.1130/0016-7606(1973)84<3815:SSTOTN>2.0.CO;2

Helmke, P., Romero, O., & Fischer, G. (2005). Northwest African upwelling and its effect on offshore organic carbon export to the deep sea. *Global Biogeochemical Cycles*, *19*(4), 1–16. https://doi.org/10.1029/2004GB002265

Henson, S. A., Sanders, R., & Madsen, E. (2012). Global patterns in efficiency of particulate organic carbon export and transfer to the deep ocean. *Global Biogeochemical Cycles*, *26*(1), 1–14. https://doi.org/10.1029/2011GB004099

Hwang, J., Kim, M., Manganini, S. J., McIntyre, C. P., Haghipour, N., Park, J., ... Eglinton, T. I. (2015). Temporal and spatial variability of particle transport in the deep Arctic Canada Basin. *Journal of Geophysical Research: Oceans*, 2813–2825. https://doi.org/10.1002/2014JC010643.Received

Hwang, J., Manganini, S., j., Park. J., Montlucon, D., B., Toole, J., M., Eglinton, T., I., (2017). Biological and physical controls on the flux and characteristics of sinking particles on the Northwest Atlantic margin, 1–15. https://doi.org/10.1002/2016JC012549.Received

Inthorn, M., Wagner, T., Scheeder, G., & Zabel, M. (2006). Lateral transport controls distribution, quality, and burial of organic matter along continental slopes in high-productivity areas. *Geology*, *34*(3), 205–208. https://doi.org/10.1130/G22153.1

Iversen, M. H., Nowald, N., Ploug, H., Jackson, G. A., & Fischer, G. (2010). High resolution profiles of vertical particulate organic matter export off Cape Blanc, Mauritania: Degradation processes and ballasting effects. *Deep-Sea Research Part I: Oceanographic Research Papers*, *57*(6), 771–784. https://doi.org/10.1016/j.dsr.2010.03.007

Iversen, M. H., & Ploug, H. (2010). Ballast minerals and the sinking carbon flux in the ocean: Carbon-specific respiration rates and sinking velocity of marine snow aggregates. *Biogeosciences*, *7*(9), 2613–2624. https://doi.org/10.5194/bg-7-2613-2010

Iversen, M. H., & Ploug, H. (2013). Temperature effects on carbon-specific respiration rate and sinking velocity of diatom aggregates – potential implications deep ocean Earth for, 4073–4085. https://doi.org/10.5194/bg-10-4073-2013

Iversen, M. H., & Robert, M. L. (2015). Ballasting effects of smectite on aggregate formation and export from a natural plankton community. *Marine Chemistry*, *175*, 18–27. https://doi.org/10.1016/j.marchem.2015.04.009

Iversen, M.H., Lampitt, R.S., (2020). Size does not matter after all: No evidence for a size-sinking relationship for marine snow, *Progress in Oceanography*, doi: https://doi.org/10.1016/j.pocean. 2020.102445

Jackson, G. A., Maffione, R., Costello, D. K., Alldredge, A. L., Logan, B. E., & Dam, H. G. (1997). Particle size spectra between 1 µm and 1 cm at Monterey Bay determined using multiple instruments. *Deep-Sea Research Part I: Oceanographic Research Papers*, *44*(11), 1739–1767. https://doi.org/10.1016/S0967-0637(97)00029-0

Jackson, G. A., & Jr, D. M. C. (2011). Deep-Sea Research I Particle size distributions in the upper 100 m water column and their implications for animal feeding in the plankton. *Deep-Sea Research Part I*, *58*(3), 283–297. https://doi.org/10.1016/j.dsr.2010.12.008

Jacox, M. G., Bograd, S. J., Hazen, E. L., & Fiechter, J. (2015). Sensitivity of the California Current nutrient supply to wind, heat, and remote ocean forcing. *Geophysical Research Letters*, *42*(14), 5950–5957. https://doi.org/10.1002/2015GL065147

Jahnke RA (2009) Global synthesis. In: Liu KK, Atkinson L, Quinones R, Talaue-McManus L (eds) (2010) Carbon and nutrient fluxes in continental margins: A global synthesis. Springer, New York

Johnson, R. (1976). Current Profiles in the Canary Current Upwelling Region Near Cape Blanc, March and April 1974, *81*(36), 6429–6439.

Karakaş, G., Nowald, N., Blaas, M., Marchesiello, P., Frickenhaus, S., & Schlitzer, R. (2006). High-resolution modeling of sediment erosion and particle transport across the northwest African shelf. *Journal of Geophysical Research: Oceans*, *111*(6), 1–13. https://doi.org/10.1029/2005JC003296

Kindler, K., Khalili, A., & Stocker, R. (2010). Diffusion-limited retention of porous particles at density interfaces, *107*(51). https://doi.org/10.1073/pnas.1012319108

Lalande, C., Nöthig, E. M., Bauerfeind, E., Hardge, K., Beszczynska-Möller, A., & Fahl, K. (2016). Lateral supply and downward export of particulate matter from upper waters to the seafloor in the deep eastern Fram Strait. *Deep-Sea Research Part I: Oceanographic Research Papers*, *114*, 78–89. https://doi.org/10.1016/j.dsr.2016.04.014

Lam, P. J., Lee, J. M., Heller, M. I., Mehic, S., Xiang, Y., & Bates, N. R. (2018). Size-fractionated distributions of suspended particle concentration and major phase composition from the U.S. GEOTRACES Eastern Pacific Zonal Transect (GP16). *Marine Chemistry*, *201*(September), 90–107. https://doi.org/10.1016/j.marchem.2017.08.013

Lovecchio, E., Gruber, N., Münnich, M., & Lachkar, Z. (2017). On the long-range offshore transport of organic carbon from the Canary Upwelling System to the open North Atlantic. *Biogeosciences*, *14*(13), 3337–3369.

Lovecchio, E., Gruber, N., & Münnich, M. (2018). Mesoscale contribution to the long-range offshore transport of organic carbon from the Canary Upwelling System to the open North Atlantic. *Biogeosciences* (Vol. 15). https://doi.org/10.5194/bg-15-5061-2018

Lutz, M., Dunbar, R., & Caldeira, K. (2002). Regional variability in the vertical flux of particulate organic carbon in the ocean interior. *Global Biogeochemical Cycles*, *16*(3), 11-1-11–18. https://doi.org/10.1029/2000gb001383

Macintyre, S., Alldredge, A. L., & Gotschalk, C. C. (1995). Accumulation of marine snow in the water column, *40*(May).

Marchant, H. K., Holtappels, M., Lavik, G., Ahmerkamp, S., Winter, C., & Kuypers, M. M. M. (2016). Coupled nitrification-denitrification leads to extensive N loss in subtidal permeable sediments. *Limnology and Oceanography*, *61*(3), 1033–1048.

Markussen, T. N., Konrad, C., Waldmann, C., Becker, M., Fischer, G., & Iversen, M. H. (2020). Tracks in the Snow – Advantage of Combining Optical Methods to Characterize Marine Particles and Aggregates. *Frontiers in Marine Science*, *7*(June), 1–12.

Martin, J. H., Knauer, G. A., Karl, D. M., & Broenkow, W. W. (1987). VERTEX: carbon cycling in the northeast Pacific. *Deep Sea Research Part A, Oceanographic Research Papers*, *34*(2), 267–285. https://doi.org/10.1016/0198-0149(87)90086-0

Martínez-Pérez, C., Mohr, W., Löscher, C. R., Dekaezemacker, J., Littmann, S., Yilmaz, P., Lehnen, N., Fuchs, B. M., Lavik, G., Schmitz, R. A., LaRoche, J., Kuypers, M. M. M. (2016). The small unicellular diazotrophic symbiont, UCYN-A, is a key player in the marine nitrogen cycle. *Nature Microbiology*, *1*(11), 16163. https://doi.org/10.1038/nmicrobiol.2016.163

Moradi, N., Klawonn, I., Iversen, M. H., Wenzhöfer, F., Grossart, H. P., Ploug, H., Fischer, G., Khalili, A. (2021). A Novel Measurement-Based Model for Calculating Diffusive Fluxes Across Substrate-Water Interfaces of Marine Aggregates, Sediments and Biofilms. *Frontiers in Marine Science*, *8*(August), 1–12. https://doi.org/10.3389/fmars.2021.689977

Nowald, N., Karakas, G., Ratmeyer, V., Fischer, G., Schlitzer, R., Davenport, R. A., & Wefer, G. (2006). Distribution and transport processes of marine particulate matter off Cape Blanc (NW-Africa): results from vertical camera profiles. *Ocean Science Discussions*, *3*(4), 903–938. https://doi.org/10.5194/osd-3-903-2006

Nowald, N., Iversen, M. H., Fischer, G., Ratmeyer, V., & Wefer, G. (2015). Time series of in-situ particle properties and sediment trap fluxes in the coastal upwelling filament off Cape Blanc, Mauritania. *Progress in Oceanography*, *137*, 1–11. https://doi.org/10.1016/j.pocean.2014.12.015

Ohde, T., Fiedler, B., & Körtzinger, A. (2015). Spatio-temporal distribution and transport of particulate matter in the eastern tropical North Atlantic observed by Argo floats. *Deep-Sea Research Part I: Oceanographic Research Papers*, *102*, 26–42.

Passow, U. (2002). Transparent exopolymer particles (TEP) in aquatic environments. *Progress in Oceanography*, *55*(3–4), 287–333. https://doi.org/10.1016/S0079-6611(02)00138-6

Pauly, D., & Christensen, V. (1995). Primary production required to sustain global fisheries. *Nature*, *374*(6519), 255–257. https://doi.org/10.1038/374255a0

Pelegrí, J. L., Arístegui, J., Cana, L., González-Dávila, M., Hernández-Guerra, A., Hernández-León, S., Marrero-Díaz, A., Montero, M.F., Sangrá, P., Santana-Casiano, M. (2005). Coupling between the open ocean and the coastal upwelling region off northwest Africa: Water recirculation and offshore pumping of organic matter. *Journal of Marine Systems*, *54*(1-4 SPEC. ISS.), 3–37. https://doi.org/10.1016/j.jmarsys.2004.07.003

Ploug, H., & Jørgensen, B. B. (1999). A net-jet flow system for mass transfer and microsensor studies of sinking aggregates. *Marine Ecology Progress Series*, *176*(1987), 279–290. https://doi.org/10.3354/meps176279

Puig, P., Madron, X. D. de, Salat, J., Schroeder, K., Martín, J., Karageorgis, A. P., ... Houpert, L. (2013). Thick bottom nepheloid layers in the western Mediterranean generated by deep dense shelf water cascading. *Progress in Oceanography*, *111*, 1–23. https://doi.org/10.1016/j.pocean.2012.10.003

Ransom, B., Shea, K. F., Burkett, P. J., Bennett, R. H., & Baerwald, R. (1998). Comparison of pelagic and nepheloid layer marine snow: Implications for carbon cycling. *Marine Geology*, *150*(1–4), 39–50. https://doi.org/10.1016/S0025-3227(98)00052-8

Romero, O., Ramondenc, S., & Fischer, G. (2020). A two-decades (1988–2009) record of diatom fluxes in the Mauritanian coastal upwelling: Impact of low-frequency forcing and a two-step shift in the species composition. *Biogeosciences Discussions*, 1–32. https://doi.org/10.5194/bg-2020-336

Roullier, F., Berline, L., Guidi, L., Durrieu De Madron, X., Picheral, M., Sciandra, A., ... Stemmann, L. (2014). Particle size distribution and estimated carbon flux across the Arabian Sea oxygen minimum zone. *Biogeosciences*, *11*(16), 4541–4557. https://doi.org/10.5194/bg-11-4541-2014

Santana-Falcón, Y., Mason, E., & Arístegui, J. (2020). Offshore transport of organic carbon by upwelling filaments in the Canary Current System. *Progress in Oceanography*, *186*(March), 102322. https://doi.org/10.1016/j.pocean.2020.102322

Santschi, P. H., Balnois, E., Wilkinson, K. J., Zhang, J., Buffle, J., & Guo, L. (1998). Fibrillar polysaccharides in marine macromolecular organic matter as imaged by atomic force microscopy and transmission electron microscopy. *Limnology and Oceanography*, *43*(5), 896–908. https://doi.org/10.4319/lo.1998.43.5.0896

Schindelin, J., Arganda-Carreras, I., Frise, E., Kaynig, V., Longair, M., Pietzsch, T., … Cardona, A. (2012). Fiji: An open-source platform for biological-image analysis. *Nature Methods*, *9*(7), 676–682.

Sichert, A., Corzett, C. H., Schechter, M. S., Unfried, F., Markert, S., Becher, D., … Hehemann, J. H. (2020). Verrucomicrobia use hundreds of enzymes to digest the algal polysaccharide fucoidan. *Nature Microbiology*, *5*(8), 1026–1039.

Steinberg, D. K., & Landry, M. R. (2017). Zooplankton and the Ocean Carbon Cycle. *Annual Review of Marine Science*, *9*(1), 413–444.

Thiele S., Fuchs B. M, Amann R., Iversen M. H. (2015) Colonization in the photic zone and subsequent changes during sinking determines bacterial community composition in marine snow. *Applied and Environmental Microbiology*. 81:1463-1471, doi:10.1128/AEM.02570-14

Thiele, S., Basse, A., Becker, J. W., Lipski, A., Iversen, M. H., & Mollenhauer, G. (2019). Microbial communities in the nepheloid layers and hypoxic zones of the Canary Current upwelling system. *MicrobiologyOpen*, *8*(5), 1–13. https://doi.org/10.1002/mbo3.705

Turner, J. T. (2015). Progress in Oceanography Zooplankton fecal pellets , marine snow , phytodetritus and the ocean ' s biological pump. *Progress in Oceanography*, *130*, 205–248. https://doi.org/10.1016/j.pocean.2014.08.005

Van Camp, L., Nykjaer, L., Mittelstaedt, E., & Schlittenhardt, P. (1991). Upwelling and boundary circulation off Northwest Africa as depicted by infrared and visible satellite observations. *Progress in Oceanography*, *26*(4), 357–402. https://doi.org/10.1016/0079-6611(91)90012-B

van der Jagt, H., Iversen, M. H., Friese, C., & Stuut, J. W. (2018). The ballasting effect of Saharan dust deposition on aggregate dynamics and carbon export : Aggregation , settling ,. https://doi.org/10.1002/lno.10779

van der Jagt, H., Wiedmann, I., Hildebrandt, N., Niehoff, B., & Iversen, M. H. (2020). Aggregate Feeding by the Copepods Calanus and Pseudocalanus Controls Carbon Flux Attenuation in the Arctic Shelf Sea During the Productive Period. *Frontiers in Marine Science*, *7*(September). https://doi.org/10.3389/fmars.2020.543124

Waldron, H. N., Monteiro, P. M. S., & Swart, N. C. (2009). Carbon export and sequestration in the southern Benguela upwelling system: Lower and upper estimates. *Ocean Science*, *5*(4), 711–718. https://doi.org/10.5194/os-5-711-2009

Manuscript III

Release of ballast material during sea-ice melt enhances carbon export in the Arctic Ocean

Steffen Swoboda[1*], Thomas Krumpen[2], Eva-Maria Nöthig[2], Katja Metfies[2], Simon Ramondenc[1,2], Jutta Wollenburg[2], Kirsten Fahl[2], Ilka Peeken[2], Morten H. Iversen[1,2*]

[1]MARUM - Center for Marine Environmental Sciences, University of Bremen, Leobener Str. 8, 28359 Bremen, Germany.
[2]Alfred Wegener Institute, Alfred Wegener Institute Helmholtz Centre for Polar and Marine Research, Am Handelshafen 12, 27570 Bremerhaven, Germany.

Corresponding authors:
Steffen Swoboda
Morten Iversen

Abstract

Globally, the most intense uptake of anthropogenic carbon dioxide occurs in the Atlantic part of the Arctic Ocean, however, little is known about how carbon uptake and export will be impacted by pan-Arctic sea-ice decline. We investigated how sea-ice derived material affects particle ballasting and carbon export in the Fram Strait by combining 13-years of flux measurements with benthic eDNA analysis, laboratory experiments and sea-ice distributions. We show that melting sea-ice in the Fram Strait releases cryogenic gypsum and terrigenous material, which ballasts sinking particles and thereby enhances their settling velocities by up to 10-fold. This resulted in up to 30% higher carbon export in the vicinity of the ice edge where both gypsum and terrigenous material were released to the water column during ice-melt. Cryogenic gypsum is formed within sea-ice during ice-formation and ballasting by gypsum is expected to persist in the future as long as sea-ice melting and release of gypsum is consistent with phytoplankton phenology. However, terrigenous material is primarily incorporated into sea-ice when ice is formed on the Arctic continental shelfs. Since, less sea-ice is currently formed on shelfs, terrigenous fluxes from melting sea-ice in the Fram Strait are here shown to be reduced by >80% per decade. We predict that terrigenous flux will ultimately cease when intensified sea-ice melt interrupts transarctic sea-ice transport, thus limiting particle ballasting when the ice melts in the Fram Strait. Therefore, sea-ice loss will likely reduce carbon export in the Fram Strait and generally in the future Arctic Ocean.

Introduction

The biological pump drives the export of organic matter from the surface to the deep ocean, mediating carbon sequestration and delivering organic matter to subsurface and benthic ecosystems (*1, 2*). The main vectors for organic matter export are zooplankton fecal pellets and marine snow particles which are composed of the prevailing material in the water column, including inorganics (e.g. minerals), living and/or detrital organic material (*3*). The efficiency with which marine snow particles and zooplankton fecal pellets are transferred to the deep ocean is largely determined by their settling velocity and the rate at which the contained organic matter is degraded. The most common degradation mechanisms are zooplankton grazing and microbial remineralization (*4*). Typically, most flux attenuation occurs in the upper 100 m of the water column (*5*). Therefore, fast settling particles are more likely to overcome high degradation by sinking rapidly through the water column. As a result, particle settling velocities are a controlling factor for the extent of particle degradation in the water column (*4*).

In the sea-ice covered Arctic, brine channels in the ice (*6*), ice ridges and the snow-ice interface act as a habitat for ice- and cryopelagic algae (*7, 8*). In addition, sea-ice melt induces surface stratification which promotes the formation of phytoplankton blooms that form long narrow belts along the ice edge (*9, 10*). The diverse phytoplankton communities associated to sea-ice may therefore sustain an enhanced primary production and have been observed to increase flux of particulate organic carbon (POC) in the vicinity of the ice edge compared to ice free areas (*11-14*). This enhanced POC flux was explained by increased sinking velocities in the sea-ice vicinity (*14, 15*).

Increased particle settling velocities can be caused by the incorporation of ballasting components (e.g. sediments or minerals) into marine particles (*4, 16-18*). Recently, cryogenic gypsum was discovered as a sea-ice mediated ballasting component in the Arctic Ocean (*19*). Cryogenic gypsum crystals form during ion precipitation in sea-ice brine (20) and were observed to be released during ice melt (*19, 21*). The released cryogenic gypsum was incorporated into marine particles in the water column, including slow sinking colonies of *Phaeocystis* spp., which enhanced their settling velocities and led to their rapid export to the seafloor (*19*).

In addition to cryogenic gypsum, Arctic sea-ice can contain large amounts of sediments (Nürnberg et al. 1994), which can also serve as a ballasting component. During the formation of sea-ice on the shallow Siberian shelf, terrigenous material is incorporated by suspension freezing or by anchor ice which plows through shallow sediments (*22*, *23*). Subsequently, the sea-ice is transported across the Arctic Ocean by the Transpolar Drift and the ice rafted sediments are released during sea-ice melt, which typically occur in the Atlantic sector of the Arctic (*24*, *25*).

Sea-ice rafted sediments are mostly composed of quartz and clay minerals (*22*, *26*, *27*), which were observed to efficiently ballast marine snow particles in laboratory experiments, resulting in 2-fold higher particle settling velocities compared to non-ballasted particles (*17*, *22*). Typically, terrigenous and POC flux are high in the vicinity of the sea-ice edge (*11*), and it was suggested that ballasting sediments may drive a more efficient POC export in the Arctic Ocean (*28*).

The continuous reduction of Arctic sea-ice area and the transition from multi-year towards first-year sea-ice may have strong repercussions on sea-ice mediated particle ballasting. Since only shelf formed ice contains terrigenous material, the reduced sea-ice formation on the Siberian shelf decreases the release from melting sea-ice (*24*, *29*). Cryogenic gypsum precipitation is not restricted to sea-ice formation in shelf areas, but a decline of the annual sea-ice formation will reduce the production and hence, ballasting potential by cryogenic gypsum. However, while the sea-ice decline in the Arctic Ocean appears to overall reduce the potential for sea ice ballasting, the lowered sea-ice cover also leads to more light availability in the upper water column which increases primary production (30). It is therefore unclear what impact a reduction of sea-ice ballasting may have on carbon export in a more productive future Arctic Ocean.

In this study, we utilize continuous flux measurements from sediment traps at station HG-IV (in the central Fram Strait) between 2000 – 2013 in combination with eDNA sediment samples, remote sensing data on sea-ice distributions as well as laboratory experiments to assess the role of sea-ice mediated ballasting. We focus on the export of the marine haptophyte *Phaeocystis* spp. as model organism, as it is neutrally buoyant and therefore does not contribute considerably to export flux below 100 m water depth if not ballasted (*19*, *31*-*34*). We assessed the role of the sea-ice edge for carbon export and consequential sympagicpelago-benthic coupling and predict that future sea-ice decline may reduce carbon export in the Arctic Ocean.

Results

Sea-ice cover and export fluxes at station HG-IV in the central Fram Strait

Analyzed sediment trap fluxes cover the sampling period from 2000 – 2013. Sediment trap fluxes of POC and numbers of 18S-sequences of *Phaeocystis spp.* (*Phaeocystis* spp. Operational Taxonomic Units, respectively *Phaeocystis* spp. OTUs) between March and September were significantly higher when the distance to the ice edge was a 0 – 40 km from the trap compared to POC flux and Phaeocystis spp. OTUs that were collected while the ice edge was 40 – 80 km from the trap (Wilcoxon signed-rank test; $p < 0.05$; Fig 2c, 2d). The flux of POC and sterol based terrigenous markers from March to September was significantly positively correlated (Spearman's rank correlation coefficient; $p < 0.001$; Fig. 2e). The monthly export flux of POC, terrigenous marker and sequence abundance of *Phaeocystis* spp. OTUs in the sediment traps were highest in April and August with a drop in export fluxes from May to July (Fig. 3a & 3b).

The occurrence of 0.15 µg/L sea-ice campesterol and 0.41 µg/L sea-ice sitosterol in the studied sea-ice samples (including *Melosira arctica* aggregates) from the Amundsen Basin can be considered to support the association between sympagic biota and terrigenous biomarkers entrained in the sea-ice.

The sea-ice coverage was integrated to the duration of the respective sampling periods from the sediment trap and increased from ~0-5% in March to ~20% in June and decreased afterwards to 0% during ice-free conditions in September (Fig. 3c). Terrigenous marker fluxes decreased significantly over the sampling period from 2000 – 2013 (Seasonal Mann-Kendall test; $p < 0.001$; Fig. 5d).

Seafloor DNA samples

Sequence abundances of *Phaeocystis* spp. were measured from deep ocean sediment samples (collected with multi-corer sediment samplers) across a latitudinal transect of the Fram Strait over the time period 2003 – 2016. Sequence abundances indicated an enhanced *Phaeocystis spp.* deposition at the ice-covered stations located in the east Greenland current (EG stations) compared to the HG stations located in mainly ice-free Atlantic waters of the WSC (fig. S1). However, due to the limited sample availability for the EG stations (n = 8) compared to the HG stations (n = 37) and a large variability was observed in the sequence abundances of *Phaeocystis* spp. OTUs and our interpretation of higher export of *Phaeocystis spp*. at the EG stations compared to the HG stations could not be verified by statistical testing.

Gypsum scavenging experiment

We incubated in situ formed organic aggregates that were collected 10 m below the depth of the chlorophyll maximum layer in roller tanks with large (>63 µm) and small (>30 to <63 µm) sized gypsum crystals to test how scavenging of the gypsum affected the size-specific settling velocities of formed aggregates. The scavenging experiment with large sized gypsum crystals (> 63 µm) showed a significantly higher particle settling velocities (two-way ANOVA, $p < 0.05$) over the entire 15h of the experiment, when compared to the control treatment (Fig. 4a). Further, particle settling velocities did not decrease over time, i.e. between 0h and 15h of incubation.

In contrast, the scavenging experiment with small sized gypsum crystals (≥30 to ≤63 µm) showed a noticeable, but not significant increase of particle settling velocities 3h and 5h after the addition of gypsum, and decreased afterwards to similar settling velocities as the control treatment (Fig. 4b). A detailed overview of measured settling velocities is listed in table S3.

Sea-ice tracking

Satellite-based trajectories of sea-ice leaving Fram Strait were calculated in monthly intervals over the period from 1997 – 2021. The age of sea-ice exiting through the Fram Strait significantly decreased over the sampling period from 1997 to 2021 (Seasonal Mann-Kendall test, $p < 0.01$, tau = -0.24; Fig. 5a). This is in line with the significant reduction of the modelled sea-ice thickness from 1997 to 2021 (Seasonal Mann-Kendall test, $p < 0.001$, tau = -0.40; Fig. 5b). The area in which the exported sea-ice was formed significantly shifted from shallow areas close on the shelf to areas of greater depth in the open Arctic Ocean from 1997 to 2021 (Seasonal Mann-Kendall test, $p < 0.05$, tau = -0.103; Fig. 5c).

Discussion

Increased POC export in the sea-ice vicinity

POC fluxes measured over a period of 13 years during the productive season at HG-IV were significantly higher with sea-ice proximity of 0 – 40 km compared to periods when the sea-ice proximity was 40 – 80 km ($p < 0.05$, Fig 2c). Additionally, we observed that POC flux was positively correlated to terrestrial marker flux ($p < 0.05$, Fig 2e). This was especially pronounced during April and August when sea-ice melting occurred at HG-IV when sea-ice approached and retreated, respectively. The sea-ice melt and release of terrigenous material caused a ballasting of settling organic matter and resulted in elevated POC and terrestrial marker flux compared to periods with larger distance to the ice-edge, i.e. no terrigenous material released from sea-ice (Fig. 3a & 3b). Similar observations have been made in previous studies where elevated POC and ice-rafted sediment fluxes were found in the vicinity of the sea-ice edge compared to ice-free regions (*11*, *14*). This suggests that the release of terrestrial and lithogenic material from melting sea-ice at the ice-edge can ballast organic matter, causing it to sink faster and thereby increase POC flux. This is supported by direct observations of higher particle settling velocities in ice-associated regions compared to ice-free areas (*14*, *15*). While a correlation between POC and terrigenous fluxes alone does not confirm ballasting of organic aggregates by ice-rafted material, these combined observations of elevated POC, terrigenous material flux as well as higher particle settling velocities in ice-associated areas, suggest particle ballasting as an important driver for elevated POC export at or near the ice-edge during ice-melt.

Ballasting potential by cryogenic gypsum

We observed a temporary increase of particle settling velocities when gypsum crystals were incorporated (Fig. 4), supporting the proposed ballasting effect of gypsum (*19*). Ballasting by small gypsum crystals (>30 to < 63 µm) caused a 1.5-fold increase in settling velocities, however, this effect was short-lived (3-5 h), due to the rapid dissolution of gypsum crystals in sea water and within the aggregates (*21*). Nevertheless, this could still enhance POC fluxes out of the upper water column, where organic matter is most vulnerable to attenuation due to the high zooplankton grazing in the upper few hundred meters of the water column (5). It should also be noted that these results are conservative, as we incubated at a temperature of 2°C, which is comparable to Atlantic water temperatures in Fram Strait (*21*), whereas other Arctic waters are colder (-1°C). As gypsum dissolution decreases with decreasing water temperature, gypsum ballasting by small crystals would have a longer and more pronounced ballasting potential in the colder Arctic waters.

In contrast, ballasting by large gypsum crystals (> 63 µm) caused a 10-fold increase in sinking velocities, which lasted until the end of the incubation (after 15 h), presumably due to their smaller surface to volume ratio which results in a slower dissolution (*21*). Hence, > 63 µm sized gypsum crystals have the potential to enhance POC flux to the deep ocean and mediate POC deposition on the sea floor in both relatively warm Atlantic and cold Arctic waters.

Considering that we added a similar mass of small and large sized gypsum crystals in the experiments, this implies that the ballasting effect by gypsum is largely dependent on the size distribution of gypsum crystals, i.e. the dissolution time, and not the quantity of the gypsum crystals released during sea-ice melt. In contrast to gypsum, the ballasting effect by terrigenous material is not temporarily limited by dissolution (*17*) and therefore, the quantity of released terrigenous material is likely the determining factor of its ballasting potential. Consequentially, particles that are ballasted by terrigenous material may have a higher potential to mediate deposition of POC on the seafloor, especially in the warmer Atlantic waters where sea-ice typically melt.

Phaeocystis **spp. export as an indicator for sea-ice mediated ballasting**

To further assess potential particle ballasting from the bulk samples of the sediment trap time series, we used the export flux of the algae *Phaeocystis* spp. as an indirect indication of particle ballasting. *Phaeocystis* spp. forms colonies with large amounts of gelatinous polysaccharides, which increase buoyancy and therefore lower their sinking velocities to ~10 m day^{-1}, with reports of *Phaeocystis* spp. colonies even rising to the surface (*35*, *36*). As a result, *Phaeocystis* spp. is usually considered to be retained within the upper 100 m of the water column and does not contribute notably to export flux without being ballasted (*31*- *34*). However, we observed flux of *Phaeocystis* spp. to 180 – 340 m at the vicinity of the ice edge (Fig. 2d). This suggests that the *Phaeocystis* spp. flux must have been ballasted, which supports previous observations of export of ballasted *Phaeocystis* spp. (*13*). While it should be noted that vertical mixing (*32*) and downwelling (*12*) were suggested to export *Phaeocystis* spp. to water layers ≥ 100 m, only an increase in density by ballasting was observed to export *Phaeocystis* spp. to greater depths and even deposition on the sea floor in >2000 m (*19*).

To further verify the possibility of ice mediated ballasting, we analyzed sediment samples across an east-west transect along the Fram Strait for the deposition of *Phaeocystis* spp.. We observed *Phaeocystis* spp. across the entire transect, with a notably enhanced deposition in the more frequently ice associated part of the western Fram Strait (EG stations), despite the common occurrence of *Phaeocystis* spp. throughout the entire Fram Strait (fig. S1; *13*, 37, *38*). Therefore, we suggest that the efficient export and deposition of *Phaeocystis* spp. at depths >2000 m was due to ballasting by cryogenic gypsum and/or ice rafted sediments, which were released during sea-ice melt in the Fram Strait.

Sea-ice derived ballasting – an overlooked process in the Arctic?

The efficient export of organic matter in ice covered regions has previously been observed as mass sedimentation events of the cryopelagic algae *Melosira arctica* (*39*) and indications towards high carbon transfer efficiencies from the surface to the seafloor by benthic remineralization rates (40). The effective transport of *M. arctica* might have been increased by additional ballasting through terrigenous material. This was supported by the presence of campesterol and sitosterol in algae aggregates sampled from sea-ice leads during the same campaign where the mass sedimentation of *M. arctica* was observed. In addition, *M. arctica* has also been shown to incorporate cryogenic gypsum, when it is released from the sea-ice during the melting season (*21*). This suggests that sea-ice mediated particle ballasting may be a common, but overlooked, driver for efficient carbon export in the Arctic.

The proposed processes of particle ballasting by ice rafted material are summarized in figure 6. Terrigenous material is incorporated during sea-ice formation while cryogenic gypsum may form in first year ice from ion precipitation in the sea-ice brine. The ice rafted material is transported along the Arctic Transpolar Drift and released during sea-ice melt at the outflow gateways of the Arctic Ocean, e.g. Fram Strait. When the released material encounters organic matter as it sinks through the water column, it may act as a ballasting component, which increases POC flux and therefore drives a more efficient export of carbon to the deep ocean.

Recently it has been shown that primary production in the Fram Strait is linked to the mixed layer depth (MLD) and the sea-ice edge (*10*). In direct proximity of the sea-ice edge, meltwater forms a strong halocline with a narrow MLD which vertically limits primary production while maintaining the phytoplankton in surface waters, thus delaying carbon export until late summer (*10*). In contrast, less sea-ice melt formed a deeper reaching MLD which supported a higher phytoplankton biomass that was exported earlier in the season (*10*). The limited carbon export during the narrow MLD regime matches well with our observations, that showed that POC export is limited when sea-ice cover is ≥ 15%. However, despite a potentially limited primary production by a narrow MLD, this does not rule out a more efficient and direct export closer to the ice edge under less sea-ice cover. Though it should be noted that during the period of the observations (2017 & 2018), ballasting by terrigenous material was likely limited since the sea-ice exported through the Fram Strait was not formed on the shallow shelf and therefore did not incorporate shelf sediment during ice-formation (fig. 5c). In conclusion we suggest, that the mechanisms that promote primary production and drive carbon export gradually alter in the marginal ice zone according to the amount of sea-ice cover. The MLD promotes a gradually increasing primary production from >20%– 0% sea-ice cover, while the onset of particle ballasting when sea-ice cover drops ≤ 15% leads to a direct and efficient carbon export.

Implications of global warming on sea-ice mediated ballasting

Rising temperatures in the Laptev Sea and central Arctic Ocean are leading to a reduction of sea-ice formation in shallow areas and thereby reduced potential for the entrainment of terrigenous material from shallow shelf regions (Fig. 5c, *22*, *23*). Coupled to the continuous reduction of long-range sea-ice transport and a premature release of ice-rafted material in the Central Arctic (*24*, *41*), we conclude that the continuous decrease of terrigenous marker fluxes between 2000 – 2013 in the Fram Strait (Fig. 5d; *29*) resulted in the reduced POC export. As temperatures in the Arctic continue to rise, we expect that the uptake and transport of ice-rafted material and thus the effect of terrestrial ballasting to further reduce and ultimately cease when the transarctic sea-ice transport from the Siberian shelf is disrupted (Fig. 5c). However, there are substantial uncertainties as to how cryogenic gypsum ballasting might impact POC flux during the transition period to an ice-free Fram Strait. Increased proportions of melting first year sea-ice (*42*), which contains higher gypsum contents (*21*), might enhance POC flux. However, the progressively earlier onset of sea-ice melt may result in a phenological mismatch between ice melt and bloom formation (*43*, *44*), reducing the potential for gypsum ballasting. Combined with a projected ice-free Arctic Ocean during summer seasons at the end of this century or even earlier (*44*), gypsum ballasting is expected to reduce to negligible amounts, thus reducing POC export in the Arctic Ocean.

Material and Methods

Sediment trap fluxes and sea-ice concentrations at station HG-IV

Field samplings were performed at the long-term ecological research (LTER) observatory HAUSGARTEN located in the eastern Fram Strait (Fig. 1). Flux measurements were obtained from moored sediment traps at station HG-IV (~ 79° N; 04° E) of the observatory. Here, sinking particles including marine microorganism from all size classes were sampled by modified automatic Kiel sediment traps (SMT 230 K/MT), with a sampling area of ~ 0.5 m^2, and 20 liquid-tight sampling cups (*45- 47*). The moored long-term sediment traps were deployed annually from 2001 - 2013 (not every year and month were fully covered, see Table S1) between 180 – 340 m depth (except from 20.07.2009 – 15.07.2010 where the deployment depth was 80 m; see table S1). The collection period of sampling cups lasted for 10-31 days, respective, with shorter intervals timed during the productive season (table S1).

Details on sample handling and measurements of particulate organic carbon (POC) fluxes can be obtained from "(*10*)". Terrigenous marker fluxes included campesterol (24-methylcholest-5-en-ß-ol) and sitosterol (24-ethylcholest-5-en-3ß-ol) and were obtained according to "(*47*)". To support the concept of these terrigenous markers in association with sea-ice derived biota, samples of different sea-ice habitats including melt ponds (with and without *Melosira arctica* aggregates), collected in the Amundsen Basin (for details see "(*48*)") were also analyzed for campesterol and sitosterol.

Data of sea-ice concentration and extent were obtained from NSIDC/NOAA and estimated according to "(*10*)", where the sea-ice edge was defined as areas with 15% sea-ice concentration. Consequentially, the distance to the ice-edge was defined as the distance from the area with 15% sea-ice concentration to the station HG-IV in central HAUSGARTEN. Sediment trap fluxes obtained during periods with an average sea-ice edge distance >150 km to station HG-IV were not considered for analysis. An overview of sediment trap fluxes and sea-ice distributions are given in table S1.

eDNA analyses: Sampling and DNA-isolation:

Sediment trap samples for eDNA-analyses, covered the deployment years 2001, 2006 and 2012 as well as peak productive periods between 2000 and 2013 (sample details shown in table S1). The samples were split by a wet splitting procedure after removal of zooplankton (swimmers) > 0.5 mm, which were manually removed under a dissecting microscope at a magnification of 20 and 50. Subsequent molecular analyses are based on 1/32 splits of the original sediment trap sample. We collected cells for DNA isolation of DNA by filtration of a split fraction from the original sample onto a 0.22 µm Sterivex-Filter (Millipore, Schwalbach, Germany). Filters were washed with sterile North Sea water (~50 ml). Genomic DNA was isolated from the samples with the PowerWater DNA Isolation Kit (Qiagen, Hilden, Germany) according to the manufacturers protocol.

Benthic eDNA analyses were based on processing samples from the upper 1 cm of sediment cores collected with a TV-guided multicorer at 45 stations along an east-west transect covering 5.6° E and 6° W at ~79° N (table S2) between 2003 – 2016. Tip-less syringes were used to collect three smaller subsamples from the original core. Subsequent to sampling, the syringes containing the sediment were stored at -20°C until further processing. For DNA-isolation, the first top centimeter (0-1 cm) of core in the syringe was cut off using a sterile scalpel. From each of the three subsamples, ~0.5 g sediment was pooled, while 0.25 g of this pool was subjected to further processing. Genomic DNA was isolated using the DNeasy PowerSoil Kit (Qiagen, Hilden, Germany) following the manufacturer’s protocol. DNA concentrations of both, sediment trap- and benthic samples, were determined using the Quantus Fluorometer (Promega, Germany) according to the manufacturer’s protocol for measuring double stranded DNA. The resulting DNA-extracts were stored at -80 °C until further analyses.

Illumina-Sequencing 18S rDNA: For Illumina-Sequencing, a fragment of the 18S rDNA containing the hypervariable V4 region was amplified with the primer set 528iF (5’-GCGGTAATTCCAGCTCC-3’) (*49*) and: 938iR (5’-GGCAAATGCTTTCGC-3’). All PCRs (polymerase chain reaction) had a final volume of 25 µLand contained 12.5 µl mastermix (KAPA HiFi HotStart ReadyMix, KAPABiosystems, Roche), 2.5 µl of each primer (1 µMol) and 2.5 µl genomic DNA (~ 5 ng/µl). PCR amplification was performed in a thermal cycler (Eppendorf, Germany) with an initial denaturation (95 °C, 3 min) followed by 25 cycles of denaturation (95 °C, 30 sec), annealing (55 °C, 30 sec), and extension (72 °C, 30 sec) with a single final extension (72 °C, 5 min). The PCR products were purified from an agarose gel 1% [w/v] with the AMPure

XP PCR purification kit (Beckman Coulter, Ing., USA) according to the manufactuer's protocol. Subsequent to purification of the 18S rDNA fragment the DNA concentrations of the samples were determined using the Quantus Fluorometer (Promega, USA). Indices and sequencing adapters of the Nextera XT Index Kit (Illumina, USA) were attached via the Index PCR. All PCRs had a final volume of 50 µl and contained contained 25 µl of KAPA HIFI Mix (Kapa Biosystems, Roche, Germany), 5 µl of each Nextera XT Index Primer [1 µmol/L], 5 µl DNA-template [~5ng] and 10 µl PCR grade water. PCR amplification was performed in a thermal cycler (Eppendorf, Germany) with an initial denaturation (95 °C, 3 min) followed by 8 cycles of denaturation (95 °C, 30 sec), annealing (55 °C, 30 sec), and extension (72 °C, 30 sec) with a single final extension (72 °C, 5 min). Prior to quantification of the PCR products with the Quantus Fluorometer (Promega, USA) for sequencing with the MiSeq-Sequencer (Illumina, USA), the final library was cleaned up using the AMPure XP PCR purification kit (Beckman Coulter, Ing., USA). Sequencing of the DNA-fragments was carried out with the MiSeq Reagent Kit V3 (2 x 300 bp) according to the manufacturer's protocol (Illumina, USA). Raw sequences generated in this study have been deposited at the European Nucleotide Archive (ENA) with the accession number xxx (accession number will be provided subsequent to acceptance of the manuscript).

Sequence analyses: Raw reads were quality trimmed with Trimmomatic (*50*). Thus, reads were scanned with a 4-base wide sliding window and cut when the average quality dropped below 15. For merging paired-end reads, the script join-paired-ends within the open-source bioinformatics pipeline QIIME v.1.8.0 (*51*) was used with a minimum read overlap of 20 bases. Further analyses were performed using QIIME v.1.8.0 (*51*). In short, reads were quality-filtered according to recommended settings (*52*). Only sequences that fully matched the primer sequences at the beginning and end of the sequence, respectively, and which were between 200 and 500 bp in length were further processed. For chimera detection and clustering of sequences into OTUs we used the QIIME workflow 'usearch.qf', which incorporates UCHIME (*53*). Pre-clustered sequences were checked for chimeras (de novo and with Silva 119 SSU Ref NR). The remaining sequence set was clustered (de novo) into OTUs with a similarity threshold of 98%. The taxonomy of OTUs were classified using the QIIME default sequence classifier UCLUST (*54*) Normalization, analyses and visualization of the sequence data was carried out in R (R Development Core Team, 2008). The sequence data set was normalized to the lowest number of OTUs in the study using the rarefy function from the

Vegan package. 18S sequences of *Phaeocystis* spp. OTUs are published in Genbank and sequence abundances in the samples are published in PANGAEA. Accession numbers will be provided subsequent to acceptance of the manuscript.

Gypsum scavenging experiment

To study the ballasting effect of cryogenic gypsum crystals on particle settling, we used a modified approach of the "scavenging experiment" from "(*18*)" where we observed settling velocities of *in-situ* marine snow particles which were encountered with gypsum crystals. Cryogenic gypsum crystals used in the experiments were collected *in-situ* during research expedition PS106 1/2 in 2017 (see "(21)" for further details). Experiments were performed during research expedition PS121 in 2019.

For the experiment, *in-situ* marine snow aggregates were collected with a marine snow catcher (MSC). The collection depth was set 10 m below the chlorophyll maximum layer, which was detected from fluorescence readings and ranged between 40 – 60 m. Captured marine snow aggregates were let to settle for 8h within the MSC, before the overlying water was gently drained. Collected aggregates were evenly divided into 6 roller tanks (1.15 l tank^{-1}) filled with filtered seawater from the MSC, of which one was used as a control while a gypsum suspension was added to the remaining 5 tanks. A total of 4 experiments were carried out in a temperature-controlled laboratory set at 2°C, with two utilizing a gypsum suspension with crystals $\geq$ 30 µm - $\leq$ 63 µm (24.32 mg L^{-1} and 20.06 mg L^{-1}) and two with crystals $\geq$ 63 µm (21.12 mg L^{-1} and 23.33 mg L^{-1}). The gypsum crystals were suspended in 50 ml filtered seawater from which 10 ml was added to each roller tank respectively. The gypsum treated roller tanks were designated to one of 5 time points respectively (3h, 5h, 7h, 10h, 15h) and placed on a roller table set at 3 RPM. For each time point, video recordings of the designated tank and the control tank were taken (Sony alpha a7II; Zeiss Loxia 50mm f2.2). Measurements of particle size and settling velocity were obtained from the captured video recordings according to "(*55*)". Measured settling velocities from roller tank experiments with gypsum crystals $\geq$ 30 µm - $\leq$ 63 µm and crystals $\geq$ 63 µm were grouped respectively for further analysis.

Sea-Ice tracking

In order to determine trajectories and origin of sea-ice passing the sediment trap position at 79°N/4.3°E, we applied a Lagrangian approach called ICETrack. The approach traces sea-ice backward in time using a combination of low-resolution satellite and atmospheric reanalysis data products. So far, ICETrack has been used in a number of publications to examine sea-ice sources, pathways, thickness changes and atmospheric processes acting on the ice cover (*56-58*).

In summary, IceTrack uses a combination of the following three different ice drift products for the tracking of sea-ice: (i) motion estimates provided by the Centre for Satellite Exploitation and Research (CERSAT; *59*), (ii) the OSI-405-c motion product from the Ocean and Sea Ice Satellite Application Facility (OSI SAF; Lavergne, 2016), and (iii) Polar Pathfinder Daily Motion Vectors (v.4) from the National Snow and Ice Data Center (NSIDC; *60*). The IceTrack algorithm first checks for the availability of CERSAT motion data, since CERSAT provides the most consistent time series of motion vectors starting from 1991 to present and has shown reliable performance (*61*). During the summer months (June–July), when drift estimates from CERSAT are missing, motion information is bridged with the OSI SAF product (2012 to present). Prior to 2012, or if no valid OSI SAF motion vector is available within the search range, NSIDC data are applied. Along track, several additional parameters from various satellite- and reanalysis products are derived. E.g. sea-ice concentration is retrieved from a CERSAT product (*62*), while the thermodynamic ice thickness was calculated by means of NCEP reanalysis 2m-air temperature data (*63*) following "(*64*)". The model was tested and applied in "(*58*)".

The reconstruction of sea-ice trajectories works as follows: Sea-ice is traced backward in time on a monthly basis starting on the 1st of each month (1997 - 2021). Tracking is discontinued if sea-ice concentration, at a specific location along the trajectory drops below 25%, which the algorithm defines as the position at which the ice is formed. Since the study of "(*65*)" indicated a limited performance of IceTrack in the Fram Strait, tracking performed in this study is initiated at a position located further north. This position (83°N/11°E) was chosen to be in the catchment area of the sediment trap, which was determined in a separate tracking experiment.

Statistical analysis

Statistical analysis of long-term trends in sediment trap fluxes and environmental data were performed with a seasonal non-parametric Kendall rank correlation coefficient. The monthly difference of export fluxes measured in a distance of 0-40 km and 40-80 km from the ice edge were tested with a Wilcoxon rank sum test. The correlation between POC and terrigenous marker flux measured with the sediment traps was tested with a spearman rank correlation. For the gypsum ballasting experiments, settling velocities where Log$_{10}$ transformed to assure a normal distribution after which a two-way ANOVA and Tukey test were performed to test for difference in settling velocity between control and gypsum added treatments. All statistical testing was performed in R (R Core Team 2021).

References

1. Volk, T., & Hoffert, M. I. (1985). Efficiencies in ocean-driven carbon pumps: Analysis of relative strengths and efficiencies in ocean-driven atmospheric CO$_2$ changes. *The Carbon Cycle and Atmospheric CO2: Natural Variations Archean to Present*, *32*, 99–110.
2. Boyd, P. W., Claustre, H., Levy, M., Siegel, D. A., & Weber, T. (2019). Multi-faceted particle pumps drive carbon sequestration in the ocean. *Nature*, *568*(7752), 327–335.
3. Turner, J. T. (2015). Progress in Oceanography Zooplankton fecal pellets, marine snow , phytodetritus and the ocean ' s biological pump. *Progress in Oceanography*, *130*, 205–248. https://doi.org/10.1016/j.pocean.2014.08.005
4. Iversen, M. H., Nowald, N., Ploug, H., Jackson, G. A., & Fischer, G. (2010). High resolution profiles of vertical particulate organic matter export off Cape Blanc, Mauritania: Degradation processes and ballasting effects. *Deep-Sea Research Part I: Oceanographic Research Papers*, *57*(6), 771–784. https://doi.org/10.1016/j.dsr.2010.03.007
5. Jackson, G. A., & Checkley Jr, D. M. (2011). Deep-Sea Research I Particle size distributions in the upper 100 m water column and their implications for animal feeding in the plankton. *Deep-Sea Research Part I*, *58*(3), 283–297.
6. Krembs, C., Eicken, H., & Deming, J. W. (2011). Exopolymer alteration of physical properties of sea ice and implications for ice habitability and biogeochemistry in a warmer Arctic. *Proceedings of the National Academy of Sciences of the United States of America*, *108*(9), 3653–3658.
7. Horner, R., Ackley, S. F., Dieckmann, G. S., Gulliksen, B., Hoshiai, T., Legendre, L., Melnikov, I. A., Reeburgh, W. S., Spindler M., Sullivan, C. W. (1992). Ecology of sea ice biota - 1. Habitat, terminology, and methodology. *Polar Biology*, *12*(3–4), 417–427. https://doi.org/10.1007/BF00243113
8. Fernández-Méndez, M., Olsen, L. M., Kauko, H. M., Meyer, A., Rösel, A., Merkouriadi, I., Mundy, C. J., Ehn, J. K., Malin Johansson, A., Wagner, P. M., Ervik, Å., Sorrel, B. K., Duarte, P., Wold, A., Hop, H., Assmy, P. (2018). Algal hot spots in a changing Arctic Ocean: Sea-ice ridges and the snow-ice interface. *Frontiers in Marine Science*, *5*(MAR).
9. Perrette, M., Yool, A., Quartly, G. D., & Popova, E. E. (2011). Near-ubiquity of ice-edge blooms in the Arctic. *Biogeosciences*, *8*(2), 515–524. https://doi.org/10.5194/bg-8-515-2011
10. von Appen, W. J., Waite, A. M., Bergmann, M., Bienhold, C., Boebel, O., Bracher, A., Cisewski, B., Hagemann, J., Hoppema, M., Iversen, M. H., Konrad, C., Krumpen, T., Lochthofen, N., Metfies, K., Niehoff, B., Nöthig, E., Purser, A., Salter, I., Schaber, M., Scholz, D., Soltwedel, T., Torres-Valdes, S., Wekerle, C., Wenzhöfer, F., Wietz, M., Boetius, A. (2021). Sea-ice derived meltwater stratification slows the biological carbon pump: results from continuous observations. *Nature Communications*, *12*(1), 1–16. https://doi.org/10.1038/s41467-021-26943-z
11. Ramseier, R. O., Garrity, C., & Martin, T. (2001). An Overview of Sea-Ice Conditions in the Greenland Sea and the Relationship of Oceanic Sedimentation to the Ice Regime. *The Northern North Atlantic*, *2*, 19–38. https://doi.org/10.1007/978-3-642-56876-3_2

12. Lalande, C., Bauerfeind, E., & Nöthig, E. M. (2011). Downward particulate organic carbon export at high temporal resolution in the eastern Fram Strait: Influence of Atlantic Water on flux composition. *Marine Ecology Progress Series*, *440*, 127–136.
13. Le Moigne, F. A. C., Poulton, A. J., Henson, S. A., Daniels, C. J., Fragoso, G. M., Mitchell, E., Richier, S., Russell, B. C., Smith, H. E. K., Tarling, G. A., Young, J. R., Zubkov, M. (2015). Carbon export efficiency and phytoplankton community composition in the Atlantic sector of the Arctic Ocean. *Journal of Geophysical Research: Oceans RESEARCH*, *175*(4449), 238. https://doi.org/10.1038/175238c0
14. Fadeev, E., Rogge, A., Ramondenc, S., Nöthig, E. M., Wekerle, C., Bienhold, C., Salter, I., Waite, A. M., Hehemann, L., Boetius, A., Iversen, M. H. (2021). Sea ice presence is linked to higher carbon export and vertical microbial connectivity in the Eurasian Arctic Ocean. *Communications Biology*, *4*(1), 1–13. https://doi.org/10.1038/s42003-021-02776-w
15. Wekerle, C., Krumpen, T., Dinter, T., von Appen, W. J., Iversen, M. H., & Salter, I. (2018). Properties of sediment trap catchment areas in the Fram strait: Results from Lagrangian modeling and remote sensing. *Frontiers in Marine Science*, *9*(NOV). https://doi.org/10.3389/fmars.2018.00407
16. Iversen, M. H., & Ploug, H. (2010). Ballast minerals and the sinking carbon flux in the ocean: Carbon-specific respiration rates and sinking velocity of marine snow aggregates. *Biogeosciences*, *7*(9), 2613–2624. https://doi.org/10.5194/bg-7-2613-2010
17. Iversen, M. H., & Robert, M. L. (2015). Ballasting effects of smectite on aggregate formation and export from a natural plankton community. *Marine Chemistry*, *175*, 18–27.
18. van der Jagt, H., Iversen, M. H., Friese, C., & Stuut, J. W. (2018). The ballasting effect of Saharan dust deposition on aggregate dynamics and carbon export: Aggregation, settling,. https://doi.org/10.1002/lno.10779
19. Wollenburg, J., Katlein, C., & Nehrke, G. (2018). Ballasting by cryogenic gypsum enhances carbon export in a Phaeocystis under-ice bloom, (May), 0–9. https://doi.org/10.1038/s41598-018-26016-0
20. Geilfus, N., Galley, R. J., Cooper, M., Halden, N., Hare, A., Wang, F., Søgaard, D. H., Rysgaard, S. (2013). Gypsum crystals observed in experimental and natural sea ice, *40*(October), 1–6.
21. Wollenburg, J. E., Iversen, M., Katlein, C., Krumpen, T., Nicolaus, M., Castellani, G., Peeken, I., Flores, H. (2020). New observations of the distribution, morphology and dissolution dynamics of cryogenic gypsum in the Arctic Ocean. *Cryosphere*, *14*(6), 1795–1808. https://doi.org/10.5194/tc-14-1795-2020
22. Nürnberg, D., Wollenburg, I., Dethleff, D., Eicken, H., Kassens, H., Letzig, T., Reimnitz, E., Thiede, J. (1994). Sediments in Arctic sea ice: Implications for entrainment, transport and release. *Marine Geology*, *119*(3–4), 185–214. https://doi.org/10.1016/0025-3227(94)90181-3
23. Darby, D. A., Myers, W. B., Jakobsson, M., & Rigor, I. (2011). Modern dirty sea ice characteristics and sources: The role of anchor ice. *Journal of Geophysical Research: Oceans*, *116*(9). https://doi.org/10.1029/2010JC006675
24. Krumpen, T., Belter, H. J., Boetius, A., Damm, E., Haas, C., Hendricks, S., Nicolaus, M., Nöthig, E., Paul, S., Peeken, I., Ricker, R., Stein, R. (2019). Arctic warming interrupts the Transpolar Drift and affects long-range transport of sea ice and ice-rafted matter. *Scientific Reports*, *9*(1), 1–9. https://doi.org/10.1038/s41598-019-41456-y
25. Krumpen, T., Birrien, F., Kauker, F., Rackow, T., Von Albedyll, L., Angelopoulos, M., Belter, J. H., Bessonov, V., Damm, E., Dethloff, K., Haapala, J., Haas, C., Harris, C., Hendricks, S., Hoelemann, J., Hoppmann, M., Kaleschke, L., Karcher, M., Kolabutin, N., Lei, R., Lenz, J., Morgenstern, A., Nicolaus, M., Nixdorf, U., Petrovsky, T., Rabe, B., Rabenstein, L., Rex, M., Ricker, R., Rohde, J., Shimanchuck, E., Singha, S., Smolyanitsky, V., Sokolov, V., Stanton, T., Timofeeva, A., Tsamados, M., Watkins, D. (2020). The MOSAiC ice floe: Sediment-laden survivor from the Siberian shelf. *Cryosphere*, *14*(7), 2173–2187. https://doi.org/10.5194/tc-14-2173-2020
26. Kempema, E. W., Reimnitz, E., & Barnes, P. W. (1989). Sea ice sediment entrainment and rafting in the Arctic. *Journal of Sedimentary Petrology*, *59*(2), 308–317. https://doi.org/10.1306/212F8F80-2B24-11D7-8648000102C1865D
27. Hebbeln, D. (2000). Flux of ice-rafted detritus from sea ice in the Fram Strait. *Deep-Sea Research Part II: Topical Studies in Oceanography*, *47*(9–11), 1773–1790.
28. Knies, J., & Stein, R. (1998). New aspects of organic carbon deposition and its paleoceanographic implications along the Northern Barents Sea Margin during the last 30,000 years. *Paleoceanography*, *13*(4), 384–394. https://doi.org/10.1029/98PA01501
29. Soltwedel, T., Bauerfeind, E., Bergmann, M., Bracher, A., Budaeva, N., Busch, K., Cherkasheva, A., Fahl, K., Grzelak, K., Hasemann, C., Jacob, M., Kraft, A., Lalande, C., Metfies, K., Nöthig, E., Maeyer, K., Quéric, N., Schewe, I., Wlodarska-Kowalczuk, M., Klages, M. (2016). Natural variability or anthropogenically-induced variation? Insights

from 15 years of multidisciplinary observations at the arctic marine LTER site HAUSGARTEN. *Ecological Indicators*, *65*, 89–102.

30. Arrigo, K. R., & Dijken, G. L. Van. (2015). Progress in Oceanography Continued increases in Arctic Ocean primary production. *Progress in Oceanography*, *136*, 60–70. https://doi.org/10.1016/j.pocean.2015.05.002
31. Wassmann, P. (1994). Significance of sedimentation for the termination of Phaeocystis blooms. *Journal of Marine Systems*, *5*(1), 81–100.
32. Reigstad, M., & Wassmann, Æ. P. (2007). Does Phaeocystis spp . contribute significantly to vertical export of organic carbon?, 217–234.
33. Wolf, C., Iversen, M., Klaas, C., & Metfies, K. (2016). Limited sinking of Phaeocystis during a 12 days sediment trap study. *Molecular Ecology*, *25*(14), 3428–3435. https://doi.org/10.1111/mec.13697
34. Assmy, P., Fernández-Méndez, M., Duarte, P., Meyer, A., Randelhoff, A., Mundy, C. J., ... Granskog, M. A. (2017). Leads in Arctic pack ice enable early phytoplankton blooms below snow-covered sea ice. *Scientific Reports*, (December 2016), in review.
35. Ploug, H., Stolte, W., Epping, E. H. G., & Jørgensen, B. B. (1999). Diffusive boundary layers, photosynthesis, and respiration of the colony-forming plankton algae, Phaeocystis sp., *44*(8), 1949–1958.
36. Skreslet, S. (1988). Buoyancy in Phaeocystis pouchetii (Hariot) Lagerheim. *Journal of Experimental Marine Biology and Ecology*, *119*(2), 157–166. https://doi.org/10.1016/0022-0981(88)90230-4
37. Nöthig, E. M., Bracher, A., Engel, A., Metfies, K., Niehoff, B., Peeken, I., Bauerfeind, E., Cherkasheva, A., Gäbler-Schwarz, S., Hardge, K., Kilias, E., Kraft, A., Kidane, Y. M., Lalande, C., Piontek, J., Thomisch, K., Wurst, M. (2015). Summertime plankton ecology in Fram Strait-a compilation of long-and short-term observations. *Polar Research*, *34*(1).
38. Orkney, A., Platt, T., Narayanaswamy, B. E., Kostakis, I., & Bouman, H. A. (2020). Bio-optical evidence for increasing Phaeocystis dominance in the Barents Sea: Increasing Phaeocystis in Barents Sea. *Philosophical Transactions of the Royal Society A: Mathematical, Physical and Engineering Sciences*, *378*(2181).
39. Boetius, A., Albrecht, S., Bakker, K., Bienhold, C., Felden, J., Fernandez-Mendez, M., Hendricks, S., Katlein, C., Lalande, C., Krumpen, T., Nicolaus, M., Peeken, I., Rabe, B., Rogacheva, E., Somavilla, R., Wenzhöfer, F. (2013). Export of Algal Biomass from the Melting Arctic Sea Ice. *Science*, *339*(6126), 1430–1432.
40. Hoffmann, R., Braeckman, U., Hasemann, C., & Wenzhöfer, F. (2018). Deep-sea benthic communities and oxygen fluxes in the Arctic the Fram Strait controlled by sea-ice cover and water depth. *Biogeosciences*, *15*(16), 4849–4869.
41. Kipp, L. E., Charette, M. A., Moore, W. S., Henderson, P. B., & Rigor, I. G. (2018). Increased fluxes of shelf-derived materials to the central arctic ocean. *Science Advances*, *4*(1), 1–10.
42. Ricker, R., Kauker, F., Schweiger, A., Hendricks, S., Zhang, J., & Paul, S. (2021). Evidence for an increasing role of ocean heat in arctic winter sea ice growth. *Journal of Climate*, *34*(13), 5215–5227. https://doi.org/10.1175/JCLI-D-20-0848.1
43. Tedesco, L., Vichi, M., & Scoccimarro, E. (2019). Sea-ice algal phenology in a warmer Arctic. *Science Advances*, *5*(5). https://doi.org/10.1126/sciadv.aav4830
44. Lannuzel, D., Tedesco, L., van Leeuwe, M., Campbell, K., Flores, H., Delille, B., Miller, L., Stefels, J., Assmy, P., Bowman, J., Brown, K., Castellani, G., Chierici, M., Crabeck, O., Damm, E., Else, B., Fransson, A., Fripiat, F., Geilfus, N., Jacues, C., Jones, E., Kaartokallio, H., Kotovich, M., Meiners, K., Moreau, S., Nomura, D., Peeken, I., Rintala, J., Steiner, N., Tison, J., Vancoppenolle, M., Van der Linden, F., Vichi, M., Wongpan, P. (2020). The future of Arctic sea-ice biogeochemistry and ice-associated ecosystems. *Nature Climate Change*, *10*(11), 983–992. https://doi.org/10.1038/s41558-020-00940-4
45. Kremling, K., Lentz, U., Zeitzschel, B., Schultz-Bull, D. E., and Duinker, J. C. 1996. New type of time-series sediment trap for the reliable collection of inorganic and organic trace chemical substances. *Review of Scientific Instruments 67*, 4360-4363.
46. Zeitzschel, B., Diekmann, P., and Uhlmann, L. 1978. A new multisample sediment trap. *Marine Biology 45*, 285-288.
47. Fahl, K., & Nöthig, E. M. (2007). Lithogenic and biogenic particle fluxes on the Lomonosov Ridge (central Arctic Ocean) and their relevance for sediment accumulation: Vertical vs. lateral transport. *Deep-Sea Research Part I: Oceanographic Research Papers*, *54*(8), 1256–1272.
48. Fernández-Méndez, M., Wenzhöfer, F., Peeken, I., Sørensen, H. L., Glud, R. N., & Boetius, A. (2014). Composition, buoyancy regulation and fate of ice algal aggregates in the Central Arctic Ocean. *PLoS ONE*, *9*(9). https://doi.org/10.1371/journal.pone.0107452

49. Elwood, H. J., Olsen, G. J., & Sogin, M. L. (1985). The small-subunit ribosomal RNA gene sequences from the hypotrichous ciliates Oxytricha nova and Stylonychia pustulata. *Molecular Biology and Evolution*, *2*(5), 399–410. https://doi.org/10.1093/oxfordjournals.molbev.a040362
50. Bolger AM, Lohse M, Usadel B. Trimmomatic: a flexible trimmer for Illumina sequence data. Bioinformatics (Oxford, England) 2014;30(15):2114-2120.
51. Caporaso JG, Kuczynski J, Stombaugh J, Bittinger K, Bushman FD, Costello EK, et al. QIIME allows analysis of high-throughput community sequencing data. *Nature Methods* 2010;7(5):335-336.
52. Bokulich NA, Subramanian S, Faith JJ, Gevers D, Gordon JI, Knight R, et al. Quality-filtering vastly improves diversity estimates from Illumina amplicon sequencing. Nature Methods 2013;10 (1):57-59.
53. Edgar RC, Haas BJ, Clemente JC, Quince C, Knight R. (2011) UCHIME improves sensitivity and speed of chimera detection. Bioinformatics;27(16):2194-2200.
54. Edgar RC. (2010) Search and clustering orders of magnitude faster than BLAST. Bioinformatics;26 (19):2460-2461.
55. Ploug, H., Terbrüggen, A., Kaufmann, A., Wolf-Gladrow, D., & Passow, U. (2010). A novel method to measure particle sinking velocity in vitro, and its comparison to three other in vitro methods. *Limnology and Oceanography: Methods*, *8*(AUG), 386–393.
56. Peeken, I., Primpke, S, Beyer, B., Guetermann, J., Katlein, C., Krumpen, T., Bergmann, M., Hehemann, L., and Gerdts, G.: Arctic sea ice is an important temporal sink and means of transport for microplastic, Nat. Commun., 9, 1509, 2018.
57. Damm, E., Bauch, D., Krumpen, T., Rabe, B., Korhonen, M., Vinogradova, E., and Uhlig, C.: The Transpolar Drift conveys methane from the Siberian Shelf to the central Arctic Ocean, Sci. Rep., 8, 4515, https://doi.org/10.1038/s41598-018-22801-z, 2018.
58. Belter, H. J., Krumpen, T., Von Albedyll, L., Alekseeva, T. A., Birnbaum, G., Frolov, S. V., Hendricks, S., Herber, A., Polyakov, I., Raphael, I., Ricker, R., Serovetnikov, S. S., Webster, M., Haas, C. (2021). Interannual variability in Transpolar Drift summer sea ice thickness and potential impact of Atlantification. *Cryosphere*, *15*(6), 2575–2591. https://doi.org/10.5194/tc-15-2575-2021
59. Girard-Ardhuin, F. and Ezraty, R.: Enhanced arctic sea ice drift estimation merging radiometer and scatterometer data, IEEE T. Geosci. Remote., 50, 2639–2648, 2012.
60. Tschudi, M., Fowler, C., Maslanik, J., and Stewart, J. S.: Polar Pathfinder Daily 25 km EASE-Grid Sea Ice Motion Vectors, Version 3. Technical report, NASA National Snow and Ice Data Center Distributed Active Archive Center, Boulder, Colorado USA, 2016.
61. Krumpen, T., Janout, M., Hodges, K. I., Gerdes, R., Girard-Ardhuin, F., Hölemann, J. A., & Willmes, S. (2013). Variability and trends in Laptev Sea ice outflow between 1992-2011. *Cryosphere*, *7*(1), 349–363. https://doi.org/10.5194/tc-7-349-2013
62. Ezraty, R., Girard-Ardhuin, F., Piolle, J. F., Kaleschke, L., Heygster, G.: Arctic and Antarctic Sea Ice Concentration and Arctic Sea Ice Drift Estimated from Special Sensor Microwave Data, Technical Report, Departement d'Oceanographie Physique et Spatiale, IFREMER, Brest, France, 2007.
63. Kanamitsu, M., Ebisuzaki, W., Woollen, J., Yang, S. K., Hnilo, J. J., Fiorinom M., and Potter, G., H.: NCEP-DOE AMIP-II Reanalysis (R-2), B. Am. Meteorol. Soc., 83, 1631–1643, 2002.
64. Thorndike, A. S.: A toy model linking atmospheric thermal radiation and sea ice growth, J. Geophys. Res.-Oceans, 97, 9401–9410, 1992.
65. Krumpen, T., Von Albedyll, L., Goessling, H. F., Hendricks, S., Juhls, B., Spreen, G., Willmes, S., Belter, H. J., Dethloff, K., Haas, C., Kaleschke, L., Katelin, C., Tian-Kunze, X., Ricker, R., Rostosky, P., Rückert, J., Singha, S., Sokolova, J. (2021). MOSAiC drift expedition from October 2019 to July 2020: Sea ice conditions from space and comparison with previous years. *Cryosphere*, *15*(8), 3897–3920. https://doi.org/10.5194/tc-15-3897-2021

Acknowledgements: We thank captain and crew from *RV Polarstern* and *RV Maria S. Merian* for their support during the research expeditions. We thank Nadine Knüppel, Christiane Lorenzen, and Swantje Rogge for their technical support in the laboratory. We thank Hannah Marchant for commenting on the manuscript. **Funding:** This work was funded by the DFG-

Research Center/Cluster of Excellence "The Ocean in the Earth System": EXC-2077-390741603, the Alfred Wegener Institute Helmholtz Center for Polar Marine Research through the PoF IV program "Changing Earth - Sustaining our Future" Topic 6.1 & 6.3 of the German Helmholtz Association, the German Federal Ministry of Education and Research (project: 03F0629A), the Helmholtz Excellence Network for the project "Polar System and its effects on the Ocean Floor (POSY)", and the framework of the HGF Infrastructure Program FRAM of the Alfred-Wegener-Institute Helmholtz Center for Polar and Marine Research. Additional funding came from the HGF Young Investigator Group SeaPump "Seasonal and regional food web interactions with the biological pump": VH-NG-1000. **Competing Interest:** The authors declare that they have no competing interest. **Data availability Statement:** Data used in this study are made available at PANGEA. 18S sequences of *Phaeocystis* spp. OTUs are published in Genbank and sequence abundances in the samples are published in PANGAEA. Accession numbers will be provided subsequent to acceptance of the manuscript.

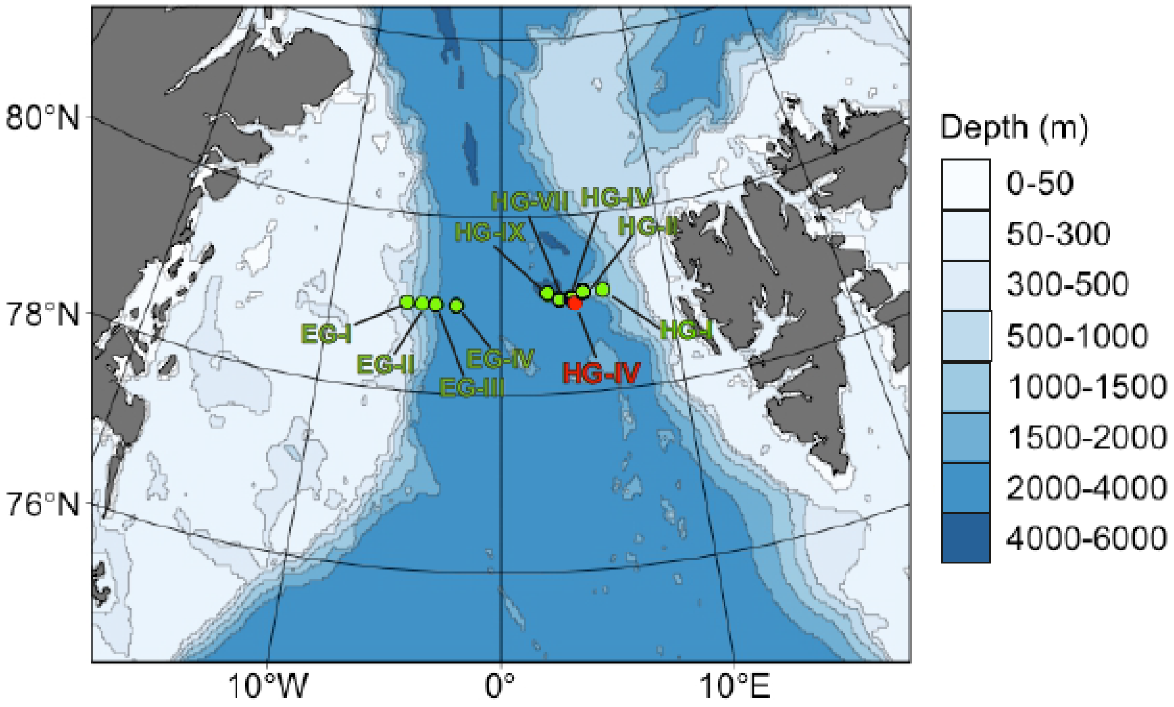

Fig. 1. Overview map of the sampling stations located in the long-term ecological research observatory HAUSGARTEN in the Fram Strait. The red circle indicates station HG-IV where the sediment trap mooring was deployed. Green circles indicate the benthic sediment sample sites.

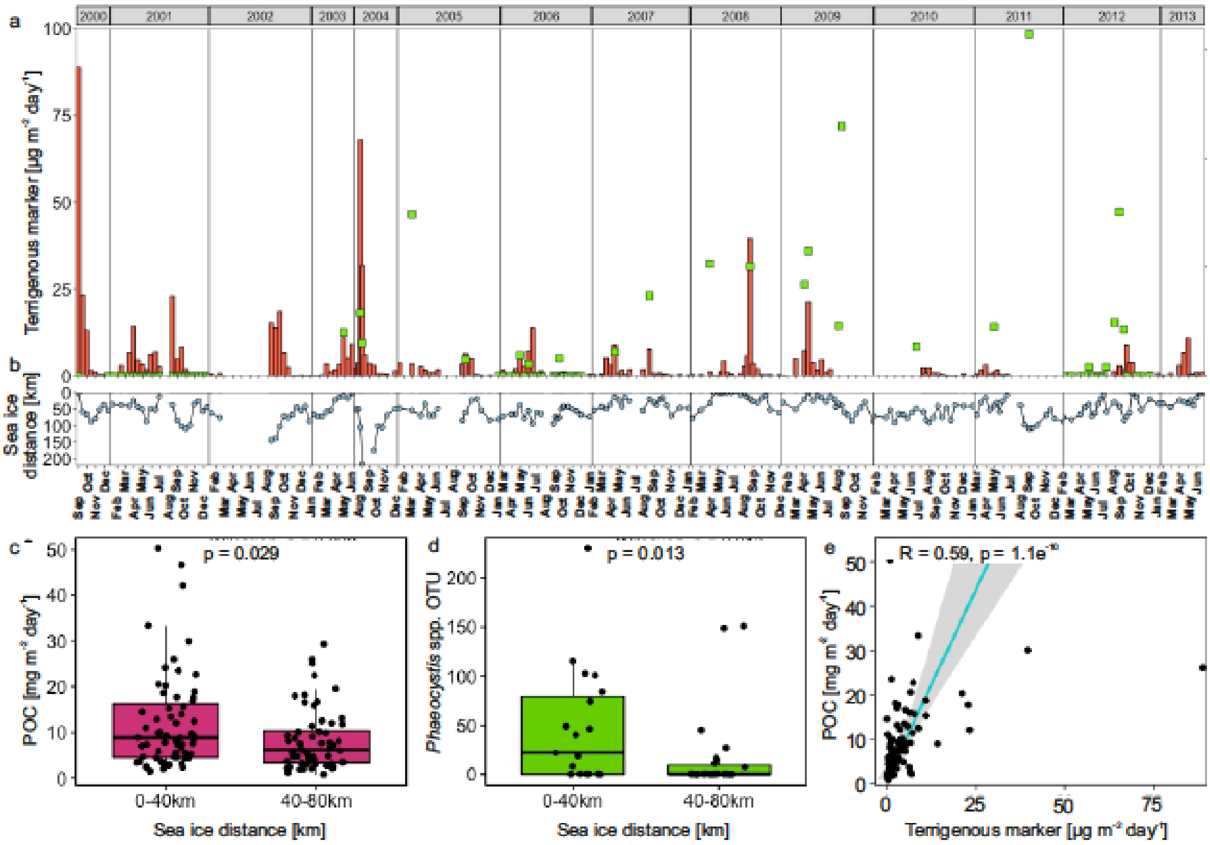

Fig. 2. Sediment trap fluxes and sea-ice dynamics measured at the mooring station HG-IV from 2000 – 2013. Panel a shows sediment trap mooring fluxes of terrigenous marker (orange bars) and *Phaeocystis* OTUs (green squares). Panel b shows the average distance of the sea-ice edge (defined as ≥15% sea-ice cover) to the mooring location. Panel c and d respectively shows POC flux and sequence abundance of *Phaeocystis* OTUs at HG-IV, grouped according to the distance of the sea-ice edge at the time of individual flux measurements. Panel e shows fluxes of POC against terrigenous marker collected at HG-IV (linear regression, grey area shows the 95% confidence interval). No sediment trap was deployed at HG-IV between July 2003 and June 2004 which leads to the missing flux measurements in panel a and b (see table S1 for details). Due to irregular sampling frequency, the sampling months are stated in panel a. For panel c-e only flux values during the productive season from March – September were used.

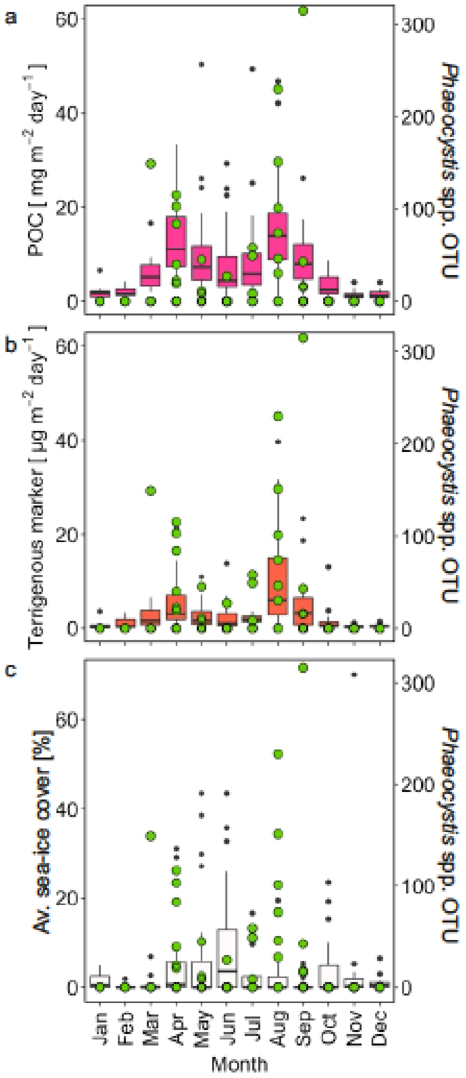

Fig. 3. Monthly sediment trap fluxes and sea-ice cover measured at the mooring station HG-IV from 2000 – 2013. Panels a and b depict the monthly POC and terrigenous marker flux. Panel c shows the monthly average sea-ice cover over the mooring location at HG-IV. Green circles in panel a – c show the sequence abundance of *Phaeocystis* OTUs in the sediment trap samples.

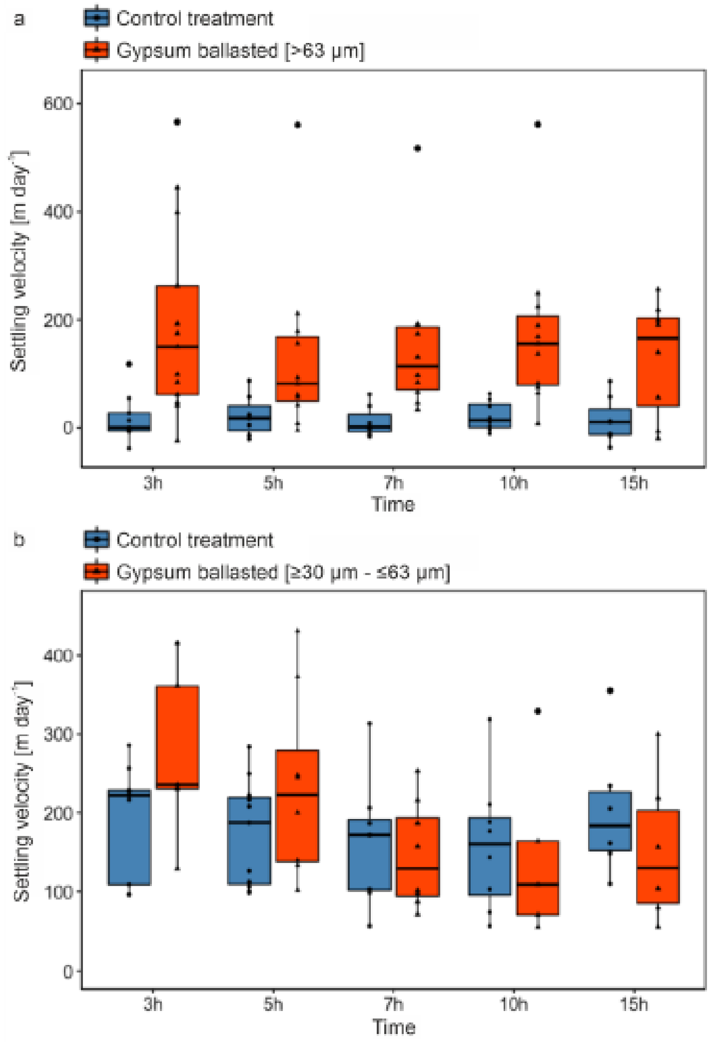

Fig. 4. Measured settling velocities of *in-situ* particles over time from a ballasting experiment with and without added gypsum crystals during research expedition PS121. Gypsum crystals were added at 0h for the ballasting treatments (red) while no gypsum was added in the control treatment (blue). Panel a compares particle settling velocities of a control treatment with particles ballasted with large gypsum crystals (>63 µm). Panel b compares particle settling velocities of a control treatment with particles ballasted with small gypsum crystals (≥30 µm - ≤63 µm). Settling velocities of the large sized ballasting treatment (panel a) were significantly higher as the control treatment (ANOVA, $p = < 0.05$). Settling velocities of the small sized ballasting treatment (panel b) were not elevated enough to show a significant increase over the control treatment (ANOVA, $p = > 0.05$).

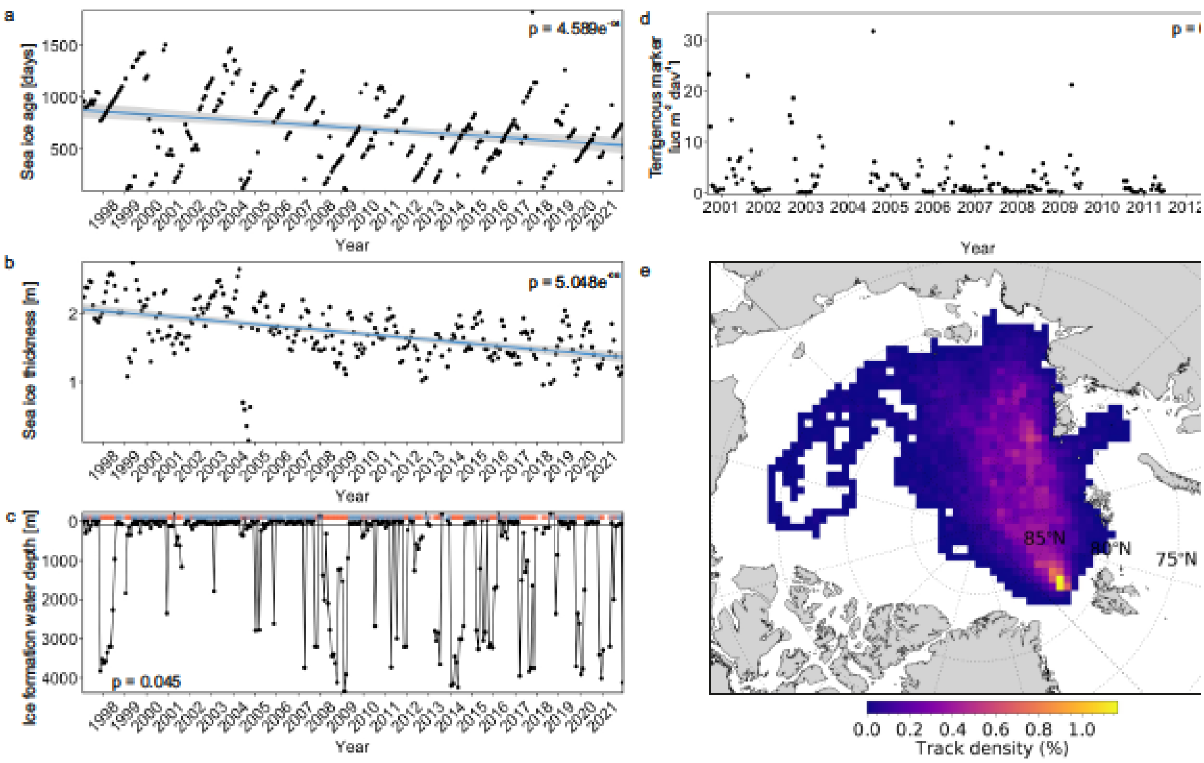

Fig. 5. Characteristics of sea-ice exported through the Fram Strait from 1997 - 2021, derived from a sea-ice backtracking experiment and terrigenous marker fluxes at HG-IV from 2000 – 2013. Panel a shows the average ice age of exported sea-ice. Panel b shows the modelled average sea-ice thickness of exported sea-ice. Panel c shows the water depth at the area where exported sea-ice was formed. Orange bars indicate sea-ice formation in areas with a water depth >100 m, while blue bars indicate a sea-ice formation depth in shallow regions with < 100 m depth. Panel d shows the terrigenous marker flux over the sampled period from 2000 – 2013. Note the change of x-axis values between panel d and a-c. Panel e shows the areal track density of sea-ice that was exported through the Fram Strait from 1997 – 2021. Levels of statistical significance for a reduction over time in panel a - d were tested with a seasonal non-parametric Kendall rank correlation coefficient and are indicated by p-values.

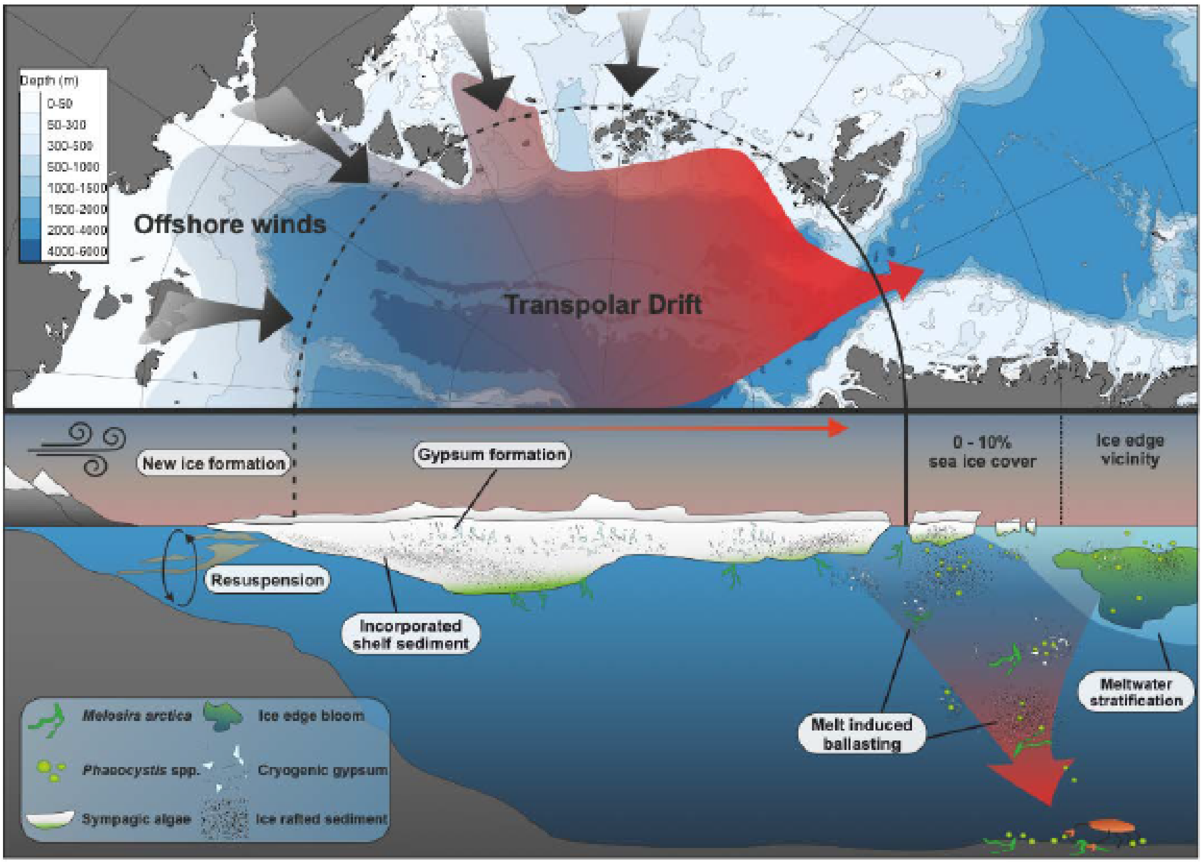

Fig. 6. Overview schematic of the proposed process of sea-ice mediated ballasting. Newly formed sea-ice incorporates resuspended sediments over the shallow Siberian shelf and cryogenic gypsum precipitates within the highly saline brine channels. The sea-ice is transported by the transpolar drift across the Arctic Ocean and is consequentially exported through the Fram Strait where it melts. During melt, incorporated sediments and cryogenic gypsum are released. When encountered with organic matter that forms in, under or in the vicinity of the sea-ice, the released ice rafted material may ballast the organic matter which increases the settling velocity which drives a more efficient drawdown of carbon to the deep ocean and support prevailing communities with food.

Discussion

Particle and aggregate settling velocities are a key aspect for the mode and quantity of carbon export via the biological carbon pump (e.g. Iversen et al. 2010, Iversen and Ploug 2010). In particular, fast particle and aggregate settling velocities through the incorporation of dense components such as ballast minerals, as well as slow-settling or suspended particles with high amounts of low-density polysaccharides (e.g. TEP), mark two extremes for particle and aggregate export. In this dissertation, new insights on the implications of fast- and slow-settling particles and aggregates for the biological pump are presented. In **Manuscript I**, a novel method for the three-dimensional representation of internal and external structures from aggregates is presented, which improves our understanding of small-scale hydrodynamics and their implications for particle aggregation. In **Manuscript II,** we observed the contrasting settling behaviour and export contribution of fast- and slow-settling particles and aggregates from the shallow shelf to the deep ocean in the canary current eastern boundary upwelling system (CC-EBUS) of Cape Blanc. In **Manuscript III**, we identify a new sea-ice mediated ballasting mechanism which enhances carbon export at the sea-ice edge in the arctic.

In the following, potential implications and relevant directions for future research for each of the presented studies are presented separately. Subsequently, I combine the presented findings to give a broader perspective on particle aggregation and ballasting throughout the water column and propose the concept of hydrodynamic dependent aggregation potential as a tool to predict particle encounter probability and thus aggregation in the water column.

Contributions from lateral advection and vertical transport to deep ocean carbon flux

Surface and subsurface sources for marine particles and aggregates

In a dynamic ocean, the settling of aggregates and particles is a three-dimensional process that is dependent on the vertical settling and the horizontal movement of water masses, forming particle trajectories that follow vectors rather than a vertical line (Wekerle et al. 2018, **Manuscript II**). The composition of an aggregate or particle largely determines its settling velocity and is therefore dependent on its source (**Manuscript II**). In the open ocean, aggregate settling velocities are largely determined by the composition of the prevailing phytoplankton community. For instance, aggregates that include the haptophyte *Phaeocystis* spp. tend to have slower settling velocities and are thus more prone to horizontal advection by water currents (**Manuscript I**, **Manuscript II**, Reigstad & Wassmann 2007), while a large proportion of calcifiers e.g. diatoms tend to increase settling velocities (Iversen & Ploug 2010, Ploug et al. 2008). In addition, areas with elevated intrusion of ballasting components such as the release of sea-ice rafted material (**Manuscript III**), aeolian dust deposition or resuspended sediments (**Manuscript II**), tend to form faster settling particles.

A subsurface source to aggregates and particles is the offshore advection of (re)suspended material from shelf margins, which were shown to contribute to deep ocean carbon export throughout the global oceans (Kim et al. 2020, Gardner et al. 2018, Karakas et al. 2006, **Manuscript II**). These particles and aggregates can originate from continental shelves, river- or glacial-discharge (**Manuscript II**, Halbach et al. 2020, Mouyen et al. 2018). These aggregates and particles form large spanning particle clouds (Manuscript II) which separate vertically dependent on their density, forming intermediate particle clouds (IPC) with relatively slow settling velocities and faster settling benthic particle clouds (BPC; Romero et al. 2020, Fischer et al. 2009, **Manuscript II**).

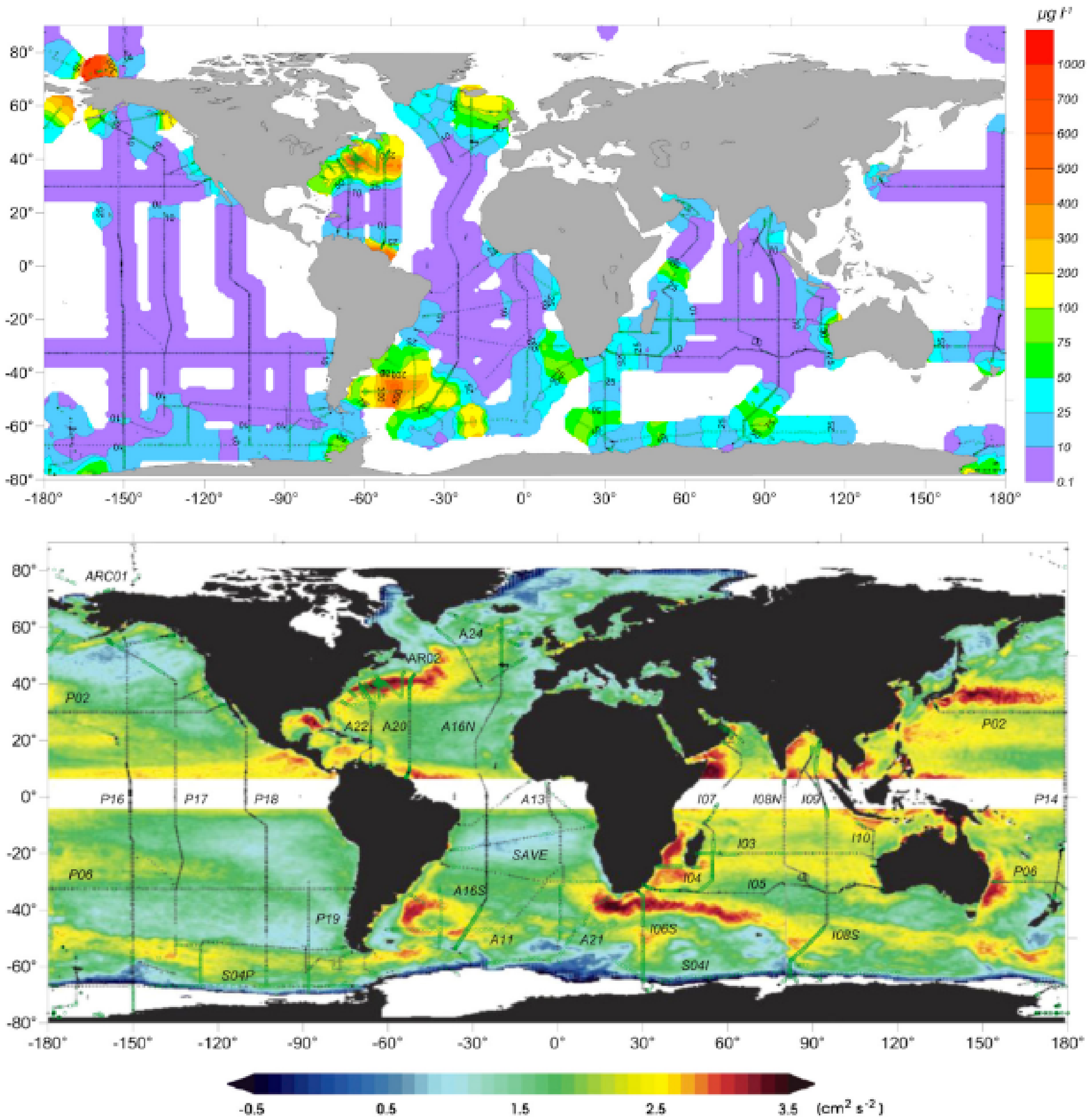

Fig. 1. Distributions of particle clouds in the global oceans. (a) Particulate matter concentration averaged from the bottom 10 m of individual profiles. (b) Map of surface eddie kinetic energy from 2002 – 2006. Figures obtained and modified from Gardner et al. 2018.

Coastal currents may drive the patchy distribution of particle clouds in the water column

In the case of the CC-EBUS off Cape Blanc, offshore advected shelf particles and aggregates contributes approx. 80% of deep ocean carbon export (**Manuscript II**). Considering the remaining three major EBUSs exhibit high rates of primary production (Carr 2001), similar current regimes (Garcia-Reyes et al. 2015, Jacox et al. 2015) and the presence of subsurface particle clouds (Ransom et al. 1998, Fischer et al. 2009, Inthorn et al. 2006, Lam et al. 2018), a substantial contribution of shelf production to deep ocean carbon export can be expected in all EBUSs.

The particle clouds that are typically observed in the region off Cape Blanc were suggested to be sourced from benthic resuspension on the shallow shelf (Karakas et al. 2006, **Manuscript II**). In general, shelf systems have dynamic current regimes which lead to the resuspension of sediments (Kim et al. 2020, Gardner et al. 2018). In the CC-EBUS, offshore directed wind leads to a stable offshore flow in the surface waters, and a subsurface shoreward flow in deeper waters above the shelf sediment (Johnson 1976, Arístegui et al. 2009). However, occasionally the wind direction shifts to a shoreward direction, thus reversing the directions of the current flow (Johnson 1976). As a result, deeper waters on the shallow shelf are "pushed" offshore which may carry organic matter that accumulated on the shelf sediment, past the shelf break. This would lead to occasional pulses of offshore transported organic matter from the shallow shelf, which may explain the patchy occurrence of slow settling particle clouds rather than a constant stream of shelf sourced particles (Nowald et al. 2006).

Internal waves have been suggested to form nepheloid layers at continental slopes and thus are expected to contribute to the formation of lateral advected particle clouds (Puig et al. 2004, Gardner et al. 2018). In the CC-EBUS, internal waves have been observed offshore (Jackson 2007) and sediment waves on the continental slope off Cape Blanc suggests that internal waves may from the sediment topography in the region (Sanz et al. 2017). However, carbon to nitrogen ratios of export fluxes in the deep ocean traps where relatively low, suggesting the presence of largely undegraded material (**Manuscript II**). While this does not rule out a potential contribution of internal waves to the formation of the intermediate and benthic particle clouds of Cape Blanc, it indicates that internal waves are likely not the dominant mechanism driving lateral export of Cape Blanc.

Potential bias of flux measurements by slow sinking and suspended particles

A fundamental issue when measuring carbon fluxes via the biological pump, is that commonly applied methodologies do not allow for the differentiation between fast settling and slow settling or suspended particles (Giering et al. 2020). As a result, the amount and therefore relative importance of slow settling and lateral advected particles cannot be differentiated from fast vertical settling particles in flux measurements, making it difficult to interpret flux characteristics such as origin, composition or age. For instance, the mooring location at station HG-IV in Fram strait which was used to identify sea-ice ballasting in the vicinity of the ice edge in **Manuscript III**, has a sediment trap mounted at 1250 & 2600 m. However, strong lateral advection of shelf material leads to high input of lateral advected material (Lalande et al. 2016). As a result, the measured fluxes from the deep ocean traps could not be implemented in **Manuscript III**, since the contribution and characteristics from vertical settling particles from the surface ocean could not be differentiated from laterally sourced particles originating from the shelf.

Recent advances in the detection and classification of particles and their fluxes are more and more reliant on image-based detection systems which capture vertical particle distribution profiles, including ship- or glider- based particle camera systems, or moored winch systems (Trudnowska et al. 2021, Giering et al. 2020). However, particle settling velocities cannot be obtained from camera images. Therefore, settling velocities are estimated by deriving the equivalent spherical diameter from the particle area in the image, and calculating the theoretical settling velocity for a similar sized sphere according to stokes law (e.g. Guidi et al. 2008, McDonnell & Buesseller 2012). Using this approach is problematic for a few reasons: (I) As outlined in **Manuscript I**, the use of geometric shapes to derive particle size estimates is likely biased and may underestimate true particle sizes; (II) the drag force generated on particles with heterogenous surface structures is considerably higher as for a model sphere, resulting in an overestimation when deriving settling velocities with stokes law (**Manuscript I**); (III) by applying stokes law, particle settling velocities are dependent on their size and larger sized particles will settle faster than smaller particles. However, in-situ particles do not show a relationship between their size and settling velocity when particle shapes are derived from geometric volume estimates (**Manuscript I**, **Manuscript II**, Iversen & Lampitt 2020); (IV) as it is not possible to differentiate between suspended and sinking particles from camera images, suspended particles are included into vertical flux estimates. Therefore, the use of camera images for the estimation particle settling and thus export fluxes bear large uncertainties.

New tools are needed for the determination of settling velocities and lateral particle flux

A newly developed approach by Moradi et al. (in prep.) uses particle size-distributions from flux measurements (sediment gel-traps) in combination with particle size-distributions from particle camera deployments to distinguish between settling and suspended particles in the water column. Applying this method to the area around the Cap-Verde islands off the coast of Mauritania, revealed, that the concentration of suspended particles in size classes below <100 µm is ~10-fold higher as for similar sized sinking particles. An advantage of this method is, that particle camera systems such as the underwater vision profiler (UVP) and particle size-distributions from sediment traps equipped with gel-traps are commonly assessed parameters and already have a relatively large data base of recorded particle size-spectra. Therefore, areas with long lasting datasets such as the Fram Strait (**Manuscript III**) and the CC-EBUS off the coast of Cape Blanc (**Manuscript II**) can be revisited and the contribution of suspended vs. settling particles assessed.

Algorithms for POC flux estimations are commonly based on the interpolation of sediment trap fluxes, combined with an estimation for particle and aggregate settling velocities and their rate of degradation (Lutz et al. 2002). However, as outlined in the previous paragraph, a common issue with sediment traps is that vertical and lateral sourced flux of aggregates and particles cannot be differentiated. Therefore, when lateral sourced particles and aggregates contribute to the flux, the parameterization of the interpolation may overestimate the amount of vertical flux. In our study (**Manuscript II**), we accounted for this methodological issue by using multiple trap measurements from different depths to verify interpolated fluxes and quantify the amount of lateral input. As verification for the contribution of lateral flux input, we used particle camera deployments, satellite chlorophyll estimates and satellite measurements of aerosol optical depth. In addition, we made a full carbon budget from the shallow shelf to the open ocean in order to quantify the potential amount of lateral advected carbon from our direct measurements. Using over two decades of sediment trap fluxes, we estimated the potential long-term impact from laterally advected particles and aggregates to the deep ocean carbon flux off Cape Blanc. As a result, we were able to show that lateral sourced particles and aggregates contributed 80% of deep ocean export off Cape Blanc and that shallow shelf production directly links to deep ocean carbon export in the region **(Manuscript II)**

New approaches like these are crucial for the accurate determination of POC export in the ocean and offer valuable information on particle characteristics e.g., fast vs. slow settling velocities, composition, origin etc.. Lateral particle fluxes are a persistent and wide spread feature in the global oceans (**Manuscript II**, fig. 1), yet their importance in the marine carbon cycle is not known and rarely recognized since we lack the tools to assess them. In addition, suspended particles and aggregates need to be excluded in vertical flux estimates which are based on gravitational settling, while new approaches for the determination of particle shapes and composition may improve our capability to parameterize settling velocities (**Manuscript I**). The wide-spread implementation of the presented approaches (**Manuscript II**, Moradi in prep.) will therefore help to better understand particle fluxes and enable us to understand the marine carbon cycle as a three dimensional rather than a strictly vertical system.

Mineral ballasting of settling aggregates

Aeolian dust deposition as a ballasting source in upwelling regimes

In the CC-EBUS, aeolian deposition of Sahara dust was suggested to incorporate into marine particles which promotes aggregation and enhances carbon export by particle ballasting (Nowald et al. 2015, van der Jagt et al. 2018). Overall, aeolian dust deposition is a common feature in all of the major EBUS (Dansie et al. 2017, Jardine et al. 2021, van der Does et al. 2020). While a direct link between events of dust deposition and deep ocean export fluxes has not been observed in the CC-EBUS, it was suggested that dust deposits accumulate in the surface ocean and when encountering with organic matter, form fast-settling aggregates (Fischer et al. 2009, Fischer et al. 2016). This is supported by measured sediment trap fluxes from the California EBUS which showed a strong correlation between lithogenic sediments and POC flux (Thunell et al. 2007). However, this may also suggest that aeolian dust deposition may contribute to sediment incorporation of marine particles on the shallow shelf in EBUS, and thus contribute to the formation of BPCs (**Manuscript II**). As a result, dust deposition may lead to an enhanced carbon flux as suggested from trap records (Thunell et al. 2007), but is temporarily decoupled between deposition events and POC flux measurements (Fischer et al. 2009, Fischer et al. 2016).

Sea-ice mediated ballasting can be expected in Antarctica

Gypsum crystals with sulphur isotope ratios similar to sea-water sourced sulphate, have been observed in Antarctic sea-ice (Wellman & Willson 1963), and coastal aerosol samples (Hara et al. 2012), thus indicating the seasonal formation of cryogenically formed gypsum in sea-ice brine in the Antarctic. In addition, the majority of seasonally formed Antarctic sea-ice melts during summer (Eayrs et al. 2019), thus suggesting a more pronounced first-year ice formation and thus gypsum formation, as in the Arctic (Wollenburg et al. 2020). Therefore, a seasonal formation and release of cryogenic gypsum into the water column with a ballasting effect can be expected (**Manuscript III**).

Apart from indications for gypsum formation, the considerable deposition of up to 24,000 kg aeolian sediment per km^2 on the Antarctic sea-ice surface has been reported (Atkins & Dunbar 2009). Further, sea floor sediment showed great similarities with aeolian sediments, indicating that the deposited sediments on the sea-ice were released during ice melt and settled through the water column (Atkins & Dunbar 2009). It can therefore be expected that similar to the CC-EBUS off Cape Blanc (**Manuscript II**, van der Does et al. 2020) annual aeolian sediments that accumulated on the sea ice cover are released during sea-ice melt and ballast organic matter in the water column, thus enhancing particle settling velocities and carbon export.

Release of calcium ions may enhance the aggregation potential of cryogenic gypsum

As outlined in the introduction, factors for the potential of aggregation according to coagulation theory are the particle size, concentration, adhesion force i.e. stickiness and encounter rate (Burd & Jackson 2009). While stickiness is in general empirically provided with a number from 0-1 (Kiørboe et al. 1994), no clear mechanism for the actual adhesion of a particle to another is measured and parameterized. Here, concepts of polymer gel theory may be useful for the parameterization of the term stickiness, since the connection between two particles is defined by chemical or physical bonds such as covalent bonds, hydrogen bonding etc. (Verdugo et al. 2004). Under this consideration, the dissolution of cryogenic gypsum may enhance the adhesion force of TEP and thus its potential for aggregation. Gypsum is a mineral with the chemical formula $CaSO_4 \bullet H_2O$, thus releasing calcium ions under dissolution in water (Wollenburg et al. 2020). Calcium ions have been identified as a crucial element for the formation of polymer gels by creating Ca-Bonds which stabilize gel networks and increase the adhesion force of TEP (Verdugo 2012, Meng & Liu 2016). Therefore, the increased adhesion force i.e., stickiness, by the dissolution of gypsum in the water column may enhance the probability for gypsum crystals to aggregate with an encountered marine particle. Further, the release of free calcium ions from gypsum dissolution may indirectly increase the stickiness of marine aggregates and thus the formation of larger gel networks such as TEP filaments, or the aggregation potential with potentially inert particles in the water column such as quartz i.e., sand grains. Therefore, the release and dissolution of cryogenic gypsum may have two opposing effects: (I) increased stickiness due to the dissolution of cryogenic gypsum increases the probability for gypsum to attach to aggregates and therefore enhance their settling velocity (**Manuscript III**); (II); the increased formation of TEP filaments enhances particle buoyancy (Azetzu-Scott & Passow 2004) and drag (**Manuscript I**), which may reduce settling velocities. As a result, chemical composition and reaction potential of particles and the surrounding water column are an important factor that needs further consideration for the understanding of particle aggregation and polymer gel or TEP properties (Verdugo 2012).

The formation of cryogenic minerals other than gypsum may enhance particle ballasting in the upper water column

During the formation of sea ice, excess ions are secreted as a salty brine, forming pores and brine channels within the newly formed ice (Underwood et al. 2010). Cryogenic mineral formation in sea-ice occurs from ion precipitation when the salinity of the brine exceeds its saturation state (Geilfus et al. 2013). The minerals that consequentially precipitate are determined by the ambient temperature (Wollenburg et al. 2018). These minerals include gypsum, ikaite, mirabilite, hydrohalite, sylvite, $MgCl_2$ and Antarcticite (Wollenburg et al. 2020). Cryogenic gypsum is considered the most stable among these minerals and once precipitated from sea-ice brine, it may be released from the sea-ice during melting and can ballast organic aggregates if it encounters and incorporates into them as it sinks through the water column (Wollenburg et al. 2018, **Manuscript III**).

Brine channels in sea-ice inhabit a wide variety of biota which fill brine channels with extracellular polymeric substance (EPS, Underwood et al. 2010, Juhl et al. 2011). The presence of EPS has been shown to affect sea-ice brine morphology and increased bulk salinity by 11-59%. Therefore, prevailing biota might enhance the potential for cryogenic mineral precipitation. Further, it has been suggested that EPS may cover cryogenic minerals and thus limit their dissolution when released into the water column (Wollenburg, personal correspondence). Therefore, despite that cryogenic minerals other than gypsum may be less stable once released in the water column, a “shielding effect” of EPS may delay their dissolution and make an incorporation into marine aggregates possible. Considering that flux attenuation is strongest in the upper 100 m of the water column (Jackson & Checkley 2012), even a short-term ballasting effect of more instable cryogenic minerals within this depth range may have a notable impact on carbon export.

Implications from aggregate structure on microbial degradation and aggregation potential

Internal diffusion of aggregates measured by nuclear magnetic resonance

The establishment of NMR spectroscopy for the three-dimensional visualisation of marine snow aggregates offers a step forward towards understanding sub-aggregate scale processes. In **Manuscript I**, the three-dimensional structure of a marine snow aggregate was visualized, which allowed for detailed analysis of the internal structure, area, volume and hydrodynamic properties of aggregates when settling through the water column.

While **Manuscript I** focused on the NMR derived structural representation of marine snow aggregates, preliminary data collected from NMR measurements show a three-dimensional representation of the diffusion-coefficients of water within the Aggregate (Fig. 2). These observations suggest that most of the aggregate structure is not considerably limited in its diffusion of water and solutes. This is in line with previous studies which showed that apparent diffusivity within marine snow is nearly similar to the free diffusion coefficients in seawater (Ploug & Passow 2007). Further, it has been shown that the majority of aggregate structures are composed of TEP which are suggested to not limit diffusion within aggregates (Zetsche et al. 2020).

In addition, the three-dimensional visualisation of diffusion coefficients may give indications to the formation of anoxic micro niches where diffusion is limited and microbial activity may transition towards anaerobic metabolism (Klawonn et al. 2015). Further, in combination with the modelled hydrodynamic properties around the aggregate (**Manuscript I**), the influence of flow and resulting over- and under-pressure above and below a settling aggregate may give valuable insights on the distribution of solutes e.g. oxygen or respiratory products into and out of the aggregate.

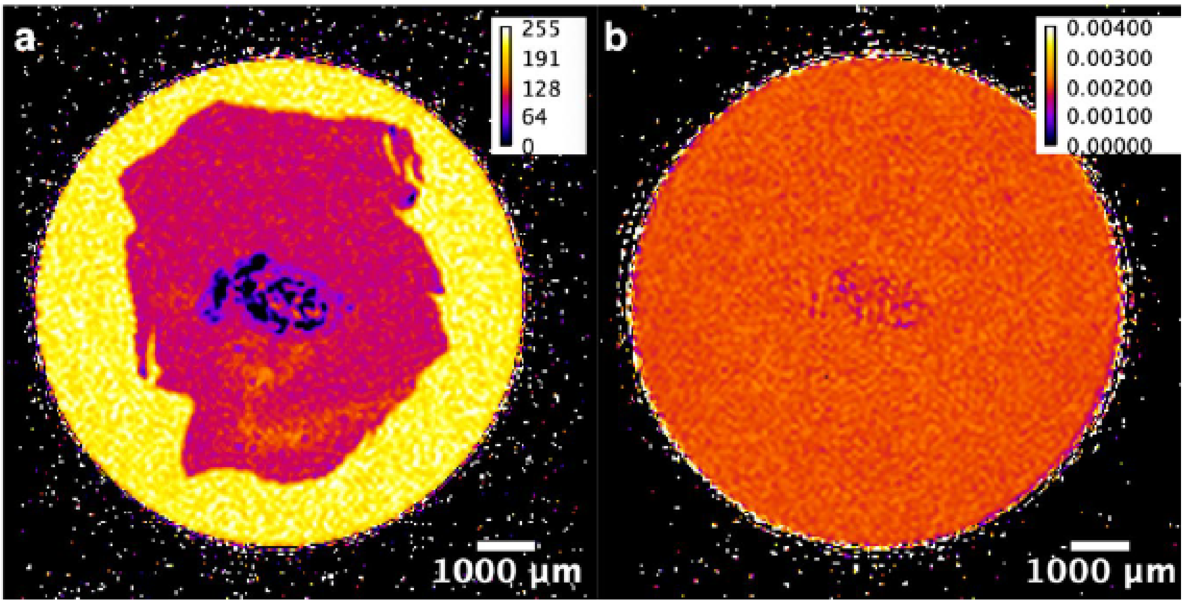

Fig. 2. Preliminary NMR measurements of aggregate structure and free diffusion of water across a z-plane within an embedded aggregate. Panel a shows the structural measurement of the embedded aggregate. The signal intensity is derived from greyscale values. Panel b shows the free diffusion coefficients of water (mm² s⁻¹). The aggregate was embedded in agar and subsequently placed in a reaction tube, filled with water and contrast agent (**Manuscript I**). The black surrounding area is air around the reaction tube. In panel a, yellow areas show surrounding water, pink areas depict the agar and dark purple/black areas show the structure of the embedded aggregate.

Impact of hydrodynamics for aggregation – a concept for selective aggregation throughout the water column

The hydrodynamic environment around a settling aggregate may act as a shielding layer which deflects approaching particles and thus limits the potential for aggregation (Kiørboe et al. 2002, Secchi et al. 2020). When an aggregate sinks, the water velocity of the surrounding boundary layer is close or equal to the terminal settling velocity of the aggregate. Therefore, if the settling aggregate encounters a particle or another aggregate, the surrounding water may act as a barrier by "pushing away" the approached particle or aggregate and thus decelerate the collision speed. Thereby, the encountering particles or aggregates' trajectories may be redirected by the shear between the boundary layer and the water flow surrounding the aggregate. As a result, the encountering particle or aggregate is deflected and therefore prevented from collision and thus aggregation. This implies that the hydrodynamic environment around a settling aggregate must be overcome in order for colliding particles and aggregates to successfully encounter and potentially aggregate. Further, it has been shown that the attachment efficiency of bacteria onto a pillar in laminar flow conditions decreased with increasing flow velocity and increasing diameter of the pillar (Secchi et al. 2020). This outlined limitation in aggregation implies two things: (1) the potential for a particle to overcome the hydrodynamic environment around an aggregate and collide, is dependent on the relative size difference between the encountering particle and the aggregate and the settling velocity, i.e. a large and fast-settling aggregate forms a stronger "hydrodynamic shield" than a small and slow-settling particle. (2) In a setting where the terminal settling velocity of an aggregate is not reached, this "hydrodynamic shield" is not or only partly established, thus increasing the potential for aggregation with other particles and aggregates.

As a consequence, this aggregation behaviour of small sized particles may have a substantial impact on the way aggregate ballasting occurs in the water column. Considering that a limitation in the attachment of a non-motile mutant of the bacterium *Pseudomonas aeruginosa* (up to 5 µm in length; Diggle & Whitelay 2020) has been shown at a flow speed of 12.5 m day^{-1} (Secchi et al. 2020), it may be suggested that fine grained minerals in the silt (50 – 2 µm sized) or clay (< 2 µm) size fraction are limited in their probability to attach to a settling aggregate.

A potentially relevant observation for the ballasting behaviour of fine-grained minerals has been made by van der Jagt et al. (2018). In their study, they conducted experiments to investigate the ballasting impact of wind collected Saharan dust on the settling velocity of marine aggregates. Their study showed that if particles are formed in sea water with added Saharan dust, the average settling velocities of the formed aggregates where significantly higher (430 ± 280 m day^{-1}) than for similar non-ballasted aggregates (133 ± 108 m day^{-1}). However, if in situ collected aggregates were incubated with Saharan dust, there were no significant differences in size-specific settling velocities between ballasted and non-ballasted aggregates (non-ballasted aggregates = 319 ± 210 m day^{-1}; Saharan dust ballasted aggregates = 402 ± 280 m day^{-1}), thus implying that only little to none of the suspended dust attached to the already formed aggregates. In the study, the authors argued that the carrying capacity of the preformed aggregates was already exploited, which prevented the dust to attach. However, given that the peak diameter of the dust size distribution was 30 µm (given in volume %), an alternative explanation may be that the high settling velocities of the marine aggregates formed a hydrodynamic environment that deflected the dust particles and therefore prevented them from encountering and, thus, ballasting the aggregates. On the other hand, if aggregates were formed within the dust suspension the size and settling velocity of the organic matter was small and low, thus enabling the encounter with the dust particles with a consequential ballasting effect on the aggregates that were formed. A conceptual overview of potential mechanisms for aggregation of small sized particles on aggregates is shown in fig. 3.

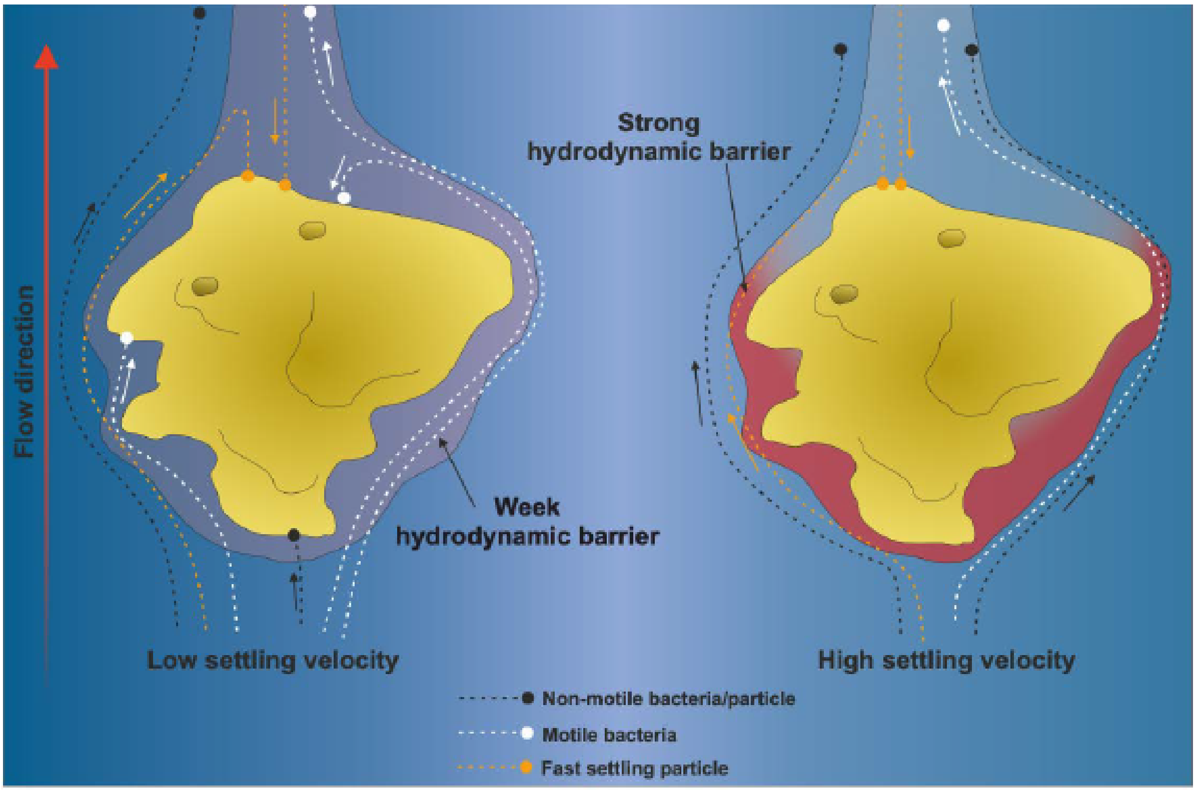

Fig. 3. Conceptual overview of aggregation mechanisms which may allow small sized particles and bacteria to attach on a settling aggregate at low and high settling velocities. At low settling velocities, non-motile bacteria/ particles may attach in the front of a settling aggregate. Motile bacteria may attach from behind if their motility velocity exceeds the speed of the wake flow behind the aggregate. Fast settling particles with near terminal of faster settling velocities may either attach from behind if their motility velocity exceeds the speed of the wake flow behind the aggregate, or vertically settle on the aggregate from behind. At high aggregate settling velocities, the only expected mechanism for particle attachment is that for fast settling particles.

If we consider a size limitation for aggregation by the hydrodynamic environment, this would imply that particle aggregation and thus ballasting is selective throughout the water column. In particular water layers with non-laminar fluid conditions such as turbulence that impact the formation of the boundary layer (Bergkvist et al. 2018), and areas where particle and/or aggregate settling is decelerated, may be potential "hotspots" for aggregation. This may encompass the turbulent ocean surface that is exposed to atmospheric forcing (Richman et al. 1987), density layers such as haloclines that temporarily slow down settling velocities (Kindler et al. 2010, MacIntyre et al. 1995), margins of counter current flow such as poleward undercurrents (Fischer et al. 2020, Kämpf et al. 2016) and benthic boundary layers that form above the sea floor (Thomsen & McCave 2000). An example would be the aeolian deposition of dust off north-west coast of Africa (van der Does et al. 2020), which would enter the upper mixed layers with high phytoplankton abundances and thus form ballasted aggregates in the upper water column (van der Jagt et al. 2018).

On the other hand, in areas with limited water movement and a uniform water column composition, particles and aggregates would reach their terminal settling velocity. Therefore, hydrodynamic environment would be expected to fully develop in these areas, thus reducing the potential for aggregation. This may explain why settling particles have limited or no impact on the distribution of particle clouds (Iversen et al. 2010, van der Jagt et al. 2020). While particle clouds do have a broad particle size-distribution with up to millimetre sized aggregates (Ransom et al. 1998, Santschi et al. 1998, Puig et al. 2013, **Manuscript II**), the majority of particles are ≤ 30 µm in diameter, thus limiting a potential encounter with vertical settling aggregates (McCave 1983, Puig et al. 2013, **Manuscript II**). Therefore, vertical settling particles and aggregates may interact with the large size fraction of particles from particle clouds, however, they are unlikely to collide with small sized particles.

From the suggested impact of the hydrodynamic environment and in particular the boundary layer on particle encounter probability and thus aggregation, a conceptual overview is given in fig. 4 to depict the potential role of the hydrodynamic dependent aggregation potential throughout the water column.

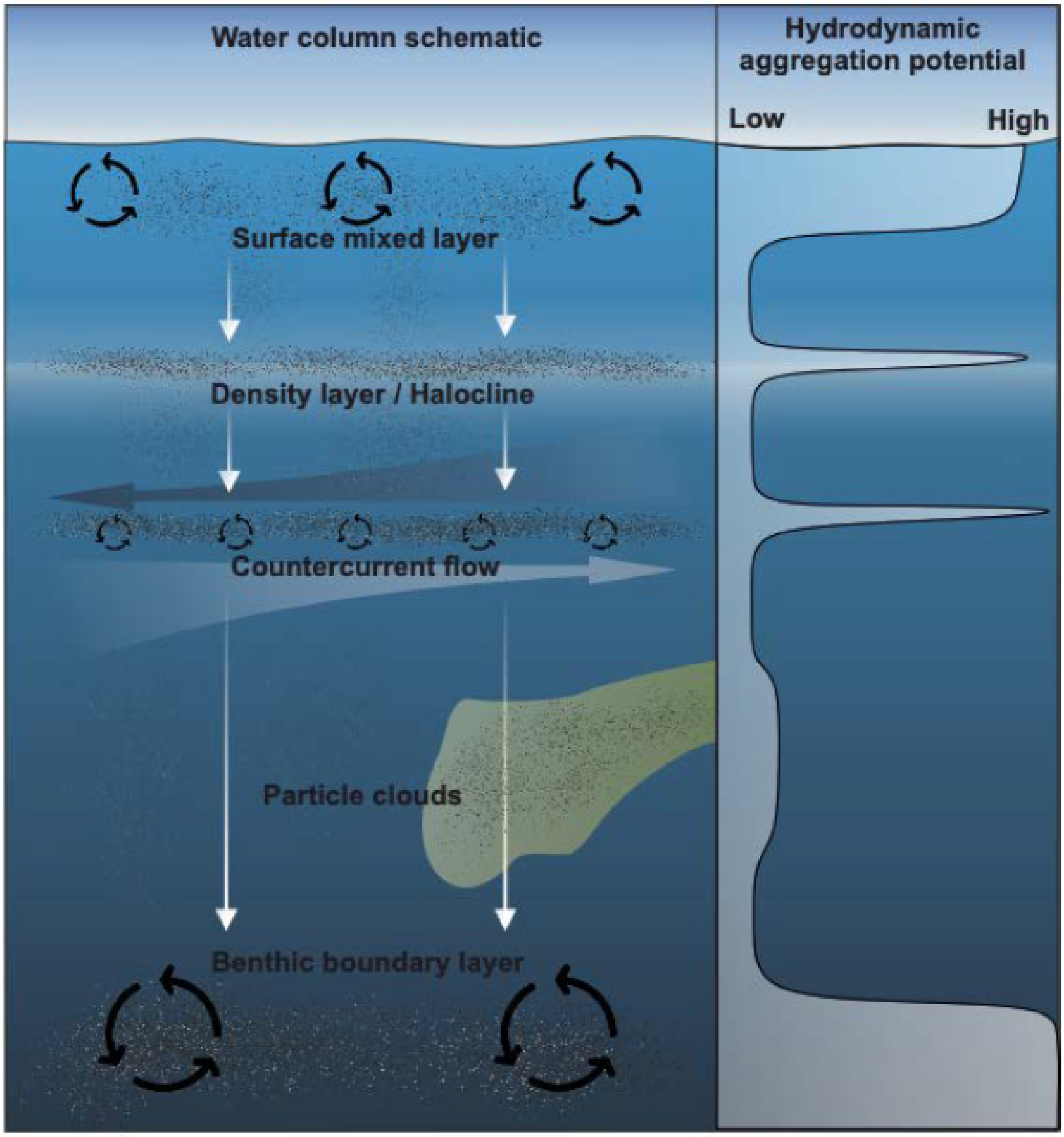

Fig. 4. Conceptual overview how the hydrodynamic dependent aggregation potential may affect particle aggregation within the water column. Proposed key areas of potentially higher hydrodynamic aggregation potential areas with increased turbulence, including the surface mixed layer, counter current flows and the benthic boundary layer above the seafloor. High particle and aggregate concentrations in particle clouds may enhance aggregation potential with larger sized particles and aggregates.

A potential case of aggregation despite high settling velocities may occur when the approached particle has a settling velocity close to the terminal settling velocity of the aggregate. As previously described, motile-bacteria may attach in the leeward side of an aggregate if their motility velocity exceeds the wake flow behind the aggregate (Secchi et al. 2020). Similarly, a settling particle with near terminal settling velocity of the aggregate may be redirected to the leeward side and accelerated by the reduced drag of the wake flow, thus allowing to attach from behind (Fig. 3).

A general assumption that has been made in the previous discussion on particle aggregation is, that larger sized aggregates have a higher settling velocity than small-sized aggregates. Therefore, large sized aggregates approach the small sized particle via differential settling which will cause an encounter with the potential for them to stick together and aggregate. However, recent studies have shown that in-situ marine aggregates do not show a size-to-settling relationship (**Manuscript II**, Iversen & Lampitt 2020) and that settling velocities of ballasting minerals such as cryogenic gypsum or sand grains exceed that of marine particles when similarly, or even smaller sizes (Wollenburg et al. 2020, Komar 1978). Therefore, situations where a small sized fast settling particle or aggregate approaches a large sized slow settling aggregate are likely to occur in situ. Potential examples would be the release of cryogenic gypsum from sea-ice with common sizes around 1 mm or the aeolian deposition of large sized sediment grains (Wollenburg et al. 2020, Atkins & Dunbar 2009). As a result, the hydrodynamic effect of the boundary layer would be much less pronounced since the larger area and thus friction of the large aggregate would result in a higher inertia, which would prevent it from being deflected by the fast settling but small particle. In the case of sea-ice mediated ballasting, including terrigenous material and cryogenic gypsum, we expect this to be likely the most common mechanism of aggregate ballasting (**Manuscript III**). This was indicated by the deposition of relatively large sized *Phaeocystis* spp. colonies at the sea-floor with incorporated cryogenic gypsum minerals (Wollenburg et al. 2018).

Conclusion

Estimations on the carbon export via the biological pump commonly only consider the surface ocean as a source for particles and aggregates (e.g. Henson et al. 2012, Boyd et al. 2019, Buesseler et al. 2020, Maerz et al. 2020) and recent estimates for annual carbon export range between 5 -17 GT C, implying a large uncertainty in our ability to detect and quantify carbon export via the biological pump (Boyd et al 2019). As outlined in this thesis, subsurface sourced aggregates and particles from the continental shelves are an additional source which contributes to global carbon fluxes. Studies that attempted to differentiate between surface and lateral sourced export in deep ocean traps suggest lateral sourced export contributes between 20-80% of collected carbon export (Hwang et al. 2015, Lalande et al. 2016, Fahl & Nöthig 2007, Schulz et al. 2021, Hwang et al. 2017, Conte et al. 2019, Blattmann et al. 2018, **Manuscript** II) and global observations show the consistent presence of coastal formed particle clouds which expand throughout the global oceans (Gardner et al. 2018). Further, material exported from the euphotic zone to the shallow sea-floor is incorporated into these lateral expanding particle clouds, giving already sedimented organic matter a "second chance" to export at deeper depths and sequester carbon for longer timescales (Boyd et al. 2019, **Manuscript** II). Therefore, as long as carbon flux estimates are considered to form exclusively in the surface ocean and export vertically, we are only considering a "part of the picture" and thus will not be able to understand the functioning, nor accurately predict the total amount of carbon export by the biological pump.

In addition, the parameterization of particles and aggregates in currently established methodologies introduces considerable uncertainties, from the study of small scale sub-aggregate processes to estimates of carbon fluxes throughout the water column. In particular, the accurate determination of the internal and external aggregate morphology is a crucial advancement that has implications for observations on microbial respiration, microbial colonization, aggregation and ballasting, and estimations of settling velocities and carbon content (**Manuscript I, Manuscript II, Manuscript** III). Further, new approaches for the separation between settling and non- settling particles will improve our capability to accurately determine export fluxes and thus our understanding of the biological pump (Moradi et al. in press). However, these observations also reveal that as long as we have not revised the parameterization of marine particles and aggregates, direct measurements of carbon export i.e. with sediment traps are crucial as a reference for flux estimations.

Only if we manage to close the gap of current uncertainties on oceanic carbon export, we will be able to project the response of earth's climate on increasing atmospheric CO_2 concentrations. The new observations outlined in this work provides new insights and may act as a guideline for relevant directions of future research to improve our attempts to understand carbon export by the biological pump.

References

Arístegui, J., Barton, E. D., Álvarez-Salgado, X. A., Santos, A. M. P., Figueiras, F. G., Kifani, S., Hernández-León, S., Mason, E., Machú, E., & Demarcq, H. (2009). Sub-regional ecosystem variability in the Canary Current upwelling. *Progress in Oceanography*, *83*(1–4), 33–48. https://doi.org/10.1016/j.pocean.2009.07.031

Atkins, C. B., & Dunbar, G. B. (2009). Aeolian sediment flux from sea ice into Southern McMurdo Sound, Antarctica. *Global and Planetary Change*, *69*(3), 133–141.

Azetsu-Scott, K., & Passow, U. (2004). Ascending marine particles: Significance of transparent exopolymer particles (TEP) in the upper ocean. *Limnology and Oceanography*, *49*(3), 741–748. https://doi.org/10.4319/lo.2004.49.3.0741

Bergkvist, J., Klawonn, I., Whitehouse, M. J., Brüchert, V., & Ploug, H. (2018). *Turbulence simultaneously stimulates small- and large-scale CO2 sequestration by chain-forming diatoms in the sea*. 1–10.

Blattmann, T. M., Zhang, Y., Zhao, Y., Wen, K., Lin, S., Li, J., Wacker, L., Haghipour, N., Plötze, M., Liu, Z., & Eglinton, T. I. (2018). Contrasting Fates of Petrogenic and Biospheric Carbon in the South China Sea. *Geophysical Research Letters*, *45*(17), 9077–9086. https://doi.org/10.1029/2018GL079222

Boyd, P. W., Claustre, H., Levy, M., Siegel, D. A., & Weber, T. (2019). Multi-faceted particle pumps drive carbon sequestration in the ocean. *Nature*, *568*(7752), 327–335. https://doi.org/10.1038/s41586-019-1098-2

Buesseler, K. O., Boyd, P. W., Black, E. E., & Siegel, D. A. (2020). Metrics that matter for assessing the ocean biological carbon pump. *Proceedings of the National Academy of Sciences of the United States of America*, *117*(18), 9679–9687. https://doi.org/10.1073/pnas.1918114117

Burd, A. B., & Jackson, G. A. (n.d.). *Particle Aggregation*. https://doi.org/10.1146/annurev.marine.010908.163904

Carr, M. E. (2001). Estimation of potential productivity in Eastern Boundary Currents using remote sensing. *Deep-Sea Research Part II: Topical Studies in Oceanography*, *49*(1–3), 59–80.

Conte, M. H., Carter, A. M., Koweek, D. A., Huang, S., & Weber, J. C. (2019). The elemental composition of the deep particle flux in the Sargasso Sea. *Chemical Geology*, *511*(March 2018), 279–313. https://doi.org/10.1016/j.chemgeo.2018.11.001

Dansie, A. P., Wiggs, G. F. S., Thomas, D. S. G., & Washington, R. (2017). Measurements of windblown dust characteristics and ocean fertilization potential: The ephemeral river valleys of Namibia. *Aeolian Research*, *29*(July), 30–41.

Diggle, S. P., & Whiteley, M. (2020). Microbe profile: Pseudomonas aeruginosa: Opportunistic pathogen and lab rat. *Microbiology (United Kingdom)*, *166*(1), 30–33. https://doi.org/10.1099/mic.0.000860

Eayrs, C., Holland, D., Francis, D., Wagner, T., Kumar, R., & Li, X. (2019). Understanding the Seasonal Cycle of Antarctic Sea Ice Extent in the Context of Longer-Term Variability. *Reviews of Geophysics*, *57*(3), 1037–1064. https://doi.org/10.1029/2018RG000631

Fahl, K., & Nöthig, E. M. (2007). Lithogenic and biogenic particle fluxes on the Lomonosov Ridge (central Arctic Ocean) and their relevance for sediment accumulation: Vertical vs. lateral transport. *Deep-Sea Research Part I: Oceanographic Research Papers*, *54*(8), 1256–1272. https://doi.org/10.1016/j.dsr.2007.04.014

Fischer, G., Reuter, C., Karakas, G., Nowald, N., & Wefer, G. (2009). Offshore advection of particles within the Cape Blanc filament , Mauritania : Results from observational and modelling studies. *Progress in Oceanography*, *83*(1–4), 322–330.

Fischer, G., Romero, O., Merkel, U., Donner, B., Iversen, M., Nowald, N., Ratmeyer, V., Ruhland, G., Klann, M., & Wefer, G. (2016). Deep ocean mass fluxes in the coastal upwelling off Mauritania from 1988 to 2012: Variability on seasonal to decadal timescales. *Biogeosciences Discussions*, *12*(21), 17643–17692. https://doi.org/10.5194/bgd-12-17643-2015

Fischer, G., Neuer, S., Ramondenc, S., Müller, T. J., Donner, B., Ruhland, G., Ratmeyer, V., Meinecke, G., Nowald, N., Klann, M., & Wefer, G. (2020). Long-Term Changes of Particle Flux in the Canary Basin Between 1991 and 2009 and Comparison to Sediment Trap Records Off Mauritania. *Frontiers in Earth Science*, *8*(July), 1–21. https://doi.org/10.3389/feart.2020.00280

García-Reyes, M., Sydeman, W. J., Schoeman, D. S., Rykaczewski, R. R., Black, B. A., Smit, A. J., & Bograd, S. J. (2015). Under pressure: Climate change, upwelling, and eastern boundary upwelling ecosystems. *Frontiers in Marine Science*, *2*(DEC), 1–10. https://doi.org/10.3389/fmars.2015.00109

Gardner, W. D., Richardson, M. J., & Mishonov, A. V. (2018). Global assessment of benthic nepheloid layers and linkage with upper ocean dynamics. *Earth and Planetary Science Letters*, *482*(November 2017), 126–134.

Geilfus, N., Galley, R. J., Cooper, M., Halden, N., Hare, A., Wang, F., Søgaard, D. H., & Rysgaard, S. (2013). *Gypsum crystals observed in experimental and natural sea ice*. *40*(October), 1–6. https://doi.org/10.1002/2013GL058479

Giering, S. L. C., Cavan, E. L., Basedow, S. L., Briggs, N., Burd, A. B., Darroch, L. J., Guidi, L., Irisson, J., Iversen, M. H., Kiko, R., Lindsay, D., Marcolin, C. R., & Robinson, C. (2020). *Sinking Organic Particles in the Ocean — Flux Estimates From in situ Optical Devices*. *6*(February). https://doi.org/10.3389/fmars.2019.00834

Guidi, L., Jackson, G. A., Stemmann, L., Miquel, J. C., Picheral, M., & Gorsky, G. (2008). Relationship between particle size distribution and flux in the mesopelagic zone. *Deep-Sea Research Part I: Oceanographic Research Papers*, *55*(10), 1364–1374. https://doi.org/10.1016/j.dsr.2008.05.014

Halbach, L., Vihtakari, M., Duarte, P., Everett, A., Granskog, M. A., Hop, H., Kauko, H. M., Kristiansen, S., Myhre, P. I., Pavlov, A. K., Pramanik, A., Tatarek, A., Torsvik, T., Wiktor, J. M., Wold, A., Wulff, A., Steen, H., & Assmy, P. (2019). Tidewater Glaciers and Bedrock Characteristics Control the Phytoplankton Growth Environment in a Fjord in the Arctic. *Frontiers in Marine Science*, *6*(May), 1–18.

Hara, K., Osada, K., Yabuki, M., & Yamanouchi, T. (2012). Seasonal variation of fractionated sea-salt particles on the Antarctic coast. *Geophysical Research Letters*, *39*(17), 1–5. https://doi.org/10.1029/2012GL052761

Henson, S. A., Sanders, R., & Madsen, E. (2012). Global patterns in efficiency of particulate organic carbon export and transfer to the deep ocean. *Global Biogeochemical Cycles*, *26*(1), 1–14. https://doi.org/10.1029/2011GB004099

Hwang, J., Kim, M., Manganini, S. J., McIntyre, C. P., Haghipour, N., Park, J., Krishfield, R. A., Macdonald, R. W., McLaughlin, F. A., & Eglinton, T. I. (2015). Temporal and spatial variability of particle transport in the deep Arctic Canada Basin. *Journal of Geophysical Research: Oceans*, 2813–2825.

Hwang, J., Manganini, S. J., Park, J., Montluçon, D. B., Toole, J. M., & Eglinton, T. I. (2017). *Biological and physical controls on the flux and characteristics of sinking particles on the Northwest Atlantic margin*. 1–15. https://doi.org/10.1002/2016JC012549.Received

Inthorn, M., Wagner, T., Scheeder, G., & Zabel, M. (2006). Lateral transport controls distribution, quality, and burial of organic matter along continental slopes in high-productivity areas. *Geology*, *34*(3), 205–208. https://doi.org/10.1130/G22153.1

Iversen, M. H., Nowald, N., Ploug, H., Jackson, G. A., & Fischer, G. (2010). High resolution profiles of vertical particulate organic matter export off Cape Blanc, Mauritania: Degradation processes and ballasting effects. *Deep-Sea Research Part I: Oceanographic Research Papers*, *57*(6), 771–784. https://doi.org/10.1016/j.dsr.2010.03.007

Iversen, M. H., & Ploug, H. (2010). Ballast minerals and the sinking carbon flux in the ocean: Carbon-specific respiration rates and sinking velocity of marine snow aggregates. *Biogeosciences*, *7*(9), 2613–2624.

Iversen, M.H., Lampitt, R.S., 2020. Size does not matter after all: No evidence for a size-sinking relationship for marine snow. *Prog. Oceanogr.* 189, 102445.

Jackson, C. (2007). Internal wave detection using the Moderate Resolution Imaging Spectroradiometer (MODIS). *Journal of Geophysical Research: Oceans*, *112*(11), 1–13.

Jackson, G. A., & Checkley JR, D. M. (2011). Deep-Sea Research I Particle size distributions in the upper 100 m water column and their implications for animal feeding in the plankton. *Deep-Sea Research Part I*, *58*(3), 283–297. https://doi.org/10.1016/j.dsr.2010.12.008

Jardine, G. E., Crocker, A. J., Bailey, I., Cooper, M. J., Milton, J. A., & Wilson, P. A. (2021). The imprint of windblown dust from the North American Southwest on the California Channel Islands and Pacific Ocean sediments. *Quaternary Science Reviews*, *261*(January), 106934. https://doi.org/10.1016/j.quascirev.2021.106934

Jacox, M. G., Bograd, S. J., Hazen, E. L., & Fiechter, J. (2015). Sensitivity of the California Current nutrient supply to wind, heat, and remote ocean forcing. *Geophysical Research Letters*, *42*(14), 5950–5957. https://doi.org/10.1002/2015GL065147

Johnson, R. (1976). *Current Profiles in the Canary Current Upwelling Region Near Cape Blanc, March and April 1974. 81*(36), 6429–6439.

Juhl, A. R., Krembs, C., & Meiners, K. M. (2011). Seasonal development and differential retention of ice algae and other organic fractions in first-year Arctic sea ice. *Marine Ecology Progress Series*, *436*, 1–16. https://doi.org/10.3354/meps09277

Kämpf, J., & Chapman, P. (2016). Upwelling Systems of the World. In *Upwelling Systems of the World*. https://doi.org/10.1007/978-3-319-42524-5

Karakaş, G., Nowald, N., Blaas, M., Marchesiello, P., Frickenhaus, S., & Schlitzer, R. (2006). High-resolution modeling of sediment erosion and particle transport across the northwest African shelf. *Journal of Geophysical Research: Oceans*, *111*(6), 1–13. https://doi.org/10.1029/2005JC003296

Kim, M., Hwang, J., Eglinton, T. I., & Druffel, E. R. M. (2020). Lateral Particle Supply as a Key Vector in the Oceanic Carbon Cycle. *Global Biogeochemical Cycles*, *34*(9), 1–14.

Kindler, K., Khalili, A., & Stocker, R. (2010). *Diffusion-limited retention of porous particles at density interfaces*. *107*(51). https://doi.org/10.1073/pnas.1012319108

Kiørboe, T., Lundsgaard, C., Olesen, M., & Hansen, J. L. S. (1994). Journal of Marine Research, 52, 297-323,1994. *Journal of Marine Research*, 297–323.

Kiørboe, T., Grossart, H. P., Ploug, H., & Tang, K. (2002). Mechanisms and rates of colonisation of sinking aggregates. *Applied and Environmental Microbiology*, *68*(8), 3996–4006. https://doi.org/10.1128/AEM.68.8.3996

Klawonn, I., Bonaglia, S., & Bru, V. (2015). *Aerobic and anaerobic nitrogen transformation processes in N 2 -fixing cyanobacterial aggregates*. 1456–1466. https://doi.org/10.1038/ismej.2014.232

Komar P.D. (1978) Grain settling. In: Middleton G.V., Church M.J., Coniglio M., Hardie L.A., Longstaffe F.J. (eds) Encyclopedia of Sediments and Sedimentary Rocks. Encyclopedia of Earth Sciences Series. Springer, Dordrecht. https://doi.org/10.1007/978-1-4020-3609-5_103

Lam, P. J., Lee, J. M., Heller, M. I., Mehic, S., Xiang, Y., & Bates, N. R. (2018). Size-fractionated distributions of suspended particle concentration and major phase composition from the U.S. GEOTRACES Eastern Pacific Zonal Transect (GP16). *Marine Chemistry*, *201*(September), 90–107. https://doi.org/10.1016/j.marchem.2017.08.013

Lalande, C., Nöthig, E. M., Bauerfeind, E., Hardge, K., Beszczynska-Möller, A., & Fahl, K. (2016). Lateral supply and downward export of particulate matter from upper waters to the seafloor in the deep eastern Fram Strait. *Deep-Sea Research Part I: Oceanographic Research Papers*, *114*, 78–89.

Lutz, M., Dunbar, R., & Caldeira, K. (2002). Regional variability in the vertical flux of particulate organic carbon in the ocean interior. *Global Biogeochemical Cycles*, *16*(3), 11-1-11–18.

Macintyre, S., Alldredge, A. L., & Gotschalk, C. C. (1995). *Accumulation of marine snow in the water column*. *40*(May).

Maerz, J., Six, K. D., Stemmler, I., Ahmerkamp, S., & Ilyina, T. (2020). Microstructure and composition of marine aggregates as co-determinants for vertical particulate organic carbon transfer in the global ocean. *Biogeosciences*, *17*(7), 1765–1803. https://doi.org/10.5194/bg-17-1765-2020

McCave, I. N. (1983). Particulate size spectra, behavior, and origin of nepheloid layers over the Nova Scotian continental rise (North Atlantic). *Journal of Geophysical Research*, *88*(C12), 7647–7666. https://doi.org/10.1029/JC088iC12p07647

Mcdonnell, A. M. P., & Buesseler, K. O. (2012). *OCEANOGRAPHY : METHODS A new method for the estimation of sinking particle fluxes from measurements of the particle size distribution , average sinking velocity , and carbon content*. 329–346.

Meng, S., & Liu, Y. (2016). New insights into transparent exopolymer particles (TEP) formation from precursor materials at various Na + /Ca 2+ ratios. *Scientific Reports*, *6*(January), 1–9. https://doi.org/10.1038/srep19747

Moradi et al. (in prep.) A novel data-driven scale-bridging model for addressing carbon flux attenuation in the water column: An application to carbon export in mesoscale eddies off Cape Verde Islands.

Mouyen, M., Longuevergne, L., Steer, P., Crave, A., Lemoine, J. M., Save, H., & Robin, C. (2018). Assessing modern river sediment discharge to the ocean using satellite gravimetry. *Nature Communications*, *9*(1), 1–9. https://doi.org/10.1038/s41467-018-05921-y

Nowald, N., Karakas, G., Ratmeyer, V., Fischer, G., Schlitzer, R., Davenport, R. A., & Wefer, G. (2006). Distribution and transport processes of marine particulate matter off Cape Blanc (NW-Africa): results from vertical camera profiles. *Ocean Science Discussions*, *3*(4), 903–938. https://doi.org/10.5194/osd-3-903-2006

Nowald, N., Iversen, M. H., Fischer, G., Ratmeyer, V., & Wefer, G. (2015). Time series of in-situ particle properties and sediment trap fluxes in the coastal upwelling filament off Cape Blanc, Mauritania. *Progress in Oceanography*, *137*, 1–11. https://doi.org/10.1016/j.pocean.2014.12.015

Ploug, H., & Passow, U. (2007). Direct measurement of diffusivity within diatom aggregates containing transparent exopolymer particles. *Limnology and Oceanography*, *52*(1), 1–6. https://doi.org/10.4319/lo.2007.52.1.0001

Ploug, H., Iversen, M. H., Koski, M., & Buitenhuis, E. T. (2008). Production, oxygen respiration rates, and sinking velocity of copepod fecal pellets: Direct measurements of ballasting by opal and calcite. *Limnology and Oceanography*, *53*(2), 469–476.

Puig, P., Palanques, A., Guillén, J., & El Khatab, M. (2004). Role of internal waves in the generation of nepheloid layers on the northwestern Alboran slope: Implications for continental margin shaping. *Journal of Geophysical Research: Oceans*, *109*(9), 1–11. https://doi.org/10.1029/2004JC002394

Puig, P., Madron, X. D. de, Salat, J., Schroeder, K., Martín, J., Karageorgis, A. P., Palanques, A., Roullier, F., Lopez-Jurado, J. L., Emelianov, M., Moutin, T., & Houpert, L. (2013). Thick bottom nepheloid layers in the western Mediterranean generated by deep dense shelf water cascading. *Progress in Oceanography*, *111*, 1–23. https://doi.org/10.1016/j.pocean.2012.10.003

Ransom, B., Shea, K. F., Burkett, P. J., Bennett, R. H., & Baerwald, R. (1998). Comparison of pelagic and nepheloid layer marine snow: Implications for carbon cycling. *Marine Geology*, *150*(1–4), 39–50. https://doi.org/10.1016/S0025-3227(98)00052-8

Reigstad, M., & Wassmann, Æ. P. (2007). *Does Phaeocystis spp . contribute significantly to vertical export of organic carbon ?* 217–234.

Richman, J. G., de Szoeke, R. A., and Davis, R. E. (1987), Measurements of near-surface shear in the ocean, *J. Geophys. Res.*, 92(C3), 2851– 2858, doi:10.1029/JC092iC03p02851.

Romero, O., Ramondenc, S., & Fischer, G. (2020). A two-decades (1988–2009) record of diatom fluxes in the Mauritanian coastal upwelling: Impact of low-frequency forcing and a two-step shift in the species composition. *Biogeosciences Discussions*, 1–32.

Santschi, P. H., Balnois, E., Wilkinson, K. J., Zhang, J., Buffle, J., & Guo, L. (1998). Fibrillar polysaccharides in marine macromolecular organic matter as imaged by atomic force microscopy and transmission electron microscopy. *Limnology and Oceanography*, *43*(5), 896–908. https://doi.org/10.4319/lo.1998.43.5.0896

Sanz, J. L., Maestro, A., & Luis, M. A. (2017). Deep-sea ecosystems off Mauritania: Research of marine biodiversity and habitats in the northwest African margin. In *Deep-Sea Ecosystems Off Mauritania: Research of Marine Biodiversity and Habitats in the Northwest African Margin*.

Schulz, K., Büttner, S., Rogge, A., Janout, M., Hölemann, J., & Rippeth, T. P. (2021). Turbulent Mixing and the Formation of an Intermediate Nepheloid Layer Above the Siberian Continental Shelf Break. *Geophysical Research Letters*, *48*(9), 1–11. https://doi.org/10.1029/2021GL092988

Secchi, E., Vitale, A., Miño, G. L., Kantsler, V., Eberl, L., Rusconi, R., & Stocker, R. (2020). The effect of flow on swimming bacteria controls the initial colonization of curved surfaces. *Nature Communications*, *11*(1), 1–12. https://doi.org/10.1038/s41467-020-16620-y

Thomsen, L. A., & McCave, I. N. (2000). Aggregation processes in the benthic boundary layer at the Celtic Sea continental margin. *Deep-Sea Research Part I: Oceanographic Research Papers*, *47*(8), 1389–1404. https://doi.org/10.1016/S0967-0637(99)00110-7

Thunell, R., Benitez-Nelson, C., Varela, R., Astor, Y., & Muller-Karger, F. (2007). Particulate organic carbon fluxes along upwelling-dominated continental margins: Rate and mechanisms. *Global Biogeochemical Cycles*, *21*(1), 1–12. https://doi.org/10.1029/2006GB002793

Trudnowska, E., Lacour, L., Ardyna, M., Rogge, A., Irisson, J. O., Waite, A. M., Babin, M., & Stemmann, L. (2021). Marine snow morphology illuminates the evolution of phytoplankton blooms and determines their subsequent vertical export. *Nature Communications*, *12*(1), 1–13.

Underwood, G., Fietz, S., Papadimitriou, S., Thomas, D., & Dieckmann, G. (2010). Distribution and composition of dissolved extracellular polymeric substances (EPS) in Antarctic sea ice. *Marine Ecology Progress Series*, *404*, 1–19. https://doi.org/10.3354/meps08557

van der Does, M., Brummer, G. J. A., van Crimpen, F. C. J., Korte, L. F., Mahowald, N. M., Merkel, U., Yu, H., Zuidema, P., & Stuut, J. B. W. (2020). Tropical Rains Controlling Deposition of Saharan Dust Across the North Atlantic Ocean. *Geophysical Research Letters*, *47*(5). https://doi.org/10.1029/2019GL086867

van der Jagt, H., Iversen, M. H., Friese, C., & Stuut, J. W. (2018). *The ballasting effect of Saharan dust deposition on aggregate dynamics and carbon export : Aggregation , settling ,*.

van der Jagt, H., Wiedmann, I., Hildebrandt, N., Niehoff, B., & Iversen, M. H. (2020). Aggregate Feeding by the Copepods Calanus and Pseudocalanus Controls Carbon Flux Attenuation in the Arctic Shelf Sea During the Productive Period. *Frontiers in Marine Science*, *7*(September). https://doi.org/10.3389/fmars.2020.543124

Verdugo, P., Alldredge, A. L., Azam, F., Kirchman, D. L., Passow, U., & Santschi, P. H. (2004). The oceanic gel phase: A bridge in the DOM-POM continuum. *Marine Chemistry*, *92*(1–4), 67–85. https://doi.org/10.1016/j.marchem.2004.06.017

Verdugo, P. (2012). Marine Microgels. *Annual Review of Marine Science*, *4*(1), 375–400. https://doi.org/10.1146/annurev-marine-120709-142759

Wellman, & Wilson. (1963). *Salts on Sea Ice in McMurdo Sound, Antarctica. 200*, Nature, vol. 200, 1962–1963.

Wekerle, C., Krumpen, T., Dinter, T., von Appen, W. J., Iversen, M. H., & Salter, I. (2018). Properties of sediment trap catchment areas in fram strait: Results from Lagrangian modeling and remote sensing. *Frontiers in Marine Science*, *9*(NOV).

Wollenburg, J., Katlein, C., & Nehrke, G. (2018). *Ballasting by cryogenic gypsum enhances carbon export in a Phaeocystis under-ice bloom*. *May*, 0–9. https://doi.org/10.1038/s41598-018-26016-0

Wollenburg, J. E., Iversen, M., Katlein, C., Krumpen, T., Nicolaus, M., Castellani, G., Peeken, I., & Flores, H. (2020). New observations of the distribution, morphology and dissolution dynamics of cryogenic gypsum in the Arctic Ocean. *Cryosphere*, *14*(6), 1795–1808. https://doi.org/10.5194/tc-14-1795-2020

Zetsche, E. M., Larsson, A. I., Iversen, M. H., & Ploug, H. (2020). Flow and diffusion around and within diatom aggregates: Effects of aggregate composition and shape. *Limnology and Oceanography*, *65*(8), 1818–1833. https://doi.org/10.1002/lno.11420

Additional Publications

Pauli, N. C., Flintrop, C. M., Konrad, C., Pakhomov, E. A., Swoboda, S., Koch, F., Wang, X. L., Zhang, J. C., Brierley, A. S., Bernasconi, M., Meyer, B., & Iversen, M. H. (2021). Krill and salp faecal pellets contribute equally to the carbon flux at the Antarctic Peninsula. *Nature Communications*, *12*(1), 1–12. https://doi.org/10.1038/s41467-021-27436-9

Abstract

Krill and salps are important for carbon flux in the Southern Ocean, but the extent of their contribution and the consequences of shifts in dominance from krill to salps remain unclear. We present a direct comparison of the contribution of krill and salp faecal pellets (FP) to vertical carbon flux at the Antarctic Peninsula using a combination of sediment traps, FP production, carbon content, microbial degradation, and krill and salp abundances. Salps produce 4-fold more FP carbon than krill, but the FP from both species contribute equally to the carbon flux at 300 m, accounting for 75% of total carbon. Krill FP are exported to 72% to 300 m, while 80% of salp FP are retained in the mixed layer due to fragmentation. Thus, declining krill abundances could lead to decreased carbon flux, indicating that the Antarctic Peninsula could become a less efficient carbon sink for anthropogenic CO2 in future.

Author contributions:

N.C.P., E.A.P., M.H.I. and B.M. conceptualised the study. N.C.P., M.H.I., C.M.F., C.K., E.A.P., F.K. and B.M. performed fieldwork. F.K. provided the measurements of primary production. M.B. and A.S.B. calibrated the acoustic system and collected acoustic data on board of RV Polarstern. X.L.W. and J.C.Z. conducted hydroacoustic analyses and krill biomass estimates. S.S. and N.C.P. conducted work in the home laboratory. N.C.P. and M.H.I. performed data analyses. N.C.P. drafted the manuscript, with the help of all authors.

Acknowledgments

The scientific work presented in this thesis is not the product of a single person, but the joint effort of many, and I would like to give my sincere thanks to all of you which made this work possible.

First and foremost, I would like to thank my supervisor Morten Iversen for his guidance during the period of the Ph.D.. His mentoring allowed me to sharpen my critical assessment, broadened my perception on the ocean and allowed me to explore my full potential, which made me grow as an aspiring scientist but also as a person. Thank you, Morten!

I would also like to thank the members of my Ph.D. thesis committee Hannah Marchant, Helle Ploug, Jan-Hendrik Hehemann, Eva-Maria Zetsche and Clara Flintrop for their guidance and support. I would like to thank the members of the Ph.D. defence committee for the critical evaluation of my thesis.

Great thanks go to the co-authors and contributors I had the pleasure to work with. Special thanks go's to Ekkehard Küstermann who with great patience and unflagging enthusiasm helped drive the method development with MR imaging. Special thanks go's also to Gerhard Bartzke for his great support towards the end of the thesis and patience when explaining the principles of small-scale fluid dynamics. I want to thank my former and current colleges in the SeaPump group which always created a nice and supportive atmosphere and with which I shared countless laughs and fun moments.

Special thanks go's to my friends which have been a great support and source of encouragement during the Ph.D.. In particular I want to thank Thanos, Julian, Swantje, Rieke, Patricia and Vero for the countless wonderful moments and support during the Ph.D., but also during the at times harsh periods during the pandemic. I want to thank my family for their endless support during my university times and period of the Ph.D..

Last but certainly not least, I want to thank Laura for the many wonderful years we have shared, grown and supported each other. I certainly would not be where and who I am without you.

Supplementary information for manuscript I

Three-dimensional visualization of marine snow using magnetic resonance imaging

Steffen Swoboda[1*], Ekkehard Küstermann[2], Gerhard Bartzke[1], Ricarda Gatter[1], Nasrollah Moradi[1], Anna Biastoch[1], Wolfgang Dreher[2], Morten H. Iversen[1,3]

[1]MARUM – Center for Marine Environmental Sciences, University of Bremen, 28359 Bremen, Germany.

[2]Chemistry Department, University of Bremen, 28359 Bremen, Germany.

[3]Section for Polar Biological Oceanography, Alfred Wegener Institute Helmholtz Centre for Polar and Marine Research, 27570 Bremerhaven, Germany.

Corresponding authors:
Steffen Swoboda
Morten Iversen

Contents:

Figures S1 to S3

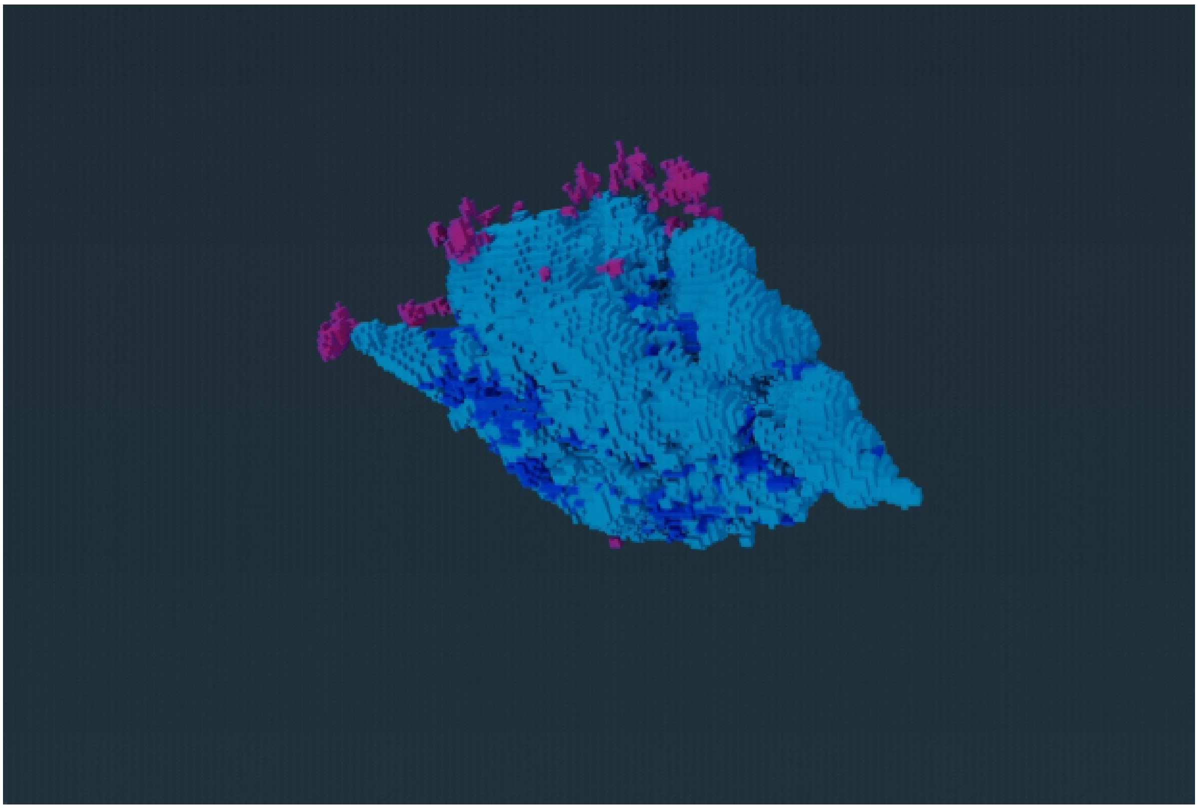

Fig. S1. NMR derived aggregate volume with manually included (dark blue) and excluded (purple) voxels.

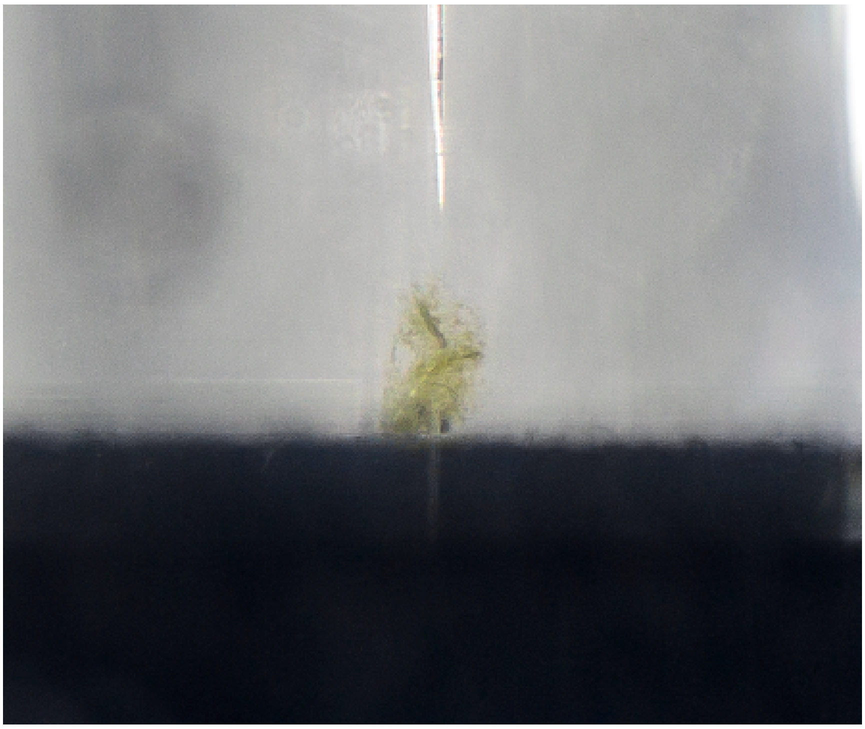

Fig. S2. Camera image of the measured aggregate during respiration measurements in the flow chamber. Set in relation to the NMR-derived model, the aggregate is facing the direction of the x-axis (Fig. 1 d in the main text).

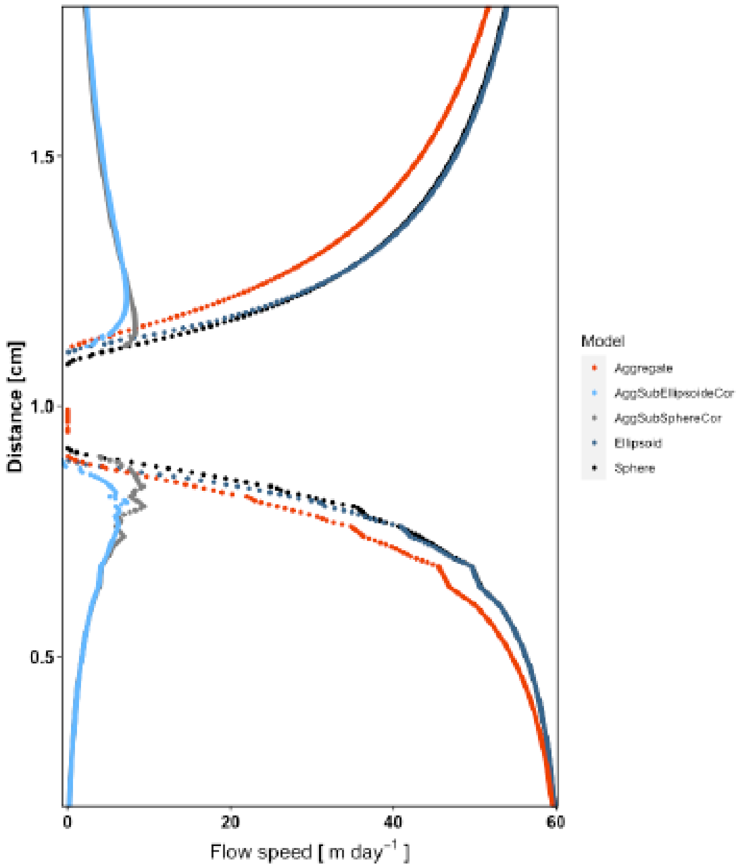

Fig. S3. Flow velocity profiles along the Z axis from the model output. Individual flow velocities from the model aggregate (red), optical derived ellipsoid (dark blue) and sphere (black) as well as the difference in flow velocity between model aggregate and the ellipsoid (light blue) and model aggregate and the sphere (grey) are depicted respectively.

Supplementary information for manuscript II

Lateral advection of shelf produced organic matter is the main contributor to deep ocean carbon flux in the Cape Blanc Upwelling region

Steffen Swoboda[1*], Hannah Marchant[1,2], Soeren Ahmerkamp[1,2], Jan-Hendrik Hehemann[1,2], Hagen Buck-Wiese[1,2], Farooq Moin Jalaluddin[1,2], Marius Becker[3], Arjun Chennu[4], Oscar E. Romero[1,6], Kai Schwalfenberg[5], Simon Ramondenc[1,6], Morten H. Iversen[1,6*]

[1]MARUM and University of Bremen, Leobener Str. 8, 28359 Bremen, Germany

[2]Max Planck Institute for Marine Microbiology, Celsiusstraße 1 ,28359 Bremen, Germany

[3]Kiel University, Institute of Geosciences, Otto-Hahn-Platz 1, 24118 Kiel, Germany

[4]Leibniz Centre for Tropical Marine Research Fahrenheitstraße 6, 28359 Bremen, Germany

[5]Institute for Chemistry and Biology of the Marine Environment, Carl-von-Ossietzky-Straße 9-11, 26129 Oldenburg, Germany

[6]Alfred Wegener Institute, Alfred Wegener Institute Helmholtz Centre for Polar and Marine Research, Am Handelshafen 12, 27570 Bremerhaven, Germany

*Corresponding authors:

Steffen Swoboda

Morten H. Iversen

Contents:

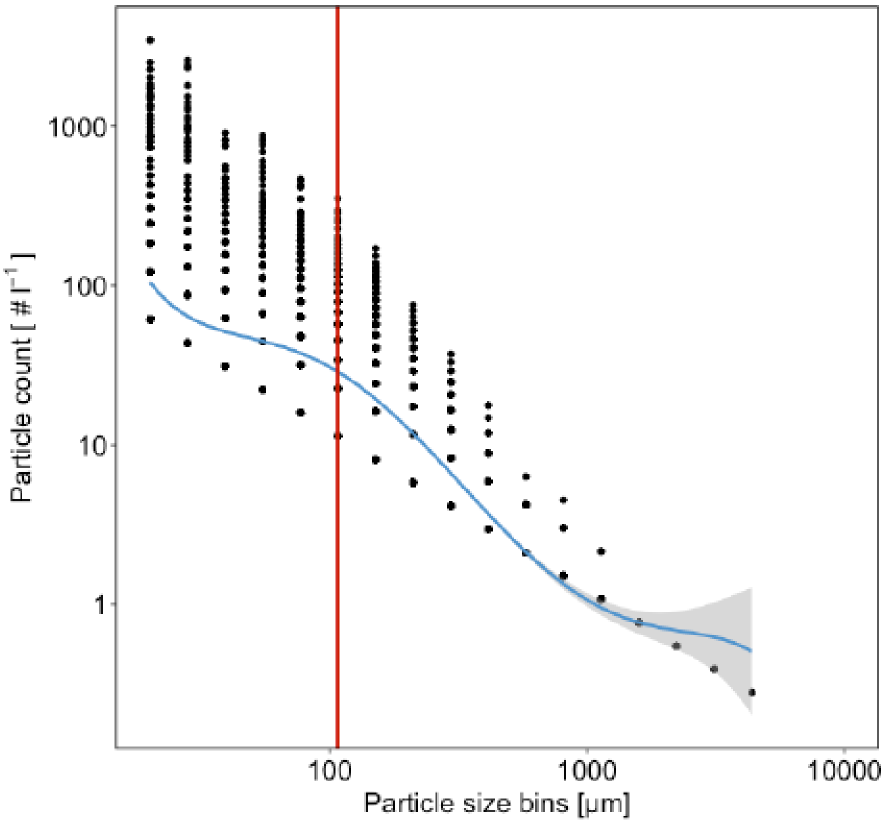

Figure S1. Representative particle size distribution as a function of particle count derived from particle camera profile GeoB23604_01 (blue line shows a polynomial regression, degree = 5, grey area shows 95% confidence interval; Profile shown in Fig.S6 & Table S1). The red vertical line indicates the threshold size of 107 µm as the minimum size for an accurate representation of particles in the water column. The decreasing slope for smaller size particles size bins indicates that only a fraction of particles could be observed below a size of 107 µm. Axis are log10 transformed. Zero values from particle camera images that included no particles from a respective size class were removed.

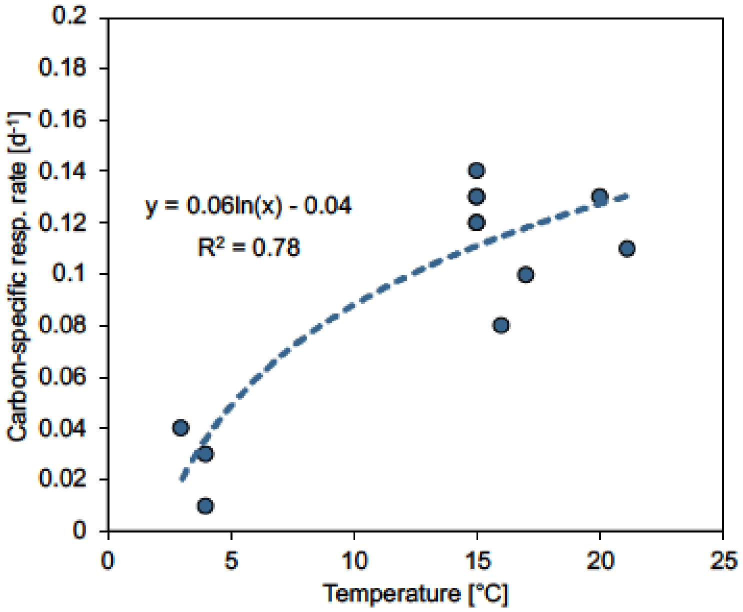

Figure S2. Logarithmic curve fit on carbon specific respiration rates of marine aggregates obtained from the literature and process study in 2019. Detailed values are listed in supplementary table S2.

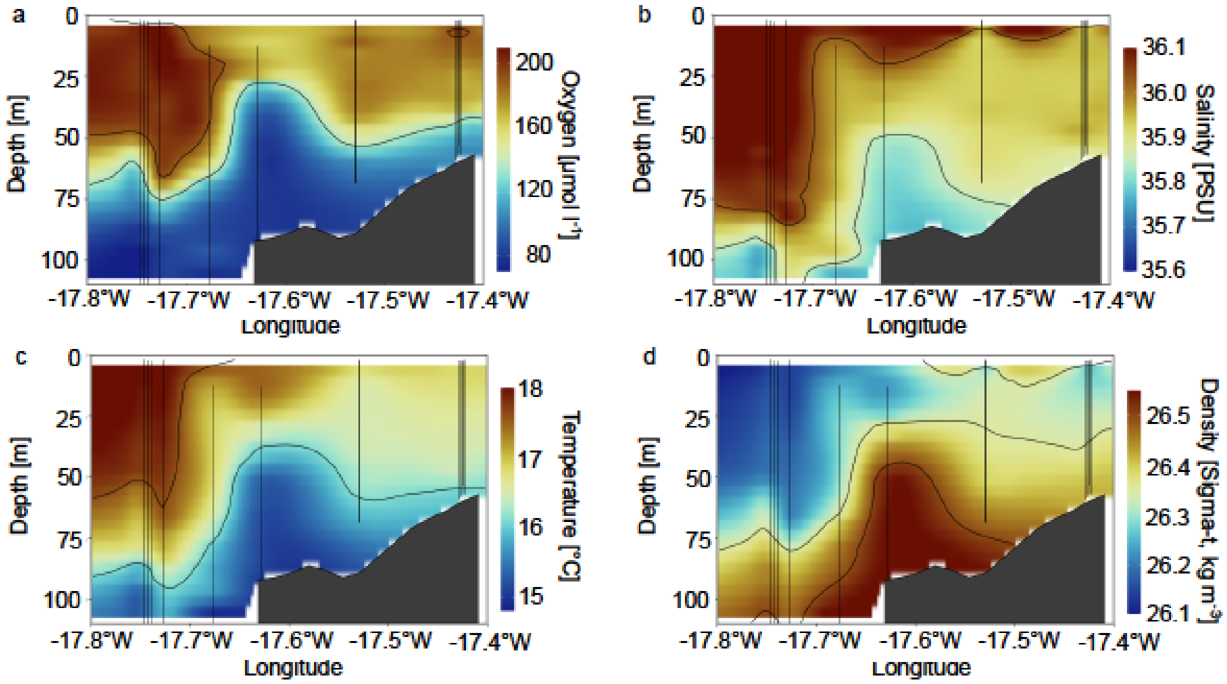

Figure S3. Profiles (black lines) of oxygen (a), salinity (b), temperature (c) and density (d) along a cross-shelf transect. The denser water with lowered values of Oxygen, Salinity and Temperature in the bottom 50 m indicates deep water is upwelled and advected on the shallow shelf in a ~50 m thick bottom layer. Profiles were obtained during the process study (January 2019)

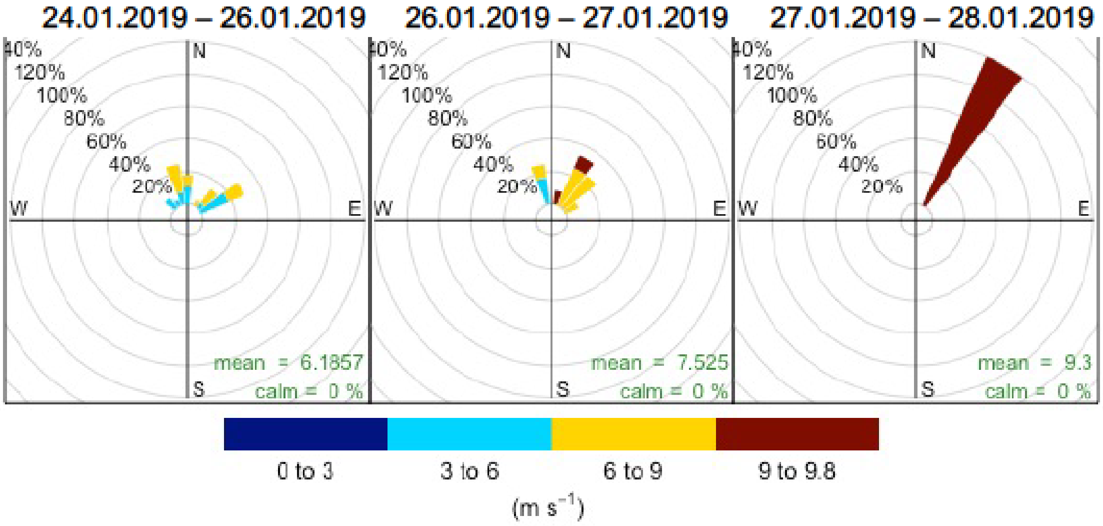

Figure S4. Ship based anemometer measurements of wind direction and speed during sampling on the shallow shelf (CB$_{sh}$) during the process study (January 2019). Spoke angle indicates the direction the wind blew from and spoke size indicates the duration in %. The wind speed of spokes is indicated by their respective colour.

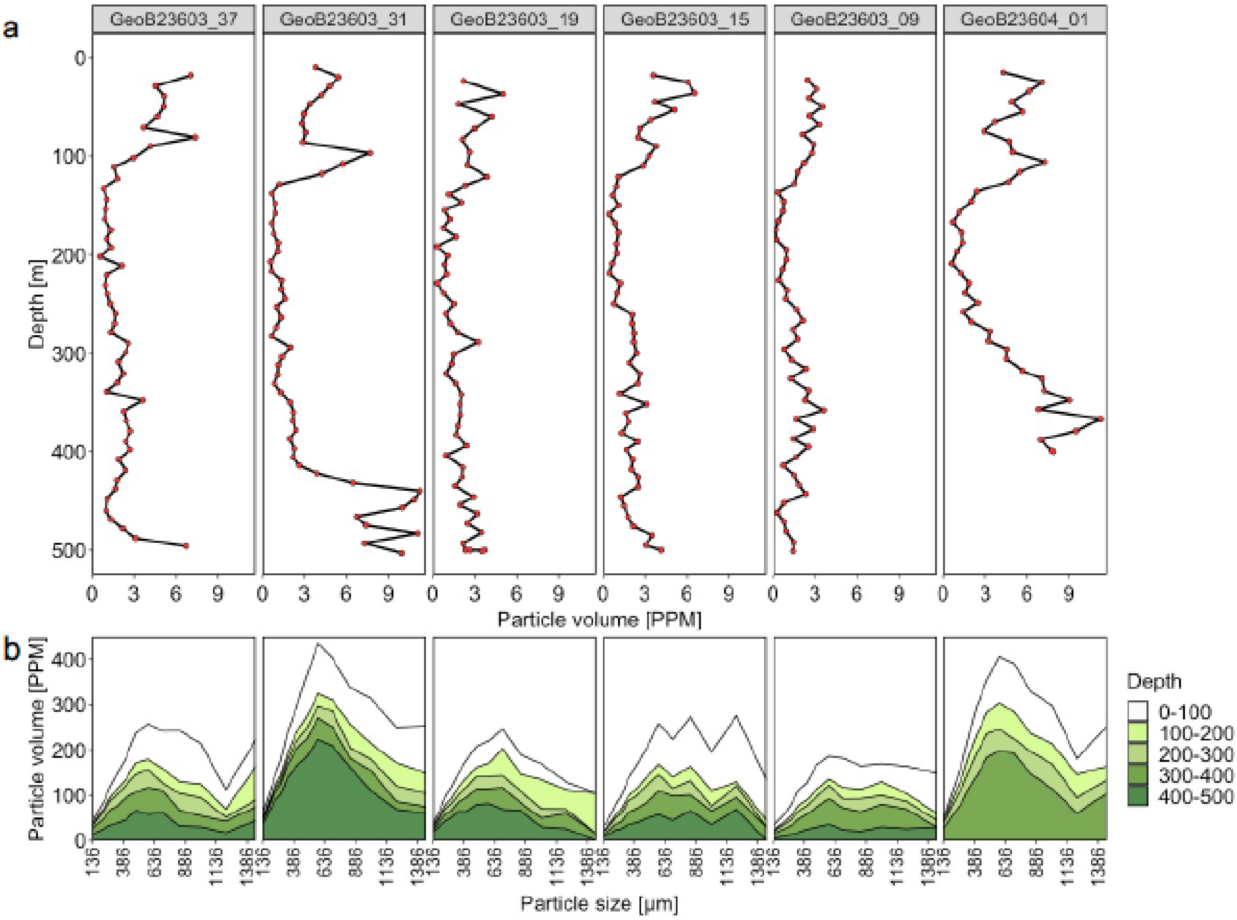

Figure S5. Measured particle volume from each individual particle camera profile at CB$_s$ during the process study (January 2019) are shown as (a) total particle volume in the 400 – 1000 µm size classes averaged over 9 m vertical steps and (b) stacked area of particle volume from particle size classes between 136 – 1386 µm. Numbers above individual profiles indicate the cast number (see details in table S1).

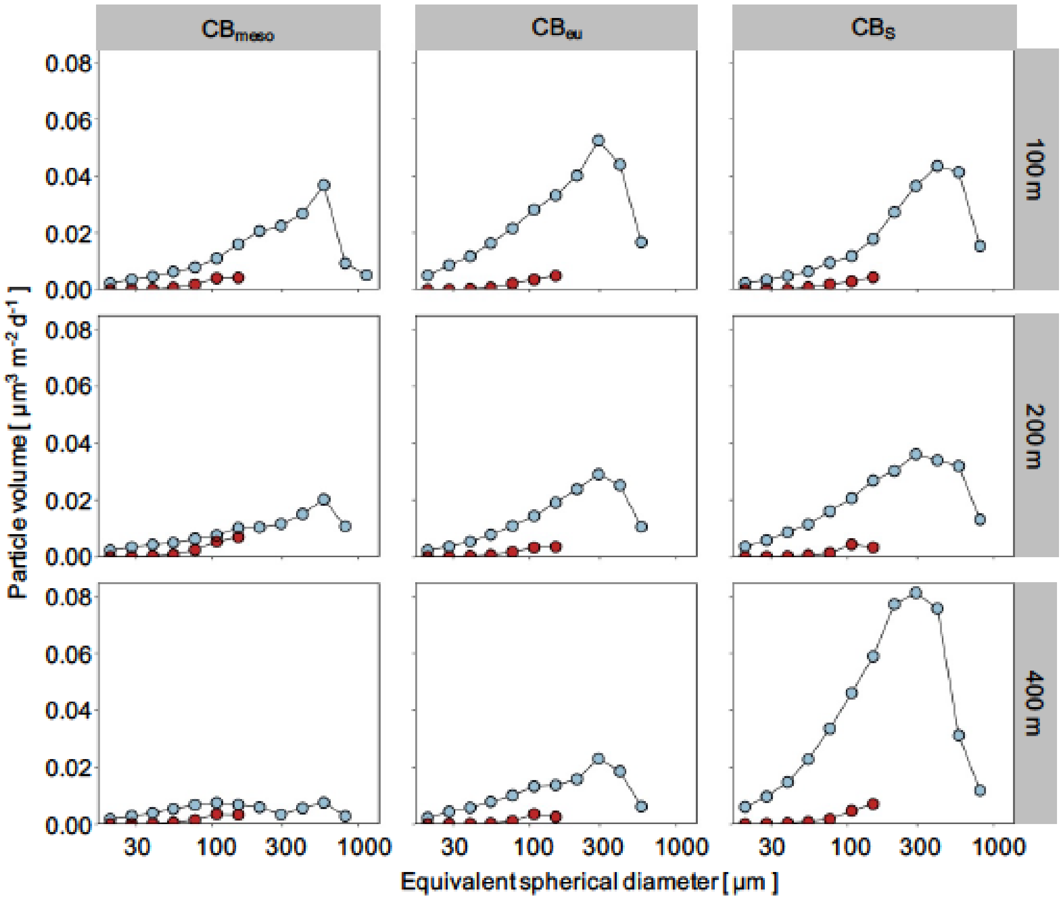

Figure S6. Particle volume flux within each particle size-class determined from the gel traps deployed as part of the drifting sediment traps during the process study (January 2019). The top grey panels show the stations of deployment while the right grey panels show the depth from which the particle volume flux was collected. Blue points depict marine snow particle volume while red points depict fecal pellet volume.

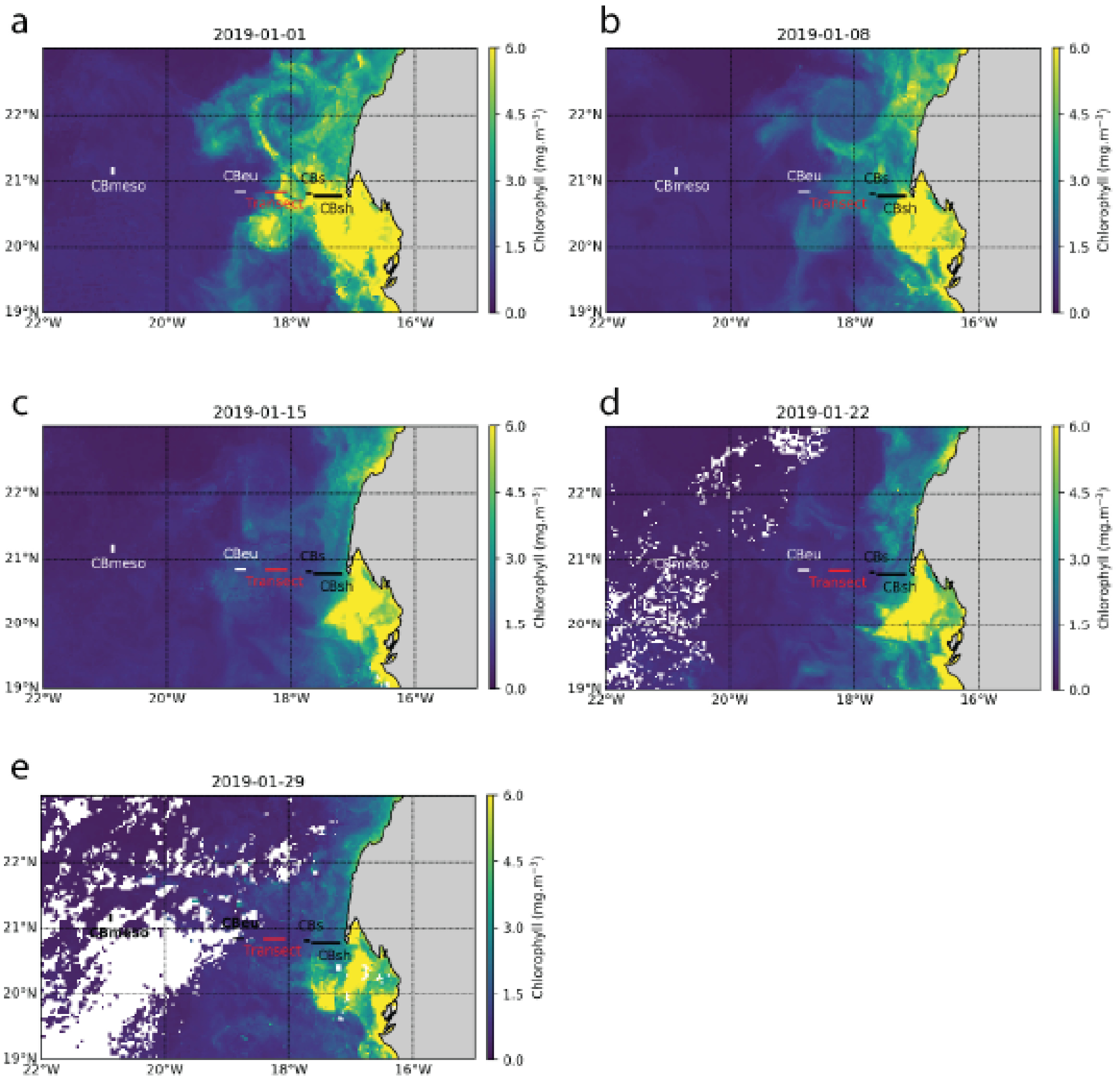

Figure S7. Weekly average chlorophyll values during January 2019, derived from VIIRS (Visible Infrared Imaging Radiometer Suite) with a spatial resolution of 4.17 km^2. Labels indicate the sampling area during the process study (January 2019).

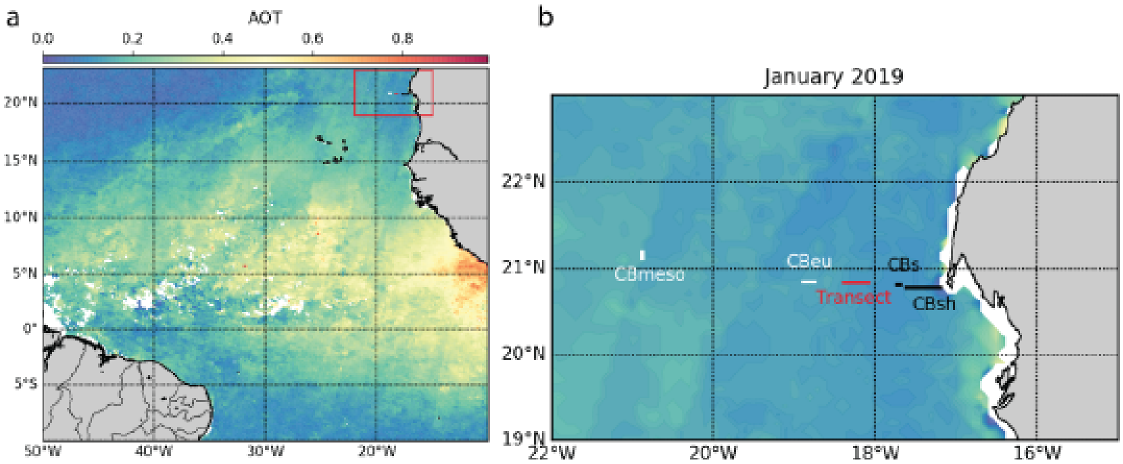

Figure S8. Monthly average Aerosol Optical Thickness (AOT) during January 2019, derived from MODIS (Moderate Resolution Imaging Spectroradiometer sensor) with a spatial resolution of 0.1°. Panel a shows the average AOT across the tropical and subtropical Atlantic. Panel b shows average AOT in the sampling region of the process study with labels indicating the sampling area.

Figure S9. Large non-sinking gelatinous (possibly transparent exopolymer particles, TEP) aggregates obtained from Marine Snow Catcher deployments on the shallow shelf at CB_{sh}.

Table S1. Detailed sampling overview during the process study on research expedition POS531 aboard RV *Poseidon* in 2019. The table shows the deployment area, station number, time of deployment, deployed instrument, latitude and longitude of the deployment, total water depth (bottom depth), wind direction, and wind velocity. For the drifting sediment traps we provide the parameters at the time of deployment. All traps were recovered ~24 h after deployment.

Area	Station number	Timestamp at deployment	Deployed device	Latitude	Longitude	Bottom depth (m)	Wind Direction (°)	Wind Velocity (m s⁻¹)
CBsh	Geo823602_19	24/01/2019 11:08	Marine snow catcher	20° 46,345' N	017° 10,859' W	27.7	59.5	7.1
CBsh	Geo823602_18	24/01/2019 09:41	Particle camera	20° 46,356' N	017° 10,861' W	26.8	67.8	10.8
CBsh	Geo823602_17	24/01/2019 09:01	CTD	20° 46,324' N	017° 10,912' W	27.2	62	8.8
CBsh	Geo823602_08	23/01/2019 19:19	Marine snow catcher	20° 46,329' N	017° 10,912' W	27.8	355.9	8.5
CBsh	Geo823602_06	23/01/2019 18:26	Particle camera	20° 46,314' N	017° 10,917' W	28.5	343.6	8
CBsh	Geo823602_07	23/01/2019 18:55	CTD	20° 46,326' N	017° 10,919' W	28.2	353.9	6.9
CBsh	Geo823602_21	24/01/2019 13:30	CTD	20° 46,365' N	017° 10,924' W	29.2	1.2	5.8
CBsh	Geo823609_02	26/01/2019 20:15	Particle camera	20° 46,372' N	017° 11,007' W	28.1	352.9	7.4
CBsh	Geo823609_01	26/01/2019 19:56	CTD	20° 46,342' N	017° 11,025' W	28.3	348.5	6.4
CBsh	Geo823608_01	26/01/2019 18:42	Particle camera	20° 46,251' N	017° 14,404' W	39.1	354.9	5.5
CBsh	Geo823608_02	26/01/2019 18:55	CTD	20° 46,256' N	017° 14,409' W	38.1	356.4	6.2
CBsh	Geo823607_01	26/01/2019 17:30	CTD	20° 46,315' N	017° 19,348' W	46.5	339.5	6.1
CBsh	Geo823607_02	26/01/2019 17:50	Particle camera	20° 46,304' N	017° 19,365' W	46.5	342.4	7.9
CBsh	Geo823610_31	28/01/2019 04:19	Particle camera	20° 46,738' N	017° 25,353' W	58.2	30.4	8.5
CBsh	Geo823610_29	28/01/2019 03:52	CTD	20° 46,711' N	017° 25,367' W	58	30	9.3
CBsh	Geo823610_23	27/01/2019 16:41	Particle camera	20° 46,718' N	017° 25,462' W	58.7	353.4	6.1
CBsh	Geo823610_25	27/01/2019 21:00	Particle camera	20° 46,523' N	017° 25,474' W	58.5	10.7	9.1
CBsh	Geo823610_26	27/01/2019 21:59	CTD	20° 46,559' N	017° 25,484' W	57.5	19.5	9.8
CBsh	Geo823610_18	27/01/2019 13:02	Particle camera	20° 46,762' N	017° 25,506' W	59	32	5.9
CBsh	Geo823610_17	27/01/2019 12:41	Marine snow catcher	20° 46,786' N	017° 25,525' W	58.2	26.1	5.1
CBsh	Geo823610_21	27/01/2019 16:02	CTD	20° 46,755' N	017° 25,547' W	59.2	352.5	5.8
CBsh	Geo823610_15	27/01/2019 10:51	Particle camera	20° 46,635' N	017° 25,555' W	58.5	47.6	6.1
CBsh	Geo823610_12	27/01/2019 09:58	Primary Production	20° 46,715' N	017° 25,645' W	58.7	49.3	7.3
CBsh	Geo823610_12	27/01/2019 09:58	CTD	20° 46,715' N	017° 25,645' W	58.7	49.3	7.3
CBsh	Geo823610_01	27/01/2019 07:58	CTD	20° 46,620' N	017° 25,680' W	59.2	33.1	7.3
CBsh	Geo823606_01	26/01/2019 15:36	Particle camera	20° 47,358' N	017° 31,721' W	76.2	338	2.8
CBsh	Geo823606_02	26/01/2019 15:54	CTD	20° 47,387' N	017° 31,729' W	75.9	327.5	3.3
CBsh	Geo823605_01	26/01/2019 13:36	CTD	20° 47,829' N	017° 37,692' W	93.8	65	5.2
CBsh	Geo823605_02	26/01/2019 13:59	Particle camera	20° 47,955' N	017° 37,767' W	94	69.4	5.4
CBs	Geo823604_02	26/01/2019 12:15	CTD	20° 48,591' N	017° 40,575' W	421.7	52.1	6.8
CBs	Geo823604_01	26/01/2019 11:31	Particle camera	20° 48,522' N	017° 40,589' W	428.8	60.4	6.7
CBs	Geo823603_38	26/01/2019 10:34	Marine snow catcher	20° 49,737' N	017° 43,569' W	687.9	48.9	6.9
CBs	Geo823603_37	26/01/2019 09:36	Particle camera	20° 49,868' N	017° 43,640' W	689.6	48	6.8
CBs	Geo823603_21	25/01/2019 21:59	CTD	20° 47,893' N	017° 43,648' W	636	2.2	8.1
CBs	Geo823603_37	26/01/2019 09:31	Particle camera	20° 49,879' N	017° 43,653' W	690.5	49.1	6.4
CBs	Geo823603_19	25/01/2019 20:31	Particle camera	20° 48,194' N	017° 44,024' W	671.7	9.8	7
CBs	Geo823603_03	25/01/2019 10:00	Primary Production	20° 48,299' N	017° 44,311' W	708.8	55.1	9.8
CBs	Geo823603_03	25/01/2019 10:00	CTD	20° 48,299' N	017° 44,311' W	708.8	55.1	9.8
CBs	Geo823603_31	26/01/2019 06:01	Particle camera	20° 49,292' N	017° 44,378' W	753	45.9	8.3
CBs	Geo823603_15	25/01/2019 17:30	Particle camera	20° 48,661' N	017° 44,454' W	728.7	359.1	4
CBs	Geo823603_28	26/01/2019 04:00	CTD	20° 49,157' N	017° 44,520' W	748.8	40.9	8.3
CBs	Geo823603_01	25/01/2019 09:03	Drifting sediment trap	20° 48,426' N	017° 44,550' W	739.7	38	9.6
CBs	Geo823603_09	25/01/2019 14:02	Particle camera	20° 48,208' N	017° 44,607' W	750.1	68.9	6.1
CBs	Geo823603_12	25/01/2019 16:02	CTD	20° 48,632' N	017° 44,779' W	777.9	19.7	3.3
Transect	Geo823611_01	28/01/2019 15:21	CTD	20° 50,047' N	018° 04,525' W	1318.9	37.3	11.7
Transect	Geo823611_02	28/01/2019 16:49	Particle camera	20° 50,053' N	018° 04,530' W	1570.5	18.7	11.9
Transect	Geo823612_01	28/01/2019 20:28	Particle camera	20° 50,808' N	018° 24,201' W	2098.2	27.4	12.5
Transect	Geo823612_02	28/01/2019 21:17	CTD	20° 50,827' N	018° 24,222' W	2098.9	27.2	13.1
CBeu	Geo823613_02	29/01/2019 08:43	CTD	20° 50,976' N	018° 44,219' W	2692	37.5	12.6
CBeu	Geo823613_01	29/01/2019 08:07	Drifting sediment trap	20° 50,948' N	018° 44,224' W	2693.1	38.8	11.5
CBeu	Geo823613_03	29/01/2019 10:04	Particle camera	20° 51,084' N	018° 44,493' W	2712.4	47.4	12
CBeu	Geo823613_05	29/01/2019 12:43	Marine snow catcher	20° 50,973' N	018° 44,811' W	2711.9	38.9	9.6
CBeu	Geo823613_06	29/01/2019 13:09	Particle camera	20° 50,944' N	018° 44,816' W	2724	53.4	12.7
CBeu	Geo823613_07	29/01/2019 14:04	CTD	20° 50,751' N	018° 45,045' W	2715	36.3	12
CBeu	Geo823613_08	29/01/2019 16:29	Particle camera	20° 50,303' N	018° 47,460' W	2802	30.7	12.6
CBeu	Geo823613_09	29/01/2019 20:30	Particle camera	20° 51,155' N	018° 48,735' W	2862.5	33.8	11.4
CBeu	Geo823613_10	29/01/2019 21:24	CTD	20° 51,260' N	018° 48,830' W	2847.8	41.3	12
CBeu	Geo823613_11	30/01/2019 07:02	Particle camera	20° 50,795' N	018° 53,648' W	3121.2	39.2	11.2
CBmeso	Geo823601_12	21/01/2019 12:52	Marine snow catcher	21° 12,316' N	020° 51,919' W	4148.2	70.6	9.9
CBmeso	Geo823601_15	21/01/2019 14:06	Particle camera	21° 12,152' N	020° 52,123' W	4149.6	76	10.3
CBmeso	Geo823601_07	21/01/2019 10:00	CTD	21° 12,530' N	020° 52,229' W	4169.6	63.4	9.3
CBmeso	Geo823601_18	21/01/2019 16:01	Primary Production	21° 11,510' N	020° 52,282' W	4152.1	59	9.6
CBmeso	Geo823601_18	21/01/2019 16:01	CTD	21° 11,510' N	020° 52,282' W	4152.1	59	9.6
CBmeso	Geo823601_06	21/01/2019 09:06	Drifting sediment trap	21° 12,561' N	020° 52,499' W	4153.4	73.2	10.8
CBmeso	Geo823601_02	20/01/2019 18:52	Particle camera	21° 12,604' N	020° 52,523' W	4154.1	57.4	12.1
CBmeso	Geo823601_03	20/01/2019 18:59	Particle camera	21° 12,597' N	020° 52,526' W	4153.6	58.8	11.8
CBmeso	Geo823601_01	20/01/2019 17:03	CTD	21° 12,618' N	020° 52,532' W	4151.8	57.7	9.3
CBmeso	Geo823601_20	21/01/2019 17:32	Particle camera	21° 11,016' N	020° 52,734' W	4151.1	57.3	9.4
CBmeso	Geo823601_43	22/01/2019 09:22	Particle camera	21° 07,034' N	020° 53,282' W	4224.7	77.3	11.9
CBmeso	Geo823601_24	21/01/2019 20:32	Particle camera	21° 10,092' N	020° 53,489' W	4153.3	68.5	9.1
CBmeso	Geo823601_37	22/01/2019 06:04	Particle camera	21° 08,906' N	020° 53,556' W	4148.6	67	12
CBmeso	Geo823601_35	22/01/2019 04:02	CTD	21° 09,250' N	020° 53,738' W	4159.7	60.2	9
CBmeso	Geo823601_26	21/01/2019 22:00	CTD	21° 09,794' N	020° 53,818' W	4155	49.6	10.9
CBmeso	Geo823601_26	21/01/2019 22:06	CTD	21° 09,787' N	020° 53,826' W	4152.8	58.2	11.3

Table S2. Sediment characteristics and inputs for O2 flux calculation. See Ahmerkamp et al. (2017) for methodological details. Sampling stations were located on the shallow shelf in the CB_{sh} region.

Parameter	Unit	GeoB23602_02	GeoB23610_14
Median grain size	µm	687.52	183
Water temperature	°C	17	16
Water depth	m	29	59
O2 penetration depth (measured)	mm	8.4	0.1
Permeability	m^2	3.43E-10	2.43E-11
Porosity	-	0.4	0.4
Bed form height	m	0.02	0.02
Bedform Wavelength	m	0.337	0.089
Bottom water velocity, estimated from ADP	m/s	0.2	0.08
Bottom water O2 concentration	µM	200	105

Table S3. Carbon specific respiration rates from aggregate associated microbes from this study and the literature. To avoid measuring biases, listed values exclusively include measurements that were performed within an upward directed flow and with an oxygen microsensor.

Study	Temperature °C	C specific resp. rate d^{-1}	st.dev d^{-1}
Iversen et al. 2010	20	0.13	0.07
Iversen & Ploug 2010	15	0.13	0.09
Iversen & Ploug 2010	15	0.13	0.13
Iversen & Ploug 2010	15	0.12	0.07
Iversen et al. 2013	15	0.12	0.03
Iversen et al. 2013	4	0.03	0.01
Ploug 1999	17	0.1	
Ploug & Grossart 2000	16	0.08	0.03
Iversen & Robert 2015	15	0.14	0.06
Iversen et al. 2016	3	0.04	
Belcher et al. 2016	4	0.01	0.07
This study	21	0.11	0.12

Table S4. Particulate organic carbon (POC) export fluxes obtained from drifting sediment trap deployments between 2012 – 2019 off the coast of Cape Blanc. Cruises indicate the respective research expedition where fluxes were measured, with "POS" indicating research vessel *Poseidon* and "M" indicating research vessel *Meteor*. Longitude and Latitude represents the position where a given drifting sediment trap was deployed in the water. Drifting sediment traps consisted of an array of 2 – 3 individual traps and the listed depth shows the sampling depth at which individual traps collected POC fluxes within an array. Trap ID indicates respective drifting trap arrays. Calculated POC fluxes are derived according to Lutz et al. 2002 and assume the vertical settling of export fluxes measured at the uppermost trap (100 m - 150 m) to 200 m and 400 m within a respective drifttrap array. Delta POC flux is the measured POC flux, divided by the calculated POC flux.

Cruise	Deployment date	Longitude (degrees)	Latitude (degrees)	Drifting trap ID	Depth (m)	Measured POC flux (mg m^{-2} day^{-1})	Calculated POC flux (mg m^{-2} day^{-1})	Delta POC flux
POS425	22/01/2012	-18.738	20.781	DF03	100m	334.0		
POS425	22/01/2012	-18.738	20.781	DF03	400m	83.9	191.2	0.44
POS425	24/01/2012	-18.715	20.721	DF04	100m	375.9		
POS425	24/01/2012	-18.715	20.721	DF04	400m	118.6	215.1	0.55
POS445	26/01/2013	-18.728	20.606	DF05	100m	133.0		
POS445	26/01/2013	-18.728	20.606	DF05	200m	133.0	109.6	1.21
POS445	26/01/2013	-18.728	20.606	DF05	400m	90.1	76.7	1.17
POS445	27/01/2013	-18.741	20.727	DF06	100m	123.6		
POS445	27/01/2013	-18.741	20.727	DF06	200m	141.3	101.7	1.39
POS445	27/01/2013	-18.741	20.727	DF06	400m	49.5	71.1	0.70
POS464	06/02/2014	-20.832	21.261	DF07	150m	91.6		
POS464	06/02/2014	-20.832	21.261	DF07	200m	78.0	85.9	0.91
POS464	06/02/2014	-20.832	21.261	DF07	400m	100.3	67.7	1.48
POS464	08/02/2014	-19.432	20.926	DF08	100m	173.6		
POS464	08/02/2014	-19.432	20.926	DF08	200m	108.3	151.3	0.72
POS464	08/02/2014	-19.432	20.926	DF08	400m	51.7	117.6	0.44
POS464	11/02/2014	-18.742	20.800	DF09	100m	156.5		
POS464	11/02/2014	-18.742	20.800	DF09	200m	192.1	130.1	1.48
POS464	11/02/2014	-18.742	20.800	DF09	400m	97.6	91.9	1.06
POS464	14/02/2014	-17.987	20.618	DF10	100m	335.3		
POS464	14/02/2014	-17.987	20.618	DF10	200m	362.4	279.3	1.30
POS464	14/02/2014	-17.987	20.618	DF10	400m	224.5	200.1	1.12
POS481	23/02/2015	-18.725	20.797	DF11	150m	163.0		
POS481	23/02/2015	-18.725	20.797	DF11	200m	149.3	148.3	1.01
POS481	23/02/2015	-18.725	20.797	DF11	400m	85.8	104.6	0.82
POS481	26/02/2015	-18.326	20.666	DF12	150m	161.4		
POS481	26/02/2015	-18.326	20.666	DF12	200m	148.2	147.0	1.01
POS481	26/02/2015	-18.326	20.666	DF12	400m	111.0	104.4	1.06
POS495	22/02/2016	-18.725	20.888	DF13	100m	107.0		
POS495	22/02/2016	-18.725	20.888	DF13	200m	121.1	88.8	1.36
POS495	22/02/2016	-18.725	20.888	DF13	400m	62.7	62.5	1.00
POS495	25/02/2016	-18.362	20.637	DF14	100m	152.7		
POS495	25/02/2016	-18.362	20.637	DF14	200m	104.3	126.7	0.82
POS495	25/02/2016	-18.362	20.637	DF14	400m	103.5	89.7	1.15
POS508	26/01/2017	-20.868	21.212	DF15	100m	114.1		
POS508	26/01/2017	-20.868	21.212	DF15	200m	50.9	99.7	0.51
POS508	26/01/2017	-20.868	21.212	DF15	400m	39.7	77.5	0.51
POS508	29/01/2017	-18.491	20.835	DF16	100m	96.4		
POS508	29/01/2017	-18.491	20.835	DF16	200m	110.4	80.1	1.38
POS508	29/01/2017	-18.491	20.835	DF16	400m	130.0	57.1	2.28
POS508	02/02/2017	-18.604	20.853	DF17	100m	145.3		
POS508	02/02/2017	-18.604	20.853	DF17	200m	109.6	142.2	0.77
POS508	02/02/2017	-18.604	20.853	DF17	400m	93.9	85.1	1.10
M140	28/08/2017	-20.833	21.269	DF18	100m	68.7		
M140	28/08/2017	-20.833	21.269	DF18	200m	62.5	59.6	1.05
M140	28/08/2017	-20.833	21.269	DF18	400m	33.9	45.9	0.74
M140	31/08/2017	-18.783	20.886	DF19	100m	73.9		
M140	31/08/2017	-18.783	20.886	DF19	200m	74.6	61.0	1.22
M140	31/08/2017	-18.783	20.886	DF19	400m	72.0	42.9	1.68
POS531	21/01/2019	-20.875	21.209	DF20	100m	79.1		
POS531	21/01/2019	-20.875	21.209	DF20	200m	73.7	68.7	1.07
POS531	21/01/2019	-20.875	21.209	DF20	400m	54.1	53.3	1.02
POS531	25/01/2019	-17.742	20.807	DF21	100m	100.8		
POS531	25/01/2019	-17.742	20.807	DF21	200m	110.1	83.9	1.31
POS531	25/01/2019	-17.742	20.807	DF21	400m	124.0	59.7	2.08
POS531	29/01/2019	-18.737	20.849	DF22	100m	77.3		
POS531	29/01/2019	-18.737	20.849	DF22	200m	90.1	67.9	1.33
POS531	29/01/2019	-18.737	20.849	DF22	400m	98.4	52.9	1.86

Supplementary information for manuscript III

Release of ballast material during sea-ice melt enhances carbon export in the Arctic Ocean

Steffen Swoboda[1*], Thomas Krumpen[2], Eva-Maria Nöthig[2], Katja Metfies[2], Simon Ramondenc[1,2], Jutta Wollenburg[2], Kirsten Fahl[2], Ilka Peeken[2], Morten H. Iversen[1,2*]

*Corresponding author

Contents:

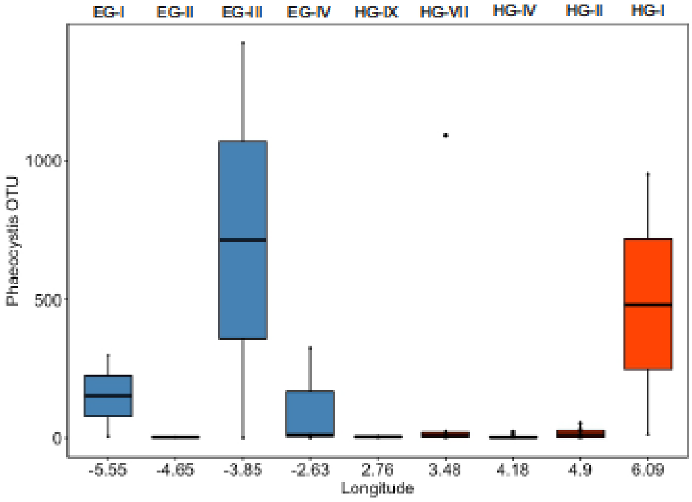

Fig. S1. Sequence abundance of *Phaeocystis* OTUs collected from sediment samples across an east-west transect in the Fram Strait. Blue colour indicates the westerly sample stations with regular sea ice cover, while red indicates easterly samples stations with rare sea ice coverage. Labels above the plot panel indicate the respective sample station.

Research expedition	Mooring location		Deployment depth (m)	Sampling interval		POC	Terrigenous marker	Phaeocystis	Ice edge distance	Ice concentration
	Latitude N	Longitude W		date start	date end	mg m^{-2} d^{-1}	µg m^{-2} d^{-1}	OTU	km	%
PS57	79°01.7	04°20.86	280	31/08/2000	15/09/2000	26.1	88.8	0	1	76
				15/09/2000	30/09/2000	12.1	23.3	NA	58	0
				14/03/2001	29/03/2001	9.1	6.5	0	41	0
				29/03/2001	14/04/2001	8.9	14.3	0	24	5
				14/04/2001	29/04/2001	4.8	4.6	0	43	0
				29/04/2001	14/05/2001	5.5	3.3	0	51	0
				14/05/2001	29/05/2001	3.4	1.8	0	87	0
				29/05/2001	14/06/2001	3.7	6.2	0	50	0
				14/06/2001	29/06/2001	2.1	6.9	0	52	1
				29/06/2001	14/07/2001	3.3	2.6	0	13	10
PS59	79°01.5	04°21,3	260	14/08/2001	31/08/2001	17.7	22.9	0	38	0
				31/08/2001	15/09/2001	6.1	4.9	0	83	0
				15/09/2001	30/09/2001	7.8	8.3	0	102	0
PS62	79°01.04	04°19.77	260	14/08/2002	29/08/2002	7.3	15.2	NA	144	0
				29/08/2002	13/09/2002	7.0	13.8	NA	138	0
				13/09/2002	28/09/2002	8.6	18.6	NA	102	0
				28/09/2002	13/10/2002	2.5	6.6	NA	71	0
				12/03/2003	27/03/2003	3.1	1.3	NA	54	0
				27/03/2003	11/04/2003	6.8	1.7	NA	22	7
				11/04/2003	26/04/2003	7.5	3.3	NA	16	9
PS64	78°59.95	04°27.44	340	26/04/2003	11/05/2003	15.3	10.9	40	12	10
				11/05/2003	26/05/2003	7.3	5.2	NA	18	7
				26/05/2003	10/06/2003	12.5	9.0	NA	3	27
PS66	79°00.99	04°20.62	280	15/07/2004	22/07/2004	1.9	2.0	NA	52	0
				22/07/2004	29/07/2004	7.2	3.7	NA	50	0
				29/07/2004	05/08/2004	49.4	67.9	58	105	0
				05/08/2004	15/08/2004	42.0	31.7	30	216	0
				15/08/2004	31/08/2004	13.9	6.1	NA	271	0
				31/08/2004	15/09/2004	12.3	3.5	NA	246	0
				15/09/2004	30/09/2004	6.5	3.0	NA	175	0

				28/02/2005	31/03/2005	7.6	3.5	149	54	0
				31/03/2005	15/04/2005	4.8	2.6	NA	69	0
				15/04/2005	30/04/2005	3.6	1.6	NA	35	0
				30/04/2005	15/05/2005	3.1	1.0	NA	69	0
				15/05/2005	31/05/2005	2.2	1.0	NA	69	0
				31/05/2005	15/06/2005	3.7	1.7	NA	49	0
PS68	79°01.00	04°20,62	179	25/08/2005	05/09/2005	9.6	3.5	NA	84	0
				05/09/2005	25/09/2005	15.9	6.4	15	61	0
				25/09/2005	15/10/2005	8.1	5.1	NA	24	4
				28/02/2006	30/03/2006	4.7	1.6	0	72	0
				30/03/2006	14/04/2006	2.8	0.7	0	66	0
				14/04/2006	29/04/2006	6.5	2.0	0	65	0
				29/04/2006	14/05/2006	13.5	4.9	19	39	2
				14/05/2006	29/05/2006	5.6	2.8	0	78	0
				29/05/2006	13/06/2006	11.4	7.2	11	56	0
				13/06/2006	28/06/2006	23.9	13.7	0	94	0
				28/06/2006	13/07/2006	0.8	0.3	0	60	0
				13/07/2006	20/07/2006	1.9	1.4	0	65	0
MSM2	79°00,82	04° 20.5	230	26/08/2006	01/09/2006	1.0	0.8	0	94	0
				01/09/2006	07/09/2006	1.2	0.6	0	73	0
				07/09/2006	15/09/2006	3.0	0.6	0	79	0
				15/09/2006	22/09/2006	4.7	0.6	16	75	0
				22/09/2006	30/09/2006	3.3	0.6	0	50	0
				28/02/2007	15/03/2007	2.5	0.5	NA	43	0
				15/03/2007	31/03/2007	16.6	5.2	NA	49	0
				31/03/2007	15/04/2007	17.8	3.0	NA	36	1
				15/04/2007	30/04/2007	33.3	8.8	22	14	8
				30/04/2007	10/05/2007	50.3	0.8	NA	24	5
				10/05/2007	20/05/2007	7.1	1.5	NA	42	0
				20/05/2007	06/06/2007	2.4	0.4	NA	16	8
				06/06/2007	20/06/2007	4.4	1.7	NA	26	5
PS70	79°00,82	04° 20,62	190	23/07/2007	15/08/2007	6.3	1.8	NA	55	0
				15/08/2007	31/08/2007	15.6	7.7	74	19	6
				31/08/2007	10/09/2007	4.6	0.7	NA	30	2
				10/09/2007	20/09/2007	1.5	0.1	NA	38	1

				20/09/2007	30/09/2007	3.4	0.9	NA	21	5
				29/02/2008	31/03/2008	5.1	0.4	NA	53	0
				31/03/2008	15/04/2008	23.5	1.3	103	33	0
				15/04/2008	30/04/2008	11.0	0.2	NA	1	29
				30/04/2008	10/05/2008	14.5	0.0	NA	0	43
				10/05/2008	20/05/2008	7.0	1.3	NA	2	30
				20/05/2008	31/05/2008	10.1	4.2	NA	0	38
				31/05/2008	15/06/2008	8.9	1.0	NA	0	36
				15/06/2008	30/06/2008	2.4	0.6	NA	1	43
PS72	79°00,4	04° 20,0	196	17/07/2008	31/07/2008	5.6	0.7	NA	7	17
				31/07/2008	10/08/2008	16.9	2.8	NA	2	20
				10/08/2008	20/08/2008	12.9	5.8	NA	15	6
				20/08/2008	31/08/2008	30.0	39.6	101	19	4
				31/08/2008	15/09/2008	8.5	3.5	NA	28	0
				15/09/2008	30/09/2008	5.3	1.9	NA	31	1
				28/02/2009	31/03/2009	9.3	5.0	NA	52	0
				31/03/2009	15/04/2009	22.7	7.4	84	20	3
				15/04/2009	30/04/2009	20.3	21.2	115	0	31
				30/04/2009	15/05/2009	12.1	3.7	NA	24	4
				15/05/2009	31/05/2009	4.6	1.6	NA	11	12
				31/05/2009	15/06/2009	9.3	4.7	NA	17	9
				15/06/2009	30/06/2009	4.3	1.0	NA	29	2
				30/06/2009	15/07/2009	3.6	1.8	NA	13	10
				15/07/2009	22/07/2009	4.5	NA	NA	21	3
PS74	79°00,43	04° 20,05	80	20/07/2009	31/07/2009	25.1	NA	NA	44	0
				31/07/2009	10/08/2009	42.2	NA	46	36	0
				10/08/2009	20/08/2009	46.7	NA	230	39	0
				20/08/2009	31/08/2009	19.5	NA	NA	59	0
				31/08/2009	15/09/2009	16.7	NA	NA	68	0
				15/09/2009	30/09/2009	8.0	NA	NA	85	0
				28/02/2010	15/03/2010	4.1	NA	NA	75	0
				15/03/2010	31/03/2010	1.9	NA	NA	54	0
				31/03/2010	15/04/2010	11.8	NA	NA	91	0
				15/04/2010	30/04/2010	11.8	NA	NA	65	0
				30/04/2010	15/05/2010	10.1	NA	NA	67	0

				15/05/2010	31/05/2010	26.0	NA	NA	77	0
				31/05/2010	15/06/2010	22.4	NA	NA	60	0
				15/06/2010	30/06/2010	29.3	NA	27	48	0
PS76	79° 00.41	04°19.90	200	10/07/2010	20/07/2010	18.2	2.3	NA	59	0
				20/07/2010	31/07/2010	11.0	0.9	NA	83	0
				31/07/2010	15/08/2010	7.7	2.3	NA	92	0
				15/08/2010	31/08/2010	8.2	0.9	NA	76	0
				31/08/2010	15/09/2010	8.7	0.9	NA	41	0
				15/09/2010	30/09/2010	6.0	0.4	NA	75	0
				28/02/2011	15/03/2011	3.5	0.6	NA	68	0
				15/03/2011	31/03/2011	7.8	1.5	NA	31	3
				31/03/2011	15/04/2011	9.3	3.1	NA	17	7
				15/04/2011	30/04/2011	8.2	0.7	NA	53	0
				30/04/2011	10/05/2011	10.0	0.9	45	40	0
				10/05/2011	20/05/2011	9.9	1.6	NA	31	1
				20/05/2011	31/05/2011	5.8	0.4	NA	58	0
				31/05/2011	15/06/2011	4.4	0.3	NA	25	3
				15/06/2011	30/06/2011	5.6	0.4	NA	11	9
PS78	79° 00.42	04°19.90	200	01/08/2011	15/08/2011	13.9	NA	NA	39	1
				15/08/2011	31/08/2011	11.5	NA	NA	97	0
				31/08/2011	10/09/2011	17.4	NA	315	109	0
				10/09/2011	30/09/2011	7.6	NA	NA	108	0
				28/02/2012	31/03/2012	5.7	NA	0	82	0
				31/03/2012	15/04/2012	7.8	NA	0	66	0
				15/04/2012	30/04/2012	18.0	NA	0	45	0
				30/04/2012	10/05/2012	24.2	NA	8	36	0
				10/05/2012	20/05/2012	7.5	NA	0	71	0
				20/05/2012	31/05/2012	4.4	NA	0	62	0
				31/05/2012	10/06/2012	19.0	NA	0	35	0
				10/06/2012	20/06/2012	9.8	NA	0	19	6
				20/06/2012	30/06/2012	7.4	NA	0	8	16
				30/06/2012	15/07/2012	3.5	NA	8	58	0
PS80	79° 00.43	04°19.78	205	29/07/2012	15/08/2012	5.9	1.3	49	30	1
				15/08/2012	31/08/2012	13.1	2.8	151	42	4
				31/08/2012	10/09/2012	15.8	1.9	43	84	0

10/09/2012	20/09/2012	12.5	8.8	0	72	0
20/09/2012	30/09/2012	9.9	3.8	NA	61	0
28/02/2013	31/03/2013	2.1	0.7	NA	44	0
31/03/2013	15/04/2013	7.3	3.0	NA	24	3
15/04/2013	30/04/2013	20.6	6.6	NA	29	1
30/04/2013	10/05/2013	18.7	10.9	NA	33	0
10/05/2013	20/05/2013	2.7	0.3	NA	23	0
20/05/2013	31/05/2013	2.8	0.6	NA	40	2
31/05/2013	10/06/2013	3.1	1.0	NA	16	12
10/06/2013	20/06/2013	2.0	0.2	NA	0	33
20/06/2013	30/06/2013	3.0	1.0	NA	1	26

Table S1. List of particulate organic carbon (POC), terrigenous marker and Phaeocystis operational taxonomic unit (OTU) fluxes obtained from moored sediment trap deployments at station HG-IV in Fram Strait. Research expeditions indicate the respective expedition where the mooring was deployed, with "PS" indicating research vessel *Polarstern* and "MSM" indicating research vessel *Maria S. Merian*. The mooring location is shown by the degrees of latitude and longitude upon deployment. Sediment traps consist of a rotating carousel of 20 sample cups which individually collected export fluxes for a designated time period. The start and end of each collection period is listed as the date start and date end respectively. Values of the distance of the sea ice edge to the mooring location are listed for each individual sampling interval. Values of sea ice cover above the mooring location are listed for each individual sampling interval.

Station	Year	Longitude E & W	Latitude N	*Phaeocystis* spp. OTU
EG1	2014	-5.55	79.00	298
EG1	2016	-5.55	79.00	5
EG2	2014	-4.65	79.00	2
EG3	2014	-3.85	79.00	1425
EG3	2016	-3.85	79.00	0
EG4	2014	-2.63	79.00	10
EG4	2015	-2.63	79.00	325
EG4	2016	-2.63	79.00	0
HG9	2003	2.76	79.14	1
HG9	2004	2.76	79.14	4
HG9	2015	2.76	79.14	5
HG7	2004	3.48	79.06	1092
HG7	2006	3.48	79.06	8
HG7	2007	3.48	79.06	15
HG7	2008	3.48	79.06	5
HG7	2011	3.48	79.06	22
HG7	2012	3.48	79.06	2
HG7	2016	3.48	79.06	1
HG4	2004	4.18	79.07	1
HG4	2007	4.18	79.07	20
HG4	2008	4.18	79.07	9
HG4	2009	4.18	79.07	1
HG4	2010	4.18	79.07	1
HG4	2012	4.18	79.07	4
HG4	2013	4.18	79.07	1
HG4	2014	4.18	79.07	4
HG4	2015	4.18	79.07	0
HG4	2016	4.18	79.07	0
HG2	2003	4.90	79.13	2
HG2	2005	4.90	79.13	30
HG2	2005	4.90	79.13	14
HG2	2006	4.90	79.13	24
HG2	2008	4.90	79.13	2
HG2	2009	4.90	79.13	10
HG2	2010	4.90	79.13	3
HG2	2011	4.90	79.13	36
HG2	2013	4.90	79.13	1
HG2	2014	4.90	79.13	3
HG2	2015	4.90	79.13	14
HG2	2016	4.90	79.13	54
HG1	2004	6.09	79.13	12
HG1	2015	6.09	79.13	951

Table S2. List of OTUs from *Phaeocystis* spp. measured in sediment samples derived from an east-west transect across Fram Strait. The station name is listed along with the location in decimal degrees longitude and latitude and the year samples where obtained.

Gypsum ballasting size	Control		Ballasted		Time
	Settling velocity (m day^{-1})	n	Settling velocity (m day^{-1})	n	
>63 µm	18 ± 45	9	173 ± 185	14	3h
>63 µm	22 ± 39	7	131 ± 158	11	5h
>63 µm	12 ± 29	7	153 ± 141	10	7h
>63 µm	21 ± 27	8	174 ± 148	11	10h
>63 µm	5 ± 49	8	129 ± 106	8	15h
≥30 µm - ≤63 µm	193 ± 73	9	274 ± 114	5	3h
≥30 µm - ≤63 µm	174 ± 67	11	234 ± 117	8	5h
≥30 µm - ≤63 µm	164 ± 80	8	146 ± 67	8	7h
≥30 µm - ≤63 µm	159 ± 85	8	146 ± 111	5	10h
≥30 µm - ≤63 µm	202 ± 87	6	152 ± 93	6	15h

Table S3. List of measured particle settling velocities from control treatments and gypsum ballasted treatments during a ballasting experiment. The gypsum ballasting size indicates the size range of gypsum crystals used for the ballasting experiments. Settling velocities show the average settling velocity and standard deviation measured over the course of the experiments, while n indicates the number of particles measured.

Erklärung

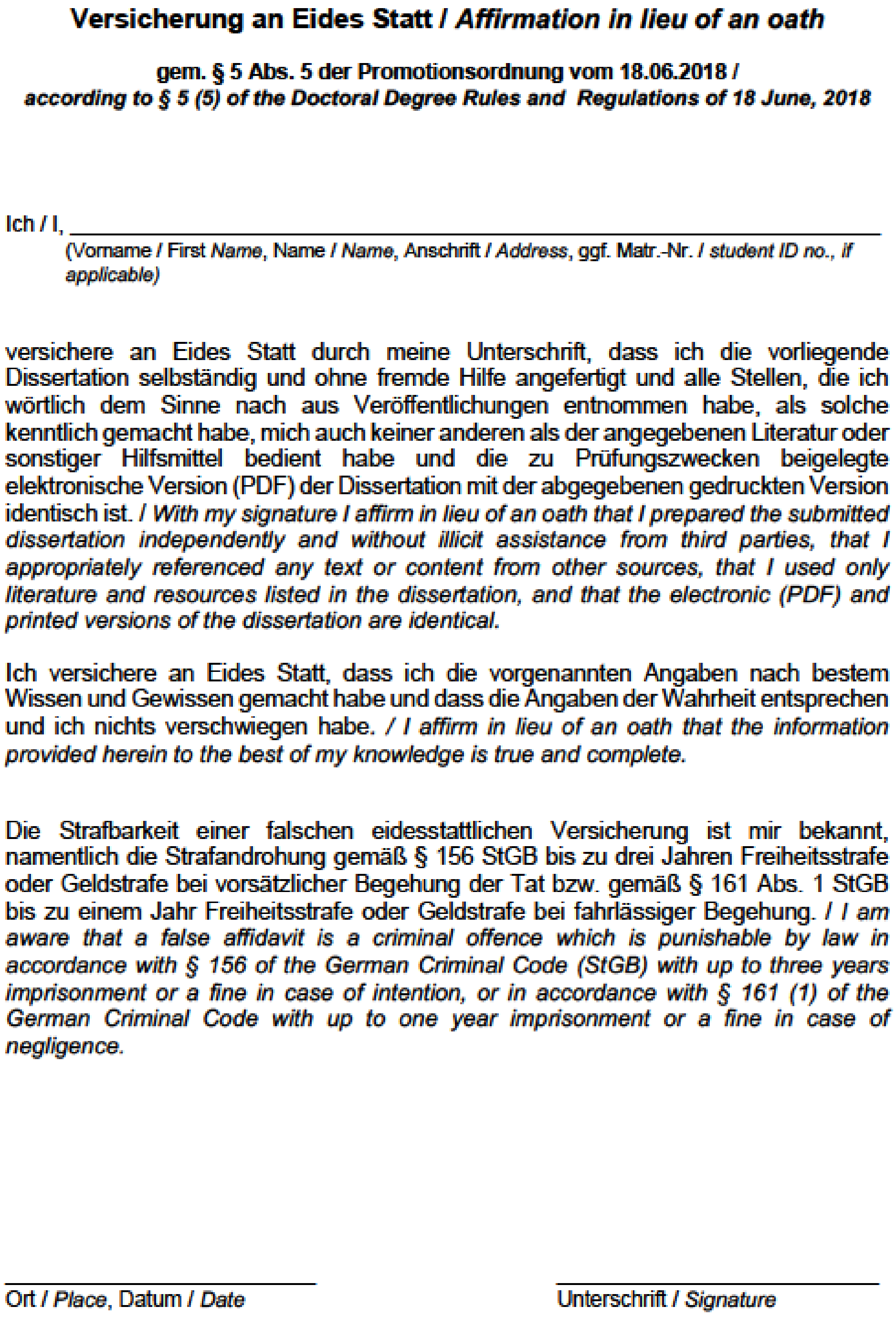

Versicherung an Eides Statt / *Affirmation in lieu of an oath*

gem. § 5 Abs. 5 der Promotionsordnung vom 18.06.2018 /
according to § 5 (5) of the Doctoral Degree Rules and Regulations of 18 June, 2018

Ich / I, ____
(Vorname / *First Name*, Name / *Name*, Anschrift / *Address*, ggf. Matr.-Nr. / *student ID no., if applicable)*

versichere an Eides Statt durch meine Unterschrift, dass ich die vorliegende Dissertation selbständig und ohne fremde Hilfe angefertigt und alle Stellen, die ich wörtlich dem Sinne nach aus Veröffentlichungen entnommen habe, als solche kenntlich gemacht habe, mich auch keiner anderen als der angegebenen Literatur oder sonstiger Hilfsmittel bedient habe und die zu Prüfungszwecken beigelegte elektronische Version (PDF) der Dissertation mit der abgegebenen gedruckten Version identisch ist. / *With my signature I affirm in lieu of an oath that I prepared the submitted dissertation independently and without illicit assistance from third parties, that I appropriately referenced any text or content from other sources, that I used only literature and resources listed in the dissertation, and that the electronic (PDF) and printed versions of the dissertation are identical.*

Ich versichere an Eides Statt, dass ich die vorgenannten Angaben nach bestem Wissen und Gewissen gemacht habe und dass die Angaben der Wahrheit entsprechen und ich nichts verschwiegen habe. / *I affirm in lieu of an oath that the information provided herein to the best of my knowledge is true and complete.*

Die Strafbarkeit einer falschen eidesstattlichen Versicherung ist mir bekannt, namentlich die Strafandrohung gemäß § 156 StGB bis zu drei Jahren Freiheitsstrafe oder Geldstrafe bei vorsätzlicher Begehung der Tat bzw. gemäß § 161 Abs. 1 StGB bis zu einem Jahr Freiheitsstrafe oder Geldstrafe bei fahrlässiger Begehung. / *I am aware that a false affidavit is a criminal offence which is punishable by law in accordance with § 156 of the German Criminal Code (StGB) with up to three years imprisonment or a fine in case of intention, or in accordance with § 161 (1) of the German Criminal Code with up to one year imprisonment or a fine in case of negligence.*

____
Ort / *Place*, Datum / *Date*

____
Unterschrift / *Signature*